Structure and Surface Energy of Blend Films of Polystyrene and Polybutadiene

Mai Salem Y Ibrahim

Thesis submitted for the degree of Doctor of Philosophy

School of Engineering

Newcastle University

September 2024

Abstract

This thesis presents data on the structure and morphology of spin-coated films of different blends of polystyrene (PS) and polybutadiene (PB). It is shown that there is a complex interrelationship between surface tension, molar mass, and film roughness that makes predicting and understanding the final morphology difficult. Both depth profiling (time-of-flight elastic recoil detection and Rutherford backscattering, as well as some cross-sectional transmission electron microscopy) and surface imaging (atomic force, optical, X-ray photoelectron, and electron microscopy) have been used alongside contact angle measurements to elucidate the three-dimensional nature and properties of these films.

Spin coating is a widely employed technique for producing uniform thin films, prized for its simplicity, speed, and cost-effectiveness. It allows for precise control over film thickness by adjusting parameters such as spin speed and solution viscosity. This method is compatible with a range of materials, enhancing its versatility for both research and industrial applications. Furthermore, spin coating yields smooth and homogeneous films, making it ideal for optical, electronic, and surface-related studies.

The polystyrene/polybutadiene (PS/PB) blend offers significant advantages for thin film fabrication, owing to its tunable phase separation behaviour that enables controlled microstructure development. The immiscibility of the two polymers facilitates the creation of well-defined morphologies, which can be tailored for specific applications. Moreover, the mechanical flexibility of PB effectively complements the rigidity of PS, resulting in films with well-balanced mechanical properties. This blend also demonstrates favourable film-forming characteristics during solution-based processes, such as spin coating, thereby enhancing reproducibility and uniformity.

The study found that surface segregation cannot be predicted solely based on surface energy. Both polystyrene (PS) and polybutylene (BP) tend to migrate to the air or substrate interface, depending on their molar mass. Notably, polystyrene with a lower molar mass shows a preference for the surface.

Acknowledgements

I would like to express my sincere gratitude to my primary supervisor, Prof. Mark Geoghegan, for his unwavering patience, encouragement, optimism, and invaluable support throughout the past seven years. I am truly grateful for his exceptional guidance and thought-provoking discussions, which have enlightened me on the significance of clear and organised thinking in research. I am also appreciative of his enduring confidence in me, beginning with our first correspondence in April 2015.

I am thankful to Prof. Sharon Velasquez Orta, my second supervisor. I also appreciate Dr. Marloes Peeters, my previous second supervisor, and Prof. Faten Al-Hazmi, my local supervisor in Jeddah.

I am grateful to Dr Sudhakar Ganta from David Fultion's lab at the School of Natural and Environmental Sciences, Newcastle University, for conducting Gel Permeation Chromatography (GPC) tests on two different polybutadienes used in this study.

I am very thankful to Dr. Matthew German for taking AFM measurements and showing me how to use the software to measure roughness.

I would also like to thank Dr Robert Crapnell, MRSC FHEA, and Dr Hayley Andrews, Faculty of Science and Engineering, Manchester Metropolitan University, Chester Street, M1 5GD, United Kingdom, for conducting SEM measurements.

I am very grateful to Tracey Davey for her work performing the TEM measurements I have shown in Figures (4.38, A and B) and the unit of BBSRC grant code BB/R013942/1.

I also thank Chris Hill, Electron Microscopy Officer at the cryo-electron Microscopy Facility at Sheffield University, England, for taking TEM measurements for one film, Figures (4.54, A and B), training me in microtoming, showing me how to put my samples in a TEM, and taking the image for it at the University of Sheffield.

I thank Dr Jake Sheriff, School of Engineering, Newcastle University, for taking XPS measurements.

I am deeply grateful to Dr Pierre Couture, Dr Callum McAleese, Dr Matthew Sharpe, and Dr Vladimir Palitsin of the Surrey Ion Beam Centre at the University of Surrey, Guildford, Surrey GU2 7XH, United Kingdom, for carrying out RBS and ToF-ERD measurements.

I want to thank my colleagues Joshua Cunday, Hosni Atout, Rachel Lee, and Emily Hall.

I am grateful to my tutor, Professor Jamie Hobbs, from the Physics department at The University of Sheffield.

I am very grateful to Dr Latifah Alfhaid for her continued support and for checking on me.

I thank Dr Pankaj Singla for handling my SEM samples, Jake McClements for giving the spin coater, Prof. Kristen for giving some glycerol and Steven Edmond for IT support.

I am grateful to the people in Saudi Arabia for their help: Prof. Zain Yamani, Dr Ahmad Shaban, Prof. Mohammed Eeda, Mr Talal, and Mrs. Ola Alahmari.

I extend my sincere thanks to King Abdul-Aziz University and the University of Jeddah for sponsoring my research, Prof. Ammar Ameen, Prof. Haifa Al-Ganas, Dr. Ahlam, Dr. Nesreen Alahmadi, Umaimah Olagi, Amal Almalki, Aishah Aljedani, Dena Tulbah, Sultana Alaboud, Hadeel Toonsi, and Mr. Mazen.

I am also grateful for the opportunity to travel and present my work through a poster at the Physical Aspects of Polymer Science meeting in London in 2022 and give an oral presentation at the fall meeting of the American Chemical Society in San Francisco in 2023.

I want to express my gratitude to my father for teaching me the values of patience, commitment, hard work, and perseverance. I am thankful for the great support of my children, who have always placed their trust in me and made me feel that they are standing by my side. I appreciate my husband’s patience and assistance, and I am also grateful to my siblings for their enduring belief in me and their support.

Abbreviations

PS	polystyrene
PB	polybutadiene
SBR	styrene-butadiene rubber
HIPS	high-impact polystyrene
PMMA	poly(methylmethacrylate)
PCBM	[6,6]-phenyl C_{61}-butyric acid methyl ester
DPPDTT	poly[2,5-(2-octyldodecyl)-3,6-diketopyrrolopyrrole-*alt*-5,5-(2,5-di(thien-2-yl)thieno [3,2-b]thiophene)]
NRA	nuclear reaction analysis
NR	neutron reflectometry
TEM	transmission electron microscopy
PANI	polyaniline
CSA	camphorsulfonic acid
PU	polyurethane
PI	polyisoprene
PT	polythiophene
THF	tetrahydrofuran
MEK	methyl ethyl ketone
d-PS	deuterated polystyrene
PVA	polyvinyl acetate
PS/PtBA	poly(tert-butyl acrylate)
3D	three-dimensional
S	entropy
k	Boltzmann constant
Ω	number of ways to arrange molecules on the lattice
n	the number of occupied lattice sites
ϕ_A and ϕ_B	volume fractions of components A and B
N_A and N_B	the numbers of lattice sites filled by each particular molecule
u_{AA}, u_{AB}, and u_{BB}	interaction energies between neighbouring lattice sites filled by two components
U_A or U_B	the average pairwise interaction energy of one component A or B monomer on a lattice site with its neighbouring monomer on one of the neighbouring sites

χ	Flory – Huggins interaction parameter
UCST	upper critical solution temperature
LCST	lower critical solution temperature
R	It characterises the size of the domains and their average distance between them
w	It characterises the width of the interface between the domains
λ_{max}	the fastest growing wavelength
G	Gibbs free energy of the total system
T	temperature
P	pressure
θ	contact angle
γ_S	surface tension between the solid and the vapour
γ_{SL}	interfacial tension between the solid and the liquid droplet
γ_{LV}	surface tension between the liquid and the vapour
β	Neumann's constant
PαMS	poly(α –methyl styrene)
AFM	atomic force microscopy
SEM	scanning electron microscopy
XPS	X-ray photoelectron microscopy
IBM	Ion beam microscopy
IBA	ion beam analysis
RBS	Rutherford backscattering
ToF-ERD	Time of Flight – Elastic Recoil Detection
Os	osmium
GPC	Gel Permeation Chromatography
M.W. or M_W	Molecular Weight

M_n	Molecular Number
PDI	polydispersity
SEC	Size Exclusion Chromatography
Si	silicon
OsO_4	osmium tetroxide
RuO_4	Ruthenium tetroxide
FFT	fast Fourier transform
γ_∞	surface tension at infinite number-average molecular weight
PEI	polyetherimide
PCL	polycaprolactone
PANI	polyaniline
CSA	camphorsulfonic acid
UV	ultraviolet

Contents

List of Tables

List of Figures

Chapter 1. Introduction

1.1 Introduction

We are surrounded by complex combinations of familiar materials, which consist of different phases, surfaces, and interfaces. These components play a vital role in determining the properties of materials, and interfaces are regions of limited thickness that contain a variety of compositions that continue from one phase to another in bulk. To create materials with improved properties at a lower cost, scientists develop materials by mixing or combining existing molecules. However, these mixtures are likely to have one component spread into another, making it essential to understand the phases that form between these components. Therefore, to comprehend material properties in such circumstances, it is necessary to begin by understanding the bulk properties and other properties close to the interfaces [1], [2].

This thesis considers studying polymer blend morphology in the bulk and surfaces. Polymers are many monomers or small molecules joining to form long-chain macromolecules. Other materials, like ceramics and metals, are less advantageous because they lack some of the features that polymers possess. Polymers have a low processing cost, are lightweight, and can possess suitable properties such as toughness and transparency. Morphology relates to an entity's structural characteristics that fall between the scale of the atomic arrangement and the size of the entire sample.

Polymers are composed of multiple monomers linked together by covalent bonds. A monomer is a small molecule repeating unit in the polymer chain. Polymerisation is the process that creates the polymer structure, where each monomer is joined to others through covalent bonding. The molar mass of a polymer, represented by *M*, can be calculated by multiplying the molar mass of a monomer, represented by M_{mon}, by the number of monomers in the polymer chain, represented by *N*.

$$M = NM_{mon} \tag{1-1}$$

During the polymerisation process, the atoms are arranged in a specific way along the polymer chain, and various repeating units and different isomers are possible along the chain. As a result, the microstructure of the polymer will remain unchanged unless the covalent bonds of the chain are broken [3].

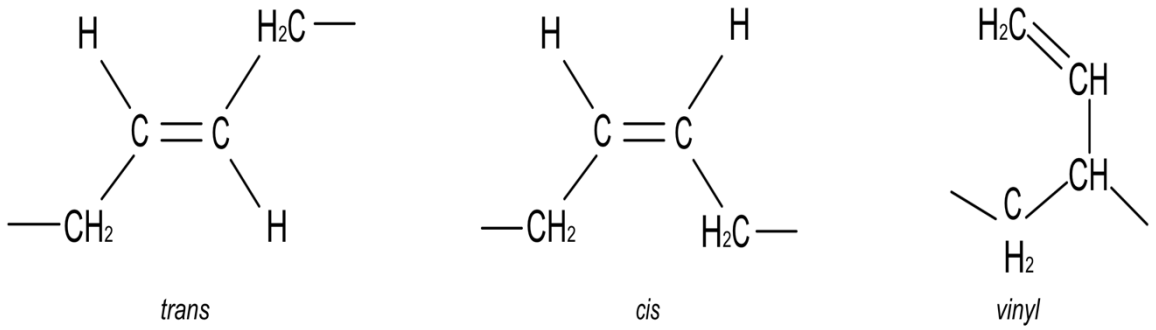

Figure 1.1 Three different structural isomers of polybutadiene (PB).

Many polymers have structural isomers along their chains, especially with double bonds in their backbone. For example, butadiene can have mixtures of trans-, cis-, and vinyl- (structural isomers) along its chain, as shown in (Figure 1.1). These structural differences can strongly affect polymeric systems' physical and chemical properties [3].

1.1.1 Polystyrene (PS) and Polybutadiene (PB)

Usually, copolymers or polymer blends are rubber-toughened polymers [4]. This thesis concerns spin-coated films of blends of two immiscible polymers, polystyrene (PS) and polybutadiene (PB), Figure 1.2. Spin-coated films are very uniform and easier to produce. PS is a rigid plastic, it is also affordable but prone to brittleness. On the other hand, PB is an elastomer resembling natural rubber. Elastomers that contain butadiene are more stress-resistant and can withstand colder temperatures than other elastomers. When the rubbery butadiene part is combined with the harder and glassy styrene part, the resulting blend makes the polymer more rigid and flexible. Combined, these mixtures separate into rubbery and harder phases due to their immiscibility. PS and PB blend spin-coated films have attracted considerable interest due to their uses in coatings, nanotechnology, and other applications in science. Their structure and surface energy play a critical role in determining their wetting and adhesion performance. Therefore, it is essential to consider the interaction between the surface phase and the bulk film structure, and this study aims to explain these films' three-dimensional nature and properties.

This work focuses on two types of amorphous polymers, PS and PB, which can also be semicrystalline. Amorphous polymers, such as glassy or rubbery, are widely used

in commercial and industrial applications that remain solid at room temperature. Many amorphous polymers are brittle and need to be mixed with additives, such as rubber, to improve toughness and crack resistance. Many chemical industries rely upon toughened plastics like styrene-butadiene rubber (SBR) and high-impact polystyrene (HIPS). These industries face challenges in designing fracture-resistant polymers, which include developing toughening mechanisms, characterising materials, and devising structure-property processes [4].

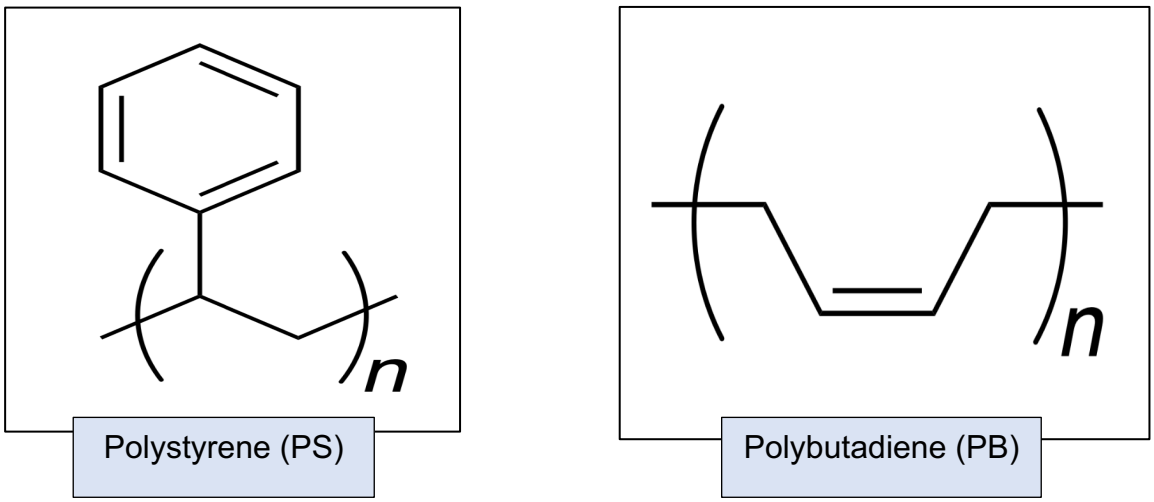

Figure 1.2 Chemical formula of polystyrene (PS) and polybutadiene (PB).

When the concentration of PS is higher than that of PB in a mixture, the resulting blend is known as high-impact polystyrene (HIPS). This is because PB serves to absorb energy, which strengthens and enhances the flexibility of HIPS beyond that of a typical polystyrene [5]. Conversely, if the blend contains more PB than PS, it is designated as styrene-butadiene rubber (SBR). The amount of PB present in SBR makes it an indispensable material due to its excellent resistance to water and abrasion, adequate stability, and cost-effectiveness. Consequently, it is widely used in various industrial applications, such as sealing and bonding in building construction, gaskets, paint systems, car tyres, and lithium-ion battery electrodes [6].

1.2 Literature Review

1.2.1 Morphology of spin-coated polymer blends thin films.

The primary goal is to understand the final three-dimensional (3D) morphology and the factors that influence it, such as substrates, the evaporation rate of the solvent, film thickness, and polymers' molecular weights [7].

According to Heriot et al., closely observing the structure during processing is crucial for understanding the unstable and complex phase separation [8]. They employed time-resolved light reflectivity during spin-coating to examine film morphology directly. Their findings revealed that phase separation commences at the surface once wetting layers are formed. They also noted that the interface becomes unstable when the thickness approaches a critical value, which they attribute to a change in solvent concentration throughout the film. Mokarian-Tabari et al. managed to control film structure by establishing a quantitative method to regulate the evaporation rate of the solvent during spin-coating [9]. Their specific system found that minimising the evaporation rate results in structured lamellar phase separation, and fast evaporation leads to lateral phase separation structures (Figure 1.2).

Another study by Walheim et al. tested the structure formation of spin-coated thin films of a symmetric blend of polystyrene (PS) and poly(methylmethacrylate) (PMMA) from a common solvent [10]. They used three different substrate surfaces (silicon oxide, gold and an organic monolayer) to understand their role in film morphology, which depends on the preferences of the PS and PMMA. They obtained topographic images using AFM, and the observed images display sharp edges with a defined structure when the solvent is commonly a better solvent for the polymer with lower surface tension. In contrast, the images reveal smooth and round surface structures if the solvent is not commonly a better solvent for the polymer with lower surface tension.

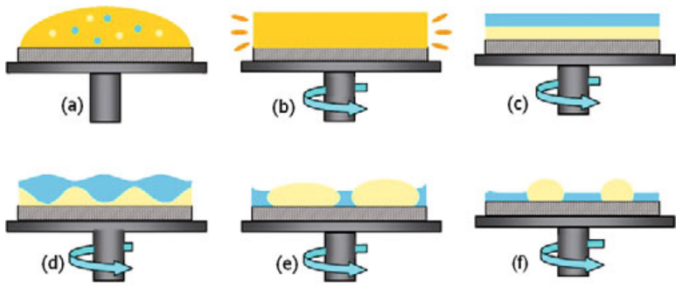

Figure 1.3 A schematic diagram shows spin-coated film formation from a polymer blend solution, how a layered structure is initiated, and how a lateral structure is created when the solvent evaporates. This image was taken from Mokarian-Tabari et al. (2010) with permission from the publisher [9].

Nilsson and colleagues modified the morphology of films of a polyfluorene copolymer blended with [6,6]-phenyl C_{61}-butyric acid methyl ester (PCBM) obtained through spin-casting [11]. A high solvent evaporation rate and strong polymer-PCBM repulsion

promote the development of a lateral structure, whereas a slow evaporation rate and poor polymer-PCBM repulsion favour a homogeneous structure.

In 2023, graphene oxide-based Janus nanosheets were employed by Cai et al. to modify the morphology of polymer blend films made of PS and PMMA by adjusting the nanosheet loading and the blend composition [12]. By doing so, the structures of the films ranging from PS network to PS droplets in the PMMA matrix were manipulated, resulting in different morphologies such as cavity-network structures, droplet-matrix structures, or bi-continuous structures.

A more recent study on using semiconductor/insulator blends to improve charge transport in transistors by inducing phase separation [13]. The study focuses on tailoring the dominant phase separation mechanism and the molecular self-assembly in a blend containing the long-chain conducting polymer poly[2,5-(2-octyldodecyl)-3,6-diketopyrrolopyrrole-*alt*-5,5-(2,5-di(thien-2-yl)thieno [3,2-b]thiophene)] DPPDTT and PMMA by adjusting the blend ratio. They found that using more than 75% concentration of the DPPDTT resulted in a surface-directed phase separation mechanism, and self-assembly leads to a nanowire or a micro-transport channel formation on the top of PMMA, enhancing device performance in transporting the charge carriers (high mobility devices). The resulting morphology is complex for blend ratios below 50% of DPPDTT. It contains surface-directed and lateral complex structures with lower mobility (obstacles to transport the carriers within the chains because of the insulating regions in between the conducting polymers).

1.2.1.1 Lamellar structure and surface segregation effect

Geoghegan et al. have studied the lamellar structure of thin films of mixtures of PS and PB in toluene [14]. They used nuclear reaction analysis (NRA), neutron reflectometry (NR), and transmission electron microscopy (TEM). They calculated the critical volume fraction and used a wide range of PS concentrations below this point. They defined the 3D morphology with layers of the different phases of ternary polymer-solvent thin films and gave a qualitative explanation of the surface effects of the phase separation.

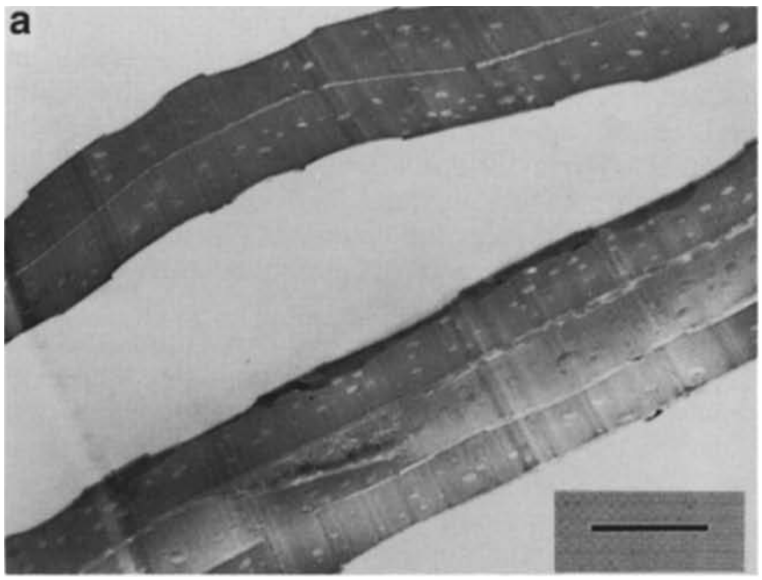

Figure 1.4 The structure of the thin film layers appears in the TEM micrograph of a section of a film with 13% PS by volume; interestingly, two thin PS layers (white colour) appear clearly between the PB layers(black colour), and the scale bar is 1μm. This image is taken from Geoghegan et al., 1994, after permission from the publisher [14].

Bernasik et al. studied the impact of phase separation in thin films insulating and conducting polymer blends [15]. The films comprised polyaniline (PANI) doped with camphorsulfonic acid (CSA), and PS, spin-coated from chloroform. While removing the solvent, the researchers observed the formation of a lamellar structure. They identified two critical processes: segregation of PANI to the substrate and substrate – directed phase separation. PS molecular weight, spinning speed, and solvent drying time control the formation of the lamellar structure.

Recently, Kang et al. investigated surface segregation behaviour in polymers with cyclic topology blended with polyurethane (PU) [16]. Their results showed 1.5 times higher surface segregation than the linear polymer, a promise for applications like antifouling effects in biomedical coatings.

1.2.1.2 Effect of different substrates on film morphology

A group of researchers (Dalnoki-Veress et al.) has studied the morphology of phase separation of thin films of a polymer blend of PS and polyisoprene (PI) in toluene, which was quenched at room temperature using the spin coating to evaporate the solvent quickly [17]. They felt that the substrate in the phase separation process had a significant effect, so they varied the PS mass fraction to determine the impact of three different substrate types: Si(001) with the native oxide layer present (Si-SiO_x), hydrogen-terminated Si(001) (Si-H), and a (Au/Pd) layer sputtered onto Si(001). They

proposed that they observed a vast difference in morphology for 1000 Å films on the Si-H and Si-SiO_x substrates because of the differences in the wetting features of PS for the surface of Si-H and Si-SiO_x substrates. However, they observed small substrate-induced morphology shifts for < 600 Å thick films of Si-SiO_x and Au / Pd substrates.

Winesett et al. have conducted a study on the impact of different substrates on the surface morphology of thin film blends of PS and PMMA [18]. The films were cast onto silicon, gold, and cobalt substrates using toluene, which were approximately 50 nm thick. Scanning transmission X-ray microscopy was then utilised to image the films. The researchers observed that the lateral shapes of PMMA differed in the initial structures due to PMMA and PS solubility in the solvent used. However, the equilibrium morphology of the films on silicon and gold substrates was altered to the one found on cobalt. This resulted in faster growth of the structure on silicon and gold substrates than on cobalt substrates.

1.2.1.3 Solvent effect and evaporation rate on film structure.

Jaczewska et al. studied spin-coated thin films of polythiophene (PT) and PS blends using three different solvents: chloroform, tetrahydrofuran (THF), and cyclohexanone. The humidity levels were controlled between 4-86% [19]. They investigated the solubility of the solvents, desorption, and adsorption by PT and PS. Based on their findings, they concluded that the higher solubility of PS compared to PT resulted in the formation of PS/PT//Si bilayers as the final structures when using chloroform. In contrast, these bilayers were not formed when using THF due to the instabilities of the surface and the interface. The instabilities of the surface resulted in the absence of a large-scale component of the morphology on the side for cyclohexanone. Furthermore, they discovered that moisture adsorption by PT and PS was minimal for chloroform and cyclohexanone. They recommended using common solvents with minimal water uptake to avoid the effects of humidity.

Jukes et al. experimented with measuring the kinetics of phase separation and film formation over time during the spin-coating process [20]. To monitor the thickness changes of the film, they utilised specular light reflectivity. Additionally, they observed the development of the phase-separated blend length using off-specular light scattering. They have demonstrated that, as phase separation progresses, the maximum scattering increases over time, but the length scale decreases instead of

growing. This is due to the unstable growth of the interface and a fluctuating composition when the morphology arises.

Dalnoki-Veress et al. studied the phase separation morphology of two ternary polymer blends in thin films: PS/PI/toluene and PS/PMMA/methyl ethyl ketone (MEK) [21]. The researchers used spin coating to restrict the geometry of the thin film and rapidly evaporated the solvent at room temperature to quench the blends. To quantify the phase separation morphology, they measured the domain area of the minority component as a function of the PS mass fraction. They identified that the significant increase in the average domain area is related to a small range of composition for both polymer blend systems. They showed a strong correlation between the average domain area and the spin speed, which enables control over the quench time of the polymer blend thin film.

1.2.1.4 Effects of the molecular weights on the surface morphology

The molecular weights of the polymers also play a role in enhancing the final morphology. A study by Geoghegan et al. has presented this effect in the morphology as polymer blend films spin spin-coated, and has suggested that changing the molecular weight of the film's components can help to make stratified films [22]. They found in their study that the low molecular weight deuterated polystyrene (d-PS) concentrates on the air and substrate interfaces while PB stays in the central region. However, when they tested the symmetric blend, they saw a bilayer structure where PB is at the air interface, and d-PS is still like the substrate interface.

Li et al. have explored the influence of molecular weights on the surface morphology of thin films made of PS/PMMA [23]. They observed three distinct surface morphologies in spin-coated films: a morphology with phase separation, a morphology with PMMA cells or PS morphology filling the net, and a sea-island morphology. However, during annealing, they found only two distinct surface morphologies.

1.2.1.5 Film thickness effect on the morphology

Kikuchi et al. have studied the effect of electrodynamic convection during the phase separation of thicker films of polymer blends to improve film morphology [24]. During the preparation of thicker polymer blend films by solvent evaporation, the phase separation often starts close to the surface and might be delayed in the bulk structure. This can result in a nonuniform morphology film. Therefore, to improve the morphology of the thicker polymer blend films, Kikuchi et al. used PS and polyvinyl acetate PVA,

and they prepared the film with solvent (toluene) evaporation. Then, they applied a DC electric field on a glass substrate with patterned electrodes. They proposed that they observed each unit of the pattern showed a well-defined structure with a regular distribution of PS/PVA polymer. PVA-rich domains were confined between each negative and positive electrode.

Wang and Koberstein conducted another study to analyse how the thickness of PS and poly(tert-butyl acrylate) (PS/PtBA) thin films affects their morphology [25]. According to their findings, the thin films, after spin-coating, exhibit laterally phase-separated wherein the thickness of PS domains is greater than that of PtBA domains. As the film thickness ranges from 58-227 nm and the PS composition in the blend increases, the morphology progresses from PS islands to PtBA holes. However, in the case of smaller film thicknesses, a PS network was observed. The study also demonstrated a consistent increase in the thicknesses of both PS and PtBA regions with the concentration of the spin-coating solution for the thicker films.

Li et al. demonstrated that the morphology of thin films of PS/PMMA blends depends on the film thickness and is influenced by annealing [26]. During the early stages of annealing, films with a thickness of 67.1 nm or 27.2 nm underwent phase separation and experienced a change in their morphologies. Over an extended annealing time, the 67.1 nm films took on a foam-like morphology, while the 27.2 nm films formed bicontinuous spinodal-like morphologies. For 16.3 nm films, distinct areas of PS-rich phases developed into a PMMA-rich phase layer, and following prolonged annealing, secondary phase separation occurred.

As previously stated in all previous studies, to gain a comprehensive understanding of the final three-dimensional (3D) morphology of polymer thin films, it is imperative to examine and analyse some of the critical factors that influence them, such as lamellar structure and surface segregation effect, substrate influence, solvent evaporation rate, polymers' molecular weights, and film thickness.

Chapter 2. Theory

2.1 Polymer Blends

A combination of different types of macromolecule that do not belong to the same polymer is known as a polymer blend [3]. Polymer blends comprise 33% of polymer usage, and their relevance is still increasing. Manufacturers can gain advantages from these materials as they offer desired properties at the most cost-effective price, enhance specific properties like impact strength, and ensure product uniformity, among other benefits [27].

One can characterise polymer blends by their polymer behaviour, which can result in either a single phase, phase separation, or partial miscibility. The miscibility range for polymer blends is relatively narrow. For example, hexane-ethanol mixtures are miscible, but polyolefin and poly(vinyl alcohol) with high molecular weight are highly immiscible. To understand this phenomenon and determine whether the blend's species will mix entirely or not, it is crucial to consider the free energy of mixing the blend [28].

2.2 Free Energy of Mixing

A binary mixture contains only two species, such as a blend of polystyrene (PS) and polybutadiene (PB). The equilibrium state of this system can be determined by the composition depending on the **entropy** and the **energy** changes in the mixing [3].

The **entropy** *S* is given by the product of Boltzmann constant k and the logarithm of Ω, which is the number of ways to arrange molecules on the lattice, meaning it is the number of occupied lattice sites n

$$S = k \ln \Omega \tag{2-1}$$

In the combined system, a homogeneous blend of A and B, where there is no volume change on mixing,

$$\Omega_{AB} = n \tag{2-2}$$

The volume fractions of components A and B are ϕ_A and ϕ_B, respectively; therefore, the number of states of each molecule of component A and B before mixing is $\Omega_A = n\phi_A$ and $\Omega_B = n\phi_B$respectively.

For one molecule of component A, the change of the entropy on mixing is

$$\Delta S_A = k \ln \Omega_{AB} - k \ln \Omega_A = k \ln \left(\frac{\Omega_{AB}}{\Omega_A}\right) = k \ln \left(\frac{1}{\phi_A}\right) = -k \ln \phi_A \tag{2-3}$$

As mentioned, the system is microscopically uniform and randomly mixed to fill all the lattice, so $\phi_A + \phi_B = 1$; from this, we can state that $\phi_A < 1$, and the change of the entropy on mixing is always positive $\Delta S_A = -k \ln \phi_A > 0$.

The contributed entropy from each molecule in the system is

$$\Delta S_{mix} = n_A \Delta S_A + n_B \Delta S_B = -k(n_A \ln \phi_A + n_B \ln \phi_B) \tag{2-4}$$

Where $n_A = \frac{n\phi_A}{N_A}$ molecules of component A and $n_B = \frac{n\phi_B}{N_B}$ molecules of component B, and N_A and N_B are the numbers of lattice sites filled by each particular molecule, i.e., the polymer chain length. Therefore, per one lattice site, the entropy of mixing is

$$\Delta \overline{S}_{mix} = \frac{\Delta S_{mix}}{n} = -k\left(\frac{\phi_A}{N_A} \ln \phi_A + \frac{\phi_A}{N_B} \ln \phi_B\right) \tag{2-5}$$

For polymer blends, N_A and N_B are large, so the entropy of mixing polymer blends is small. This is why many polymer blends demix easily.

An ideal mixture contains components that have the same interaction energy, and it is always homogenous because of the positive entropy; we can consider the volume fraction of components A and B to be $\phi_A = \phi$ and $\phi_B = 1 - \phi$ respectively. The entropy for the ideal mixture becomes [3],

$$\Delta \overline{S}_{mix} = -k\left(\frac{\phi}{N_A} \ln \phi + \frac{1-\phi}{N_B} \ln(1-\phi)\right) \tag{2-6}$$

To ultimately determine the equilibrium state of the system (polymer blend), let us consider the energetic part. There could be an attractive or repulsive interaction between the system components. The mixing mostly happened under constant pressure, and the enthalpic interaction between the components must be determined. For the sake of simplicity, assume that the components of the system are mixed at constant volume and that the monomer volume of component A and component B is identical. The mixing energy can either be positive, which indicates opposing mixing, or negative, which means promoting mixing. In addition, assuming that one lattice site can only be occupied by one component, the energy of mixing can be written in terms of three pairwise interaction energies between neighbouring lattice sites filled by two components (u_{AA}, u_{AB}, and u_{BB}). To determine the average pairwise interaction energy U_A of one component A monomer on a lattice site with its neighbouring monomer on one of the neighbouring sites, mean field theory is used. Mean field theory is the average interaction between the components A and B. The volume fraction ϕ_A is the

probability of this neighbour being a monomer of component A, where $\phi_B = 1 - \phi_A$ is the probability of the neighbour being one monomer of component B.

$$U_A = u_{AA}\,\phi_A + u_{AB}\,\phi_B \tag{2-7}$$

Similarly, one monomer of component B within a lattice site interacts with its neighbouring monomer on an adjacent site, resulting in an average pairwise interaction energy U_B,

$$U_B = u_{BB}\,\phi_B + u_{AB}\,\phi_A \tag{2-8}$$

One lattice has $z = 6$, nearest neighbours, so z is the coordination number of this lattice. The average interaction energy of a monomer of A component is $z\,U_A$ with all its z neighbours (this assumes that all its neighbours are A), where the average per monomer is the $\frac{z\,U_A}{2}$ because each pairwise interaction added up twice for one monomer and its neighbour. The energy per site filled with component B is the $\frac{z\,U_B}{2}$. As stated, the total number of the filled lattice sites in the combined system is n, and the number of lattice sites filled by components A and B is $n\phi_A$ and $n\phi_B$, respectively. To sum up, the total interaction energy of the pure unmixed components is

$$U = \frac{z\,n}{2}\,(U_A\phi_A + U_B\phi_B) \tag{2-9}$$

Indicating the volume fraction of component A as $\phi_A = \phi$, and the volume fraction of component B as $\phi_B = 1 - \phi$, and equations (2-7) and (2-8), the total energy of a binary system such a blend of PS and PB with n lattice sites:

$$U = \frac{z\,n}{2}\,\{[u_{AA}\,\phi + u_{AB}\,(1-\phi)]\phi + [u_{BB}\,(1-\phi) + u_{AB}\,\phi](1-\phi)\}$$

$$U = \frac{z\,n}{2}\,(u_{AA}\,\phi^2 + 2u_{AB}\,\phi(1-\phi) + u_{BB}\,(1-\phi)^2) \tag{2-10}$$

However, before mixing, the interaction energy of a pure component A per site is $\frac{z\,u_{AA}}{2}$ due to that each monomer before mixing is only neighbouring by component A. The total energy of component A before mixing is $\frac{z\,n}{2}u_{AA}\phi$. Similarly, the total interaction energy of pure component B before mixing is $\frac{z\,n}{2}u_{BB}(1-\phi)$. Therefore, the total interaction energy before mixing both components:

$$U_0 = \frac{z\,n}{2}\,(u_{AA}\,\phi + u_{BB}\,(1-\phi)) \tag{2-11}$$

The change of the energy on mixing is

$$U - U_0 = \frac{z\,n}{2}\left(u_{AA}\,\phi^2 + 2u_{AB}\,\phi(1-\phi) + u_{BB}\,(1-\phi)^2 - u_{AA}\,\phi - u_{BB}\,(1-\phi)\right)$$

$$U - U_0 = \frac{z\,n}{2}\left(u_{AA}\,(\phi^2 - \phi) + 2u_{AB}\,\phi(1-\phi) + u_{BB}\,(1 - 2\phi + \phi^2 - 1 + \phi)\right)$$

$$U - U_0 = \frac{z\,n}{2}\left(u_{AA}\,\phi(\phi-1) + 2u_{AB}\,\phi(1-\phi) + u_{BB}\,\phi(\phi-1)\right)$$

$$U - U_0 = \frac{z\,n}{2}\,\phi(1-\phi)(2u_{AB} - u_{AA} - u_{BB}) \qquad (2\text{-}12)$$

Therefore, the energy change per site on mixing:

$$\Delta\bar{U}_{mix} = \frac{U - U_0}{n} = \frac{z}{2}\,\phi(1-\phi)(2u_{AB} - u_{AA} - u_{BB}) \qquad (2\text{-}13)$$

The difference between the interaction energies in a unit of kT is the Flory–Huggins interaction parameter χ

$$\chi = \frac{z}{2kT}\,(2u_{AB} - u_{AA} - u_{BB}) \qquad (2\text{-}14)$$

χ depends on temperature and often has a form of $\chi = A + B/T$, A and B are constants [29]. Different forms of χ existence, which may also depend on the composition ϕ.

We can rewrite equation (2-13), which is a mean-field description of the energy equation of a binary mixture as a polymer blend

$$\Delta\bar{U}_{mix} = \chi\,\phi(1-\phi)\,k\,T \qquad (2\text{-}15)$$

The free energy of mixing is commonly known as the Flory-Huggins equation and can be obtained by combining equations (2-15) and (2-6):

$$\Delta\bar{F}_{mix} = \Delta\bar{U}_{mix} - T\,\Delta\bar{S}_{mix} = kT\left[\frac{\phi}{N_A}\ln\phi + \frac{1-\phi}{N_B}\ln(1-\phi) + \chi\,\phi(1-\phi)\right] \qquad (2\text{-}16)$$

As mentioned, the first two parts of the free energy equation of mixing are entropic, consistently promoting mixing; even with long-chain polymers, they are very small [1], [3]. The last part is the enthalpic part, which can be zero in the case of an ideal mixture (when the polymer chain length is the same as its random walk conformation, thermodynamically ideal mixtures are mixtures with no different interaction energy between components); positive opposes mixing, whereas negative promotes mixing, which depends on the χ sign. If χ is negative, there will be a net attraction between species. Therefore, the free energy of such a mixture will decrease, and the single-phase mixture is favourable for all compositions. If χ is positive, there is a net repulsion between components, increasing the free energy of the mixing. Thus, the equilibrium state in this situation depends on $\Delta\bar{F}_{mix}(\phi)$ the functional dependence of this free

energy on the composition for all compositions where $\Delta\bar{F}_{mix}(\phi)$ depends on χ and both N_A and N_B, more details in **section (2.4).** Indeed, the thermodynamic information in the Flory-Huggins equation is enough to determine the system equilibrium state [1], [3].

2.3 Phase Separation Conditions

Thermodynamic equilibrium occurs when a system has the lowest possible free energy. If a homogeneous mixture possesses a particular composition ϕ_0 and free energy $F_{mix}(\phi_0)$, its local stability may be of concave or convex nature, as depicted in (Figure 2.1). Moreover, its stability can be found where the free energy of the mixed state $F_{mix}(\phi_0)$ is greater or lesser than the phase separated state $F_{\alpha\beta}(\phi_0)$.

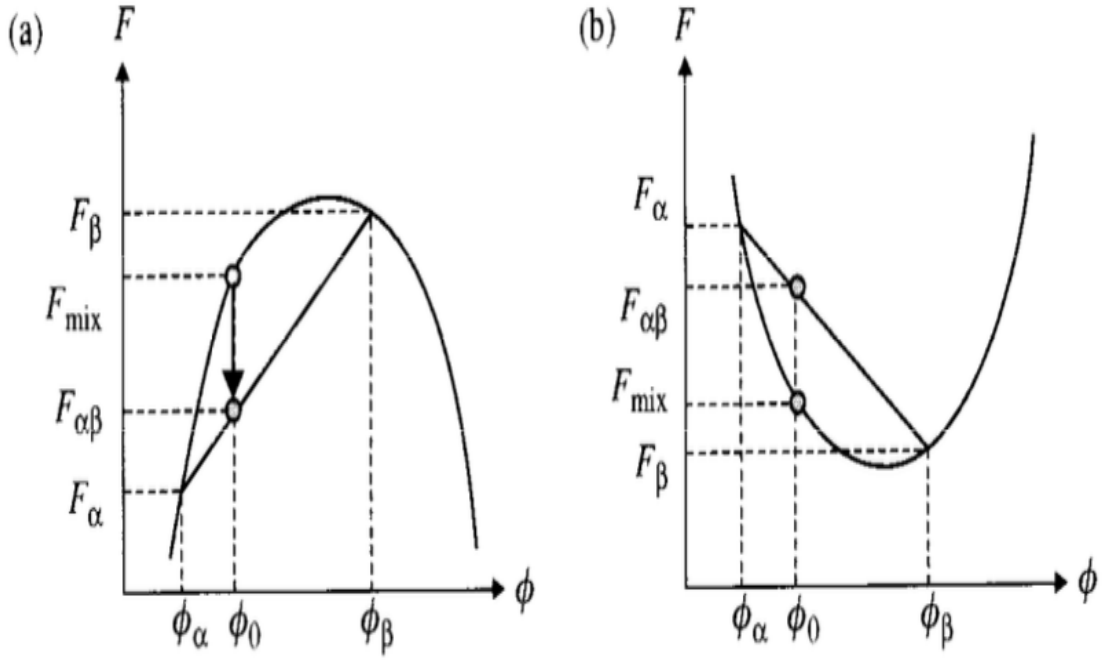

Figure 2.1 An example of an unstable system (a) and a completely stable blend (b). This figure is taken from M. Rubinstein and R.H. Colby, 2003, after permission from the publisher [3].

Consider the system with the total composition ϕ_0, which has two phases: ϕ_α volume fraction of the components has α phase, and ϕ_β volume fraction of the components has β phase. The phase-separated $F_{\alpha\beta}(\phi_0)$ state can be determined by the straight line, which links the free energies F_α and F_β of the two compositions ϕ_α and ϕ_β. The shape of the free energy curve depends on the composition, indicating stability. As in (Figure 2.1-a), the curvature is concave, and the system naturally phase-separates into two phases to decrease its total free energy since $F_{mix}(\phi_0) > F_{\alpha\beta}(\phi_0)$. Whereas

in (Figure 2.1-b), the curve is convex, and the mixed state is stable because every single-phase composition possesses a lower total free energy than any phase-separated composition since $F_{mix}(\phi_0) < F_{\alpha\beta}(\phi_0)$. Therefore, it is a mixture of a single phase. The second derivative of the free energy of mixing can determine the basis of the local stability [1], [3],

$$\frac{\partial^2 F_{mix}}{\partial \phi^2} < 0 \quad \text{unstable.} \tag{2-17}$$

$$\frac{\partial^2 F_{mix}}{\partial \phi^2} > 0 \quad \text{locally stable.} \tag{2-18}$$

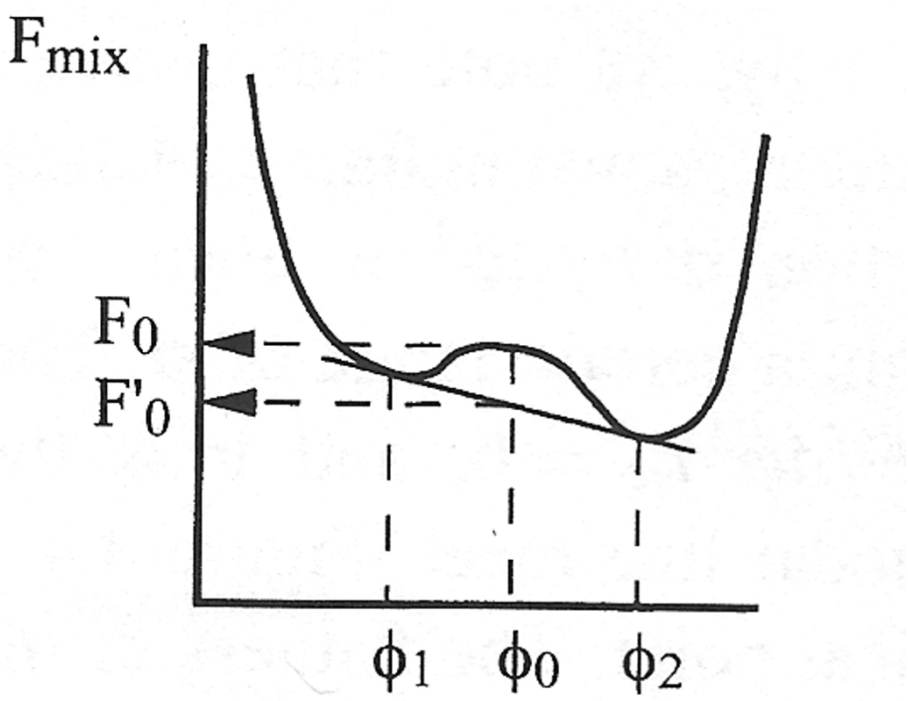

Figure 2.2 Mixtures of ϕ_1 and ϕ_2 can phase separately to lower their free energy. This figure is taken from Jones and Richards, 1999, after permission from the publisher [1].

Figure 2.2 shows that the free energy curve has a different shape. At a stable composition ϕ_0, the system will lower its free energy from F_0 to the total energy of the phase-separated system F'_0 with composition ϕ_1 and ϕ_2. However, the single phase is unstable at these two points, and we can determine the lowest free energy by drawing the tangent line between ϕ_1 and ϕ_2, as shown in Figure 2.2 [1], [30].

2.4 The Phase Diagram

To construct a phase diagram to analyse the mixture behaviour representing stability, metastability (locally stable but energetically unstable), and instability regions, we must examine the free energy of mixing for a polymer blend,

$$\Delta\bar{F}_{mix} = \Delta\bar{U}_{mix} - T\,\Delta\bar{S}_{mix} = kT[\frac{\phi}{N_A}\ln\phi + \frac{1-\phi}{N_B}\ln(1-\phi) + \chi\,\phi(1-\phi)] \qquad (2\text{-}16)$$

The boundary conditions for the two equilibrium phases can be obtained by calculating the tangent of the free energy at composition ϕ' and ϕ" [3].

$$\left(\frac{\partial\Delta\bar{F}_{mix}}{\partial\phi}\right)_{\phi=\phi'} = \left(\frac{\partial\Delta\bar{F}_{mix}}{\partial\phi}\right)_{\phi=\phi''} \qquad (2\text{–}19)$$

For a symmetric polymer blend (as top part in Figure 2.3), the tangent will be horizontal and $N = N_A = N_B$. Thus,

$$\left(\frac{\partial\Delta\bar{F}_{mix}}{\partial\phi}\right)_{\phi=\phi'} = \left(\frac{\partial\Delta\bar{F}_{mix}}{\partial\phi}\right)_{\phi=\phi''} = kT\left[\frac{\ln\phi}{N} - \frac{\ln(1-\phi)}{N} + \chi\,(1-2\phi)\right] = 0 \qquad (2\text{-}20)$$

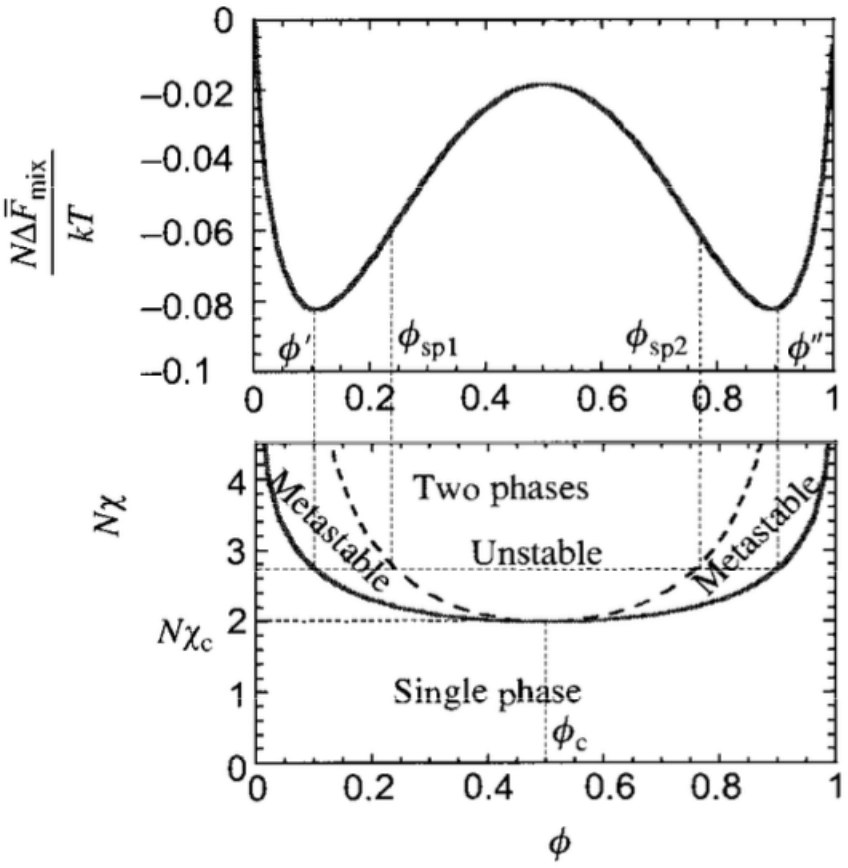

Figure 2.3 A symmetric polymer blend composition depends on the free energy of mixing with $\chi N = 2.7$ (top curve). Its phase diagram shows the solid curve for a binodal and the dashed curve for a spinodal (bottom figure). This figure is taken from M. Rubinstein and R.H. Colby, 2003, after permission from the publisher [3].

Solving the last equation for χ_b related to the phase boundary represents the binodal of a symmetric blend (as shown in the bottom of figure 2. 3 as a solid line),

$$\chi_b = \frac{1}{2\phi-1}\left[\frac{\ln\phi}{N} - \frac{\ln(1-\phi)}{N}\right] = \frac{\ln(\phi/(1-\phi)}{(2\phi-1)N} \tag{2-21}$$

Assuming $\chi = A + B/T$,

$$T_b = \frac{B}{\ln(\frac{\phi}{1-\phi})/((2\phi-1)N) - A} \tag{2-22}$$

Equation (2-22) gives the binodal of the phase diagram and the relation between the temperature and the composition. For the binary system, this describes the coexistence curve because, at the equilibrium, the binodal can be browsed by the two coexisting compositions for a curve of given temperature (or $N\chi$ as the bottom figure in Figure 2.3) and overall composition in the two phases. Moreover, any overall composition at T on the binodal has the least free energy (only for $N_A = N_B$) in the state of the phase-separated blend by the two coexisting compositions ϕ' and ϕ".

The inflection points in $\Delta\bar{F}_{mix}(\phi)$, which represent the limit of the local stability of an asymmetric blend, can be obtained by:

$$\frac{\partial^2\Delta\bar{F}_{mix}}{\partial\phi^2} = kT\left(\frac{1}{N_A\phi} + \frac{1}{N_B(1-\phi)} - 2\chi\right) = 0 \tag{2-23}$$

The curve where the inflection points occur is the boundary between the metastable and the unstable regions known as the spinodal (shown in the bottom part of Figure 2. 3, a dashed line). Solving equation (2-23) gives,

$$\chi_s = \frac{1}{2}\left(\frac{1}{N_A\phi} + \frac{1}{N_B(1-\phi)}\right) \tag{2-24}$$

Again, from the $\chi = A + \frac{B}{T}$, spinodal can transformed in the temperature-composition plane for the phase diagram by:

$$T_s = \frac{B}{\frac{1}{2}\left(\frac{1}{N_A\phi} + \frac{1}{N_B(1-\phi)}\right) - A} \tag{2-25}$$

The critical composition ϕ_c can be found from equation (2-24) in the binary blend, which is the lowest point where the coexistence curve and the spinodal meet (shown in the bottom part of Figure 2.3) and also can be defined by $\frac{\partial^3\Delta\bar{F}_{mix}}{\partial\phi^3} = 0$.

$$\frac{\partial\chi_s}{\partial\phi} = \frac{1}{2}\left(-\frac{1}{N_A\phi^2} + \frac{1}{N_B(1-\phi)^2}\right) = 0 \tag{2-26}$$

$$\phi_c = \frac{\sqrt{N_B}}{\sqrt{N_A}+\sqrt{N_B}} \tag{2-27}$$

Substituting equation (2-27) in equation(2-24),

$$\chi_c = \frac{1}{2}\left(\frac{1}{\sqrt{N_A}} + \frac{1}{\sqrt{N_B}}\right)^2 \tag{2-28}$$

Then we have the critical temperature, where the point in which the coexistence curve and the spinodal meet at the phase diagram,

$$T_c = \frac{B}{\frac{1}{2}\left(\frac{1}{\sqrt{N_A}}+\frac{1}{\sqrt{N_B}}\right)^2 - A} \tag{2-29}$$

At the critical composition, the curve of the free energy becomes flat. This implies that there will be significant fluctuations in the composition at a small amount of free energy (Figure 2.4).

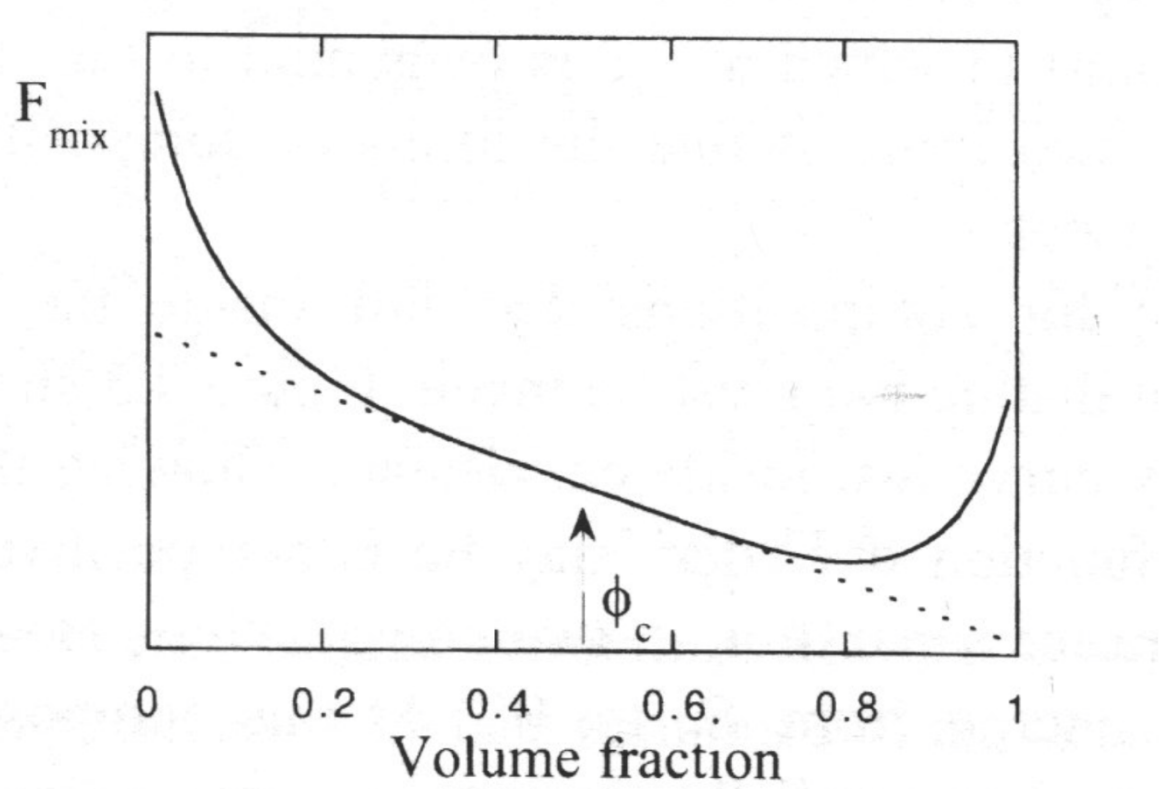

Figure 2.4 The free energy curve will vanish at the critical composition and the critical temperature, only when $N_A \neq N_B$. This figure is taken from Jones and Richards, 1999, after permission from the publisher [1].

As in Figure 2.3, the phase diagram of a symmetric polymer blend ($N = N_A = N_B$) has a critical composition $\phi_c = \frac{1}{2}$ and critical interaction parameter $\chi_c = 2/N$, which is very small for blends of long chains.

Most polymer blends are phase-separated over some composition range because they have a $\chi > \chi_c$ within the metastable region. This implies that at any given composition in the metastable region, the equilibrium comprises two phases having compositions ϕ' and ϕ" located on the two parts of the coexistence curve at the same χ.

However, if the net attraction between the mixture components is $\chi < 0$ or if there is very weak repulsion $(0 < \chi < \chi_c)$ the blends will form a single phase homogeneous mixture across all composition range $(0 \leq \phi \leq 1)$ and the mixture is stable.

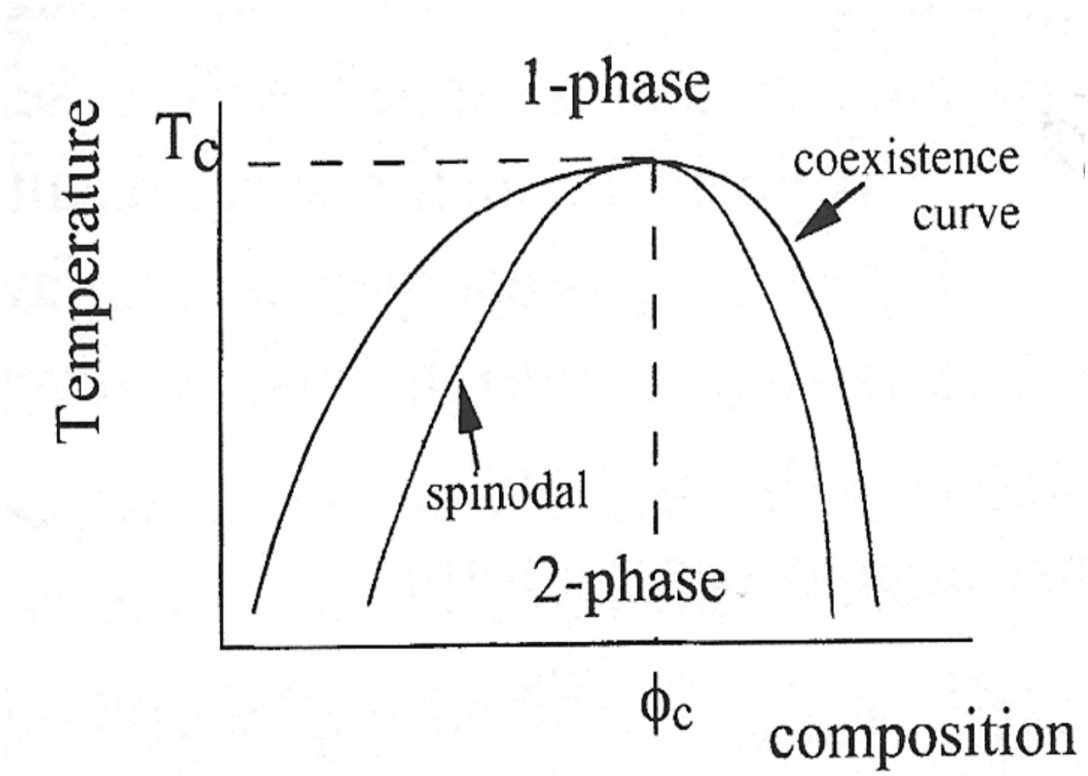

Figure 2.5 An upper critical solution temperature (UCST) phase diagram, the coexistence curve and the spinodal meet at the critical temperature. The spinodal separates the unstable composition from the metastable composition, and the coexistence curve (binodal) separates the single-phase region from the binary-phase (metastable) region. This figure is taken from Jones and Richards, 1999, after permission from the publisher [1].

Experimentally and based on equation (2.14) and the form $\chi = A + B/T$, the interaction parameter is inversely proportional to absolute temperature T. Therefore, the phase diagram is commonly presented in the temperature-composition curve, as (Figure 2.5), this diagram is known as upper critical solution temperature (UCST) phase diagram. When $B > 0$, then χ decreases as temperature increases; the highest temperature of the two phases region is T_c. The mixtures are homogenous and stable for all $T > T_c$.

On the contrary, the lower critical solution temperature (LCST) phase diagram when $B < 0$, then χ decreases as the temperature is lowered, and the lowest temperature of the two phases region is T_c. For all $T < T_c$, the mixtures are homogenous and stable [1], [3], [29]–[32]

2.5 Phase Separation Mechanisms

Knowing how to differentiate between unstable, metastable, and stable compositions is crucial in polymer science. It is equally essential to comprehend how a system can transition between these compositions and to characterise the phase-separated structures that result from this transition. If a system transitions from a single-phase region to a two-phase region, it can be said that phase separation has occurred. This transition is typically brought about by a change in temperature, either an increase or a decrease, depending on the specific system. This phenomenon is commonly observed in polymer blends. In polymer blends, achieving a complete phase-separated situation is very rare, and we have a single interface between two microscopic domains. However, phase separation structure development resulting from temperature changes can often be monitored in real-time because of the high polymer viscosity that can slow the rate of unmixing. Moreover, the phase separation process can stop at any stage due to quenching the system by decreasing its temperature to below the glass transition temperature of the two phases.

The mechanisms of phase separation are continuously changing in different compositions, and there are two ways in which it can occur: spinodal decomposition and nucleation [1], [5], [29].

2.5.1 Spinodal decomposition

Any slight deviation in composition decreases free energy within the spinodal line, rendering the system unstable. This leads to random composition fluctuations being amplified in a process known as spinodal decomposition.

Typically, materials diffuse from low-concentration to high-concentration regions to make uniform concentrations. However, in the spinodal decomposition, the case is reversed. At equilibrium, the material chemical potential must be uniform, not the concentration, so the material diffuses from high chemical potential to low chemical potential regions. The chemical potential is linked to the first derivative of the free energy concerning the concentration. Therefore, if the second derivative of the free energy concerning concentration is positive, the high-concentration region has a high

chemical potential. As a result, diffusion will occur in the usual direction. However, within the spinodal region, the second derivative of the free energy concerning concentration is negative, so the chemical potential gradient has an opposite sign to the concentration gradient, and the system will move from the low-concentration region to the high-concentration region by diffusion.

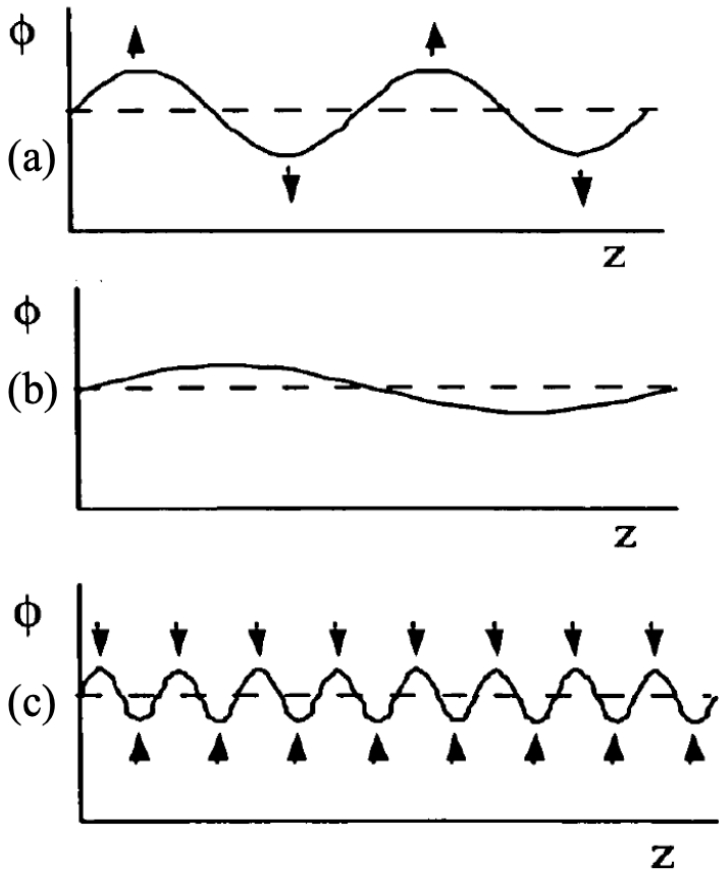

Figure 2.6 A characteristic length scale of the spinodal decomposition (a) an intermediate length scale grows quickly. (b) A long wavelength fluctuation expands slowly over a long distance of diffusion. (c) a short wavelength with many interfaces. This figure is taken from Jones, 2002, after permission from the publisher [30].

Therefore, any fluctuation in the composition will grow only in amplitude by the transport of material from the troughs to the peaks (see Figure 2.6), eventually causing a phase-separated domain at the coexisting composition. Still, fluctuations of different wavelengths increase at different rates. A common length scale results from the competition between the system entropy (approving mixing) and enthalpy (approving demixing). This should also conserve the overall energy per unit volume of the whole system constant, which can happen if the phase-separated domains' size and the distance between them are kept equal, at least in the early stages of phase separation.

Indeed, equality in domain size and homogeneity of the energy per unit volume produce a common phase separation length scale. A very short wavelength fluctuation is suppressed because it forms too many domains and, thus, new interfaces in a given volume, which means that phase separation increases the system's overall energy (see Figure 2.6 (c)).

Meanwhile, on a very large length scale, the composition fluctuation grows slowly by moving large domains from the troughs to the peaks, which requires large mass transport (see Figure 2.6 (b)), a kinetically suppressed process, i.e., it is too slow. Therefore, in the early stages, the phase separation morphology can be controlled by an intermediate length scale of fluctuations, which grows the fastest (see Figure 2.6 (a)). The competition between enthalpy and entropy resulted in a controlled length scale in spinodal decomposition. The number of small domains increases if the system is controlled by enthalpy. Conversely, if the system is controlled by entropy, there will be fewer domains and interfaces.

The typical length scale will not be confined to the formed morphology of the system. In some scenarios, the morphology is limited by concentration. For an unstable mixture in which one component is significantly less concentrated than the other, the less concentrated component's domains will be dissolved in a matrix of the more concentrated component. However, if the system is symmetrical, the morphology will assume a bicontinuous structure since no major or minor components exist. There is an exception when the less concentrated component has greater viscoelasticity than the more concentrated one; in such cases, the structure formed is also bicontinuous [29], [30].

2.5.2 Nucleation

As mentioned, the area between the binodal and spinodal on the phase diagram is considered metastable. It means that any mixture in this region can easily undergo phase separation with a small activation energy caused by fluctuations in composition or temperature. So, the continuous spinodal decomposition process will no longer be available to it. These fluctuations begin to raise the free energy of the system. As a result, a droplet from the minority phase, larger than the critical size, is formed by thermal nucleation. This droplet grows until the free energy of the system decreases again, and the phase separation occurs. This kind of thermal nucleated phase separation is a rare phenomenon known as a homogenous nucleation.

Heterogeneous nucleation is the most common form of nucleation caused by impurities. Impurities, such as dust particles, create fresh surfaces that are typically covered by one of the two components of the system. Therefore, there is an interfacial tension related to the impurities and each of the components of the system. Phase separation occurs at the interface where the nucleation site gets wetted due to the low interfacial tension controlling it. A wetting layer is likely to form at this time, and there is no activation energy. The impact of this occurrence is considered very significant; using ultrapure materials is essential to prevent this. Additionally, demixing may occur from both the container walls and the surface, making it challenging to avoid metastable liquid mixtures from demixing [1], [29], [30], [33].

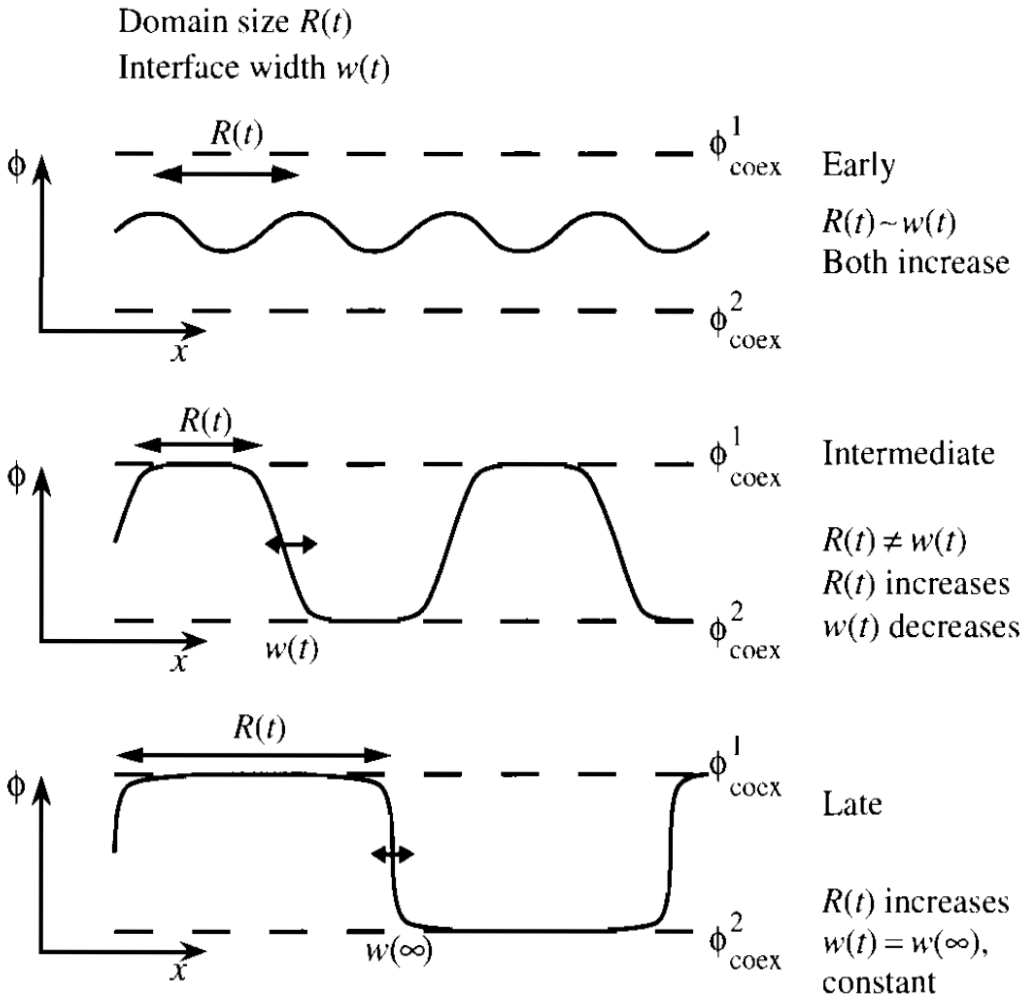

Figure 2.7 Visual representations of composition profiles in a phase-separation system demonstrate how the average domain size and interfacial width change over time. This figure is taken from Jones, 2002, with permission from the publisher [30].

2.5.3 Characterisation of Phase Separation Mechanisms

Composition fluctuations of spinodal decomposition grow in amplitude and remain with a constant wavelength, but they do not continue for an extended period (see Figure 2.6). The amplitude of the composition wave cannot increase as it reaches the coexisting compositions at their peak levels. Moreover, the system is still far from equilibrium even at this stage. Therefore, the only probability is starting the size of the domain to grow. This guides us to the stages of spinodal decomposition in Figure 2.7.

Mentioning two length scales is important to characterise phase separation mechanisms; R characterises the size of the domains and their average distance between them, and w characterises the width of the interface between the domains. Both R and w are constant during the very early stage and are related to the fastest growing wavelength λ_{max}. As we approach the end of the early stage, the peak compositions approach the coexisting compositions. At this point, we enter a complex intermediate stage of the phase separation. During this stage, the size and the separation of the domains R increases, and the interfacial width w decreases towards its equilibrium value. In the later phase separation stage, a more straightforward situation arises where distinct domains with compositions near the coexisting compositions are separated by interfaces with an equilibrium width. This late stage occurs due to a nucleation and growth mechanism. The only length scale characterising the morphology at the late stage is R [1], [30].

2.6 Surface Energy and Wetting Properties.

Thus far, we have discussed the potential outcomes of mixing polymer blends in bulk. However, the significance of surfaces and interfaces must be considered when dealing with thin films. It is crucial to recognise that material properties differ between the bulk and the vicinity of interfaces, given that the structures of the solid materials in the bulk vary from those on their surfaces and interfaces [1]. We aim to understand the final three-dimensional morphology of an immiscible polymer blend thin film. Therefore, we should be concerned about the interplay of the surface phase with the bulk film [7].

The measurement of solid surface energy or tension plays an essential role in various industries, as it is the thermodynamic quantity used to define wetting. In principle, the surface or interface is located in a region that has a definite thickness where the composition and the energy differ from the bulk phase. Therefore, the pressure in this region is inhomogeneous, whereas in the bulk, it is homogeneous. To create an

interface, a net energy is required to move the matter from the bulk phase to the interfacial region. This work, which is done to make a unit interfacial region area, is the surface tension (interfacial tension) γ, which is defined as the excess free energy per unit area, which means the energy needed to enlarge the surface area per unit. Thus, it is the thermodynamic differential with the area A of the surface

$$\gamma = (\frac{\partial \mathrm{G}}{\partial A})_{T,P,n} \tag{2-30}$$

Where G is the Gibbs free energy of the total system, T is the temperature, P is the pressure, and n is the density of the particles (the total number of moles of matter in the system) [2].

Direct solid surface tension measurement is impossible due to the motionlessness of molecules in a solid phase. Therefore, several theoretical and experimental approaches have been developed to measure solid surface tension. Among these approaches, the contact angle method is considered the most accessible [34]–[36].

2.6.1 Contact Angle Phenomenon

A liquid droplet's interaction with a solid surface is obtained by measuring the contact angle [2], [35]–[38]. This angle can be categorised as either static, which occurs when the system is at rest, or dynamic when the droplet is in motion. Our focus will be on the static contact angle. However, it's important to note that a system at rest can exist in either a stable or metastable equilibrium.

The stable equilibrium state, where the energy is at its lowest, can be achieved by ensuring the solid surface is planar, smooth, homogeneous, and rigid. Conversely, metastable equilibrium is characterised by energy barriers that separate an energy trough from adjacent states, and the solid surface may be rough or compositionally heterogeneous. A system can exist in various metastable states, and the amount of mechanical energy in the liquid droplet can determine these states. The contact angle can change in metastable equilibrium based on factors like the liquid droplet's volume, external mechanical energy (like vibration), and the method used to form the droplet (whether advancing or receding it on the solid surface).

However, in 1805, Young proposed a means of estimating solid surface tension from a contact angle [2], [35]–[38].

2.6.2 The Young Equation

The measurement of contact angle θ involves using the tangent angle of a solid surface as the base for a liquid droplet (as shown in Figure 2.8). The reason for this can be explained by the mechanical equilibrium of the liquid droplet, which is maintained through the interplay of three interfacial tensions: the surface tension between the solid and the vapour, γ_S which pulls the liquid droplet trying to wet the solid surface, the interfacial tension between the solid and the liquid droplet, γ_{SL} which causes the liquid droplet to dewet the solid surface, and the surface tension between the liquid and the vapour, γ_{LV}.

This equilibrium relationship is known as Young's equation [37]:

$$\gamma_S = \gamma_{SL} + \gamma_{LV} \cos\theta, \tag{2-31}$$

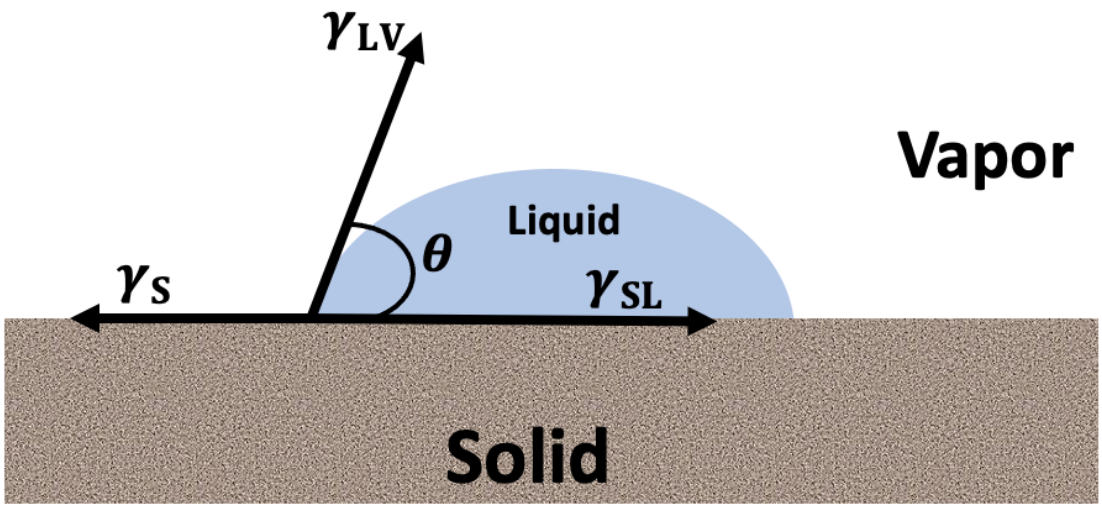

Figure 2.8 A schematic drawing of liquid droplet contact angle on a solid surface and the three interfacial tensions.

Wetting is a direct consequence of Young's equation. By gravity, the liquid droplet will reach the contact angle of equilibrium, which in turn leads to the spreading of the droplet. The wetting behaviour of a liquid on a solid surface is measured by the contact angle, which can range from zero to 180 degrees. If the contact angle is zero, it indicates complete wetting, while a contact angle of 180 degrees indicates complete non-wetting. Moreover, the surface is hydrophilic if the contact angle is less than 90°. The surface is considered hydrophobic if it is between 90° and 150°. Meanwhile, the surface is superhydrophobic if the contact angle is more significant than 150° [29].

2.6.3 Neumann's Equation of state for interfacial tensions

θ and γ_{LV} are the only two measurable quantities that are involved in Young's equation. θ is measured easily by a goniometer, and γ_{LV} is obtained through other techniques, such as a pendant droplet experiment [39]–[41]. Thus, many different methods have been researched to determine the surface energy γ_{S} by analysing the contact angle values of different liquids droplets and some established surface tensions γ_{S}. One of the well-known methods was introduced in the form of Neumann's equation [42]:

$$\gamma_{\mathrm{SL}} = \gamma_{\mathrm{S}} + \gamma_{\mathrm{LV}} - 2\sqrt{\gamma_{\mathrm{LV}}\gamma_{\mathrm{S}}}\, e^{-\beta(\gamma_{\mathrm{LV}}-\gamma_{\mathrm{S}})^2}, \tag{2-32}$$

where β = 0.000115 $(\mathrm{m}^2/\mathrm{mJ})^2$ is Neumann's constant. Using the combination of Young's and Neumann's equations (2-31) and (2-32) to eliminate γ_{SL}, resulting in [35], [36], [43]–[49]:

$$cos\,\theta = -1 + 2\sqrt{\frac{\gamma_{\mathrm{S}}}{\gamma_{\mathrm{LV}}}}\, e^{-\beta(\gamma_{\mathrm{LV}}-\gamma_{\mathrm{S}})^2}, \tag{2-33}$$

In equation (2-33), only one liquid is necessary to evaluate the surface energy of a solid polymer. In the experiments described in the thesis, we use two (water and glycerol) in order to test this relation.

2.7 Surface-caused self-assembly in thin film

The surface boundary affects the phase separation morphology in polymer blend thin films. Due to the large size of polymer molecules, the properties of materials can be significantly affected by the surface layer [7]. The interplay between phase separation and surface segregation (wetting) is responsible for creating a phase-separated film morphology. The process of phase separation is influenced by $N\chi$, where N represents the number of segments of the polymers and χ measures the unfavourable interaction between the polymers of the blend. Meanwhile, wetting is regulated by the interactions between the polymers and the boundary phases [50].

In polymer blend thin films, the usual tendency is for phase separation to result in an isotropic domain structure morphology, as shown in Figure 2.9 (a). Nevertheless, nearing the surfaces that confine the bulk, the domain structure is believed to be anisotropic. The coexisting compositions do not have precisely the same interfacial energies as the boundary surfaces. This means that the component with the lower surface energy will separate and move towards the surface to reduce the overall free energy of the system. In cases with a significant difference in the interfacial energies between the coexisting phases, the separation will result in a layered structure with

domains parallel to the surface [51], [52]. Figure 2.9 (b) provides a visual representation of this phenomenon. This surface is expected to be enriched in the lower surface energy component [53]. Also, It is assumed that the anisotropic domain structure will merge with the isotropic domain bulk structure at a certain depth beneath the surface.

However, the two flat boundary surfaces can significantly affect the film morphology, and these surfaces can determine the domain morphology (Figure 2.9 (c)) if the film is thin enough. At equilibrium, the total interfacial area between the coexisting phases has to be minimised. For that to occur and depending on the surface polymer interactions and the wetting behaviour of the different components, the layered domains are expected to coarsen over time after being quenched into the two-phase region of the phase diagram [54]. As time progresses, the domains may form a highly ordered bilayer or trilayer structure in equilibrium, similar to the one shown in Figure 2.9 (d) [55], [56].

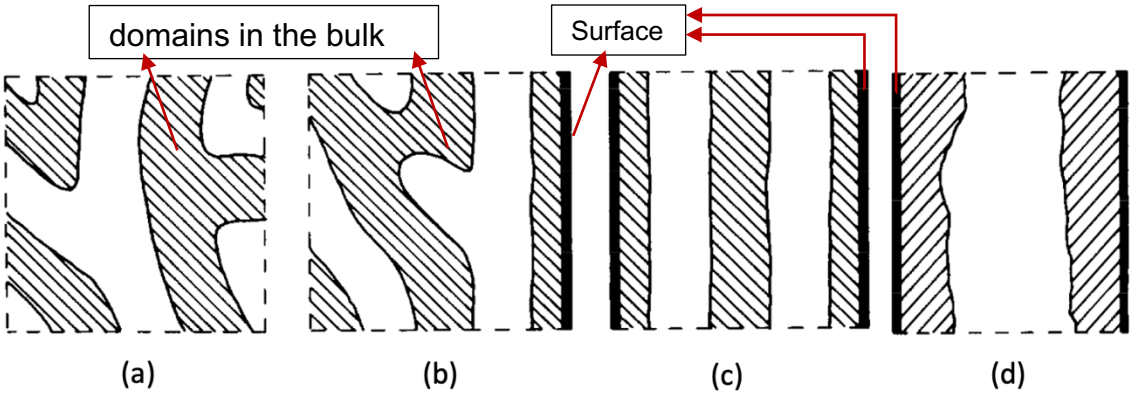

Figure 2.9 A schematic drawing of domines morphology in phase separation of polymer blends. (a) Isotropic domains in the bulk. (b) domains structures segregate close to the surface. (c) and (d) when a situation in a thin film has two boundary surfaces where the same phase attracts far from the bulk in the equilibrium, this assumes a complete wetting for both surfaces. This figure is taken from Krausch, 1995, after permission from the publisher [55].

2.7.1 Surface-directed Spinodal Decomposition

When thin films of polymer blends are quenched inside the spinodal, the surface affects them, breaking their symmetry. This leads to the phenomenon of surface-directed spinodal, where the surface pins the direction and phase of the composition waves that occur. These waves extend from the film surface into the bulk, continuing until the bulk phase separation, driven by thermal fluctuations, is the dominant phenomenon [57]–[60]. In bulk, surface-directed spinodal decomposition leads to

forming a surface-enriched structure. The first experimental evidence for such a phenomenon was given by Jones et al. [61].

Geoghegan et al. used ^{3}He nuclear reaction analysis to study the effect of the surface and the interface on the phase separation region in the thin film of a mixture of deuterated polystyrene (d-PS) and poly(α −methyl styrene) (PαMS) blend. They detected the surface-directed spinodal decomposition morphology in the unstable region of the phase diagram. They compared their work with other theoretical and experimental works. They found that the vacuum interface of d-PS-rich layers increases with time a power law exponent of 0.14 (following $z^* \propto t^{0.14}\ where\ z^* = \int(\phi - \phi_0)dz$). They also observed a second layer rich in d-PS closer to the substrate, which increased with a power law exponent of 1/3. They calculated the size of the first stage of the wetting layer and compared it with other workers. They proposed that the wavelength decreases when the films are thinner than the critical thickness [57].

This phenomenon results in the creation of distinct self-organised structures or phases that are separated laterally on the surface of a thin film [8], [62]–[64]. Self-organisation is a prominent feature in thin film polymer bends, which has led to extensive research in technological applications. For instance, researchers are targeting specific domain morphologies to improve the efficiency of photovoltaic devices. Additionally, it helps design functional polymer/fullerene solar cells [65]–[71]. Lu et al. have proposed a method to enhance the performance of transistors by introducing semiconducting polymers into insulator polymer blends. Their research has resulted in a stable polymer blend device with a lower concentration of semiconducting polymers, exhibiting very high on/off ratios [72]. More studies are also on the hollow interior structure to aid the development and design of biomedical devices and drug delivery [73].

2.8 Polymers Blends and Thin Film Preparation

Thin polymer films can be prepared from the polymer solutions. The polymer-solvent interaction can determine the solubility of a polymer in a solvent. A generally accepted rule is that a polymer could dissolve in a solvent with similar chemistry. Various properties influence this interaction, such as the constitution of the polymer, temperature, and molecular weight. For instance, adding solvent to a high molecular weight soluble polymer might cause the polymer to swell rather than dissolve because the process transits from a polymer solution to a gel-like state [74]. Polar molecules typically dissolve better in polar solvents, while nonpolar molecules prefer nonpolar solvents. For instance, polystyrene, a nonpolar molecule, can dissolve well in nonpolar

solvents like toluene but won't dissolve in polar solvents like water [75]. Therefore, due to these properties, the dissolution process can take a few minutes to several days [74].

There are many ways of creating polymer films, such as **solution-casting**, in which the solvent evaporates to form the film. Another example is **dip-coating**, where a clean substrate is soaked into the solution and then withdrawn at a constant speed from the solution. After that, a film is formed after allowing the substrate to dry [74]. Also, the **doctor blade** technique is one in which the solution is spread across the substrate by a blade, leaving a film when the remaining solvent has evaporated [76].

Moreover, obtaining a smooth and uniform thin film on a flat substrate can be reached by **spin-coating**. Spin-coating follows clear steps:

Deposition is when a pipette deposits the polymer solution on the substrate. The substrate is stable at the beginning of this step, and the polymeric solution is introduced as a continuous stream at the centre of the substrate. After operating the spin-coater, the centrifugal force spread the liquid from the centre to outwards to cover the hole substrate.

Spin-up at this step, the substrate rotates rapidly, usually several thousand rounds per minute (rpm), in the range 2000 - 8000 (rpm). The polymeric solution flows wholly and radially covers the substrate caused by centrifugal force at these high rotational speeds. This step usually takes a few seconds, and the solvent evaporates quickly.

Spin-off occurs when the film of the polymeric solution becomes thin due to convective stable outflow made by the centrifugal force, and the excess polymeric solution is removed from the edge of the substrate as droplets, leaving a thin film.

Evaporation is the drying step, where the polymeric layer occurs and the remaining solvent has evaporated.

Some parameters, such as the initial polymer concentration, the viscosity of the polymeric solution, the spin speed, and the volatility of the solvent, affect the final thickness of the films [74].

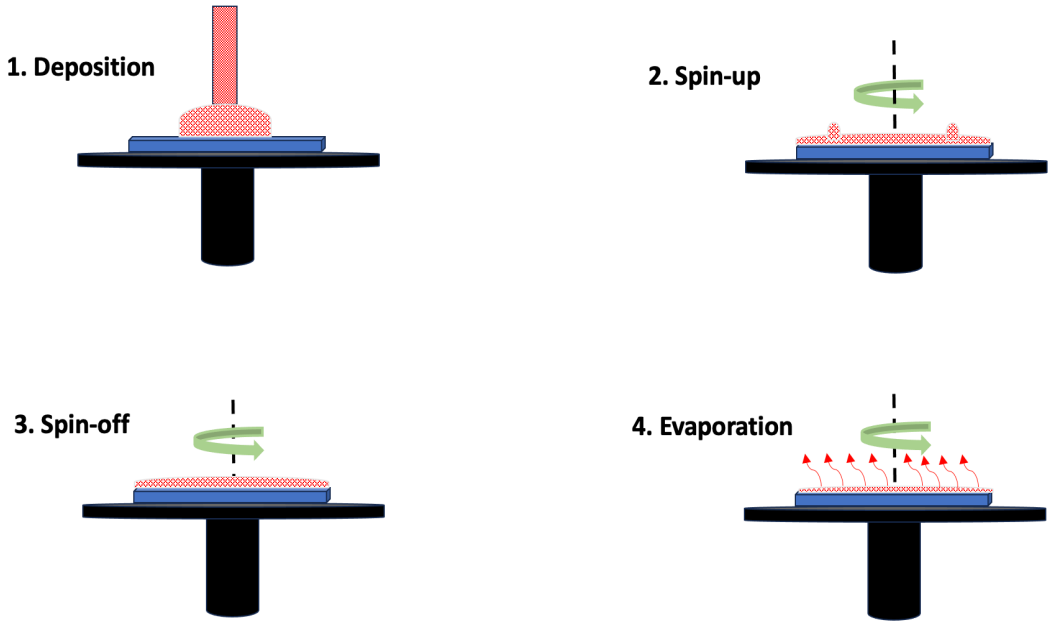

Figure 2.10 A schematic drawing of the spin coating steps.

The thin film can be removed from the substrate by floating it on distilled water. The floating film can be collected on a thin nylon loop (10 lbs breaking strength) or TEM grids (section 3.5). The film should be supported to allow it to be picked up quickly by the nylon loop underneath it (Figure 2.11 and Figure A.1 in the appendix). It is wise to trim the film using a scalpel to the specified dimensions before laying it on a grid. This will prevent any overlapping of the films when they are collected [74]. In our experiments, the more polystyrene the film has and the thicker it is, the better it floats effortlessly. We could not float almost all of the samples; we resorted to spin coating them on Kapton tape (made of polyimide), and then staining them afterwards.

Most polymer materials can be dried in air without changing their structure, and a thin film of polymers should be dried before staining (section 3.4) [4].

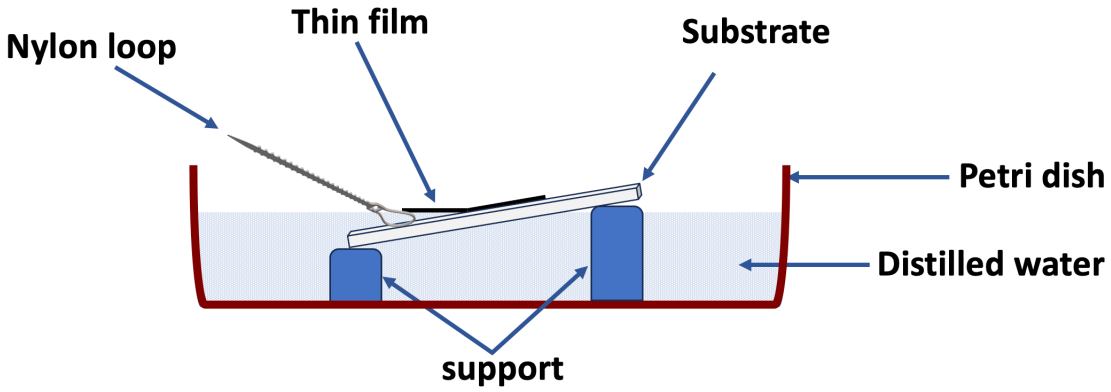

Figure 2.11 A schematic drawing of the thin film floating.

2.9 Experimental Techniques

Microscopy typically involves investigating a sample via radiation transmitted through or reflected from it. Consequently, optical and electron microscopy give complementary information about samples over different length scales. The image's information and quality depend on the microscopy's resolution and contrast. Optical microscopy allows observation of the sample over scales of tens of microns. Electron microscopy allows seeing more detail in the sample than optical microscopy because the electron wavelength is much smaller than that of light, which helps see smaller objects. However, a light microscope saves time and effort by checking the sample and getting a first view to discard any unneeded or poor samples [77].

This section gives more details and explanations about optical and electron microscopy. In addition, there is a discussion about atomic force microscopy (AFM), used in this research to study the topography of thin films and their structures on short, sub-micron length scales. Moreover, an explanation of ellipsometry was also used in this project to measure thin film thickness, besides giving some details about the contact angle measurement device (goniometer).

2.9.1 Contact Angle Goniometer

A contact angle goniometer that measures the contact angle accurately can study surface wetting and interfacial phenomena. The contact angle is essential to understanding wetting behaviour because it is influenced by liquid surface tension, the surface energy of the solid, and the intermolecular forces at the liquid-solid interface.

The contact angle refers to the angle between a liquid droplet and the solid surface it rests on (see Figure 2.8). This angle is determined for several points along the droplet perimeter, and the average is often reported for high accuracy. A low contact angle suggests substantial wetting and good adhesion between the liquid and the surface, while a high contact angle indicates poor wetting and a limited interaction [78].

The contact angle goniometer consists of a stage to hold the sample on, a light source, a micrometre syringe, and a high-resolution camera to obtain clear images that can be analysed geometrically by contact angle software (Figure 2.12) [79].

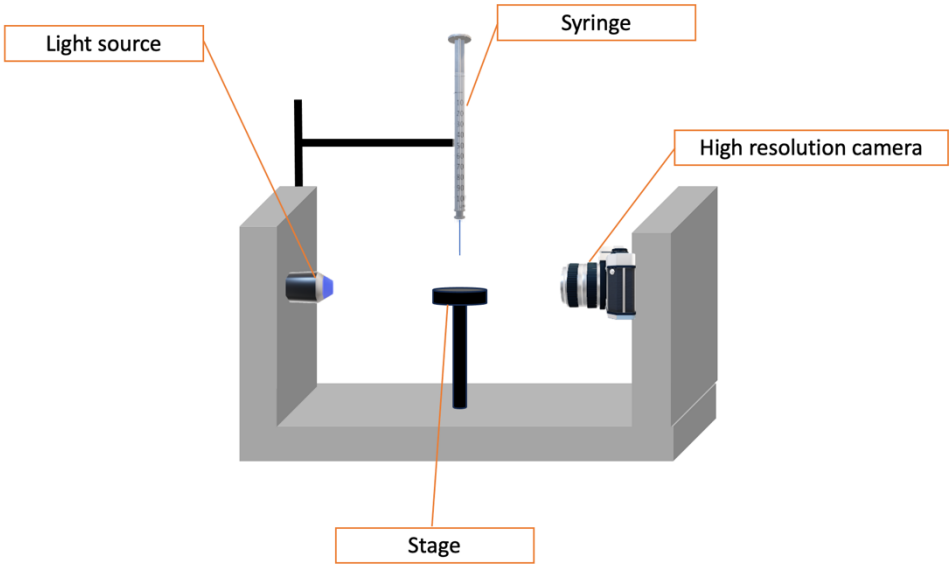

Figure 2.12 A schematic drawing of a contact angle goniometer.

2.9.2 Optical Microscopy

Optical microscopy has been used extensively in scientific research. It is a technique to provide magnified images of the sample using a series of glass lenses with visible light. The specimen is illuminated by the visible light transmitted through or reflected off the sample's surface. The light is focused on the surface by a condenser lens placed under the specimen. Then, the passing light will go through two magnifying lenses (usually, a compound microscope has at least two lenses); the first is the objective lens, and the second is the ocular lens. The magnification of the final image is usually the objective lens magnification times the ocular magnification. The magnification can be increased using more lenses or an objective lens with a short focal length [80]. A detector, the eye or a digital camera can project the final image [81]. The resolution of the optical microscope reaches from below a micron to macroscopic length scales [82].

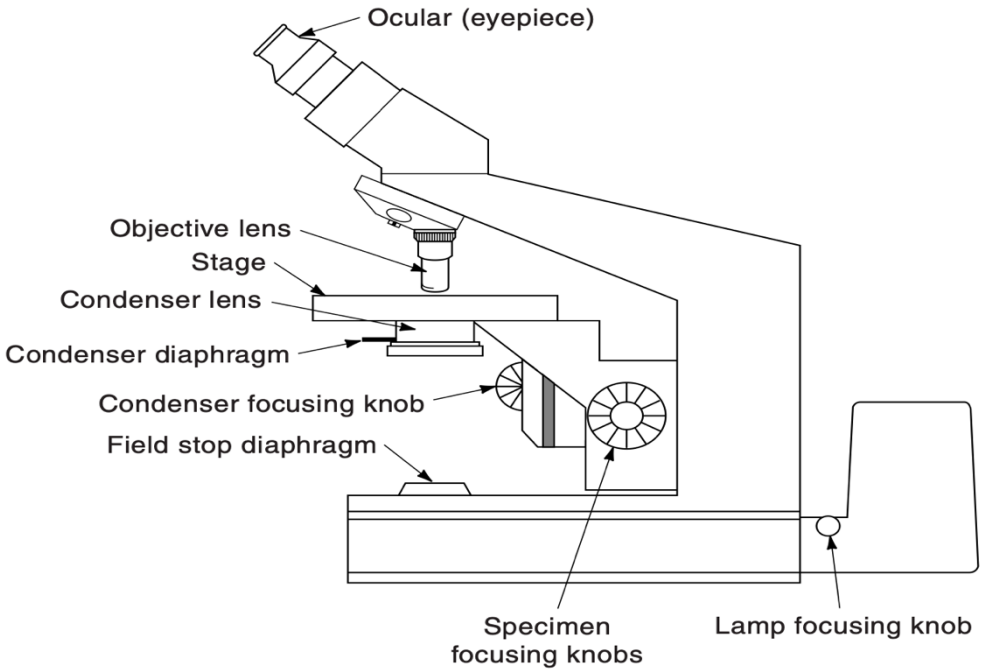

Figure 2.13 A schematic drawing of an optical microscope and its components. This figure is taken from D. B. Murphy 2001 after permission from the publisher [81].

2.9.3 Spectroscopic ellipsometry

Ellipsometry is a non-contact instrument for measuring thin film thickness. It measures the polarisation change that occurs when polarised light is reflected or transmitted after being incident on a sample. Therefore, it is an optical technique used primarily to measure this change in the polarised light, which can give information about some properties of the material, such as thickness and refractive index.

The polarisation of the light details that electric field in terms of its components: s-polarised (component oscillates perpendicular to the incident plane) and p-polarized (component oscillates parallel to the incident plane). Ψ(Psi) and Δ(Delta) are the main parameters that are measured by an ellipsometer to characterise the change in the polarised light ρ , which is the complex reflection coefficient, equation (2-34). Ψ is the amplitude ratio of s and p after reflection, and Δ is the phase difference between s and p. The central ellipsometer equation (2-34) that compares the initial and the final state of polarisation is as follows [83]–[85]:

$$\rho = \frac{r_p}{r_s} = \tan(\psi)\, \mathrm{e}^{i\Delta}, \qquad (2\text{-}34)$$

where r_p and r_s are the amplitudes of the s and p after reflection and normalised to their initial values, and they are complex numbers.

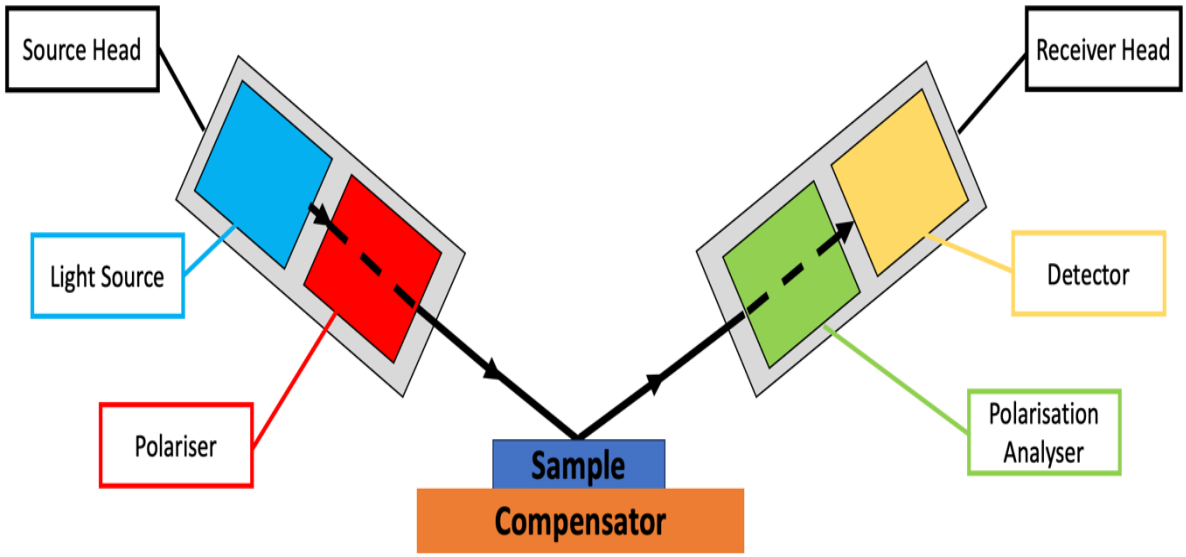

Figure 2.14 A schematic drawing of an ellipsometer and its components.

Ellipsometers typically include an unpolarised Light Source, a polariser that converts the light to linearly polarised light, a Step Scan Rotating Compensator, a polarisation analyser and a Spectrometer Detector. They also have a vacuum chuck to firmly hold the sample on the step (see Figure 2.14) [86].

2.9.4 Atomic force microscopy (AFM)

Atomic Force Microscopy (AFM) is one of the family of scanning probe microscopes (SPM) and is used to scan solid surfaces with a highly sharp cantilever. The SPM technique measures interactions between a highly localised tip and the sample as a function of position. Varying kinds of SPMs depend on the different types of these interactions [87].

AFM gives direct quantitative surface imaging of micro- and nanostructures of conductors and insulators with atomic resolution. It can be applied in different experimental conditions, such as ambient, vacuum, and increased temperature. It uses minimal interaction forces between the apex of the tip and the sample surface to control the distance between them. By applying unique investigation modes, these

interaction forces give helpful information about the sample, such as polymer properties, adhesion, friction, and elastic/ plastic mechanical properties [87], [88].

AFM scans a sharp tip over the sample's surface and measures its interaction. AFM instruments typically include (Figure 2.15):

Cantilever: It is a force-sensing device with a sharp tip integrated at its free end. When the tip interacts with the sample's surface, the cantilever deflects. This deflection is measured from a piezoelectric response to create topography images. The piezoelectric material is part of a feedback loop to control the position of the cantilever relative to the sample.

Tip: It ends with a sharp apex. The sharpness of the tip is critical to achieving high resolution. The tip types differ for each application, for example, conducting tips for electrical measurements and magnetic-coated tips for magnetic imaging.

Detection System: A laser beam is focused on the back of the cantilever, and the photodiode detects the reflected light. As the cantilever deflects, the reflected laser point on the photodiode changes, allowing precise deflection measurement.

Control System: It receives the measured signal as input and gives the controlled signal to the nano-positioning device and maybe the cantilever holder.

Nano-positioner: It holds the sample securely and allows the precise position of the sample concerning the cantilever in the x, y, and z directions [89].

AFM offers various modes of operation, each designed to meet specific experimental requirements. Three basic modes measure the attractive or the repulsive intermolecular interaction force.

In contact mode, the tip is in constant contact with the sample during measurement. Therefore, keeping the force constant at the set point, the z-piezo position will track down the sample topography. However, continuous contact may damage the sample or tip, so contact mode is suitable for rigid and flat surfaces [4], [87].

In non-contact mode, the tip is at a certain distance above the sample's surface without physical contact between them. The van der Waals interaction forces between the sample's surface and the tip are measured, and it needs to be performed most of the time in high vacuum conditions. Therefore, the non-contact mode is suitable for delicate surface samples but requires precision and a sensitive detection system. For this reason, the non-contact mode is the least popular mode of the AFM [87].

In tapping mode, which is known as intermittent contact mode, the tip intermittently contacts the sample surface, and that is what made this mode solves some of the problems of contact mode and non-contact mode. The cantilever is oscillated with constant amplitude near or at its resonant frequency. On each oscillation cycle, the tip taps the sample's surface for a very short time. Tapping mode is the standard researchers used to measure the material's morphology, such as polymer [87].

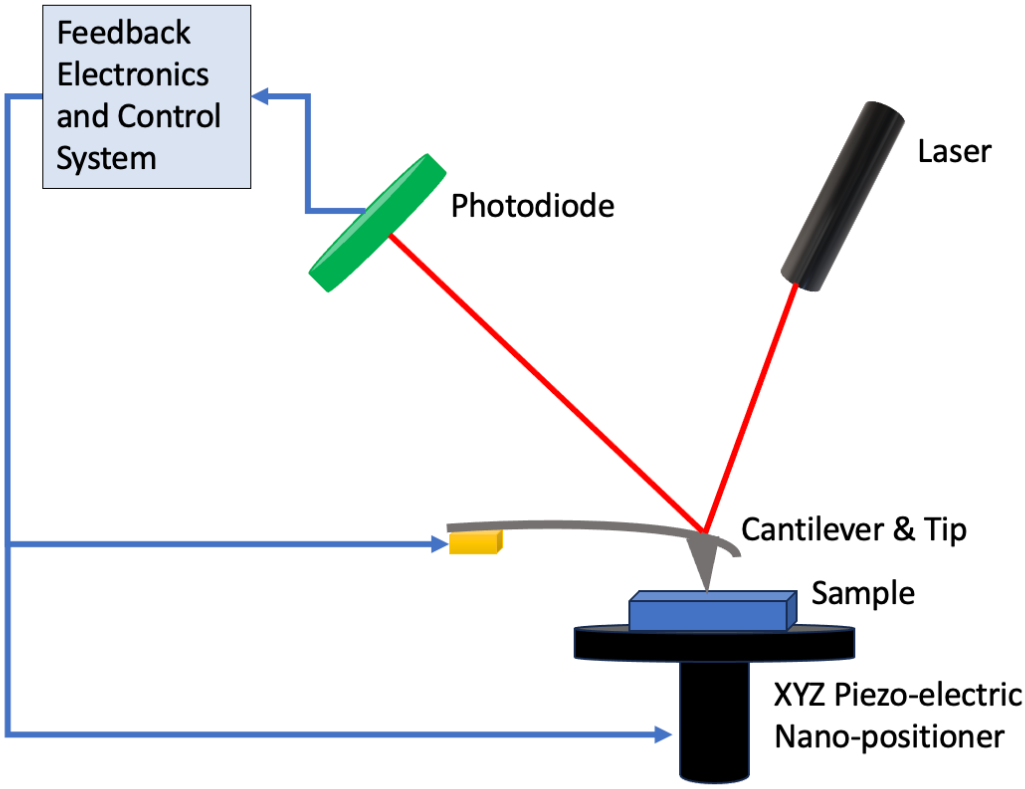

Figure 2.15 A schematic drawing of AFM and its essential components.

2.9.5 Scanning electron microscopy (SEM)

The underlying principles of an electron microscope are not dissimilar to those of an optical microscope. Both depend on a beam of radiation entering the sample, and that radiation will interact with the sample to create an image. Using an electron beam instead of a light beam has increased the magnification range [90].

To achieve good resolution, the electron microscope needs a high vacuum condition to prevent electrons from being scattered by the atmospheric particles [77]. Therefore, the electron beam travels from the gun (a cathode) to the specimen and from the

specimen to the camera or viewing screen within high vacuum conditions. The specimen should also be clean and not include contaminants, so it must be stable and prepared well to show its structure without contamination [90], [91].

The electron beam is emitted from its source (a cathode), which can be a thermionic or a field emission source. Thermionic emission occurs when the filament is heated to a high temperature to release the electrons. In contrast, field emission happens when electrons are emitted by applying a strong electric field to the filament [92].

Moreover, the electron microscope uses electromagnetic coils and a high voltage (anode) to accelerate the electron beam down toward the specimen [93]. The larger the accelerating voltage, the shorter the electron wavelength and the better the resolution. De Broglie's relation states that

$$\lambda = \frac{h}{p}, \tag{2-35}$$

where λ is the wavelength, *h* is Plank's constant and *p* is the momentum. Equation (2-36) can relate the acceleration voltage (*V*) of the electron beam with the electron wavelength as follows:

$$\lambda = \frac{h}{p} = h\left[2eVm_o + \left(\frac{eV}{c}\right)^2\right]^{-\frac{1}{2}}, \tag{2-36}$$

e is the electron charge, m_o is the electron rest mass, and *c* is the light velocity in the vacuum [92]. For instance, when the acceleration voltage is 1250 kV, the electron's wavelength reaches 0.000736 nm [94].

The electron beam is focused and directed onto the specimen using a series of electromagnetic lenses. The number and the positions of these lenses differ from one kind of electron microscope to another (Figure 2.16). Condenser lenses are the first lenses encountered by the electron beam after leaving the electron gun. They focus the electrons into a converging beam. Objective, intermediate, and projector lenses act to magnify and project the beam to the spot under study at the specimen [92]. EMs have fluorescent screens or detectors to present and detect the final image.

There are two main electron microscopy techniques: scanning and transmission electron microscopes. Their primary differences are how they work and what images they can produce (Figure 2.16).

A scanning electron microscope (SEM) scans a focused electron beam over the specimen line by line. Detectors collect the signals from the interaction between the

specimen and the electron beam [95]. The three most important signals produced from this interaction are backscattered electrons, secondary electrons and X-rays. **Backscattered electrons** are scattered back elastically by the nuclei in the specimen and then escape from the surface and have high energy. They are detected by a detector placed above the specimen, and they give information about the material composition (surface topography contrast). **Secondary electrons** result from the top few nanometres of the specimen by the interaction between the primary electrons beam and the electrons within the specimen atoms, which have low energy. The secondary electron detector provides topography information. Usually, **X-ray photons** are emitted when an electron from the outer shell of an atom falls into the inner shell after the secondary electron is released. The X-ray detector displays information about the distribution of different elements on the surface of the specimen [4], [95].

Nonconductive materials such as polymers constitute a significant problem in SEM because when the electron beam hits the sample, charge rapidly builds up. They need previous preparations, which require a conductive coating. This can be done, for example, by a sputter coater that can cover the sample with a thin layer of a conductive material such as gold or copper. This coating enhances the surface structure resolution, which can reach several nanometres. Sputter coaters have the advantages of a short preparation time of about 5-10 minutes and uniform coatings on rough-textured specimens [4], [95].

2.9.6 Transmission electron microscopy (TEM)

TEM can achieve a high resolution extending to 1nm due to the shorter wavelength of the electron beam as the applied acceleration voltage increases, usually 100-300 kV. Therefore, in TEM, the electron beam is transmitted through an ultra-thin specimen (less than 100 nm), allowing the electrons to penetrate without losing much energy (see section 3.5). Thus, internal structures may be observed and visualised on a fluorescent screen [4], [77], [90], [95].

To enhance the contrast in TEM images, samples need previous special preparation. For example, many samples are too opaque for electron microscopes to analyse. Hence, they need staining techniques with heavy elements, making their structures more visible so regions in the specimen with higher electron density appear darker than regions with lower electron density (see section 3.4) [96].

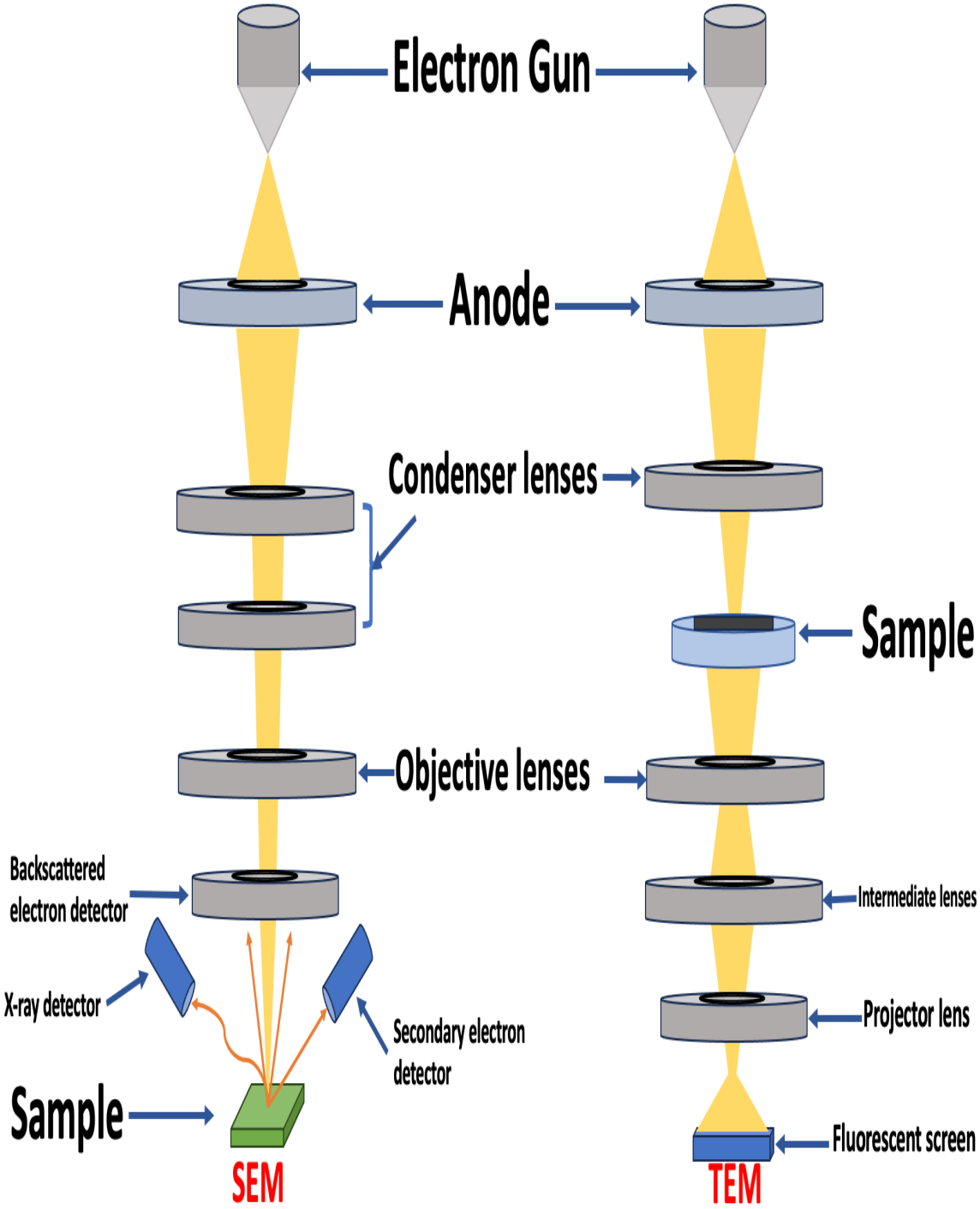

Figure 2.16 A schematic diagram of SEM and TEM.

2.9.7 X-ray Photoelectron Spectroscopy (XPS)

Surface analysis can be performed using X-ray photoelectron microscopy (XPS), in which a sample is irradiated with monoenergetic X-rays, and the energy of the detected electrons is analysed. Usually, Mg Kα (1253.6 eV) or Al Kα (1486.6 eV) X-rays are used. These photons can go into a solid on the order of 1-10 μm. They interact with the core electrons of the sample surface atoms. Electrons ejected from the surface are energy-filtered through a hemispherical analyser (HSA). After that, a detector records the intensity of a defined energy (Figure 2.17).

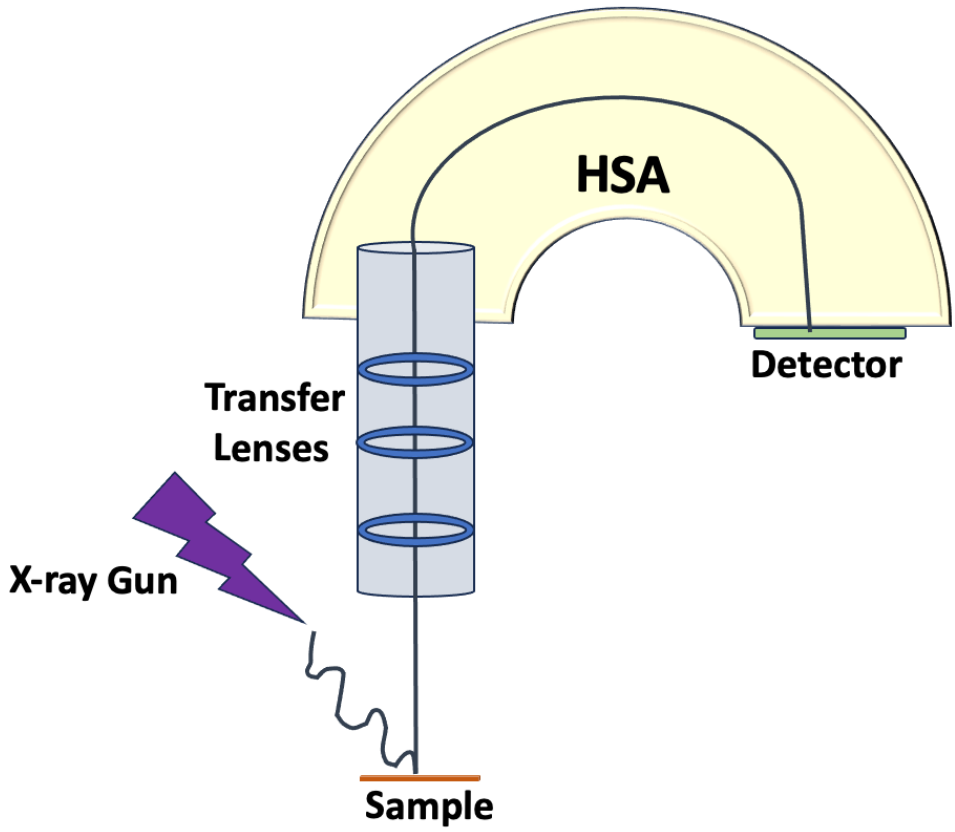

Figure 2.17 Schematic drawing of XPS instrument.

As a result, ionised states are created in the surface of the film, producing electrons that are emitted photoelectrically. Their kinetic energies can be measured by

$$\mathrm{KE} = \mathrm{h}\nu - \mathrm{BE} - \Phi \tag{2-37}$$

where $\mathrm{h}\nu$ is the energy of the incident photon, BE is the binding energy of the atomic orbital from which the electron emerges, and Φ is the material work function. The binding energy is considered as the difference between the initial and the final states

after the photoelectron has left the atom. This equation (2-37) implies that a scan of photoelectron energies provides information about the different bonds at the surface of the sample since the photon energy is constant. Also, each element has a unique set of binding energies that XPS can use to determine the concentration of the elements in the surface and give information about the chemical shift that is used to identify the chemical state of the materials being analysed, whether the electrons are of isolated atoms or if the atoms are involved in a chemical bond. The resulting spectrum from a mixture of elements is the sum of the peaks of the individual constituents, which is obtained as a plot of the number of detected electrons per time and their binding energies [29], [97]–[99].

2.9.8 Ion Beam Microscopy (IBM)

Ion beam analysis (IBA) is often used with light ions and small accelerators. These light beams, usually protons or alphas, generate backscattered ions, which are detected to indicate the depth profile [100]. The depth profile is obtained based on the energy loss of the incident beam and the energy of the scattered or recoiled nuclei.

2.9.8.1 Rutherford Backscattering Spectroscopy (RBS)

Rutherford backscattering (RBS) is a technique that uses charged particles, typically $^4He^+$ ions, to determine the depth profile of materials. It has a depth resolution of 100-300 Å in a solid region up to 1 μm deep. Based on the detected energy, RBS can distinguish the atomic masses of the elements and their distribution in depth.

The ion beam from an ion accelerator hits the sample, and α-particle beams interact with it. Some ions are elastically scattered from the sample's surface atoms, whereas others pass through the sample by losing some energy and are then backscattered at different depths. Detectors and electronics techniques detect and analyse these backscattered particles to obtain the final results (Figure 2.18). The resulting spectrum represents a function of the number of the backscattered α-particles and their energy, which gives information about the nature of the elements in the sample and their depth distribution [101], [102].

The scattered energy E is given by

$$E = K\,E_0 \tag{2-38}$$

where E_0 is the incident energy and K is the kinematic recoil factor, which gives the energy ratio before and after scattering. K depends on the target mass M and the

projectile mass m on the scattering angle θ. For example, K at $\theta = 180°$ is obtained by

$$K = \left[\frac{M-m}{M+m}\right]^2 \tag{2-39}$$

K increases with the target mass, and heavier masses are more accessible to get good data because as the ion beam passes through the sample, it loses energy in collisions, and this will, in turn, reduce the backscattered energy, which is further reduced when it goes deeper towards into the sample. For this reason, with a lighter element mass than the ion beam mass, it is difficult to detect it, and no actual backscattering can take place at all with hydrogen. Moreover, for the same reason, a heavier element close to the substrate may express equal backscattered energy to a lighter element at the surface, which makes the data analysis more complicated.

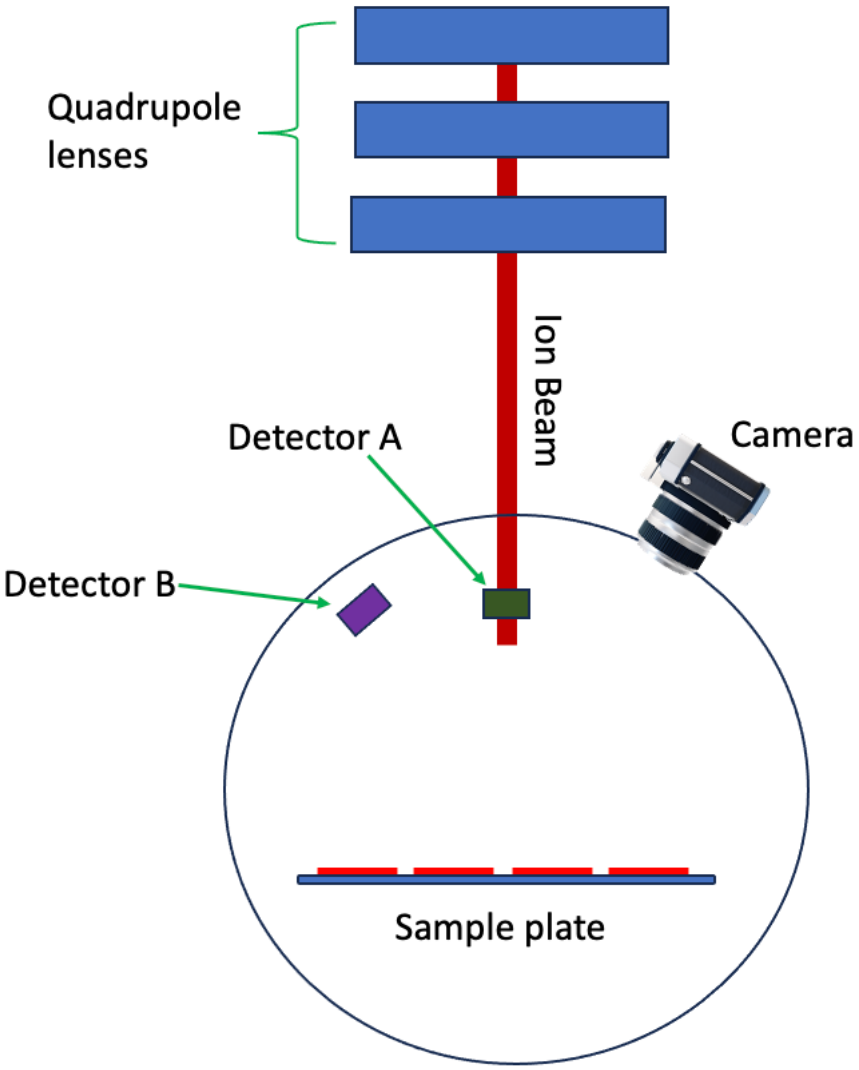

Figure 2.18 Schematic drawing of RBS experimental setup.

2.9.8.2 Time of Flight - Elastic Recoil Detection (ToF-ERD)

Time of Flight – Elastic Recoil Detection (ToF-ERD) is another technique for ion beam analysis (IBA) and is available as a thin film analytical technique. ToF-ERD can determine polymer sample compositions and give the depth distributions for most elements (including hydrogen) within the sample. ToF-ERD uses heavy ion beams such as chlorine (Cl) and iodine (I) to enter and interact with the sample. This allows the measurement of light and heavier elements, like hydrogen and osmium (Os). The sample is set on a goniometer, allowing the measurement of the incident heavy ion beam angle and the recoil atoms angle (Figure 2.19). The sample atoms are knocked out of the sample and then pass through two timing foil gates, T1 and T2. After that, the resulting beam passes through a gas ionisation chamber (GIC). Recoiled atoms' and scattered ions' energy and time of flight give information about sample individual elements' masses and depth profiles [103]–[106].

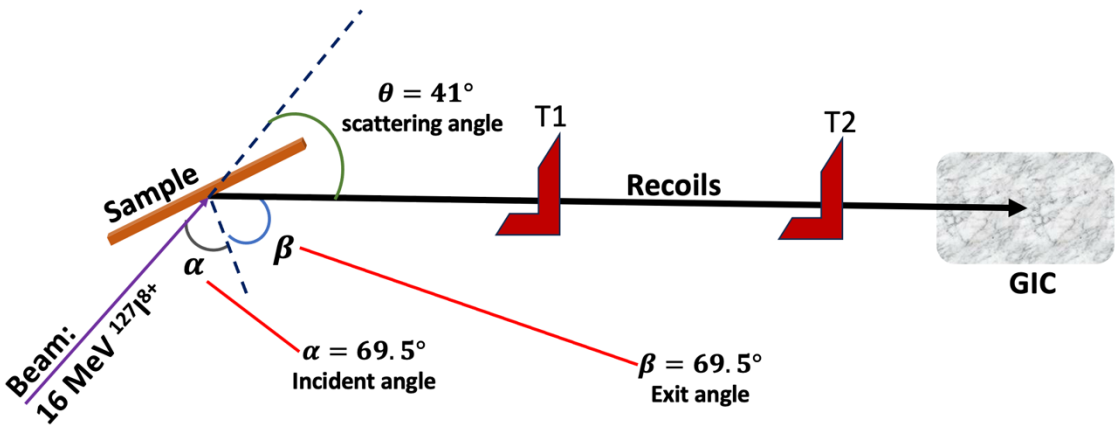

Figure 2.19 Schematic drawing of ToF-ERD experimental setup.

Chapter 3. Materials and Methods

3.1 Introduction

Polymer blends are the materials used to make our spin-coated thin films, which are thoroughly discussed and prepared in section 3.2. To delve into these films' morphology and surface energy, we have employed various techniques, which will be elaborated on in the upcoming sections.

3.2 Materials and Preparing Samples

This work studies five spin-coated thin film blends with differently concentrated solutions to obtain surface energy measurements. The blends contain two immiscible polymers: polystyrene (PS) and polybutadiene (PB).

These are PS (M.W. = 4 kg/mol) and PB (M. W. = 3 kg/mol); PS (M. W. = 50 kg/mol) and PB (M. W. = 53 kg/mol); PS (M.W. = 290 kg/mol) and PB (M.W. = 200 kg/mol); PS (M.W. = 290 kg/mol) and PB (M.W. = 3 kg/mol) and PS (M.W. = 4 kg/mol) and PB (M.W. = 200 kg/mol). Table 3.1 displays each blend specification. These were all measured at polymer mass ratios (PS:PB) of 0:1, 1:3, 1:1, 3:1, and 1:0. These ratios were selected to cover the most compositional spectrum, ranging from pure PB (0:1) to pure PS (1:0). The intermediate ratios of 1:3, 1:1, and 3:1 facilitate a thorough exploration of the blending behavior in both PS-rich and PB-rich regions, including the symmetric blend (1:1), which is often vital for detecting phase transitions, miscibility, and morphological changes. This systematic variation allows for a comprehensive understanding of how the relative proportions of each polymer impact film formation, microstructure, and physical properties. The solutions containing the solvent, toluene-anhydrous, with a purity of 99.8%, have varying concentrations of polymers ranging from 0.13 vol.% to 47 vol.%. The polymer volume fraction is calculated by first determining the volume of each chemical in the system (PS, PB, and toluene), then dividing the sum of the PS and PB volumes by the volume of toluene.

Toluene was used as the primary solvent. A spin coater, KW-4A (CHEMAT TECHNOLOGY INC.), spun the films for 30 seconds at 2000 rpm. The films were spun-cast onto glass (1 mm thick) or silicon (525 $\mp$ 25 μm thick) substrates at room temperature [14], [22]. Some solutions are left on a stirrer for one day to ensure good mixing.

Blend No.	Polymer	Label as in text and figures	Source	M_W (kg/mol)	M_n (kg/mol)	PDI M_W/M_n
1	PS[1]	PS (M.W. = 4 kg/mol)	Sigma – Aldrich, SIAL	3.97	3.88	1.02
	PB[2] liquid vinyl-1,2=80%	PB (M. W. = 3 kg/mol)	Polysciences	11.39	10.96	1.04
2	PS[1]	PS (M. W. = 55 kg/mol)	Sigma – Aldrich SIAL	55.0	54.7	1.00
	PB[3] (rich in 1,2 microstructure) (1,2=85% trans-1,4 =9% , cis 1,4 = 6%)	PB (M. W. = 53 kg/mol)	Polymer Source	53.0	50.0	1.06
3	PS[1]	PS (M.W. = 290 kg/mol)	Alfa Aesar ThermoFisher Scientific	288.8	274.6	<1.06
	PB[2] 36% cis, 55% trans, 9% 1,2-vinyl	PB (M.W. = 200 kg/mol)	Polysciences	692.2	254.8	2.7
4	PS[1]	PS (M.W. = 290 kg/mol)	Alfa Aesar ThermoFisher Scientific	288.8	274.6	<1.06
	PB[2] liquid vinyl-1,2=80%	PB (M. W. = 3 kg/mol)	Polysciences	11.39	10.96	1.04
5	PS[1]	PS (M.W. = 4 kg/mol)	Sigma – Aldrich, SIAL	3.97	3.88	1.02
	PB[2] 36% cis, 55% trans, 9% 1,2-vinyl	PB (M.W. = 200 kg/mol)	Polysciences	692.2	254.8	2.7

Table 3.1 Specification of PS and PB in each blend.

[1]Molecular Weight, Molecular Number, and polydispersity values are by Gel Permeation Chromatography (GPC).
[2]GPC values based on polystyrene standard.
[3]Molecular Weight, Molecular Number, and polydispersity values are by Size Exclusion Chromatography (SEC).

3.3 Techniques used

In this work, we used an Ossila Goniometer and its own software or a home-built apparatus using Image J software to measure the contact angle θ in degrees. Water and glycerol were the used liquids, and the droplet volume was 20 μL for all the contact angles measured in this work. For each thin film, we obtained the average contact angle of at least four different water contact angles and at least four different glycerol contact angles; all the measurements were at room temperature. Some of these contact angles were measured for films spun on glass and silicon to ensure they have the same contact angle for the same films.

Then, we calculated the surface energy for each film via MATLAB code to maintain the symmetrical contact angle resulting from water and glycerol for the identical film. MATLAB was used to solve equation (2-33), where $\gamma_{\mathrm{LV,water}}$= 72.8 mN/m and $\gamma_{\mathrm{LV,glycerol}}$= 63.4 mN/m at 20 °C. These two liquids were chosen because they were available at the lab, and they are non-toxic.

In this project, the optical microscope Olympus BX51 was used. Also, a J.A. Woollam Alpha-SE spectroscopic ellipsometer was used to measure film thickness. It has a Quartz Tungsten Halogen (QTH) light source with a 380 nm to 900 nm wavelength. The software for data acquisition is CompleteEASE, where the thickness of the thin films is measured in three steps. At least two angles of incidence were chosen (mostly 65° and 70°), and the sample was aligned after picking the model, silicon (Si) with transparent film, and the model was fitted with the sample measurement to get the thickness of the sample. This model contained the first ellipsometry measurements for the uncoated silicon wafers, which were analysed with a Si model, applying the silicon optical constants available in the instrument's software, namely Si JAW as the substrate layer [107]. The second is the Cauchy layer, which fits the film layer and gets the thin film thickness. To maintain accurate fitting, the mean-squared error (MSE) should be less than 30; MSE is the quality estimator of the difference between the measured data and the model (see Figure 3.1).

We typically use glass as a substrate for the contact angle measurements. However, we must consider the glass transparency in the visible energy range and internal reflections when using ellipsometry [86]. To address this, the backside of the glass substrate was covered with tape before attempting to measure the film thickness using a fitting model called Glass with Transparent Film (with Backside reflection). Unfortunately, the thickness measurement was inaccurate, and it was more

challenging to obtain a suitable fitting. Therefore, all the thickness-measured samples were spin-coated in silicon wafers. They are more accurate than glass due to their greater light reflectivity (not as transparent as glass), thinner, and smoother.

A Nanowizard 3, JPK Instruments (at Newcastle University) was used to perform AFM measurements, and ACTA-50 probes were used throughout. The mode used is QI mode (Quantitative Imaging mode), which allows us to control the tip-sample force fully imparted on the specimen surface and the interaction, which means the signal-to-noise ratio through the scan. This mode makes imaging straightforward and helps protect the samples and the cantilever tips. In this work, we also used the JPK analysis software to analyse the images and calculate the roughness of 21 samples.

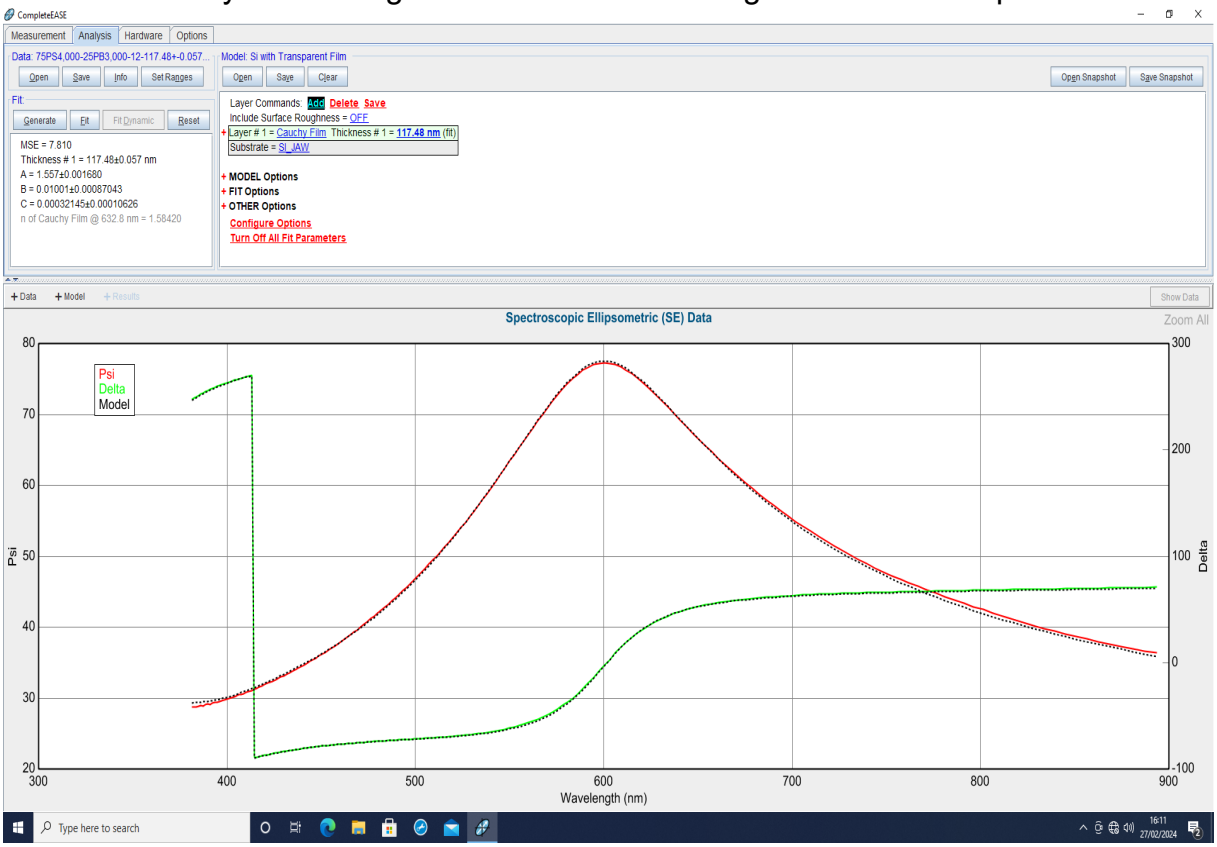

Figure 3.1 A screenshot of an example of the thin-film thickness fitting. This thin film comprises 72.2 vol.% PS (M.W. 4 kg/mol) and 27.6 vol.% PB (M.W. 3 kg/mol). Its thickness is 117.5 nm.

In this work, SEM measurements were recorded on a Supra 40VP Field Emission (Carl Zeiss Ltd., Cambridge, UK) with an average chamber and gun vacuum of 1.3×10^{-5} and 1×10^{-9} mbar respectively. Samples were mounted on the aluminium SEM pin stubs (12 mm diameter, Agar Scientific, Essex, UK). To enhance the contrast of these images, a thin layer of Au/Pd (8 V, 30 s) was sputtered onto the electrodes with the SCP7640 from Polaron (Hertfordshire, UK) before being placed in the chamber.

In TEM, the filament used in this work is lanthanum hexaboride LaB_6. It is heated to a high temperature to emit electrons (thermionic emission), and the applied acceleration voltage is 100 kV.

Generally, three problems are associated with polymers' direct investigation without previous preparation. Firstly, preparing the ultrathin specimens for TEM investigations is usually difficult; less than 1 μm thick and preferably 50-100 nm thick [95]. Secondly, polymers are sensitive to the irradiation of the electron beam. The third is that the structures of the polymer materials often have low contrast due to the same light elements (C, H, O, and others), which interact weakly with the electron beam. Several preparations are required to overcome these difficulties before investigating the polymer materials (films) [108]. The following sections focus on polystyrene (PS) and polybutadiene (PB) blend film preparation.

In addition, surface data of 18 stained samples at approximate depths of 5-10 nm was carried out on a Thermo scientific K-α XPS, using a monochromated Al Anode at 12 kV. All samples were handled with clean tweezers at all times, and three points were analysed per sample. Survey scans were carried out (Figure 3.2) with the following conditions: pass energy of 150 eV and a step size of 0.4 eV, the high resolution scans of C1s, O1s and Os 4f were taken with a pass energy of 40 eV and a step size of 0.1eV.

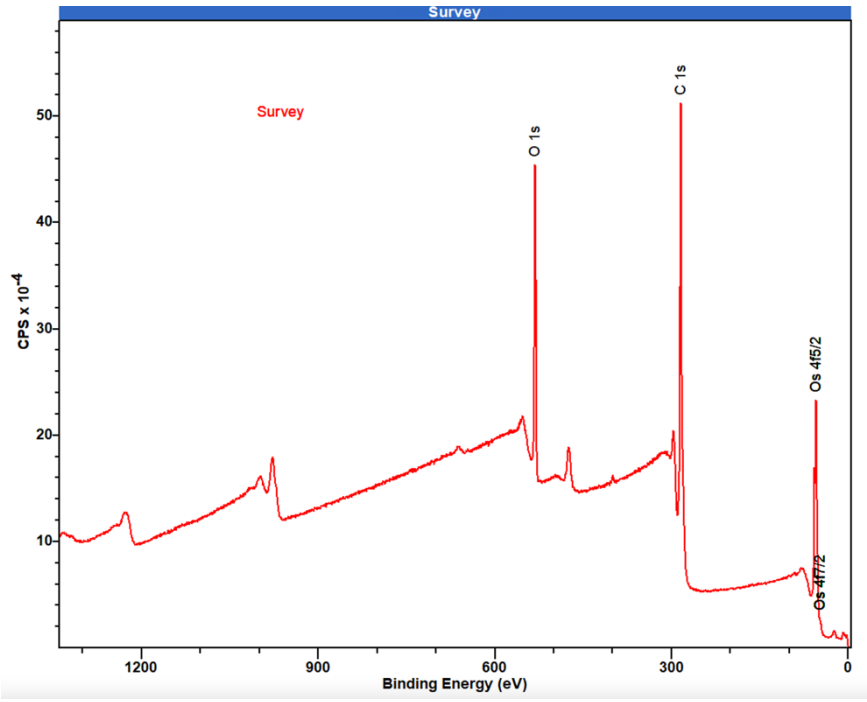

Figure 3.2 A survey spectrum is taken for the surface of a thin film sample comprising 22.4 vol.% by PS (M.W. 55 kg/mol) and 77.6 vol.% PB (M.W. 53 kg/mol). The surface contains 72.7% ∓ 8.4% PB.

The Os 4f spectrum (Figure 3.3) for the three points of all samples has been analysed by Casa XPS software to obtain the amount of PB at the surface. We have calculated the average area under the peaks of Os and then normalised it using pure PB samples.

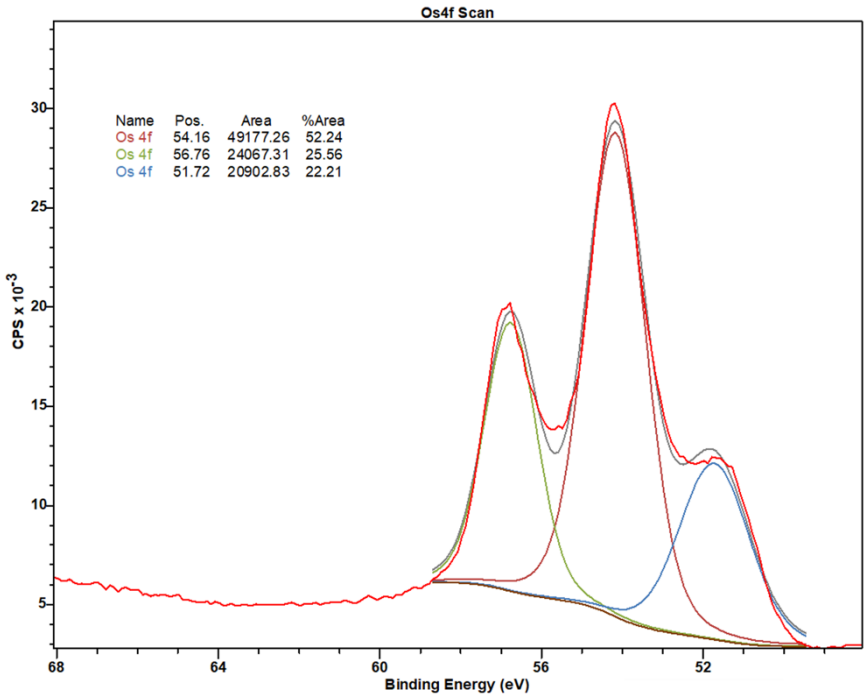

Figure 3.3 Os 4f survey scan spectrum is taken for the surface of a thin film sample comprising 22.4 vol.% by PS (M.W. 55 kg/mol) and 77.6 vol.% PB (M.W. 53 kg/mol). The surface contains 72.7% ∓ 8.4% PB.

This work examined 18 thin film samples at Surrey Ion Beam Centre. The samples were on silicon wafers and stained with osmium tetroxide OsO_4. Measurements were done using a 2 MeV $^{4}He^{+}$ incident beam accelerated by a 2 MV Tandem accelerator with a 2.5 mm beam spot.

The results, a wealth of data, are meticulously analysed using the Potku software. This powerful tool allows us to identify atoms of different masses and generate high-intensity regions, providing precise concentrations for each element within the sample [104].

At the Surrey Ion Beam Centre, 18 thin film samples were examined using ToF-ERD. The samples were carefully prepared and mounted on silicon wafers stained with OsO_4. Measurements were conducted using a 16 MeV $^{127}I^{8+}$ incident beam, while the angles during the experiment were meticulously set, as shown in Figure 3.15.

From the results, a volume fraction of PB with depth for 15 samples was obtained. The normalisation was done using the data of pure film (100 vol. %) PB (M.W. = 200 kg/mol). The Os profile was fitted with depth in a polynomial equation and then the data were divided by it. This accounts for any nonuniformity in the staining. After that, 15 samples of the blend films obtained their volume fraction of PB with their depth using the same equation of the pure (100 vol. %) PB (M.W. = 200 kg/mol). Then, RBS data were compared with ToF-ERD data for all 15 samples to ensure they agreed. Finally, RBS data were convolved with a Gaussian function of width between 5 to 20 nm to make a better comparison.

3.4 Staining and Embedding

The most common method to observe different phases in multiphase polymers is phase contrast of stained thin sections by transmission electron microscopy [4]. Osmium and ruthenium tetroxide staining can help observe dispersed phases in multiphase blends. Staining enhances the contrast due to the increased density of the unsaturated phase [109]. It also makes the sample resistant to damage by the incident electron beam. Polystyrene (PS) and polybutadiene (PB) have similar electron densities (1.04 g cm^{-3} for PS and 0.9 g cm^{-3} for PB). Polybutadiene is unsaturated. i.e. it has double bonds, making it susceptible to damage by the electron beam. However, osmium tetroxide OsO_4 reacts with the double bonds by increasing electron scattering of the heavy metal Os; this provides a good contrast and fixes PB by cross-linking it and making it hard to damage (Figure 3. 4). Ruthenium tetroxide RuO_4 is an oxidising agent similar to OsO_4 in unsaturated phases but is known to split double bonds or rings rather than bond to them. An instance of RuO_4 attacking the polystyrene benzene ring can be observed in the staining process of polystyrene. Therefore, we did not use it in our study [4].

However, we should know that both are hazardous chemicals; osmium tetroxide is more toxic, whereas Ruthenium tetroxide is the more potent oxidising agent. Thus, specific handling and special care should be taken during the staining in a fume hood with excellent ventilation [4]. Therefore, all necessary measures were taken to ensure the safe handling of OsO_4 or its vapour during preparations. These measures included carrying out the procedures in a well-ventilated fume hood and always wearing gloves and goggles. Furthermore, the equipment and glassware were thoroughly washed with water before removing them from the fume hood. A significant amount of excess waste,

including empty containers of OsO_4, was mixed with fat and disposed of following local regulations.

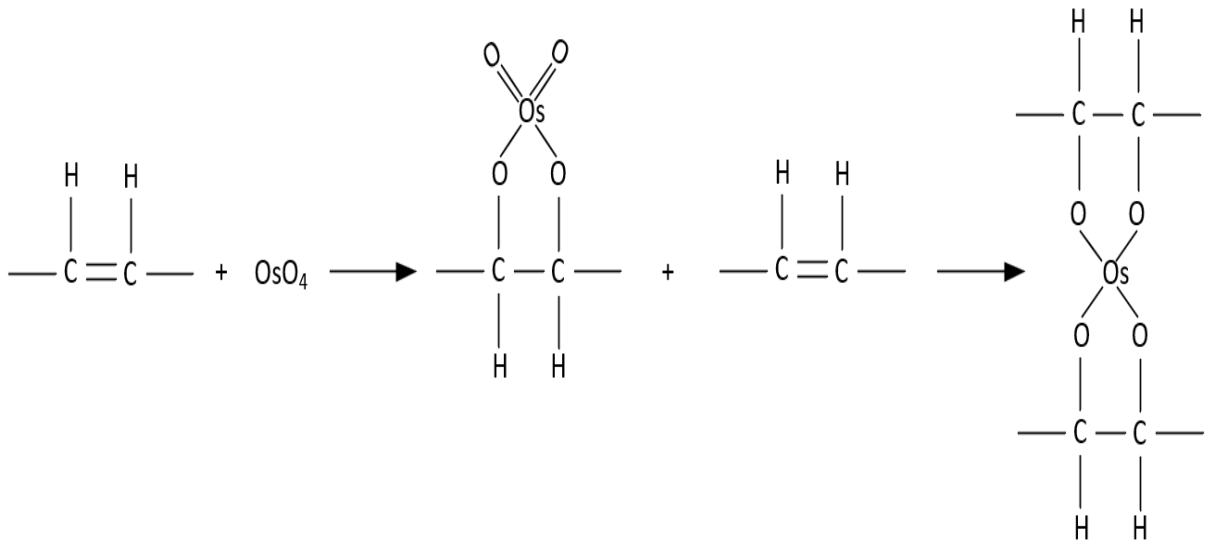

Figure 3.4 The chemical equation of how osmium tetroxide interacts with the double bond.

As previously stated, staining involves introducing dense elements into the film structure. Consequently, staining can cause changes in film thickness, which must be considered when analysing microscopy images. A study compared the lamellar structure of thin films of polystyrene-block-polyisoprene before and after staining by osmium tetroxide vapour for an hour [110]. They concluded that staining caused the stained phase to swell by a factor of 1.15 in the plane and compressed the unstained phase to 0.71 of its original size. Another study has observed an increase in the lamellar period (refers to the thickness of the individual) thin films of three symmetric deblock copolymers of polystyrene-polybutadiene, polystyrene-poly(methylmethacrylate), and polystyrene-poly(4-vinylpyridine), after staining by OsO_4, RuO_4, and Iodine I_2, respectively [109]. Similar trends in the change of the lamellar period were found in the three cases, and the maximum ratio of the stained to the untreated was close to 1.23.

In this study, spin-coated thin films that were either picked up on a net, on a silicon substrate or a glass substrate (covered with 50 μm thick Kapton tape) were left in the air for a couple of hours to be dried, then were stained using the vapour of a 2% osmium tetroxide solution in water, which was purchased from Sigma-Aldrich. After labelling each, the floated films and films on the substrate were placed in small Pyrex

petri dishes. A few drops of osmium tetroxide solution were placed in a small Pyrex petri dish with a glass pipette. All dishes were put in a large, covered petri dish. This large Pyrex petri dish was placed on a support in a beaker with water, to cover just the base of the lower Pyrex petri dish (water bath not to sink or immerse in). The beaker with water was heated to 50 °C and 60 °C under a fume hood to evaporate the OsO_4 solution. Firstly, four different blends of thin films were stained for 10, 20 and 30 minutes each (Table A.1 in the appendix). The optical microscope Olympus BX51 images were used to study film surface morphology before and after staining (Figure A.2 in the appendix). These images were used to obtain information on the structure length scale using a fast Fourier transform (FFT) analysis. Image SXM 201 software was used to get a two-dimensional FFT. The radial intensity distribution from the FFT was obtained to determine the length scale (that gives the distance between domines and the domines average size of a sample) inherent in the film structure (Figure A.3 in the appendix). At this end, we concluded that with the limit of microscopy at that time, 30 minutes would provide good staining for the surfaces and the bulk of our films without damaging the films and changing film morphology. Figure (3.5) shows a schematic drawing of the staining apparatus for one sample.

Then, the film should be embedded for ultrathin sectioning. Three media are generally used: acrylic resins, epoxy, and polyester. The essential features of the embedding medium for polymers are its hardness (a low viscosity), ease of sectioning, and stability in the high vacuum and the electron beam. The epoxy resins are the most stable. However, epoxies can distort the morphology of some surfaces. Resins are low viscosity. Therefore, changes to the recipe of the used medium can be made to get good results. In addition, while using the embedding media, one should not forget the safety information supplied and cured using the times and temperatures recommended by the supplier. Also, the film will not be damaged when the medium is poured into the mould [4], [95].

During the first attempt in this project, LR white medium acrylic resin was used. Unfortunately, this attempt was unsuccessful; it was hard to section the blocks because they were soft, and some samples were twisted after being cured. The successful attempt was with 100% resin. In both attempts, the embedding medium was pipetted into a mold hole or a beam capsule; then, dry-stained films were embedded and left to be cured at 60 °C for 24 – 48 hours. When becoming hard, the blocks are taken off the

mold (or the beam capsule was removed), and the samples are ready for sectioning (Figure A.4 in the appendix).

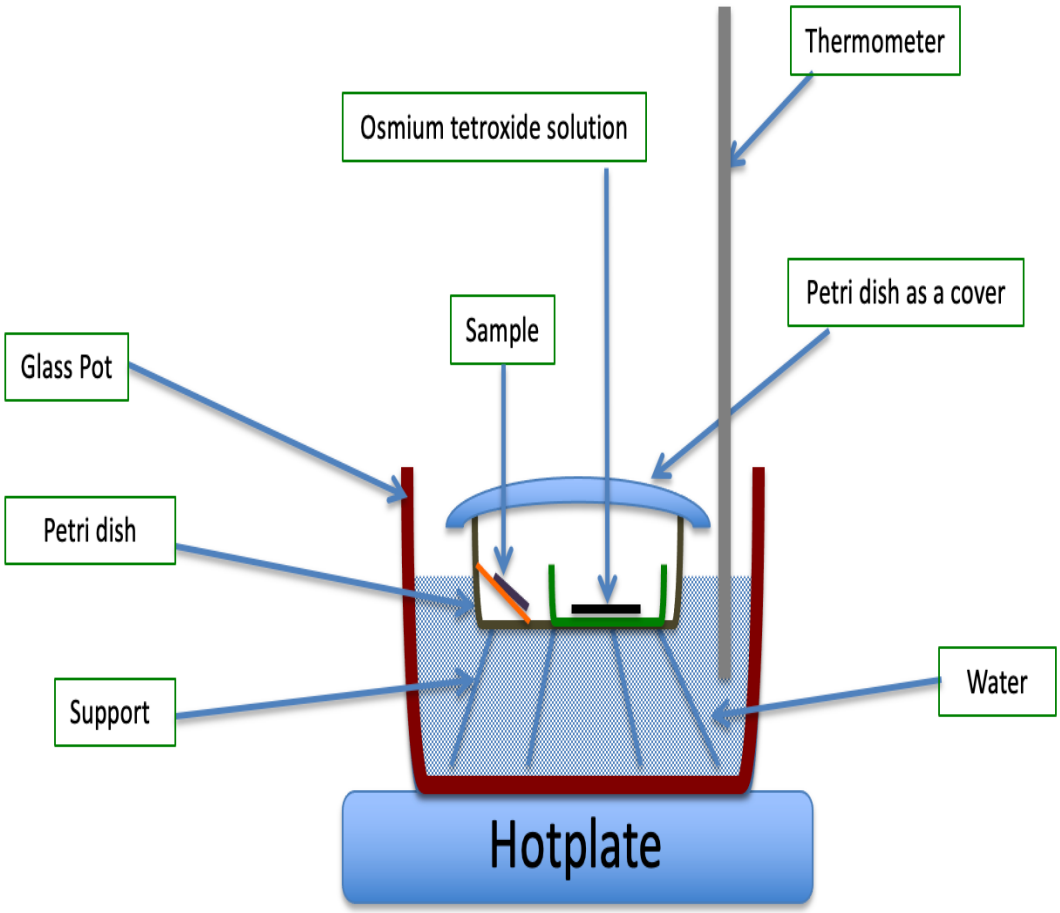

Figure 3.5 Schematic drawing of the apparatus used for staining the samples.

3.5 Ultramicrotomy

The cross-section images under the microscope can investigate the actual structure in the bulk of the thin films. Microtomy permits polymer film preparation and getting the depth profiles of the film. Therefore, the sections should represent the original bulk structure, and they should be thin, flat, not deformed, have contrast, and be easily interpreted by TEM [4].

Trimming is the first step in sectioning, which begins with trimming the excess resin from the block face and the edges of the block using a single-edged razor blade,

making the block shape a trapezium of approximately 0.5 mm^2 (Figure A.5 in the appendix). After that, the trimmed block is placed in the holder of an ultramicrotome perpendicular to the knife's motion. It is advised to begin the sectioning with the glass knife until the film is reached, and then the ultrathin sections (70 nm thick) can be made using a diamond knife. A plastic boat filled with distilled water was attached to the knife, where the ultrathin sections were floated, and some were picked up onto TEM grids. Grids are made of metal such as nickel, copper, and gold and have different shapes, such as square mesh, hexagonal mesh, and parallel bars. Copper is the common one. Then, the grids should be placed on filter paper to let them dry and be ready to be imaged by the electron microscope [111].

In this project, ultrathin sections (70 nm approx.) are cut using a diamond or glass knife on a Reichert or Leica EM UC7 ultramicrotome and collected on piliform-coated copper grids. The grids are examined on a Hitachi HT7800 transmission electron microscope using an Emsis Xarosa camera with Radius software at (Electron Microscopy Research Services, Newcastle University).

Chapter 4. Results

This study focused on studying spin-coated films with different concentrations of toluene solutions, incorporating five distinct blends of PS and PB. This enabled us to investigate wetting behaviour, depth profiles, phase separation, and surface segregation. The chapter presents the findings of our investigation for each blend, beginning with the results of contact angle experiments, followed by XPS, RBS, and ToF-ERD results, and concluding with presenting microscopic images.

We examined the spin-coated films' water and glycerol contact angles (Figure 4.1) using various concentrated solutions in toluene for all five blends. One example of this relationship is depicted in Figure 4.2.

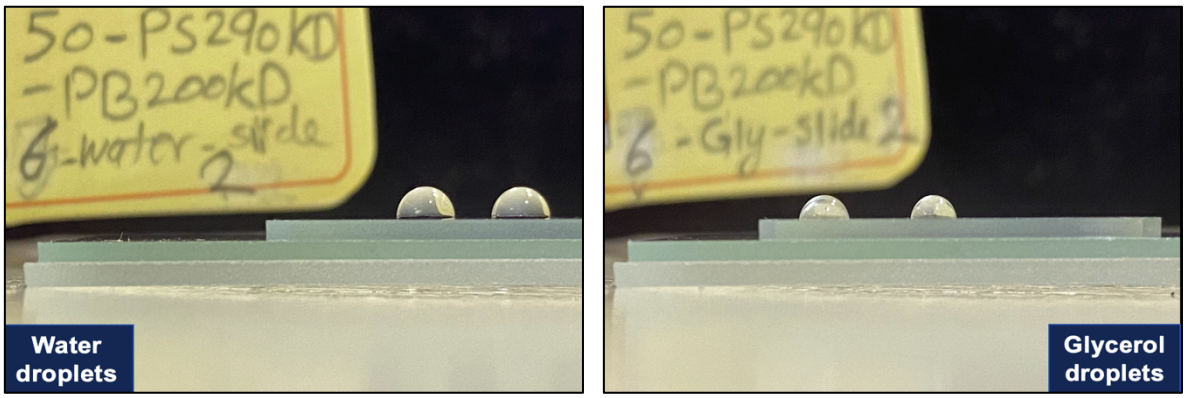

Figure 4.1 An image shows droplets of water and glycerol for the film of 46.4 vol.% PS (M.W.= 290 kg/mol) and 53.6 vol.% PB (M.W.= 200 kg/mol).

4.1 Blend films of PS (M.W.= 4 kg/mol) and PB (M.W.= 3 kg/mol)

We conducted this study to analyse the impact of film thickness on surface energy in blend films comprising 4 kg/mol PS and 3 kg/mol PB. These films were examined at various volume percentages of PB (vol.% PB), including 0 vol.% PB,27.8 vol.% PB, 53.6 vol.% PB, 77.6 vol.% PB, and 100 vol.% PB. All relevant data are available in Table 4.1. Our investigation studied the correlation between contact angles and the polymer volume fraction in toluene, ranging from approximately 0.4 vol.% to 46.6 vol.% (see Figure 4.2). The purple curve represents 100 vol.% PS, while the blue curve represents 100 vol.% PB. The observed difference in contact angles indicates that PS is more hydrophobic than PB, within the polymer volume fraction range of 1.7% to 37.5%.

Blend of	Polymer weight fraction	Polymer volume fraction	Water contact angle (°)	Surface energy((mN)/m)-water	Glycerol contact angle (°)	Surface energy((mN)/m)- glycerol	The Thickness (nm)
100 vol.% PS (M.W. 4 kg/mol)	0.50%	0.42%	19.9 ± 2.3	68.8 ± 1.7	65.5 ± 1.4	37.2 ± 1.6	4.4 ± 1.4
	1.00%	0.83%	30.7 ± 1.6	64.1 ± 1.5	69.5 ± 0.8	34.9 ± 0.9	41.7 ± 0.1
	2.00%	1.67%	83.62 ± 0.05	32.6 ± 0.1	74.5 ± 0.4	32.0 ± 0.5	80.2 ± 0.1
	2.50%	2.08%	84.2 ± 0.1	32.2 ± 0.1	74.8 ± 0.4	31.8 ± 0.5	90.52 ± 0.03
	3.50%	2.92%	85.9 ± 0.1	31.1 ± 0.1	76.6 ± 0.9	30.7 ± 1.0	141.55 ± 0.04
	4.00%	3.33%	86.6 ± 0.1	30.7 ± 0.1	76.9 ± 1.3	30.6 ± 0.4	160.7 ± 0.1
	5.00%	4.17%	87.3 ± 0.1	30.3 ± 0.1	77.66 ± 0.03	30.12 ± 0.03	197.9 ± 0.1
	7.50%	6.25%	87.8 ± 0.1	29.9 ± 0.1	78.4 ± 0.2	29.7 ± 0.3	277.0 ± 0.2
	10.00%	8.34%	88.2 ± 0.1	29.7 ± 0.1	78.4 ± 0.5	29.4 ± 0.6	399.4 ± 0.9
	25.00%	20.84%	89.4 ± 0.1	28.9 ± 0.2	79.8 ± 0.5	28.9 ± 0.6	1415.9 ± 35.1
	35.00%	29.18%	89.6 ± 0.3	28.8 ± 0.4	80.1 ± 0.1	28.7 ± 0.1	1808.5 ± 28.9
	45.00%	37.51%	90.4 ± 0.2	28.3 ± 0.3	80.2 ± 0.1	28.8 ± 0.1	3588.5 ± 3.0
72.2 vol.% PS (M.W. 4 kg/mol) and 27.8 vol.% PB (M.W. 3 kg/mol)	1.00%	0.87%	88.0 ± 0.1	29.8 ± 0.2	78.9 ± 0.3	29.4 ± 0.4	55.17 ± 0.02
	2.00%	1.73%	88.7 ± 0.2	29.4 ± 0.2	79.9 ± 0.4	28.8 ± 0.4	117.5 ± 0.1
	3.50%	3.03%	89.5 ± 0.1	28.9 ± 0.1	80.1 ± 0.1	28.7 ± 0.1	155.1 ± 4.3
	5.00%	4.33%	92.18 ± 0.05	27.2 ± 0.1	82.7 ± 0.1	27.2 ± 0.1	186.0 ± 0.5
	7.00%	6.06%	93.25 ± 0.01	26.51 ± 0.01	83.8 ± 0.3	26.6 ± 0.3	240.0 ± 6.3
	10.00%	8.66%	94.5 ± 0.2	25.7 ± 0.2	85.14 ± 0.03	25.81 ± 0.04	360.9 ± 2.3
	20.00%	17.32%	95.0 ± 0.1	25.4 ± 0.1	85.8 ± 0.1	25.5 ± 0.1	988.7 ± 17.6
	25.00%	21.65%	95.2 ± 0.1	25.3 ± 0.1	85.8 ± 0.1	25.4 ± 0.1	1192.3 ± 30.0
	30.00%	25.98%	95.2 ± 0.4	25.3 ± 0.5	86.01 ± 0.01	25.3 ± 0.01	1203.1 ± 2.6
	35.00%	30.31%	95.3 ± 0.2	25.2 ± 0.3	86.3 ± 0.2	25.2 ± 0.2	2862.9 ± 1.8
	40.00%	34.64%	95.3 ± 0.3	25.2 ± 0.4	86.4 ± 0.1	25.1 ± 0.1	2970.5 ± 2.9
	45.00%	38.97%	96.0 ± 0.1	24.8 ± 0.2	86.7 ± 0.2	24.9 ± 0.2	3618.6 ± 2.4
	50.00%	43.30%	97.5 ± 0.5	23.9 ± 0.6	87.0 ± 0.1	24.8 ± 0.1	4061.5 ± 4.8
46.4 vol.% PS (M.W. 4 kg/mol) and 53.6 vol.% PB (M.W. 3 kg/mol)	1.00%	0.90%	87.1 ± 0.3	30.4 ± 0.4	77.71 ± 0.03	30.09 ± 0.03	63.79 ± 0.05
	2.00%	1.80%	87.8 ± 0.3	30.0 ± 0.4	78.4 ± 0.1	29.7 ± 0.2	127.7 ± 0.2
	3.50%	3.14%	89.07 ± 0.05	29.1 ± 0.1	79.69 ± 0.04	28.9 ± 0.1	144.4 ± 0.1
	5.00%	4.49%	91.0 ± 0.2	27.9 ± 0.2	81.6 ± 0.1	27.8 ± 0.1	192.7 ± 1.0
	7.00%	6.29%	91.4 ± 0.6	27.7 ± 0.8	82.1 ± 0.1	27.6 ± 0.1	256.4 ± 3.0
	10.00%	8.98%	93.3 ± 0.3	26.5 ± 0.4	84.0 ± 0.3	26.5 ± 0.4	323.3 ± 3.6
	20.00%	17.97%	93.8 ± 0.1	26.2 ± 0.2	84.6 ± 0.1	26.1 ± 0.1	438.3 ± 5.3
	25.00%	22.46%	93.9 ± 0.2	26.1 ± 0.3	84.9 ± 0.1	25.9 ± 0.1	624.73 ± 23.4
	30.00%	26.95%	94.5 ± 0.1	25.8 ± 0.1	85.4 ± 0.2	25.7 ± 0.3	1019.2 ± 2.7
	35.00%	31.45%	94.6 ± 0.2	25.7 ± 0.2	85.9 ± 0.1	25.4 ± 0.1	2270.7 ± 1.9
	40.00%	35.94%	95.2 ± 0.2	25.3 ± 0.2	86.2 ± 0.1	25.2 ± 0.2	2850.2 ± 2.6
	45.00%	40.43%	95.5 ± 0.1	25.1 ± 0.1	86.5 ± 0.1	25.0 ± 0.2	2966.1 ± 6.6
	50.00%	44.92%	95.9 ± 0.1	24.9 ± 0.1	86.9 ± 0.1	24.8 ± 0.2	3253.3 ± 5.2
22.4 vol.% PS (M.W. 4 kg/mol) and 77.6 vol.% PB (M.W. 3 kg/mol)	1.00%	0.93%	87.3 ±1.0	30.2 ± 1.3	78.5 ± 1.1	29.6 ± 1.3	65.8 ± 0.1
	2.00%	1.86%	88.4 ± 0.3	29.6 ± 0.4	79.7 ± 0.2	29.0 ± 0.2	117.5 ± 0.1
	3.50%	3.26%	89.4 ± 0.2	28.9 ± 0.3	81.2 ± 0.6	28.1 ± 0.7	218.6 ± 0.6
	5.00%	4.47%	92.2 ± 0.1	27.1 ± 0.1	83.3 ± 0.2	26.9 ± 0.3	292.4 ± 0.7
	7.00%	6.52%	93.2 ± 0.2	26.5 ± 0.3	84.5 ± 0.2	26.2 ± 0.2	412.9 ± 3.8
	10.00%	9.31%	95.2 ± 0.1	25.3 ± 0.2	85.8 ± 0.5	25.5 ± 0.6	726.8 ± 1.1
	20.00%	18.62%	95.3 ± 0.1	25.2 ± 0.1	85.8 ± 0.3	25.4 ± 0.3	1768.3 ± 26.1
	25.00%	23.27%	95.5 ± 0.1	25.1 ± 0.2	86.5 ± 0.2	25.0 ± 0.2	2163.7 ± 1.3
	30.00%	27.93%	95.8 ± 0.5	24.9 ± 0.6	87.0 ± 0.3	24.8 ± 0.4	2212.1 ± 1.3
	35.00%	32.58%	95.9 ± 0.4	24.9 ± 0.5	87.3 ± 0.2	24.6 ± 0.2	2402.4 ± 1.5
	40.00%	37.24%	96.9 ± 0.3	24.2 ± 0.4	87.7 ± 0.2	24.4 ± 0.3	3940.3 ± 1.3
	45.00%	41.89%	98.0 ± 0.3	23.6 ± 0.4	88.2 ± 0.1	24.1 ± 0.1	4341.1 ± 1.6
	50.00%	46.55%	98.5 ± 0.8	23.2 ± 1.0	88.9 ± 0.2	23.7 ± 0.2	5021.0 ± 1.6
100 vol.% PB (M.W. 3 kg/mol)	0.50%	0.48%	70.5 ± 4.9	40.9 ± 6.1	69.4 ± 0.5	34.9± 0.5	4.2 ± 0.1
	1.00%	0.96%	78.8 ± 0.2	35.6 ± 0.3	70.9 ± 0.2	34.1 ± 0.3	83.5 ± 1.5
	2.00%	1.93%	79.9 ± 0.1	35.0 ± 0.1	71.3 ± 0.9	33.8 ± 1.0	193.9 ± 1.1
	2.50%	2.41%	80.1 ± 1.1	34.8 ± 1.4	73.0 ± 0.1	32.8 ± 0.1	273.2 ± 1.6
	3.50%	3.37%	80.7 ± 0.6	34.4 ± 0.7	73.1 ± 0.1	32.8 ± 0.1	395.3 ± 0.6
	4.00%	3.85%	81.8 ± 0.8	33.8 ± 1.0	73.2 ± 0.3	32.7 ± 0.3	408.2 ± 0.5
	5.00%	4.82%	82.4 ± 0.2	33.4 ± 0.2	73.5 ± 0.6	32.5 ± 0.6	513.8 ± 1.6
	7.50%	7.23%	82.8 ± 0.5	33.1 ± 0.7	73.6 ± 0.7	32.5 ± 0.8	1141.6 ± 9.0
	10.00%	9.63%	87.3 ± 0.2	30.3 ± 0.3	79.2 ± 0.2	29.2 ± 0.3	1324.9 ± 11.6
	20.00%	19.27%	88.4 ± 0.1	29.5 ± 0.8	79.6 ± 0.2	29.0 ± 0.2	1378.8 ± 31.4
	30.00%	28.90%	89.7 ± 0.2	28.8 ± 0.3	80.5 ± 0.1	28.5 ± 0.1	2433.2 ± 1.8

Table 4.1 Data from the contact angle experiment of blend films of PS (4 kg/mol) and PB (3 kg/mol).

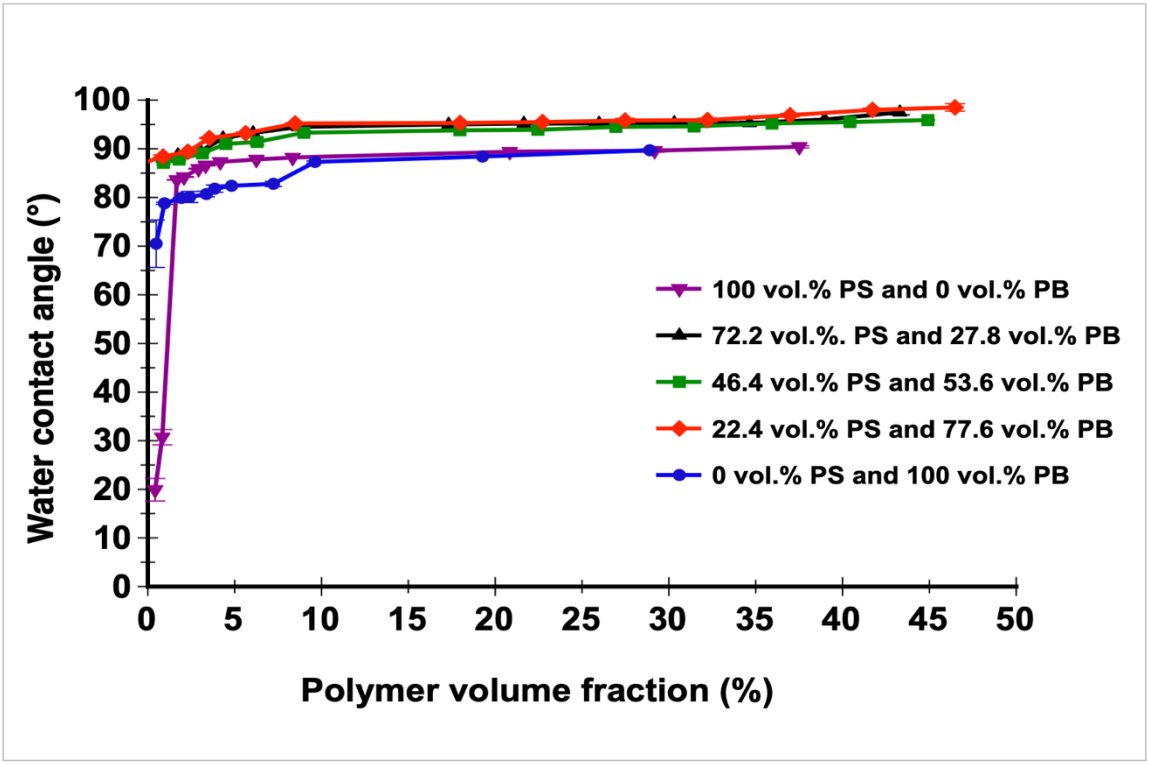

Figure 4.2 A plot of the relation of water contact angle and polymer volume fraction in toluene of blend films PS (M.W.= 4 kg/mol) and PB (M.W.= 3 kg/mol).

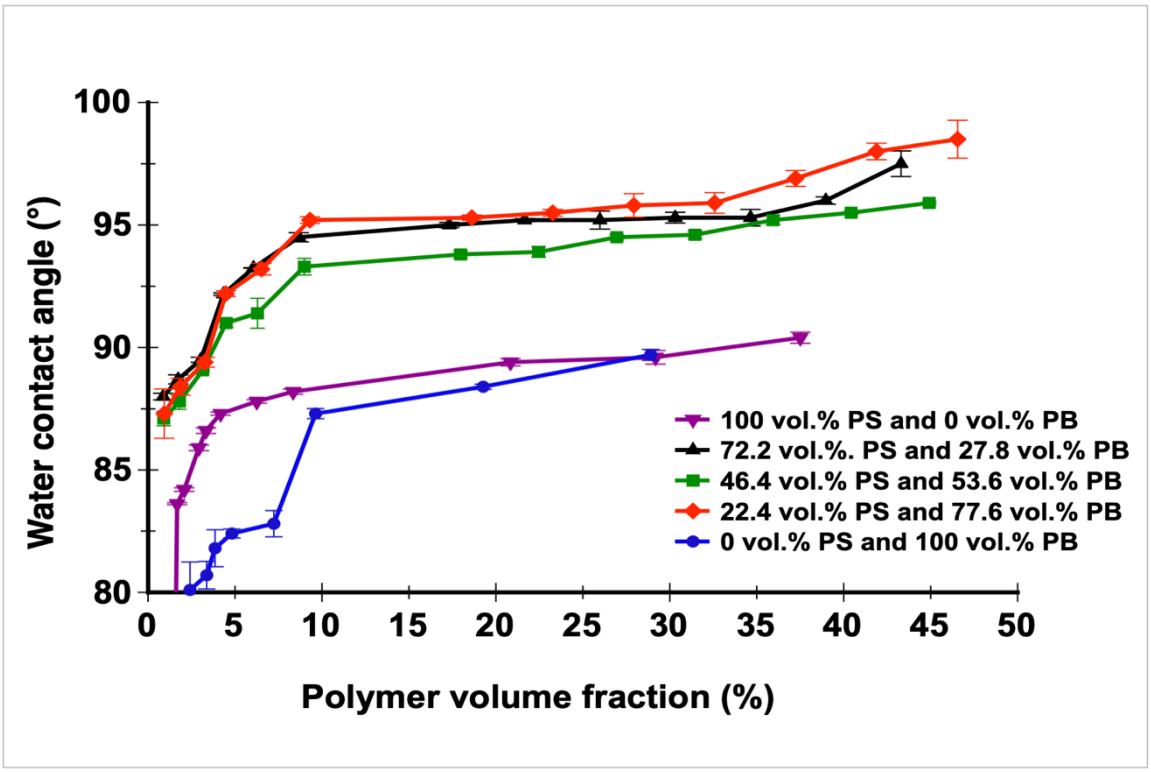

Figure 4.3 A zoomed-in plot of the relation of water contact angle and polymer volume fraction in toluene of blend films PS (M.W.= 4 kg/mol) and PB (M.W.= 3 kg/mol). The data are the same as those shown in Figure 4.2.

In addition, the black curve represents films that have a higher PS volume fraction of 72.2% compared to PB at 27.8%. Its contact angle falls between the other polymer

blends, with polymer volume fractions ranging from 8.7% to 43.3% (Figure 4.3). Films containing 53.6 vol.% PB (green curve) exhibit the lowest contact angles among the blend films. The red curve represents films consisting of 77.6 vol.% PB and 22.4 vol.% PS, showing the highest contact angles, peaking at 98.5°± 0.8° at a polymer volume fraction of 46.6%. Glycerol contact angles were also measured for the same films.

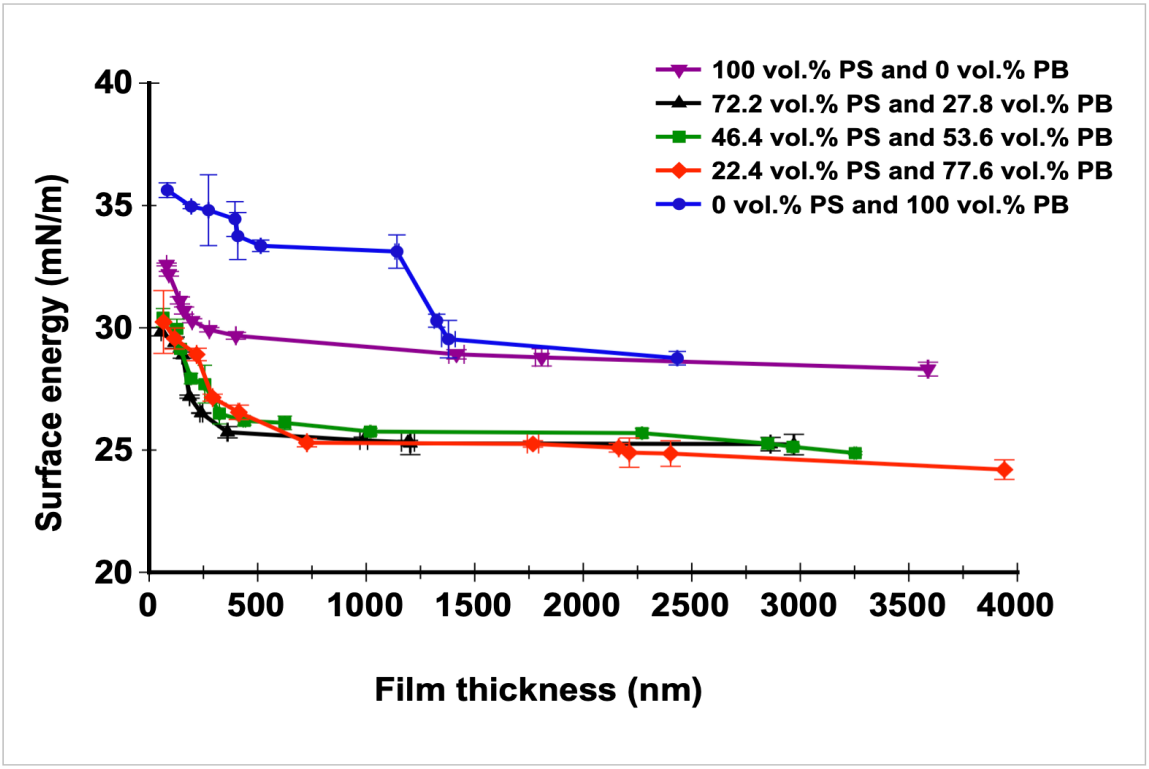

Figure 4.4 A plot of the relation of film thickness and surface energy of blend films of PS (M.W.= 4 kg/mol) and PB (M.W.= 3 kg/mol).

The investigation revealed that the surface energy (refer to 2.6.2 and equation 2-33 for the calculation of the surface energy, where $\gamma_{LV,water}$= 72.8 mN/m, $\gamma_{LV,glycerol}$= 63.4 mN/m, and β = 0.000115 $(m^2/mJ)^2$) decreases as the film thickness increases and that the mixtures have lower surface energy than the individual homopolymers (see Figure 4.4). It was observed that PB is more hydrophilic than PS. For PB, the surface energy ranges from 40.9 ± 6.1 mN/m to 28.8 ± 0.3 mN/m for film thicknesses ranging from 4.2 ± 0.1 nm to 2433.2 ± 1.8 nm (indicated by the blue curve). On the other hand, the surface energy of PS for thinner films (4.4 ± 1.4 nm to 41.7 ± 0.1 nm) is greater than that of PB (68.8 ± 1.7 mN/m and 64.1 ± 1.5 mN/m) due to the influence of the substrate, leading to instability. As a result, the surface energy for PS (indicated by the purple curve) ranges from 32.6 ± 0.1 mN/m to 28.3 ± 0.3 mN/m for film thicknesses spanning 80.2 ± 0.1 nm to 3588.5 ± 3.0 nm (refer to Table 4.1 for more details about these films surface energies and thicknesses). A similar trend was noted for polystyrene spin-

coated films on silicon wafers at room temperature (~20 °C) for PS with a molecular mass of 22 kg/mol and PS of 15.2 kg/mol [112].

The blend films with the highest hydrophobicity in this combination (red curve in Figure 4.4) have mass ratios (PS: PB) of 1:3 and thicknesses ranging from 730 nm to 3950 nm. These films show a decrease in surface energy from 30.2 ± 1.3 mN/m to 23.2 ± 1.0 mN/m as the thickness ranges from 65.8 ± 0.1 nm to 5021.0 ± 1.6 nm. In contrast, the films (black curve) with opposite mass ratios (PS: PB) of 3:1 exhibit smaller differences in surface energy, making them less hydrophobic than the 1:3 mass ratio films. The most hydrophilic blend films within this set have a mass ratio (PS: PB) of 1:1 (green curve).

XPS analysis indicates that the surface concentrations of PB in the 27.8 vol.% PB, 53.6 vol.% PB, and 77.6 vol.% PB films are 109.8 ± 2.7%, 95 ± 12%, and 108.7 ± 4.4%, respectively. These values suggest that the surface layer of each blend is composed almost entirely of PB. Values slightly exceeding 100% are attributed to experimental uncertainty and signal normalisation in XPS analysis.

PS M.W. (kg/mol)	PB M.W. (kg/mol)	PB (vol. %)	Polymers (vol. %)	Thickness (nm)	Surface energy (water) (mN/m)	Average roughness (nm)	PB amount at the surface (%)
4.0	3.0	0.0	8.3	399.4 ± 0.9	29.7 ± 0.1	1.03 ± 0.02	
		27.8	17.3	988.7 ± 17.6	25.4 ± 0.1	2.4 ± 0.6	109.8 ± 2.7
		53.6	22.5	624.7 ± 23.4	26.1 ± 0.3	82.5 ± 7.0	95.1 ± 11.6
		77.6	9.3	726.8 ± 1.1	25.3 ± 0.2	13.0 ± 1.8	108.7 ± 4.4
		100.0	4.7	513.8 ± 1.6	33.4 ± 0.2	5.0 ± 0.5	

Table 4.2 Summarising some data of five blend films PS (M.W.= 4 kg/mol) and PB (M.W.= 3 kg/mol).

ToF-ERD and RBS data analysis reveals that these surface layers (surface starts at 0 nm depth) are approximately 10 -15 nm thin (Figure 4.5), indicating that the polystyrene underneath the surface might impact the surface energy. In blend films with 27.8 vol% BP, the PB volume fraction sharply decreases to around 0.1 beneath the surface layer (Figure 4.5, A). Conversely, for a blend ratio of 53.6 vol.% PB, the PB volume fraction gradually decreases through the film (Figure 4.5, B). Additionally, in blend films with 77.6 vol.% PB, the volume fraction of PB decreases to almost 0.5 in the bulk (Figure 4.5, C).

AFM analysis shows that the surface roughness of films with 27.8 vol.% PB, 53.6 vol.% PB, and 77.6 vol.% PB is 2.4 ± 0.6 nm, 82.5 ± 7.0 nm, and 13.0 ± 1.8 nm, respectively, as illustrated in Figure 4.6 and Table 4.2. Figures 4.7 to 4.9 show these surfaces. Consequently, the films with 53.6 vol.% PB exhibit the highest surface roughness among these blends, as noted from the light yellow structure in Figure 4.8.

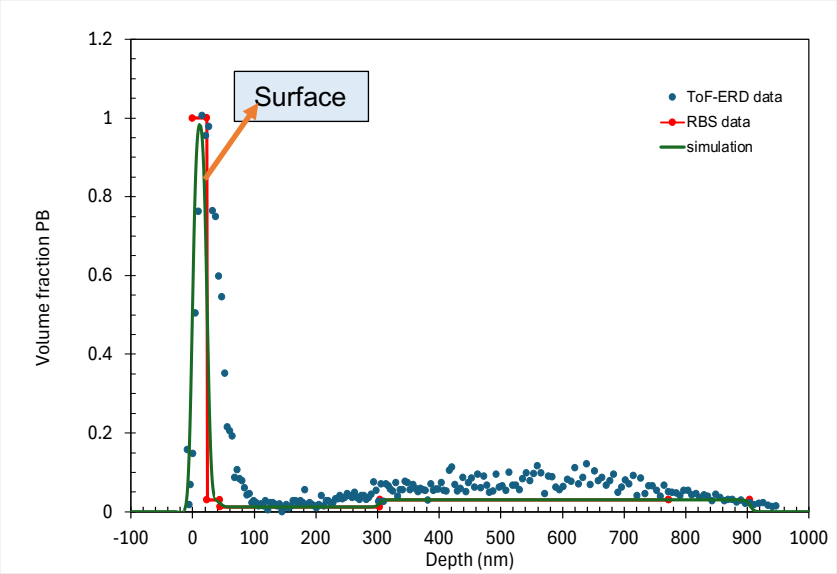

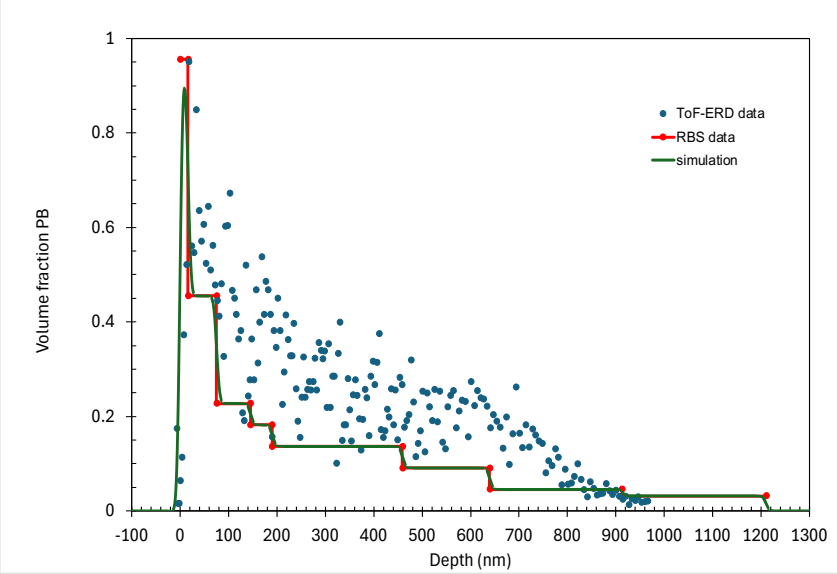

B. 53.6 vol.% PB

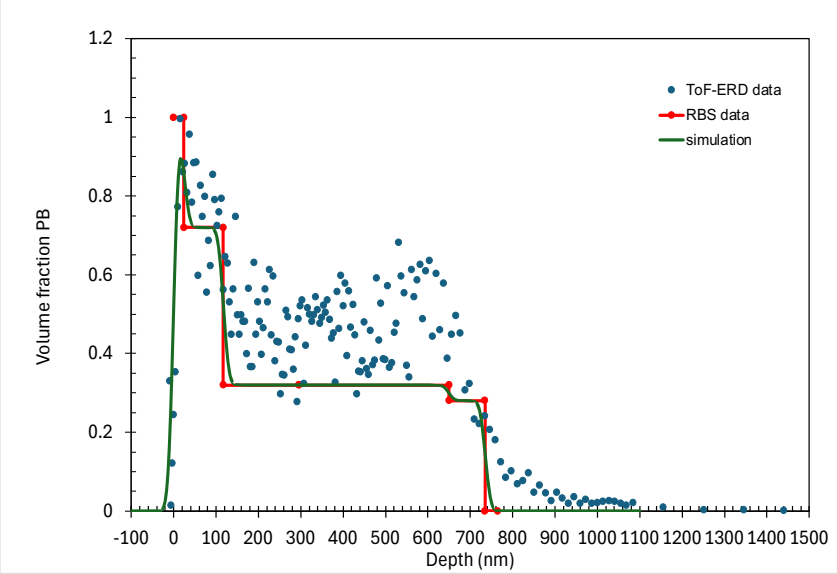

C. 77.6 vol.% PB

Figure 4.5 ToF-ERD data compared with volume fraction profiles obtained by RBS for blend films of PS (M.W.= 4 kg/mol) and PB (M.W.= 3 kg/mol).

Optical microscopy shows that the films' structure behaved differently in increasing the thickness of these blend films (Figures 4.10,11, and 12). In Figure 4.10, the presence of cracks is evident in films with thin PB surface layers and PS beneath the surface. During spin-coating, as the toluene evaporates, a PS-rich phase partially swollen with toluene begins to form a layer. Upon nearly complete evaporation of toluene, this PS-rich phase undergoes a transition to a glassy state, causing it to shrink. On the other hand, neighbouring PB-rich phases, which do not form a glass, consequently do not shrink, leading to the formation of cracks due to the different expansivities of the two layers. A similar behaviour was observed in a study involving a spin-coated thin film consisting of a mixture of 6-nm PEGylated CdSe nanoparticles in poly(methacrylate), where the CdSe nanoparticles segregated to the cracks [113].

The roughness of film surfaces plays a significant role in influencing contact angle measurements, as it affects the extent of contact between a droplet and the surface compared to flat interfaces [114]. When a droplet conforms to the contours of a rough film and maintains full contact, it demonstrates Wenzel wetting behaviour, resulting in a larger surface area in contact with the substrate than would be anticipated based solely on the projection of the droplet area. Conversely, if air pockets form beneath the droplet due to pronounced film topography, the droplet may exhibit reduced contact with the film, leading to Cassie-Baxter behaviour. Research on polymer blend films has shown potential for both behaviours. One might expect the differences between Wenzel and Cassie-Baxter behaviours to be reflected in varying contact angles for glycerol and water; however, it is somewhat unexpected that this was not observed for all films in this study.

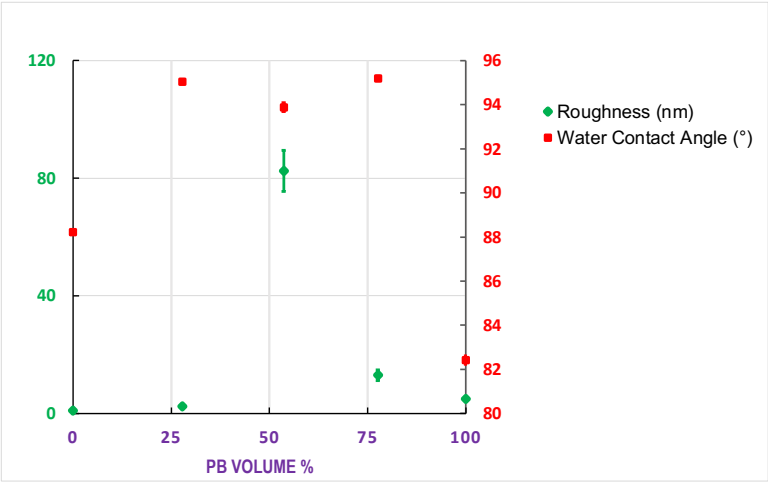

Figure 4.6 PB volume %, roughness, and water contact angle for blend films of PS (M.W.= 4 kg/mol) and PB (M.W.= 3 kg/mol).

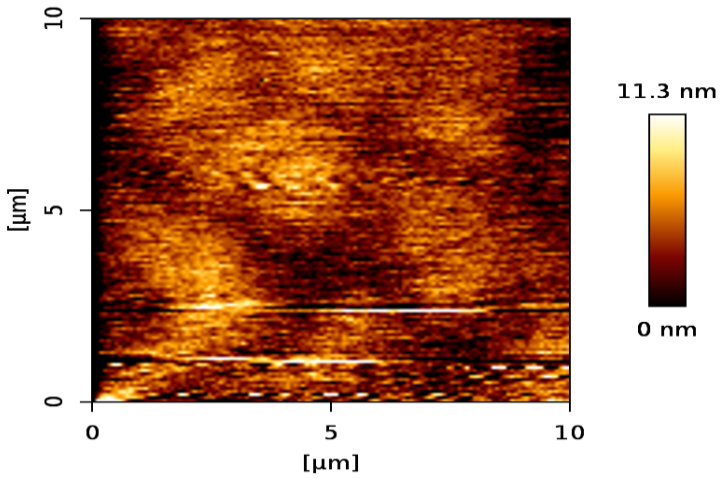

Figure 4.7 AFM topography of the unstained film surface containing 72.2 vol.% PS (M.W. 4 kg/mol) and 27.8 vol.% PB (M.W. 3 kg/mol). The roughness is 2.4 $\pm$ 0.6 nm. The thickness is 988.7 ±17.6 nm. Surface energy is 25.4 $\pm$ 0.1 mN/m.

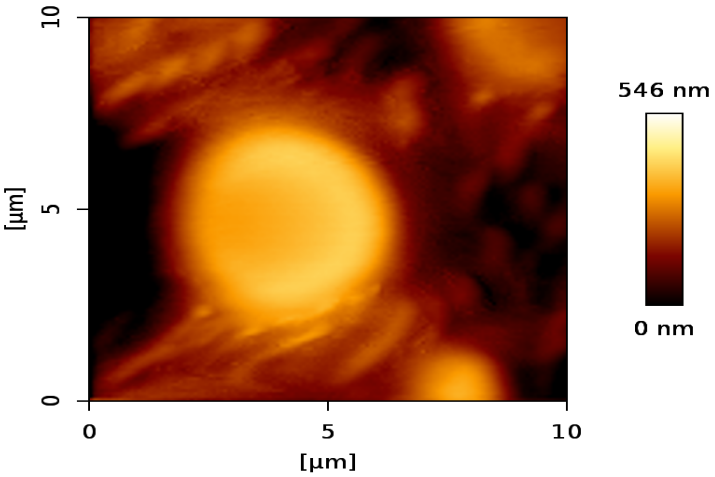

Figure 4.8 AFM topography of the unstained film surface containing 46.4 vol.% PS (M.W. 4 kg/mol) and 53.6 vol.% PB (M.W. 3 kg/mol). The roughness is 82.5 $\pm$ 7.0 nm. The thickness is 624.7 ± 23.4 nm. Surface energy is 26.1 $\pm$ 0.3 mN/m.

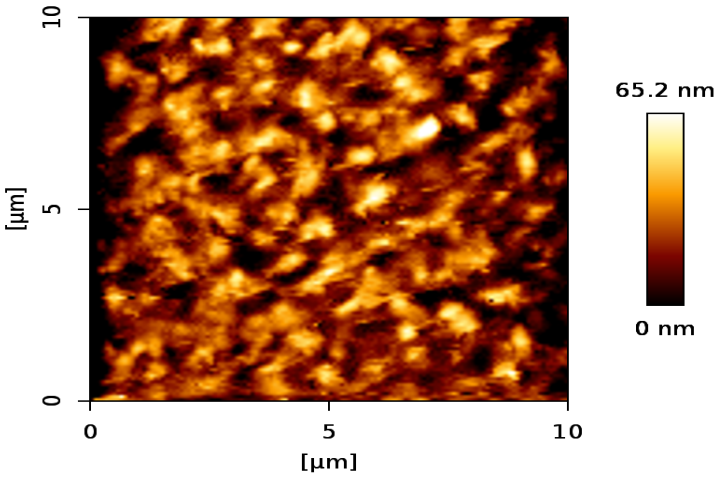

Figure 4.9 AFM topography of the unstained film surface containing 22.4 vol.% PS (M.W. 4 kg/mol) and 77.6 vol.% PB (M.W. 3 kg/mol). The roughness is 13.0 $\pm$ 1.8 nm. The thickness is 726.8 ± 1.1 nm. Surface energy is 25.3 $\pm$ 0.2 mN/m.

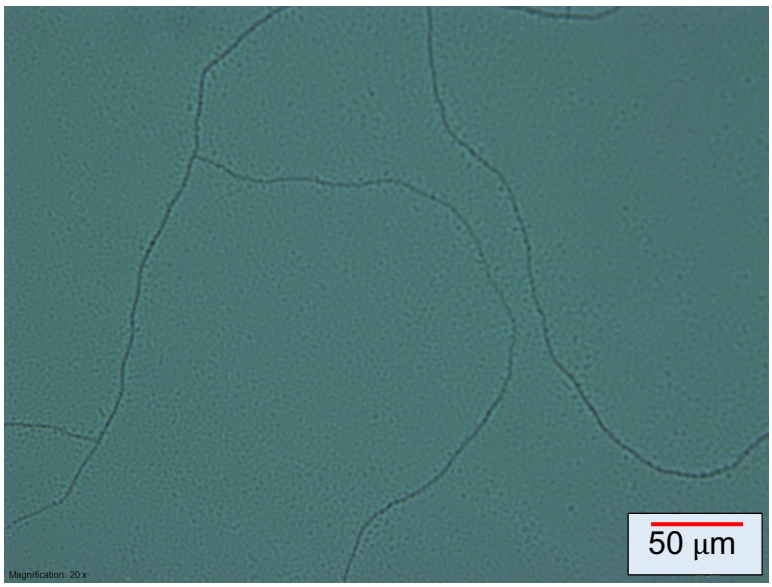

A. 2862.9 ± 1.8 nm thick

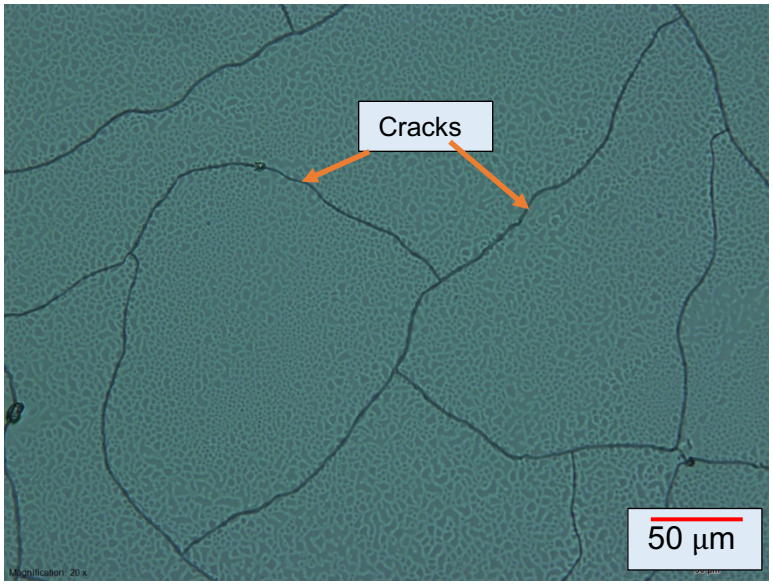

B. 3618.6 ± 2.4 nm thick

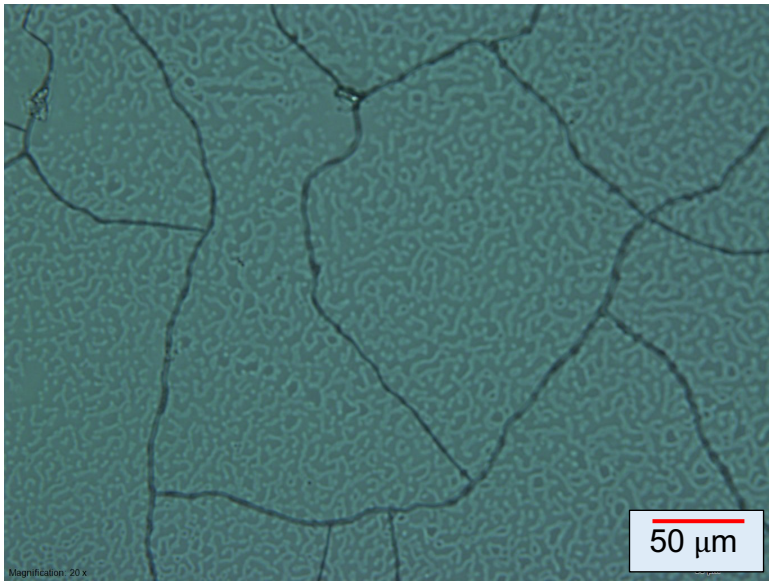

C. 4061.5 ± 4.8 nm thick

Figure 4.10 Three optical micrographs of three unstained films containing 72.2 vol.% PS (M.W. 4 kg/mol) and 27.8 vol.% PB (M.W. 3 kg/mol). The scale bar is 50 μm.

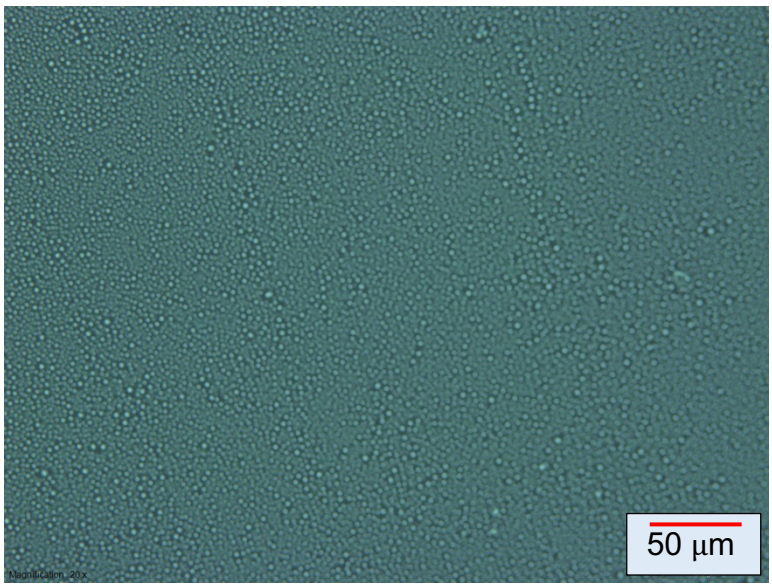

A. 2270.7 ± 1.9 nm thick

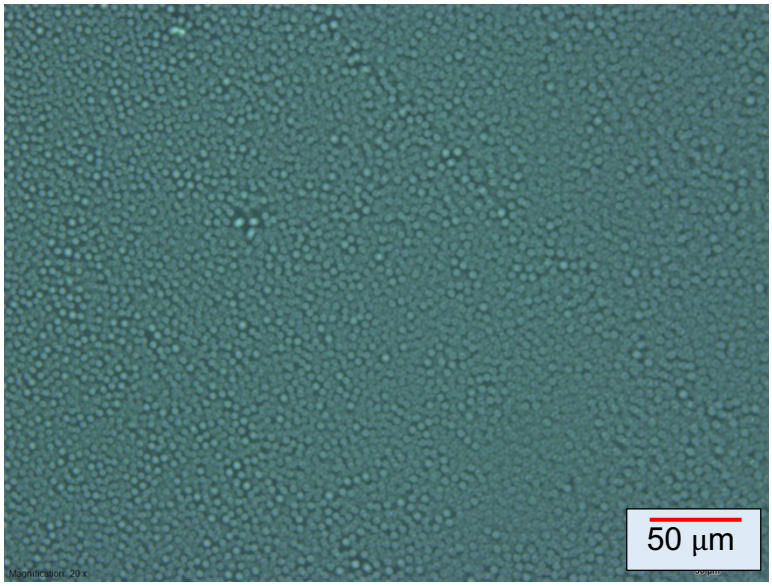

B. 2850.2 ± 2.6 nm thick

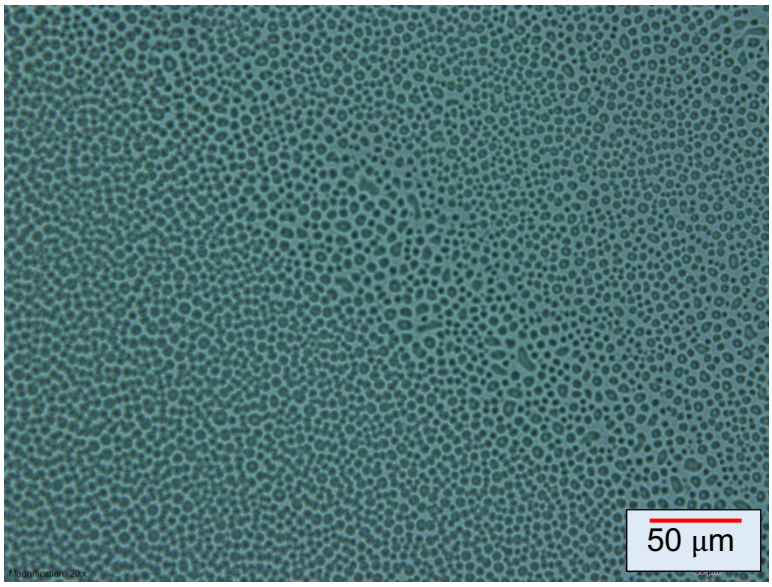

C. 3253.3 ± 5.2 nm thick

Figure 4.11 Three optical micrographs of three unstained films containing 46.4 vol.% PS (M.W. 4 kg/mol) and 53.6 vol.% PB (M.W. 3 kg/mol). The scale bar is 50 µm.

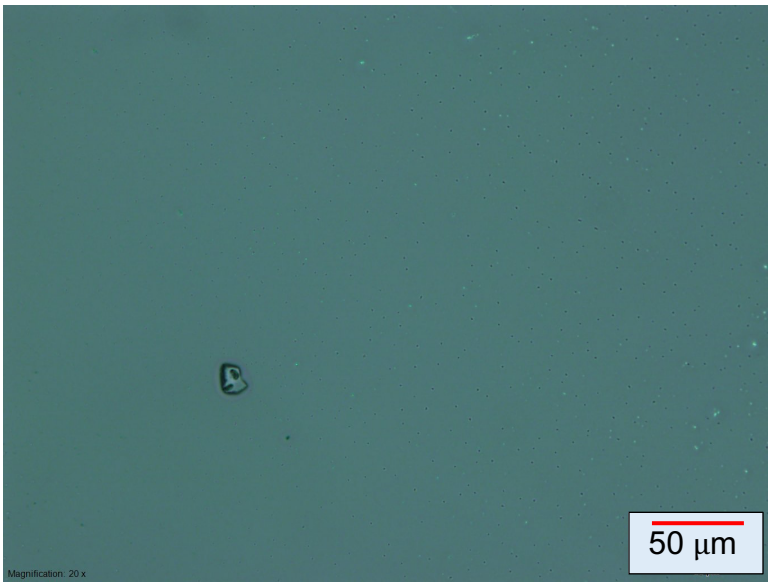

A. 292.4 ± 0.7 nm thick

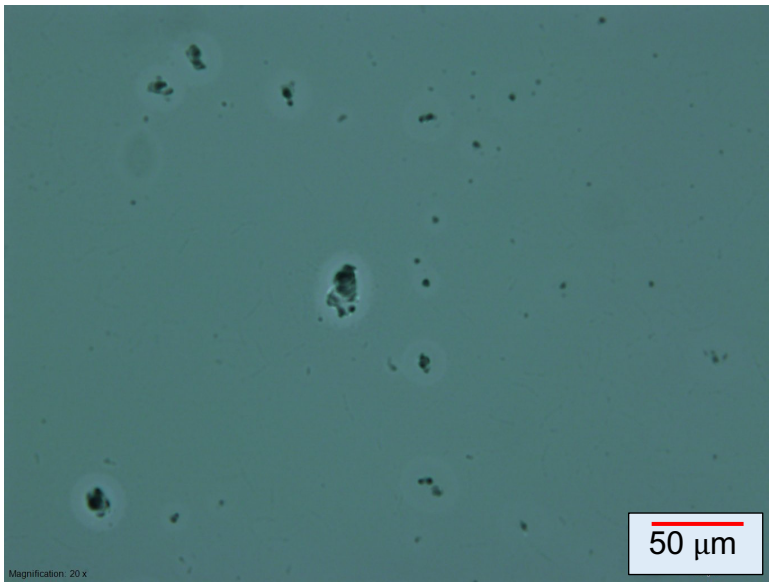

B. 726.8 ± 1.1 nm thick

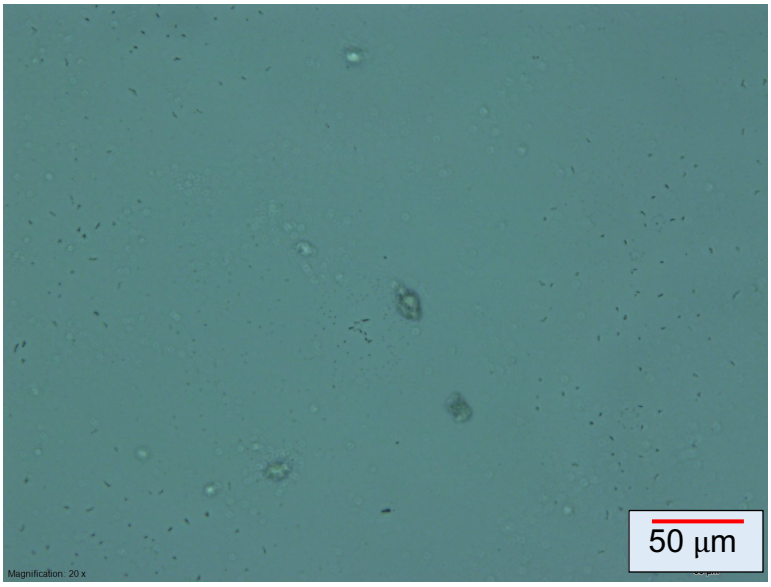

C. 2163.7 ± 1.3 nm thick

Figure 4.12 Three optical micrographs of three unstained films containing 22.4 vol.% PS (M.W. 4 kg/mol) and 77.6 vol.% PB (M.W. 3 kg/mol). The scale bar is 50 µm.

4.2 Blend films of PS (M.W.= 55 kg/mol) and PB (M.W.= 53 kg/mol)

The impact of thickness on surface energy was examined for blend films comprising 55 kg/mol PS and 53 kg/mol PB (Figure 4.13). Surprisingly, the study revealed that the blend films exhibited lower surface energy than those for the homopolymer films. This is unexpected, as one would anticipate the surface energy of the blend to fall between those of the individual polymers.

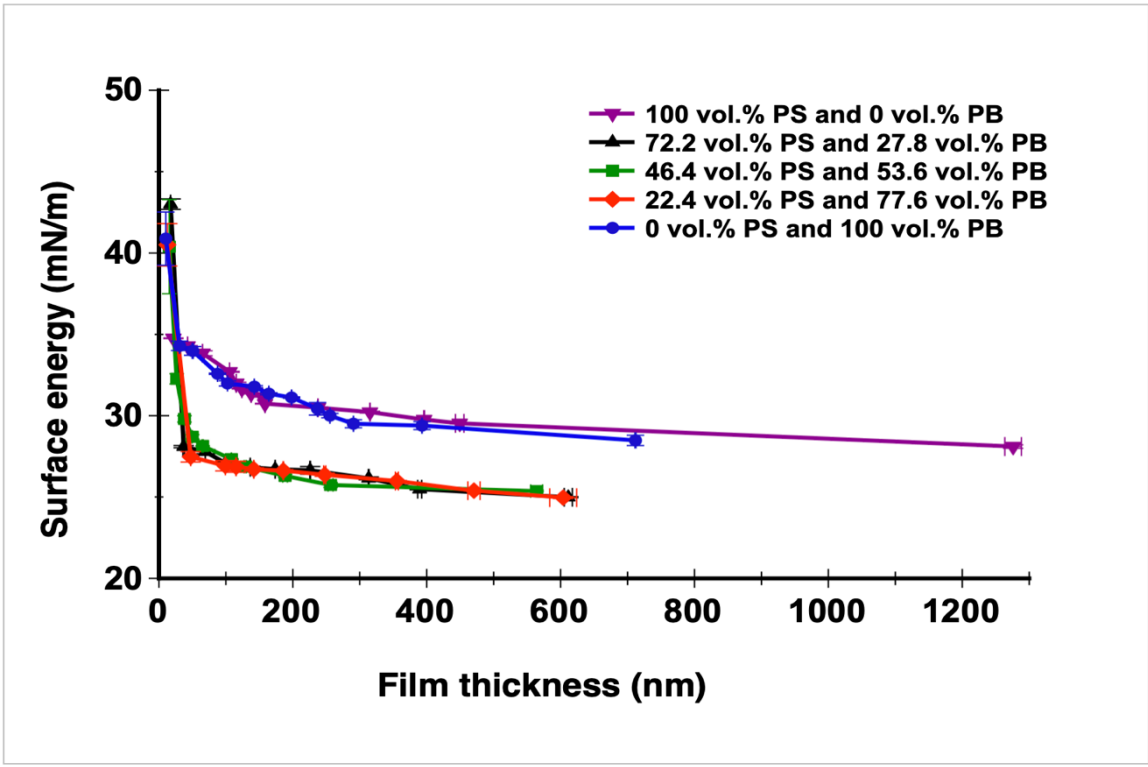

Figure 4.13 A plot of the relation of film thickness and surface energy of blend films of PS (M.W.= 55 kg/mol) and PB (M.W.= 53 kg/mol).

Films composed of a single polymer exhibit a decrease in surface energy from 34.76 ± 0.02 mN/m to 28.1 ± 0.1 mN/m for PS films with a thickness between 21.6 ± 0.1 nm to 1276 ± 12 nm and from 40.9 ± 1.6 mN/m to 28.5 ± 0.3 mN/m for PB with a thickness between 10.3 ± 0.1 nm to 711.8 ± 0.7 nm. This result also corresponds to a study of PS (M.W. 30 kg/mol) films in the air at 23 °C [115]. It shows that the surface energy decreases from 33.6 to 28.4 mN/m as the thickness ranges from 20 to 620 nm.

Conversely, the surface energy of blend films falls within a similar range, decreasing from approximately 40 mN/m to 25 mN/m with thicknesses ranging from 12 nm to 600 nm (see Table 4.3 for more details).

Blend of	Polymer weight fraction	Polymer volume fraction	Water contact angle (°)	Surface energy((mN)/m)-water	Glycerol contact angle (°)	Surface energy((mN)/m)- glycerol	The Thickness (nm)
100 vol.% PS (M.W. 55 kg/mol)	0.50%	0.42%	80.20 ± 0.02	34.76 ± 0.02	70.9 ± 0.4	34.1± 0.5	21.6 ± 0.1
	1.00%	0.83%	80.94 ± 0.02	34.29 ± 0.02	71.5 ± 0.1	33.6 ± 0.2	42.86 ± 0.03
	1.50%	1.25%	81.7 ± 0.1	33.8 ± 0.2	72.2 ± 0.1	33.3 ± 0.2	65.02 ± 0.02
	1.75%	1.46%	83.44 ± 0.02	32.70 ± 0.03	74.09 ± 0.01	32.19 ± 0.01	105.46 ± 0.02
	2.00%	1.67%	84.55 ± 0.05	32.0 ± 0.1	75.15 ± 0.02	31.58 ± 0.03	115.50 ± 0.03
	2.50%	2.08%	85.07 ± 0.02	31.67 ± 0.02	75.68 ± 0.03	31.27 ± 0.03	123.87 ± 0.03
	3.00%	2.50%	85.55 ± 0.02	31.37 ± 0.02	76.10 ± 0.03	31.03 ± 0.04	137.7 ± 0.1
	3.25%	2.71%	85.86 ± 0.02	31.17 ± 0.02	76.5 ± 0.1	30.8 ± 0.1	154.7 ± 0.1
	3.50%	2.92%	86.54 ± 0.01	30.74 ± 0.02	77.19 ± 0.03	30.39 ± 0.03	158.4 ± 0.1
	4.00%	3.33%	86.93 ± 0.03	30.49 ± 0.04	77.53 ± 0.02	30.20 ± 0.02	237.5 ± 0.1
	5.00%	4.17%	87.36 ± 0.04	30.2 ± 0.1	77.9 ± 0.1	30.0 ± 0.1	315.2 ± 0.3
	7.50%	6.25%	88.08 ± 0.02	29.76 ± 0.03	78.7 ± 0.2	29.5 ± 0.2	396.2 ± 0.5
	10.00%	8.34%	88.45 ± 0.01	29.53 ± 0.02	79.06 ± 0.03	29.31 ± 0.03	449.3 ± 6.3
	20.00%	16.67%	90.7 ± 0.1	28.1 ± 0.1	80.7 ± 0.5	28.4 ± 0.6	1276.0 ± 12.4
72.2 vol.% PS (M.W. 55 kg/mol) and 27.8 vol.% PB (M.W. 53 kg/mol)	0.25%	0.22%	67.2 ± 0.3	43.0 ± 0.3	73.84 ± 0.05	32.3 ± 0.1	17.3 ± 0.1
	0.70%	0.61%	90.7 ± 0.1	28.1 ± 0.1	81.6 ± 0.1	27.9 ± 0.1	37.0 ± 1.2
	1.50%	1.30%	91.2 ± 0.1	27.8 ± 0.1	82.4 ± 0.1	27.4 ± 0.1	69.27 ± 0.05
	2.00%	1.73%	92.3 ± 0.1	27.1 ± 0.1	82.87 ± 0.03	27.11 ± 0.03	99.5 ± 0.1
	2.50%	2.17%	92.7 ± 0.1	26.8 ± 0.1	83.75 ± 0.02	26.61 ± 0.02	136.4 ± 0.1
	3.00%	2.60%	92.9 ± 0.1	26.7 ± 0.1	83.9 ± 0.1	26.5 ± 0.1	173.6 ± 0.2
	4.00%	3.46%	93.0 ± 0.2	26.6 ± 0.2	83.9 ± 0.3	26.5± 0.3	225.9 ± 0.5
	5.00%	4.33%	93.8 ± 0.1	26.2 ± 0.1	84.5 ± 0.1	26.2 ± 0.1	313.4 ± 0.7
	7.00%	6.06%	94.90 ± 0.03	25.48 ± 0.03	85.58 ± 0.05	25.6 ± 0.1	389.5 ± 3.0
	10.00%	8.66%	95.69 ± 0.02	24.99 ± 0.03	86.2 ± 0.1	25.2 ± 0.1	611.5 ± 6.1
46.4 vol.% PS (M.W. 55 kg/mol) and 53.6 vol.% PB (M.W. 53 kg/mol)	0.25%	0.22%	71.3 ± 2.3	40.4 ± 2.9	70.5 ± 0.4	34.3 ± 0.4	15.4 ± 0.1
	0.50%	0.44%	84.1 ± 0.2	32.3 ± 0.3	74.8 ± 0.1	31.8 ± 0.2	26.57 ± 0.04
	0.70%	0.63%	88.0 ± 0.2	29.8 ± 0.2	78.6 ± 0.1	29.6 ± 0.1	38.1 ± 0.1
	1.00%	0.90%	89.8 ± 0.1	28.7 ± 0.1	80.5 ± 0.2	28.5 ± 0.2	49.72 ± 0.03
	1.50%	1.35%	90.65 ± 0.01	28.14 ± 0.02	81.3 ± 0.2	28.0 ± 0.2	65.3 ± 0.9
	2.00%	1.80%	91.94 ± 0.02	27.33 ± 0.03	82.58 ± 0.03	27.28 ± 0.03	108.2 ± 0.2
	2.50%	2.25%	92.7 ± 0.2	26.9 ± 0.3	83.5 ± 0.1	26.8 ± 0.1	128.9 ± 1.5
	5.00%	4.50%	93.6 ± 0.1	26.3 ± 0.1	84.2 ± 0.4	26.4 ± 0.5	188.4 ± 3.5
	7.00%	6.30%	94.5 ± 0.1	25.7 ± 0.2	85.1 ± 0.4	25.8 ± 0.5	256.3 ± 3.7
	10.00%	8.99%	95.08 ± 0.04	25.4 ± 0.1	85.7 ± 0.3	25.5 ± 0.3	564.2 ± 8.9
22.4 vol.% PS (M.W. 55 kg/mol) and 77.6 vol.% PB (M.W. 53 kg/mol)	0.25%	0.23%	71.1 ± 1.0	40.5 ± 1.3	73.9 ± 0.2	32.3 ± 0.2	12.5 ± 0.1
	0.70%	0.65%	91.7 ± 0.3	27.5 ± 0.3	82.1 ± 0.1	27.6 ± 0.1	47.45 ± 0.03
	1.50%	1.40%	92.6 ± 0.3	26.9 ± 0.3	83.6 ± 0.1	26.7 ± 0.1	99.2 ± 0.1
	2.00%	1.86%	92.6 ± 0.3	26.9 ± 0.3	84.0 ± 0.2	26.5 ± 0.2	115.3 ± 0.1
	2.50%	2.33%	92.9 ± 0.1	26.7 ± 0.1	84.06 ± 0.05	26.4 ± 0.1	141.7 ± 0.1
	3.00%	2.79%	93.1 ± 0.1	26.6 ± 0.1	84.2 ± 0.1	26.3 ± 0.1	185.7 ± 0.4
	4.00%	3.72%	93.5 ± 0.1	26.4 ± 0.1	84.5 ± 0.1	26.2 ± 0.1	247.6 ± 1.6
	5.00%	4.65%	94.08 ± 0.02	25.99 ± 0.03	84.67 ± 0.01	26.08 ± 0.01	355.4 ± 2.2
	7.00%	6.52%	95.04 ± 0.01	25.39 ± 0.01	85.7 ± 0.1	25.5 ± 0.2	470.6 ± 9.1
	10.00%	9.31%	95.73 ± 0.04	25.0 ± 0.1	86.27 ± 0.04	25.17 ± 0.05	603.9 ± 20.1
100 vol.% PB (M.W. 53 kg/mol)	0.10%	0.10%	70.5 ± 1.3	40.9 ± 1.6	62.6 ± 3.6	38.9± 4.1	10.3 ± 0.1
	0.50%	0.48%	80.9 ± 0.2	34.3 ± 0.3	71.1 ± 0.4	33.9 ± 0.5	30.9 ± 0.2
	1.00%	0.96%	81.4 ± 0.2	34.0 ± 0.3	71.7 ± 1.2	33.6 ± 1.4	50.4 ± 0.7
	1.50%	1.45%	83.63 ± 0.03	32.58 ± 0.04	74.2 ± 0.1	32.1 ± 0.1	87.6 ± 0.2
	1.75%	1.69%	84.6 ± 0.1	32.0 ± 0.2	75.3 ± 0.1	31.5 ± 0.1	102.41 ± 0.03
	2.00%	1.93%	84.9 ± 0.1	31.8 ± 0.1	75.4 ± 0.1	31.4 ± 0.2	142.4 ± 0.1
	2.50%	2.41%	85.56 ± 0.04	31.4 ± 0.1	76.1 ± 0.1	31.0 ± 0.2	164.2 ± 0.1
	3.00%	2.89%	85.93 ± 0.03	31.13 ± 0.04	76.5 ± 0.1	30.8 ± 0.1	198.1 ± 0.2
	3.50%	3.37%	87.0 ± 0.3	30.4 ± 0.4	77.4 ± 1.4	30.3 ± 1.6	236.9 ± 0.1
	3.75%	3.61%	87.7 ± 0.1	30.0 ± 0.1	77.8 ± 0.5	30.1 ± 0.6	255.4 ± 0.1
	4.00%	3.85%	88.5 ± 0.2	29.5 ± 0.2	78.5 ± 0.2	29.6 ± 0.2	290.5 ± 0.1
	5.00%	4.82%	88.7 ± 0.2	29.4 ± 0.2	78.9 ± 0.2	29.4 ± 0.2	393.0 ± 0.3
	7.50%	7.23%	90.1 ± 0.3	28.5 ± 0.3	80.7 ± 0.2	28.3 ± 0.2	711.8 ± 0.7

Table 4.3 Data from the contact angle experiment of blend films of PS 55 kg/mol and PB 53 kg/mol.

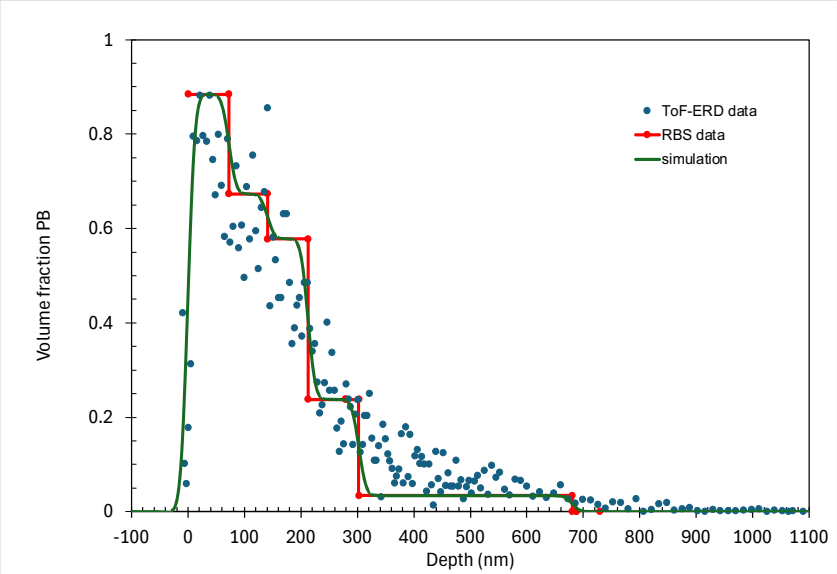

A. 27.8 vol.% PB

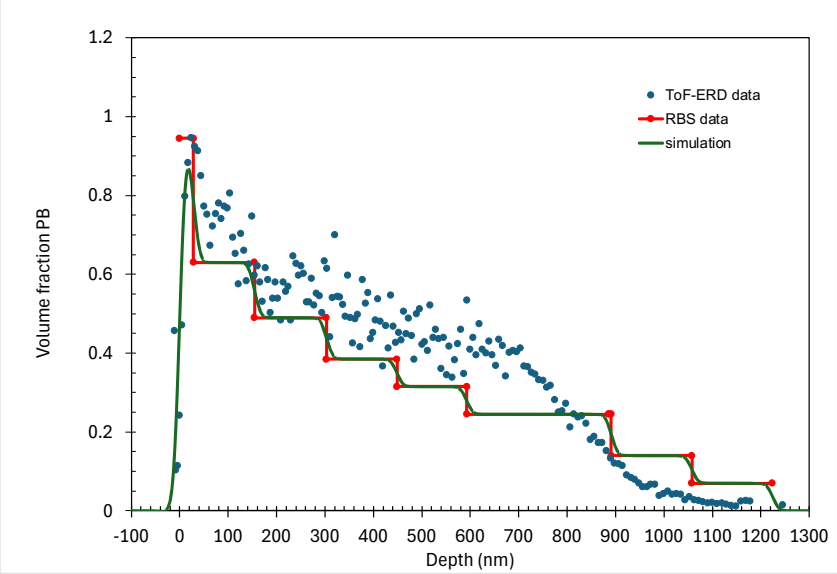

B. 53.6 vol.% PB

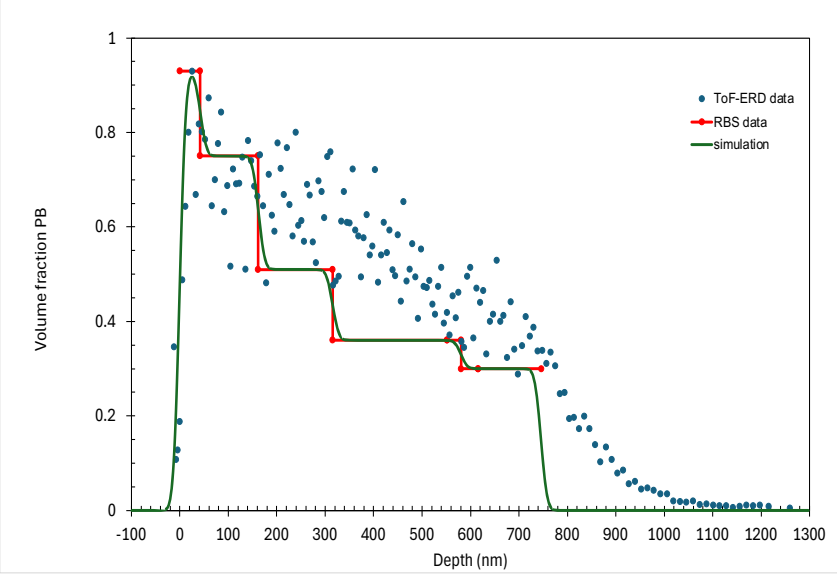

C. 77.6 vol.% PB

Figure 4.14 ToF-ERD data compared with volume fraction profiles obtained by RBS for blend films of PS (M.W.= 55 kg/mol) and PB (M.W.= 53 kg/mol).

In XPS analysis, it was observed that the amount of PB at the surface of blend films with 27.8 vol.% PB, 53.6 vol.% PB, and 77.6 vol.% PB is 90.9% ± 9.8%, 99.6% ± 6.5%, and 72.7% ± 8.4%, respectively. This indicates that the surface layer of these blends is rich in PB (Table 4.4).

PS M.W. (kg/mol)	PB M.W. (kg/mol)	PB (vol. %)	Polymers (vol. %)	Thickness (nm)	Surface energy (water) (mN/m)	Average roughness (nm)	PB amount at the surface (%)
55.0	53.0	0.0	6.3	396.2 ± 0.5	29.76 ± 0.03	1.2 ± 0.1	
		27.8	6.1	389.5 ± 3.0	25.48 ± 0.03	11.4 ± 2.9	90.9 ± 9.8
		53.6	9.0	564.2 ± 8.9	25.4 ± 0.1	57.0 ± 7.3	99.6 ± 6.5
		77.6	6.5	470.6 ± 9.1	25.39 ± 0.01	110.7 ± 2.3	72.7 ± 8.4
		100.0	4.8	393.0 ± 0.3	29.4 ± 0.2	2.6 ± 0.2	

Table 4.4 Summarising some data of five blend films PS (M.W.= 55 kg/mol) and PB (M.W.= 53 kg/mol).

Also, ToF-ERD and RBS data analysis agreed with XPS analysis and revealed that these surface layers contain approximately 0.9 volume fraction of PB (Figure 4.14, A, B, and C). The PB volume fraction gradually decreases through the bulk to reach around 0.2 at the back of the film. This may be explained by the fact that PB first segregates to the surface. Behind this surface wetting layer, there is likely to be bulk phase separation.

The AFM analysis revealed that the surface roughness of films containing 27.8 vol.% PB, 53.6 vol.% PB, and 77.6 vol.% PB is 11.4 ± 2.9 nm, 57.0 ± 7.3 nm, and 110.7 ± 2.3 nm, respectively (Figure 4.15 and Table 4.4).These results indicate increased surface roughness with higher PB ratios in the films. Specifically, the film with 77.6 vol.% PB exhibited the highest surface roughness (Figure 4.18). The following images (Figures 4.16 to 4.18) show AFM topography for those blend films.

These blend films have similar surface energy but different structures. Even when their thickness increases, they still have different structures (Figure 4.19 to 4.21).

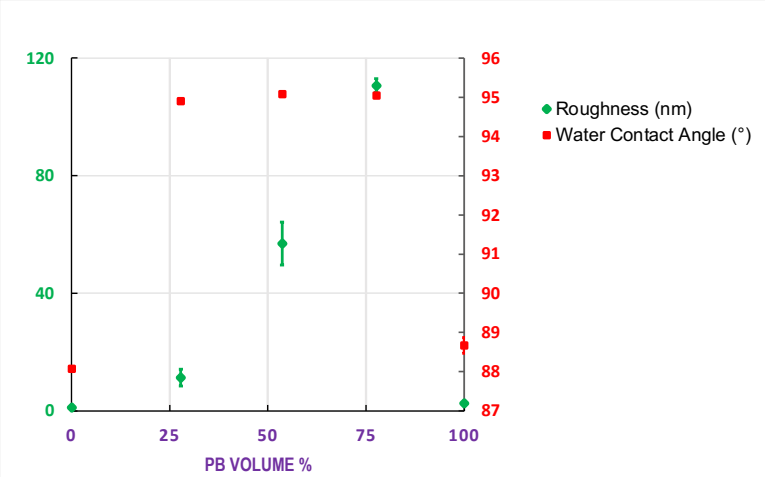

Figure 4.15 PB volume %, roughness, and water contact angle for blend films of PS (M.W.= 55 kg/mol) and PB (M.W.= 53 kg/mol).

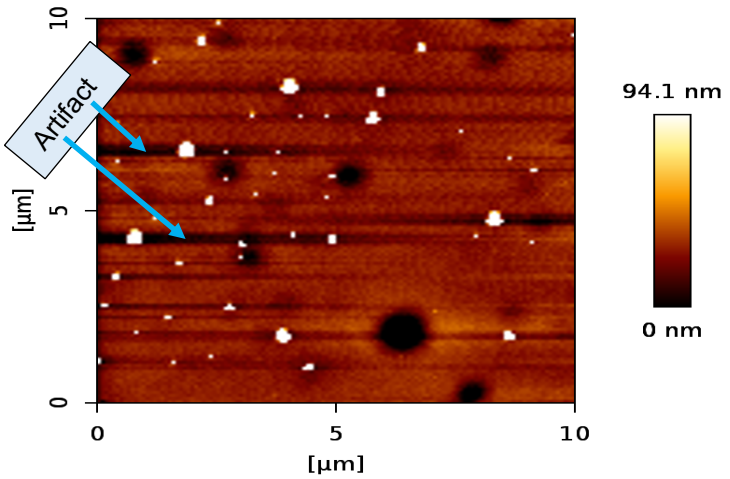

Figure 4.16 AFM topography of the unstained film surface containing 72.2 vol.% PS (M.W. 50 kg/mol) and 27.8 vol.% PB (M.W. 53 kg/mol). The roughness is 11.4 ± 2.9 nm. The thickness is 389.5 ± 3.0 nm. Surface energy is 25.48 ± 0.03 mN/m.

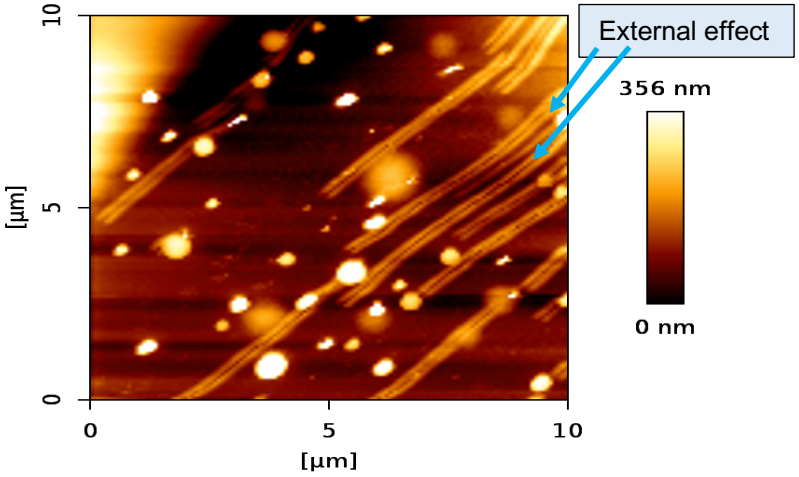

Figure 4.17 AFM topography of the unstained film surface containing 46.4 vol.% PS (M.W. 55 kg/mol) and 53.6 vol.% PB (M.W. 53 kg/mol). The roughness is 57.0 ± 7.3 nm. The thickness is 564.2 ± 8.9 nm. Surface energy is 25.4 ± 0.1 mN/m.

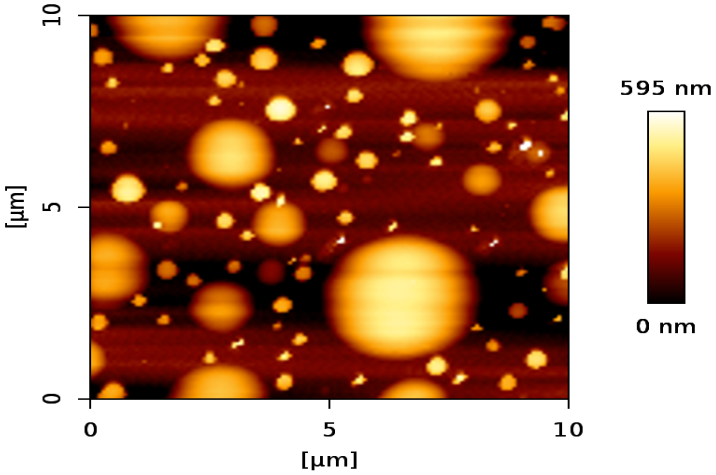

Figure 4.18 AFM topography of the unstained film surface containing 22.4 vol.% PS (M.W. 55 kg/mol) and 77.6 vol.% PB (M.W. 53 kg/mol). The roughness is 110.7 ± 2.3 nm. The thickness is 470.6 ± 9.1 nm. Surface energy is 25.39 ± 0.01 mN/m.

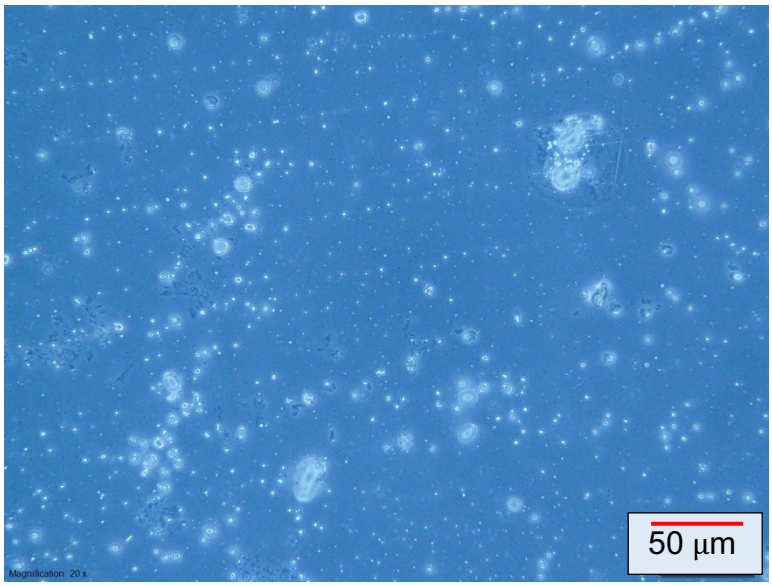

A. 17.3 ± 0.1 nm thick

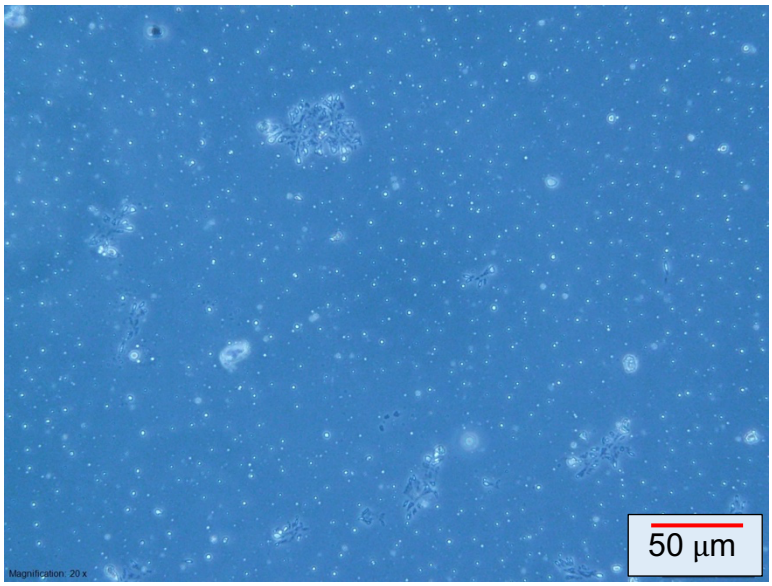

B. 37.0 ± 1.2 nm thick

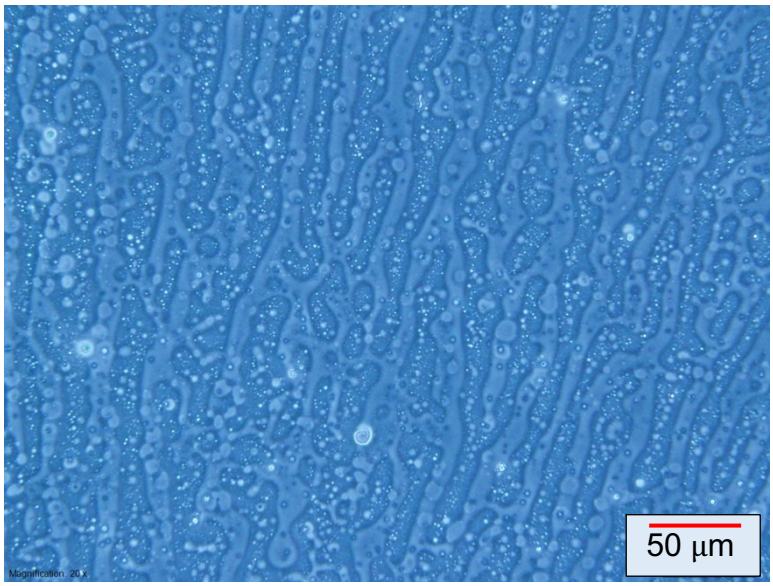

C. 611.5 ± 6.1 nm thick

Figure 4.19 Three optical micrographs of three unstained films containing 72.2 vol.% PS (M.W. 55 kg/mol) and 27.8 vol.% PB (M.W. 53 kg/mol). The scale bar is 50 μm.

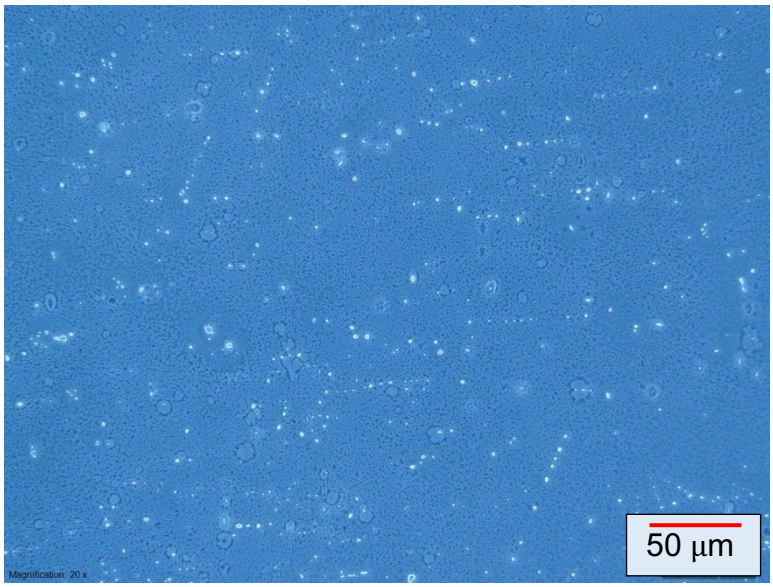

A. 38.1 ± 0.1 nm thick

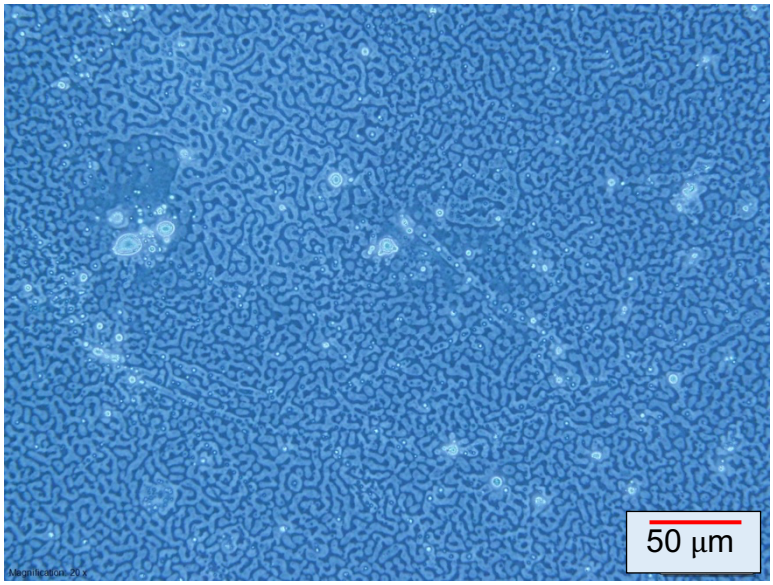

B. 188.4 ± 3.5 nm thick

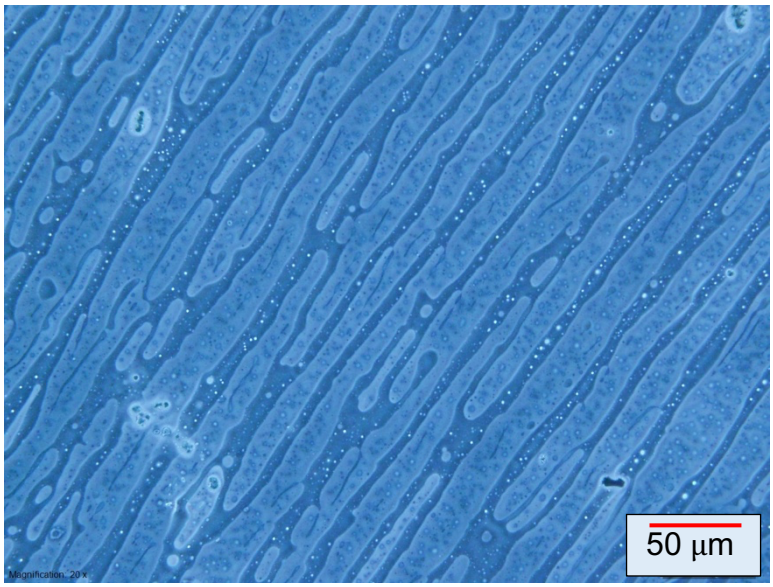

C. 564.2 ± 8.9 nm thick

Figure 4.20 Three optical micrographs of three unstained films containing 46.4 vol.% PS (M.W. 55 kg/mol) and 53.6 vol.% PB (M.W. 53 kg/mol). The scale bar is 50 µm.

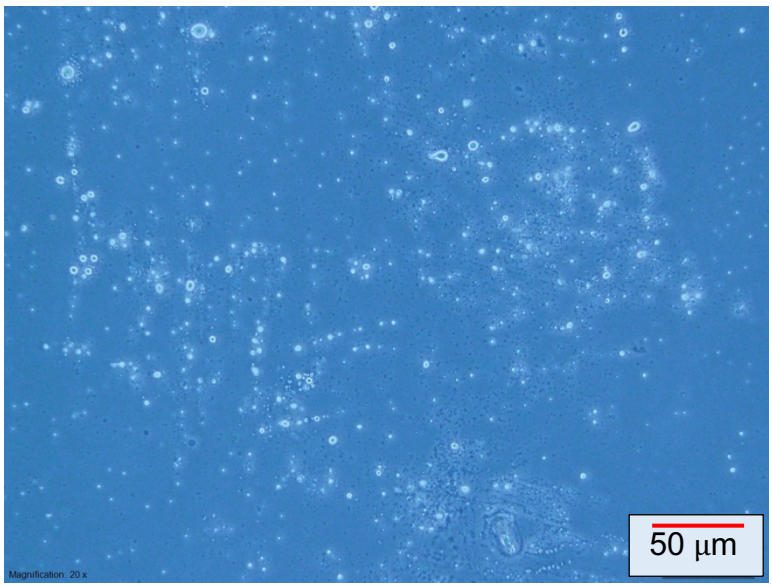

A. 47.45 ± 0.03 nm thick

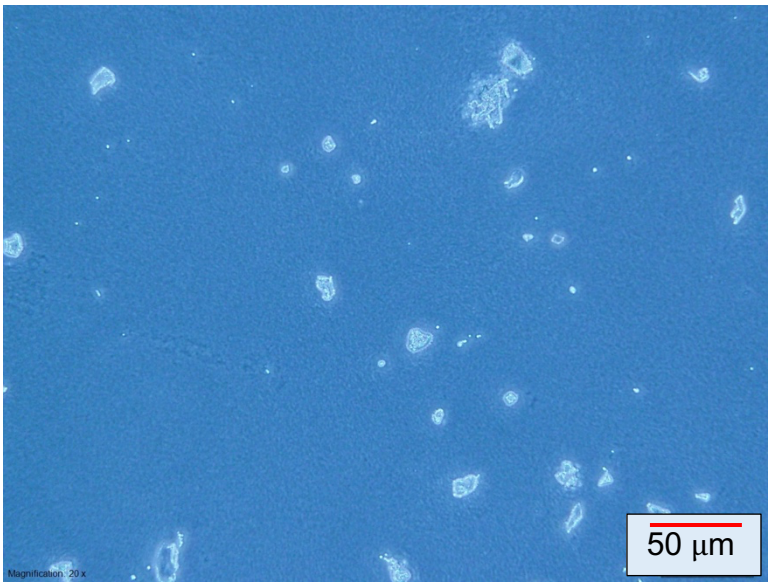

B. 335.4 ± 2.2 nm thick

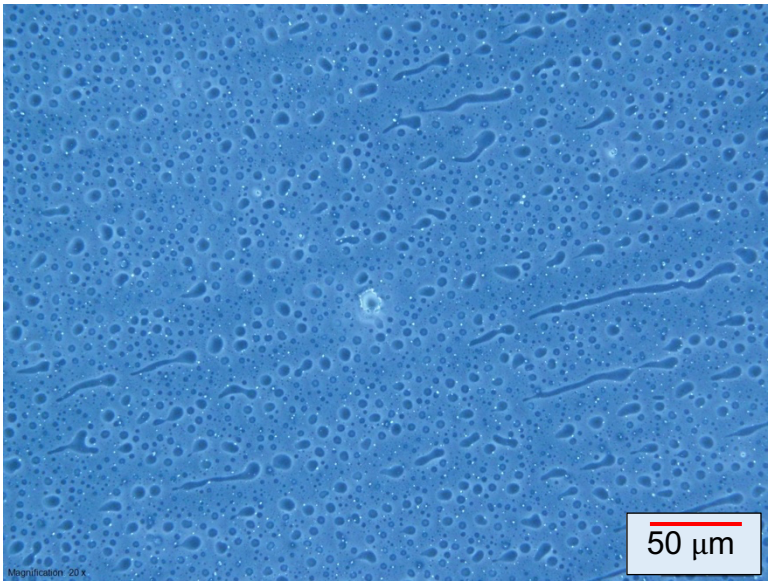

C. 603.9 ± 20.1 nm thick

Figure 4.21 Three optical micrographs of three unstained films containing 22.4 vol.% PS (M.W. 55 kg/mol) and 77.6 vol.% PB (M.W. 53 kg/mol). The scale bar is 50 μm.

4.3 Blend films of PS (M.W.= 290 kg/mol) and PB (M.W.= 200 kg/mol)

As the thickness of blend films with higher PS and PB molecular weights (290 kg/mol and 200 kg/mol, respectively) increased, a slight decrease in surface energy was observed. Films with 100 vol.% PS exhibited the highest surface energy, ranging from 31.8 ± 0.6 mN/m to 28.4 ± 0.2 mN/m, with thicknesses ranging from 141.5 ± 0.3 nm to 1143 ± 32 nm. Thinner 100 vol.% PB films (thickness 13.7 ± 0.3 nm to 92.59 ± 0.03) had higher surface energy compared to 100 vol.% PS thin films in the same range of thickness, while thicker 100 vol.% PB films (thickness 152.90 ± 0.05 nm to 1104.7 ± 8.1 nm) had lower surface energy (29.5 ± 0.9 mN/m to 28.5 ± 0.2 mN/m) than pure PS. For further details, please refer to Table 4.5.

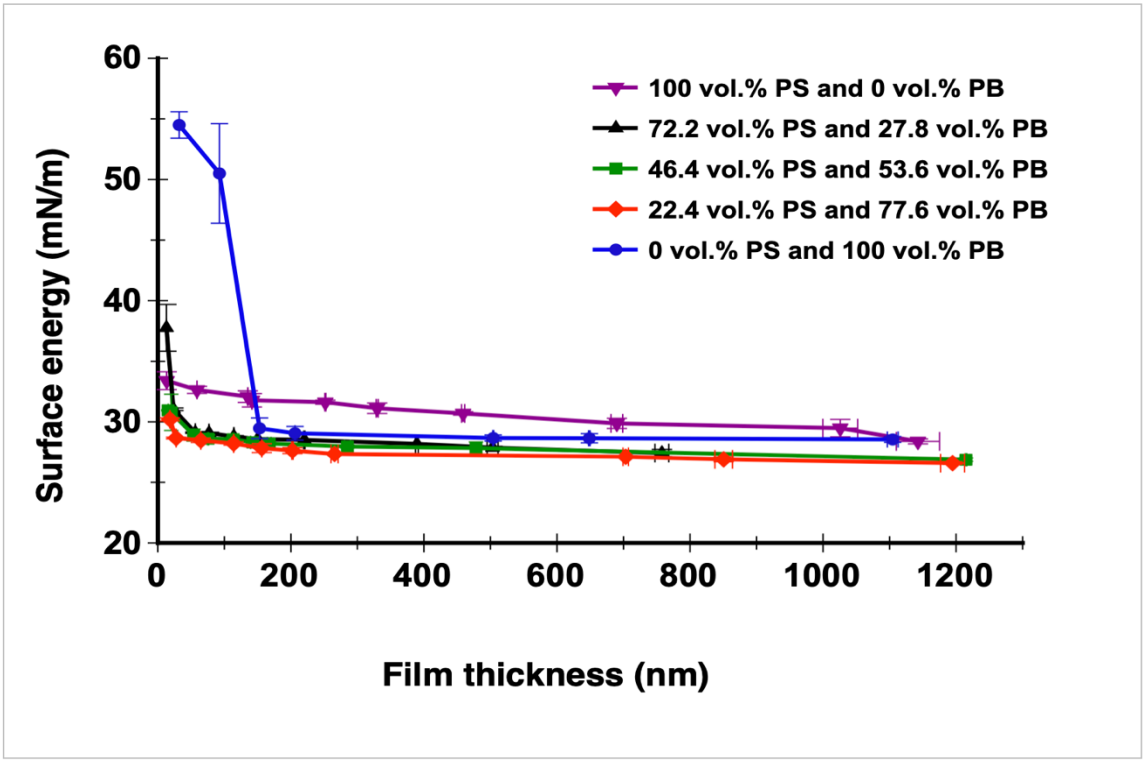

Figure 4.22 A plot of the relation of film thickness and surface energy of blend films of PS (M.W.= 290 kg/mol) and PB (M.W.= 200 kg/mol).

In this blend of PS 290 kg/mol films and PB 200 kg/mol, surface energy decreases slightly with increasing PB volume fraction (as shown in Figure 4.22 and Table 4.5).

The X-ray photoelectron spectroscopy (XPS) results indicate that the surface composition of the films with 27.8 vol.% PB and 53.6 vol.% PB is predominantly rich in polystyrene (PS), with only a small amount of polybutadiene (PB) present. In contrast, the film with 77.6 vol.% PB has a surface layer of approximately two-thirds PB and one-third PS. The respective percentages of PB at the film surfaces are 10.3 ± 0.8%, 9.2 ± 2.2%, and 63.4 ± 8.9% (Table 4.6).

Blend of	Polymer weight fraction	Polymer volume fraction	Water contact angle (°)	Surface energy((mN)/m)-water	Glycerol contact angle (°)	Surface energy((mN)/m)- glycerol	The Thickness (nm)
100 vol.% PS (M.W. 290 kg/mol)	0.15%	0.13%	82.4 ± 0.6	33.4 ± 0.7	72.6 ± 0.5	33.1 ± 0.6	13.3 ± 0.1
	0.25%	0.21%	83.6 ± 0.2	32.6 ± 0.3	73.4 ± 0.1	32.6 ± 0.2	58.85 ± 0.03
	0.50%	0.42%	84.4 ± 0.4	32.1 ± 0.5	75.2 ± 0.5	31.5 ± 0.6	135.3 ± 0.3
	1.00%	0.83%	84.9 ± 0.4	31.8 ± 0.6	75.3 ± 0.5	31.5 ± 0.6	141.5 ± 0.3
	1.50%	1.25%	85.2 ± 0.1	31.6 ± 0.2	75.6 ± 0.4	31.3 ± 0.5	251.8 ± 0.7
	2.00%	1.67%	85.9 ± 0.3	31.1 ± 0.4	76.6 ± 0.2	30.7 ± 0.2	329.8 ± 1.4
	2.50%	2.08%	86.6 ± 0.1	30.7 ± 0.1	77.3 ± 0.3	30.3 ± 0.3	459.0 ± 2.4
	3.50%	2.92%	87.9 ± 0.3	29.9 ± 0.4	78.2 ± 0.7	29.8 ± 0.8	690.0 ± 8.8
	5.00%	4.17%	88.5 ± 0.6	29.5 ± 0.7	78.9 ± 0.9	29.4 ± 1.0	1025.9 ± 26.2
	7.50%	6.25%	90.3 ± 0.2	28.4 ± 0.2	79.8 ± 0.9	28.9 ± 1.0	1142.7 ± 32.5
	10.00%	8.34%	91.5 ± 0.2	27.6 ± 0.2	82.0 ± 0.3	27.6 ± 0.4	2592.6 ± 8.2
72.2 vol.% PS (M.W. 290 kg/mol) and 27.8 vol.% PB (M.W. 200 kg/mol)	0.25%	0.22%	75.5 ± 1.5	37.8 ± 1.9	71.6 ± 2.2	33.6 ± 2.5	12.9 ± 0.1
	0.50%	0.43%	86.1 ± 0.1	31.0 ± 0.1	76.8 ± 0.1	30.6 ± 0.1	23.5 ± 0.1
	1.00%	0.87%	89.12 ± 0.04	29.1 ± 0.1	79.5 ± 0.3	29.1 ± 0.3	56.32 ± 0.02
	1.50%	1.30%	89.2 ± 0.1	29.1 ± 0.1	79.8 ± 0.1	28.9 ± 0.1	76.9 ± 0.2
	2.00%	1.73%	89.6 ± 0.1	28.8 ± 0.1	80.0 ± 0.2	28.8 ± 0.2	114.2 ± 0.2
	2.50%	2.17%	90.0 ± 0.1	28.6 ± 0.1	80.5 ± 0.1	28.5 ± 0.2	150.1 ± 0.4
	3.50%	3.03%	90.07 ± 0.01	28.51 ± 0.02	80.7 ± 0.1	28.4 ± 0.1	220.2 ± 1.0
	5.00%	4.33%	90.6 ± 0.1	28.2 ± 0.1	81.11 ± 0.04	28.1 ± 0.1	389.5 ± 2.1
	7.50%	6.50%	91.1 ± 0.1	27.9 ± 0.1	81.72 ± 0.02	27.78 ± 0.03	503.2 ± 8.2
	10.00%	8.66%	91.8 ± 0.2	27.4 ± 0.3	82.5 ± 0.1	27.3 ± 0.1	757.7 ± 10.4
46.4 vol.% PS (M.W. 290 kg/mol) and 53.6 vol.% PB (M.W. 200 kg/mol)	0.25%	0.22%	86.21 ± 0.04	30.9 ± 0.1	65.1 ± 1.3	37.4 ± 1.6	15.61 ± 0.05
	0.50%	0.45%	86.5 ± 1.2	30.8 ± 1.5	77.5 ± 0.5	30.2 ± 0.5	20.1 ± 0.1
	1.00%	0.90%	89.4 ± 0.4	28.9 ± 0.5	79.9 ± 0.1	28.8 ± 0.1	53.7 ± 0.2
	1.50%	1.35%	89.9 ± 0.3	28.6 ± 0.3	80.3 ± 0.2	28.6 ± 0.2	75.6 ± 0.8
	2.00%	1.80%	90.0 ± 0.2	28.6 ± 0.2	80.5 ± 0.1	28.5 ± 0.1	113.3 ± 1.1
	2.50%	2.25%	90.4 ± 0.1	28.3 ± 0.1	81.0 ± 0.1	28.2 ± 0.1	142.8 ± 3.4
	3.50%	3.14%	90.5 ± 0.1	28.2 ± 0.1	81.13 ± 0.01	28.12 ± 0.02	167.4 ± 2.8
	5.00%	4.49%	90.9 ± 0.1	28.0 ± 0.1	81.53 ± 0.04	27.88 ± 0.05	285.0 ± 4.6
	7.50%	6.74%	91.1 ± 0.4	27.8 ± 0.5	81.72 ± 0.03	27.78 ± 0.03	478.3 ± 7.9
	10.00%	8.98%	92.7 ± 0.1	26.9 ± 0.1	83.2 ± 0.1	26.9 ± 0.1	1214.8 ± 1.2
22.4 vol.% PS (M.W. 290 kg/mol) and 77.6 vol.% PB (M.W. 200 kg/mol)	0.25%	0.23%	87.4 ± 0.1	30.2 ± 0.1	78.0 ± 0.4	29.9 ± 0.5	18.1 ± 0.1
	0.50%	0.47%	89.8 ± 0.1	28.7 ± 0.1	80.44 ± 0.02	28.51 ± 0.02	27.51 ± 0.04
	1.00%	0.93%	90.1 ± 0.1	28.5 ± 0.2	80.8 ± 0.1	28.3 ± 0.1	64.59 ± 0.04
	1.50%	1.40%	90.5 ± 0.1	28.2 ± 0.1	81.1 ± 0.1	28.1 ± 0.1	114.0 ± 0.2
	2.00%	1.86%	91.2 ± 0.3	27.8 ± 0.4	81.73 ± 0.04	27.77 ± 0.05	156.2 ± 0.1
	2.50%	2.33%	91.5 ± 0.2	27.6 ± 0.2	82.03 ± 0.01	27.60 ± 0.01	202.3 ± 1.0
	3.50%	3.26%	91.92 ± 0.02	27.34 ± 0.03	82.57 ± 0.01	27.29 ± 0.02	265.6 ± 5.3
	5.00%	4.65%	92.3 ± 0.1	27.1 ± 0.1	82.90 ± 0.03	27.10 ± 0.03	703.3 ± 4.1
	7.50%	6.98%	92.6 ± 0.2	26.9 ± 0.2	83.24 ± 0.01	26.90 ± 0.02	850.5 ± 13.2
	10.00%	9.31%	93.1 ± 0.1	26.6 ± 0.1	83.7 ± 0.1	26.6 ± 0.1	1194.7 ± 18.0
100 vol.% PB (M.W. 200 kg/mol)	0.25%	0.24%	35.9 ± 2.1	61.4 ± 2.2	49.6 ± 2.8	46.1 ± 3.0	13.7 ± 0.3
	0.50%	0.48%	48.3 ± 0.9	54.5 ± 1.1	66.2 ± 1.1	36.8 ± 1.2	32.1 ± 0.1
	1.00%	0.96%	55.0 ± 3.4	50.5 ± 4.1	77.5 ± 0.5	30.2 ± 0.6	92.59 ± 0.03
	1.50%	1.45%	88.6 ± 0.7	29.5 ± 0.9	79.5 ± 0.2	29.1 ± 0.2	152.90 ± 0.05
	2.00%	1.93%	89.2 ± 0.4	29.1 ± 0.6	79.7 ± 0.7	28.9 ± 0.8	206.2 ± 0.1
	2.50%	2.41%	89.8 ± 0.2	28.7 ± 0.2	79.8 ± 0.2	28.9 ± 0.2	504.2 ± 0.7
	3.50%	3.37%	89.9 ± 0.3	28.6 ± 0.3	80.5 ± 0.6	28.5 ± 0.7	648.7 ± 1.1
	5.00%	4.82%	90.0 ± 0.2	28.5 ± 0.2	80.9 ± 0.8	28.2 ± 0.3	1104.7 ± 8.1
	7.50%	7.23%	90.7 ± 0.4	28.1 ± 0.5	81.3 ± 0.1	28.0 ± 0.1	2240.9 ± 2.0
	10.00%	9.63%	91.2 ± 0.2	27.8 ± 0.2	81.8 ± 0.1	27.7 ± 0.1	2640.0 ± 72.8

Table 4.5 Data from the contact angle experiment of blend films of PS 290 kg/mol and PB 200 kg/mol.

The analysis of ToF-ERD and RBS data reveals that in a blend film containing 27.8 vol.% PB, the volume fraction of PB at the surface is approximately 0.4 (Figure 4.23, A). Below the surface, the PB volume fraction remains constant, ranging from 0.4 to 0.2 towards the back of the film. Conversely, in a blend film with 53.6 vol.% PB, the surface PB volume fraction is around 0.4, then decreases to 0.2 in bulk before increasing to 0.85 close to the substrate (Figure 4.23, B). In the case of a blend film with 77.6 vol.% PB, the surface exhibits a PB volume fraction of 1.0, which gradually decreases through the bulk to approximately 0.8 and stabilises at 0.6 close to the back of the film (Figure 4.23, C).

PS M.W. (kg/mol)	PB M.W. (kg/mol)	PB (vol. %)	Polymers (vol. %)	Thickness (nm)	Surface energy (water) (mN/m)	Average roughness (nm)	PB amount at the surface (%)
290.0	200.0	0.0	2.9	690.0 ± 8.8	29.9 ± 0.4	1.4 ± 0.1	
		27.8	6.5	503.2 ± 8.2	27.9 ± 0.1	14.0 ± 5.6	10.3 ± 0.8
		53.6	6.7	478.3 ± 7.9	27.8 ± 0.5	6.2 ± 2.0	9.2 ± 2.2
		77.6	4.7	703.3 ± 4.1	27.1 ± 0.1	21.1 ± 6.6	63.4 ± 8.9
		100.0	3.4	648.7 ± 1.1	28.6 ± 0.3	2.3 ± 0.2	

Table 4.6 Summarising some data of five blend films PS (M.W.= 290 kg/mol) and PB (M.W.= 200 kg/mol).

The AFM analysis revealed that the surface roughness of the films with 27.8 vol.% PB, 53.6 vol.% PB, and 77.6 vol.% PB is 14.0 ± 5.6 nm, 6.2 ± 1.9 nm, and 21.1 ± 6.6 nm, respectively (see Figures 4.24 to 4.27). Consequently, the film with 77.6 vol.% PB exhibits the highest surface roughness among these blends (Figure 4.27). This film, containing the highest proportion of PB on the surface, also has the least surface energy. Figure 4.26 shows the lowest surface roughness among these blends.

The optical microscope revealed that the films' structure exhibited thickness-dependent behaviour (see Figures 4.28, 29, and 30). However, Figures 4.28-E, 4.29-F, and 4.30-E displayed similar surface structures. These three optical images demonstrated nearly identical surface energies of 27.4 ± 0.3 mN/m, 26.9 ± 0.1 mN/m, and 26.9 ± 0.2 mN/m, respectively.

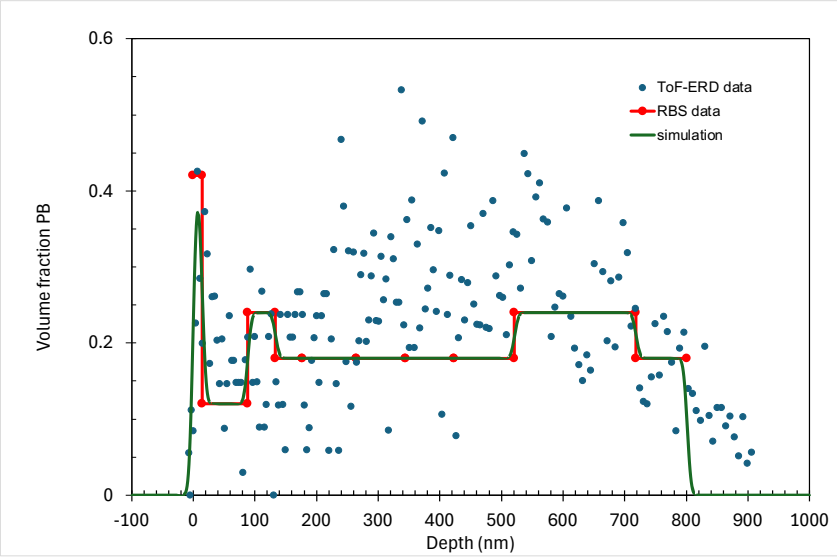

A. 27.8 vol.% PB

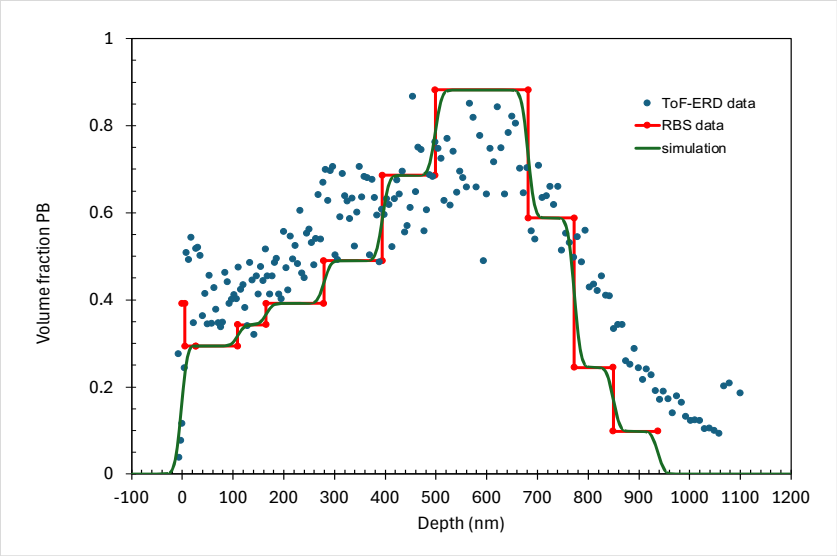

B. 53.6 vol.% PB

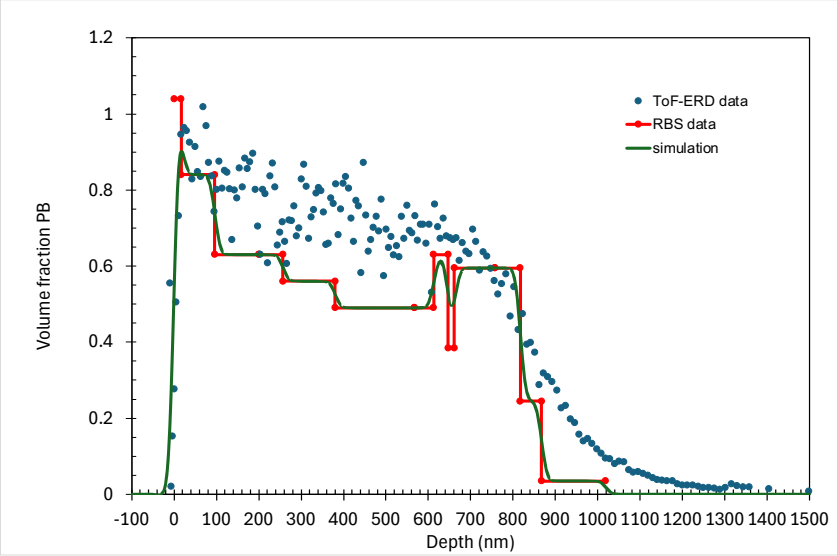

C. 77.6 vol.% PB

Figure 4.23 ToF-ERD data compared with volume fraction profiles obtained by RBS for blend films of PS (M.W.= 290 kg/mol) and PB (M.W.= 200 kg/mol).

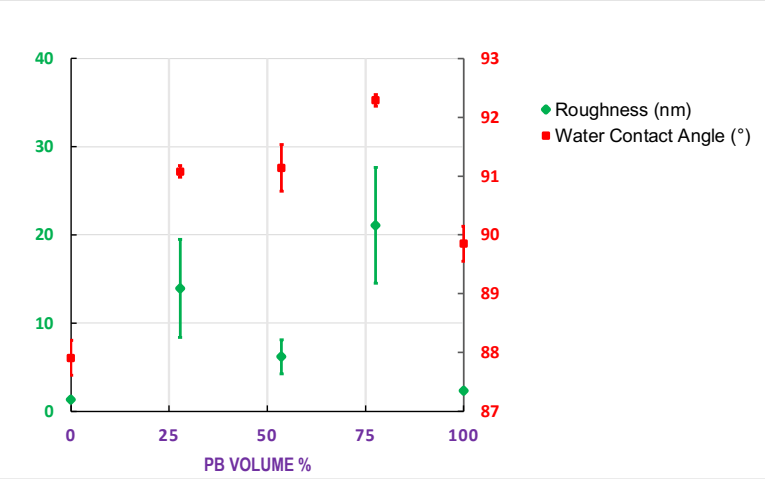

Figure 4.24 PB volume %, roughness, and water contact angle for blend films of PS (M.W.= 290 kg/mol) and PB (M.W.= 200 kg/mol).

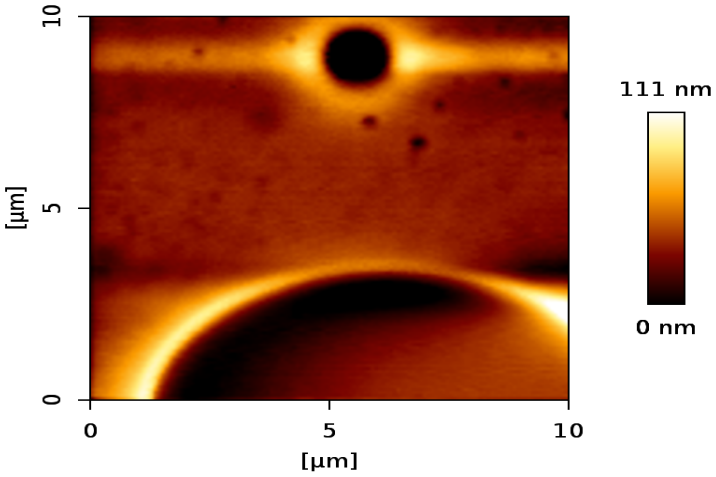

Figure 4.25 AFM topography of the unstained film surface containing 72.2 vol.% PS (M.W. 290 kg/mol) and 27.8 vol.% PB (M.W. 200 kg/mol). The roughness is 14 $\pm$ 5.6 nm. The thickness is 503.2 ± 8.2 nm. Surface energy is 27.9 $\pm$ 0.1 mN/m.

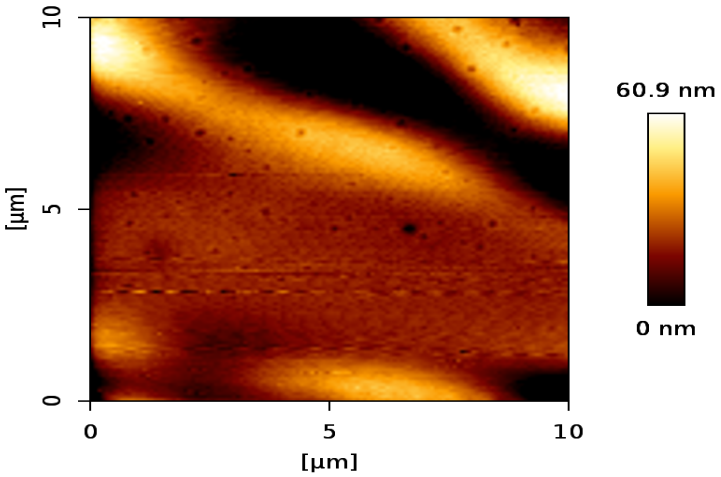

Figure 4.26 AFM topography of the unstained film surface containing 46.4 vol.% PS (M.W. 290 kg/mol) and 53.6% PB (M.W. 200 kg/mol). The roughness is 6.2 $\pm$ 1.9 nm. The thickness is 478.3 ± 7.9 nm. Surface energy is 27.8 $\pm$ 0.5 mN/m.

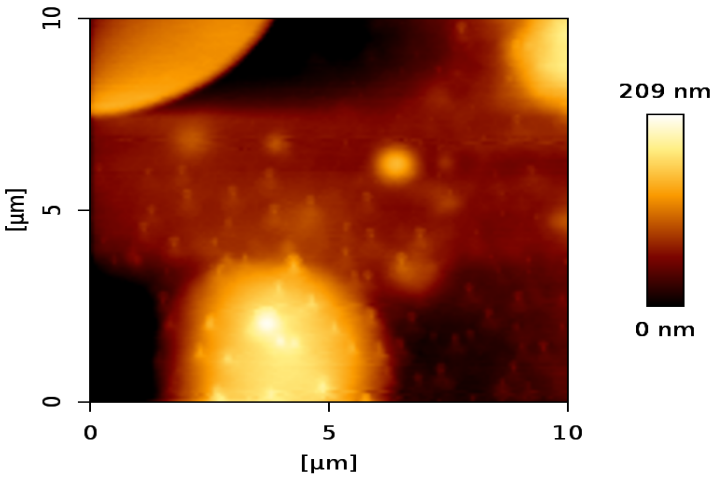

Figure 4.27 AFM topography of the unstained film surface containing 22.4 vol.% PS (M.W. 290 kg/mol) and 77.6 vol.% PB (M.W. 200 kg/mol). The roughness is 21.1 ± 6.6 nm. The thickness is 703.3 ± 4.1 nm. Surface energy is 27.1 ± 0.1 mN/m.

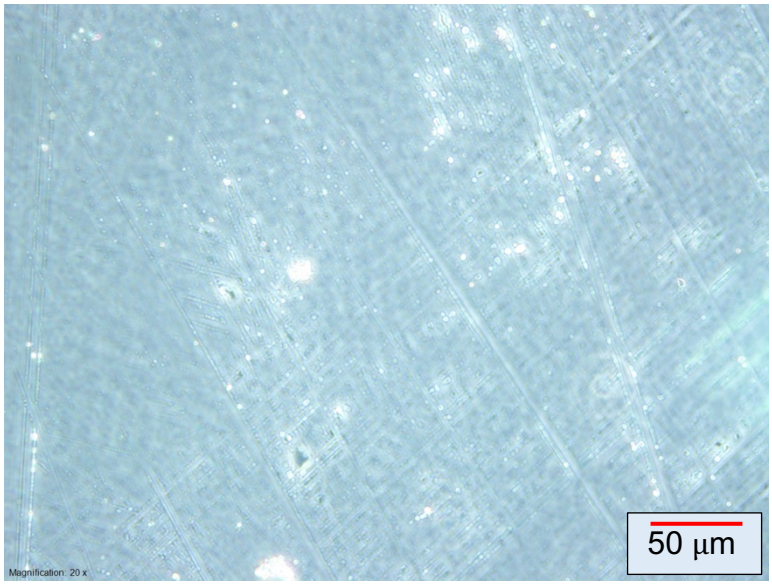

A. 114.2 ± 0.2 nm thick

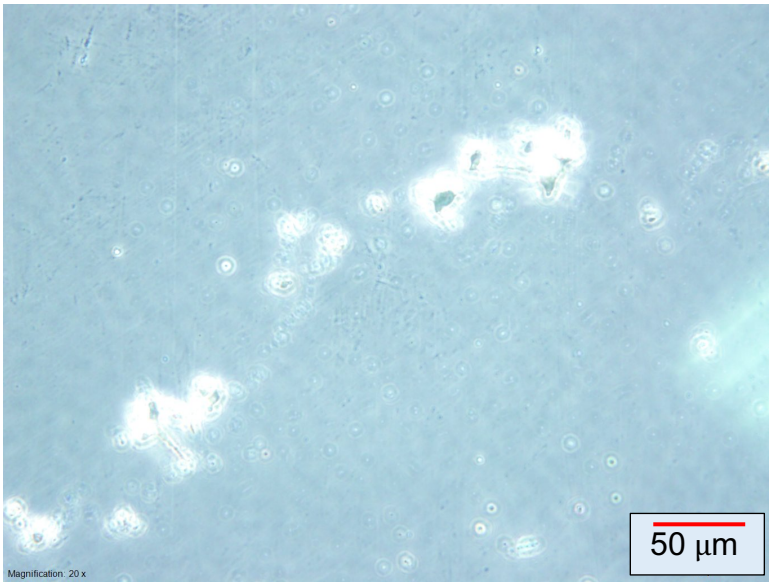

B. 389.5 ± 2.1 nm thick

Figure 4.28 Two optical micrographs of two unstained films containing 72.2 vol.% PS (M.W. 290 kg/mol) and 27.8 vol.% PB (M.W. 200 kg/mol). The scale bar is 50 µm.

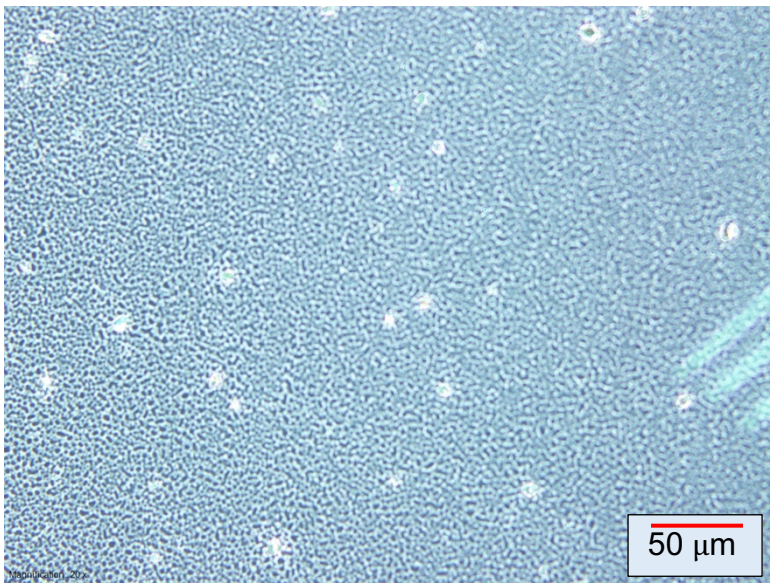

A. 142.8 ± 3.4 nm thick

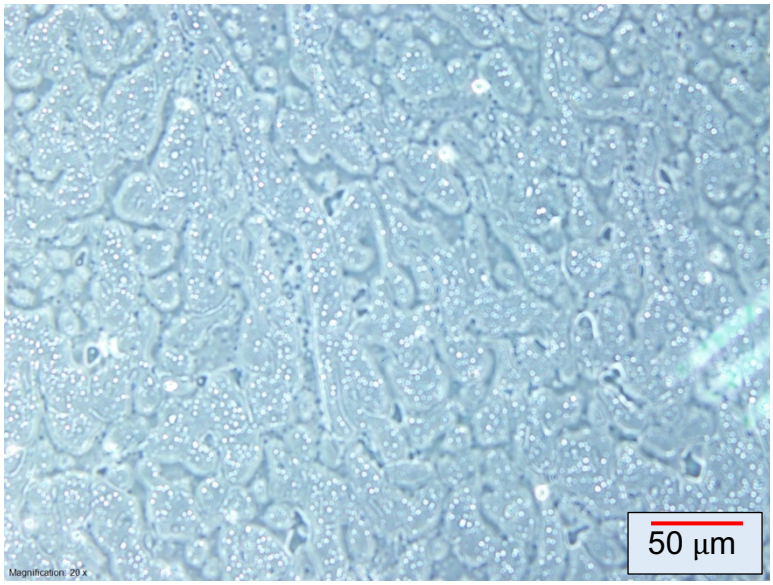

B. 285.0 ± 4.6 nm thick

Figure 4.29 Two optical micrographs of two unstained films containing 46.4 vol.% PS (M.W. 290 kg/mol) and 53.6 vol.% PB (M.W. 200 kg/mol). The scale bar is 50 μm.

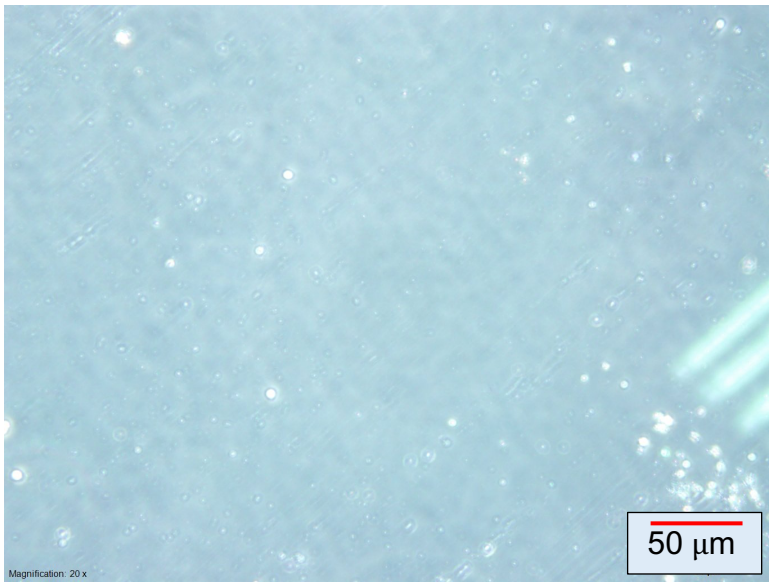

A. 64.59 ± 0.04 nm thick

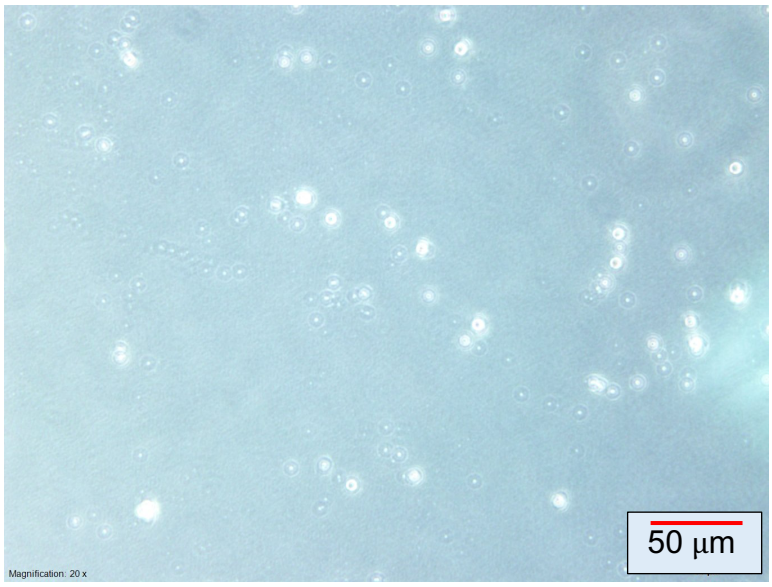

B. 202.3 ± 1.0 nm thick

Figure 4.30 Two optical micrographs of the surface of two unstained films containing 22.4 vol.% PS (M.W. 290 kg/mol) and 77.6 vol.% PB (M.W. 200 kg/mol). The scale bar is 50 μm.

4.4 Blend films of PS (M.W.= 290 kg/mol) and PB (M.W.= 3 kg/mol)

We studied blend films containing 290 kg/mol PS and 3 kg/mol PB. Films consisting of 77.6 vol.% PB and those with equal proportions of PS and PB displayed the lowest surface energy as the film thickness increased between 250 nm and 2500 nm (Figure 4.31). Meanwhile, pure PB films exhibited the highest surface energy in the same thickness range. This result indicates that single polymer films with a lower molecular weight are less hydrophobic than those in the same group for the second single polymer. Moreover, pure PS films and those containing 27.8 vol.% PB demonstrated greater hydrophobicity than pure PB films. Films thinner than 250 nm have different surface energies compared to thicker ones (refer to Figure 4.31 and Table 4.7).

To evaluate the measurement accuracy, we compared the relationship between surface energies and film thickness using water contact angle (Figure 4.31) and glycerol contact angles, and they are in agreement (Figure 4.32).

The XPS results show that the amounts of PB at the surface of films with 27.8 vol.% PB, 53.6 vol.% PB, and 77.6 vol.% PB are 85.2% ± 4.4%, 104.0% ± 5.7%, and 94.4% ± 4.5%, respectively. This indicates that the surface layer of these blends is predominantly PB, which has a lower molecular weight (3 kg/mol) than the other polymer in the same blend (290 kg/mol PS).

The analysis of ToF-ERD and RBS data reveals that a PB depth profile of blend film containing 27.8 vol.% PB has three peaks: the highest for the surface (air interface), which has a volume fraction of PB of 1, then around 0.4 at the bulk and 0.45 at the back of the film (substrate interface) (Figure 4.33, A). Conversely, a blend film with 53.6 vol.% PB has two peaks: one at the surface PB volume fraction is 1, then decreases to 0.2 in bulk before a small peak close to the substrate of PB volume fraction of 0.1 (Figure 4.33, B). In the case of a blend film with 77.6 vol.% PB, the only peak is at the surface, exhibiting a PB volume fraction of 1.0, which gradually decreases toward the film's end (Figure 4.33, C).

AFM shows that the surface roughness of films 27.8 vol.% PB, 53.6 vol.% PB, and 77.6 vol.% PB is 4.5 ± 1.6 nm, 46.0 ± 11.4 nm, and 21.1 ± 7.3 nm (Figures 4.34 to 4.37), respectively. Therefore, the highest surface roughness is found in the film of 53.6 vol.% PB of these blends, which is completely PB at the surface (Table 4.8).

Blend of	Polymer weight fraction	Polymer volume fraction	Water contact angle (°)	Surface energy((mN)/m)-water	Glycerol contact angle (°)	Surface energy((mN)/m)- glycerol	The Thickness (nm)
100 vol.% PS (M.W. 290 kg/mol)	0.15%	0.13%	82.4 ± 0.6	33.4 ± 0.7	72.6 ± 0.5	33.1 ± 0.6	13.3 ± 0.1
	0.25%	0.21%	83.6 ± 0.2	32.6 ± 0.3	73.4 ± 0.1	32.6 ± 0.2	58.85 ± 0.03
	0.50%	0.42%	84.4 ± 0.4	32.1 ± 0.5	75.2 ± 0.5	31.5 ± 0.6	135.3 ± 0.3
	1.00%	0.83%	84.9 ± 0.4	31.8 ± 0.6	75.3 ± 0.5	31.5 ± 0.6	141.5 ± 0.3
	1.50%	1.25%	85.2 ± 0.1	31.6 ± 0.2	75.6 ± 0.4	31.3 ± 0.5	251.8 ± 0.7
	2.00%	1.67%	85.9 ± 0.3	31.1 ± 0.4	76.6 ± 0.2	30.7 ± 0.2	329.8 ± 1.4
	2.50%	2.08%	86.6 ± 0.1	30.7 ± 0.1	77.3 ± 0.3	30.3 ± 0.3	459.0 ± 2.4
	3.50%	2.92%	87.9 ± 0.3	29.9 ± 0.4	78.2 ± 0.7	29.8 ± 0.8	690.0 ± 8.8
	5.00%	4.17%	88.5 ± 0.6	29.5 ± 0.7	78.9 ± 0.9	29.4 ± 1.0	1025.9 ± 26.2
	7.50%	6.25%	90.3 ± 0.2	28.4 ± 0.2	79.8 ± 0.9	28.9 ± 1.0	1142.7 ± 32.5
	10.00%	8.34%	91.5 ± 0.2	27.6 ± 0.2	82.0 ± 0.3	27.6 ± 0.4	2592.6 ± 8.2
72.2 vol.% PS (M.W. 290 kg/mol) and 27.8 vol.% PB (M.W. 3 kg/mol)	0.25%	0.22%	70.3 ± 0.3	41.1 ± 0.4	73.2 ± 0.4	32.7 ± 0.5	24.02 ± 0.03
	0.50%	0.43%	81.2 ± 0.2	34.1 ± 0.2	73.3 ± 2.8	32.6 ± 3.3	53.20 ± 0.04
	1.00%	0.87%	81.3 ± 0.2	34.0 ± 0.2	74.8 ± 0.5	31.8 ± 0.6	102.6 ± 0.1
	1.50%	1.30%	83.5 ± 0.1	32.7 ± 0.1	75.1 ± 0.5	31.6 ± 0.6	140.2 ± 0.1
	2.00%	1.73%	84.5 ± 0.3	32.0 ± 0.4	74.9 ± 0.5	31.7 ± 0.6	223.7 ± 0.3
	2.50%	2.17%	86.1 ± 0.2	31.0 ± 0.2	76.8 ± 0.1	30.6 ± 0.1	274.5 ± 0.4
	3.50%	3.03%	86.8 ± 0.3	30.6 ± 0.3	77.6 ± 0.1	30.2 ± 0.1	456.7 ± 1.2
	5.00%	4.33%	87.6 ± 0.1	30.1 ± 0.2	78.2 ± 0.8	29.8 ± 1.0	702.4 ± 4.4
	7.00%	6.06%	88.4 ± 0.2	29.6 ± 0.2	79.7 ± 0.1	29.0 ± 0.1	838.7 ± 5.1
	10.00%	8.66%	89.0 ± 0.1	29.2 ± 0.2	81.2 ± 0.3	28.1 ± 0.4	979.8 ± 20.6
	20.00%	17.32%	90.4 ± 0.2	28.3 ± 0.2	81.7 ± 0.4	27.8 ± 0.5	1828.4 ± 5.2
	30.00%	25.98%	91.0 ± 0.3	27.9 ± 0.4	82.8 ± 0.1	27.2 ± 0.1	2315.6 ± 2.2
46.4 vol.% PS (M.W. 290 kg/mol) and 53.6 vol.% PB (M.W. 3 kg/mol)	0.25%	0.22%	27.1 ± 2.0	65.8 ± 1.8	57.0 ± 3.0	42.0 ± 3.4	28.7 ± 0.1
	0.50%	0.45%	81.1 ± 0.1	34.2 ± 0.2	72.6 ± 0.1	33.1 ± 0.1	54.47 ± 0.05
	1.00%	0.90%	81.6 ± 0.3	33.9 ± 0.4	73.3 ± 0.2	32.7 ± 0.2	88.2 ± 0.9
	1.50%	1.35%	82.4 ± 0.1	33.4 ± 0.1	74.4 ± 0.2	32.0 ± 0.2	139.0 ± 2.0
	2.00%	1.80%	87.40 ± 0.03	30.19 ± 0.04	78.6 ± 0.2	29.6 ± 0.2	169.8 ± 3.7
	2.50%	2.25%	88.0 ± 0.2	29.8 ± 0.2	78.6 ± 0.1	29.6 ± 0.1	294.1 ± 4.6
	3.50%	3.14%	89.2 ± 0.4	29.1 ± 0.5	79.4 ± 0.2	29.1 ± 0.2	394.2 ± 8.3
	5.00%	4.49%	90.1 ± 0.2	28.5 ± 0.2	81.0 ± 0.6	28.2 ± 0.6	501.5± 14.1
	7.00%	6.29%	92.0 ± 0.4	27.3 ± 0.5	83.0 ± 0.3	27.0 ± 0.4	671.7 ± 12.9
	10.00%	8.98%	92.4 ± 0.3	27.0 ± 0.3	83.3 ± 0.4	26.9 ± 0.4	986.7 ± 34.7
	20.00%	17.97%	92.8 ± 0.1	26.8 ± 0.1	83.6 ± 0.3	26.7 ± 0.3	1881.5 ± 49.3
	30.00%	26.96%	93.1 ± 0.2	26.7 ± 0.2	83.8 ± 0.1	26.6 ± 0.1	2433.8 ± 5.6
22.4 vol.% PS (M.W. 290 kg/mol) and 77.6 vol.% PB (M.W. 3 kg/mol)	0.25%	0.23%	31.2 ± 1.6	63.8 ± 1.6	31.7 ± 1.0	55.2 ± 0.9	31.4 ± 0.1
	0.50%	0.47%	34.1 ± 1.8	62.4 ± 1.9	38.6 ± 0.9	51.9 ± 0.9	44.7 ± 0.1
	1.00%	0.93%	58.9 ± 5.6	48.2± 6.8	55.0 ± 2.9	43.1 ± 3.2	84.9 ± 1.1
	1.50%	1.40%	60.0 ± 2.4	47.5 ± 2.9	57.3 ± 0.3	41.9 ± 0.4	103.3 ± 2.0
	2.00%	1.86%	67.4 ± 0.4	42.8 ± 0.5	57.3 ± 4.8	41.8 ± 5.4	113.3 ± 3.7
	2.50%	2.33%	68.5 ± 0.7	42.2 ± 0.9	58.8 ± 0.9	41.0 ± 1.0	120.6 ± 3.1
	3.50%	3.26%	82.2 ± 0.4	33.5 ± 0.5	74.3 ± 0.9	32.1 ± 1.0	156.9 ± 7.1
	5.00%	4.65%	86.5 ± 0.4	30.8 ± 0.5	78.3 ± 0.1	29.8 ± 0.2	231.4 ± 7.2
	7.00%	6.52%	89.9 ± 0.7	28.6 ± 0.8	82.0 ± 0.5	27.6 ± 0.6	273.7 ± 4.2
	10.00%	9.31%	91.9 ± 0.1	27.4 ± 0.1	82.71 ± 0.05	27.2 ± 0.1	281.0 ± 6.4
	20.00%	18.62%	92.3 ± 0.2	27.1 ± 0.3	83.8 ± 0.1	26.6 ± 0.1	514.6 ± 2.0
	30.00%	27.93%	93.2 ± 0.1	26.5 ± 0.1	83.9 ± 0.4	26.5 ± 0.4	1210.9 ± 27.4
	50.00%	46.55%	94.0 ± 0.1	26.1 ± 0.1	84.6 ± 0.2	26.1 ± 0.2	2013.1 ± 2.5
100 vol.% PB (M.W. 3 kg/mol)	0.50%	0.48%	70.5 ± 4.9	40.9 ± 6.1	69.4 ± 0.5	34.9± 0.5	4.2 ± 0.1
	1.00%	0.96%	78.8 ± 0.2	35.6 ± 0.3	70.9 ± 0.2	34.1 ± 0.3	83.5 ± 1.5
	2.00%	1.93%	79.9 ± 0.1	35.0 ± 0.1	71.3 ± 0.9	33.8 ± 1.0	193.9 ± 1.1
	2.50%	2.41%	80.1 ± 1.1	34.8 ± 1.4	73.0 ± 0.1	32.8 ± 0.1	273.2 ± 1.6
	3.50%	3.37%	80.7 ± 0.6	34.4 ± 0.7	73.1 ± 0.1	32.8 ± 0.1	395.3 ± 0.6
	4.00%	3.85%	81.8 ± 0.8	33.8 ± 1.0	73.2 ± 0.3	32.7 ± 0.3	408.2 ± 0.5
	5.00%	4.82%	82.4 ± 0.2	33.4 ± 0.2	73.5 ± 0.6	32.5 ± 0.6	513.8 ± 1.6
	7.50%	7.23%	82.8 ± 0.5	33.1 ± 0.7	73.6 ± 0.7	32.5 ± 0.8	1141.6 ± 9.0
	10.00%	9.63%	87.3 ± 0.2	30.3 ± 0.3	79.2 ± 0.2	29.2 ± 0.3	1324.9 ± 11.6
	20.00%	19.27%	88.4 ± 0.1	29.5 ± 0.8	79.6 ± 0.2	29.0 ± 0.2	1378.8 ± 31.4
	30.00%	28.90%	89.7 ± 0.2	28.8 ± 0.3	80.5 ± 0.1	28.5 ± 0.1	2433.2 ± 1.8

Table 4.7 Data from the contact angle experiment of blend films of PS (290 kg/mol) and PB (3 kg/mol).

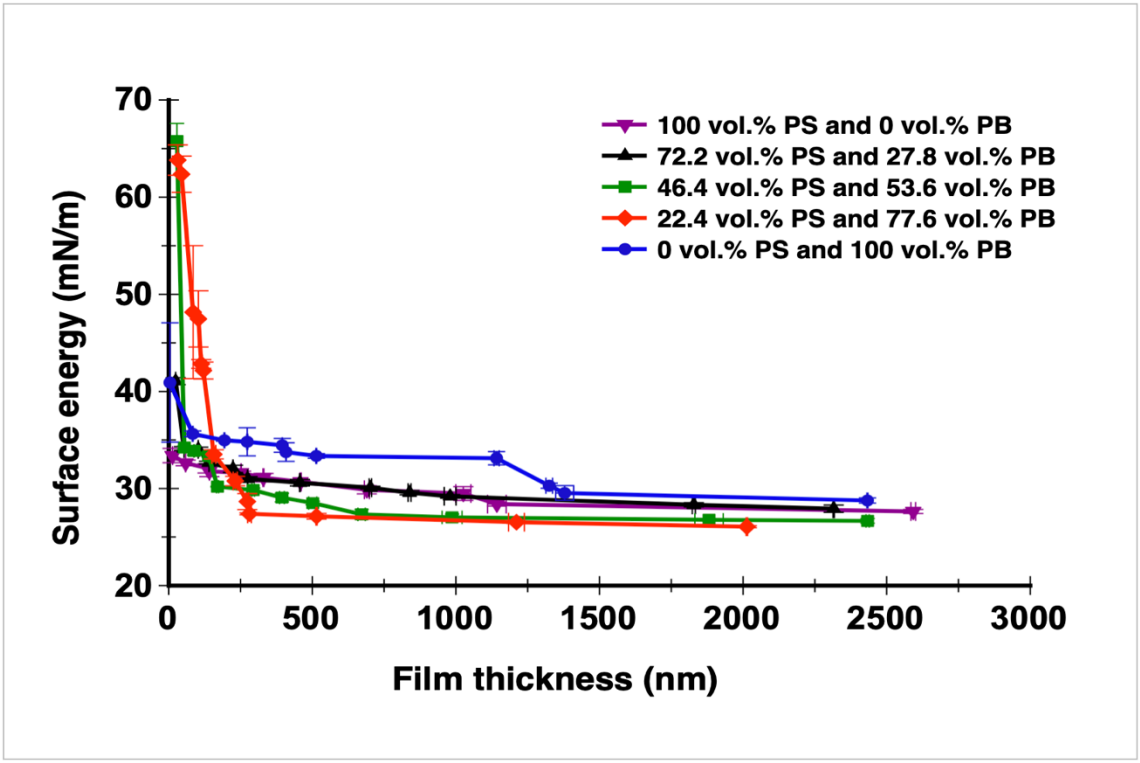

Figure 4.31 A plot of the relation of film thickness and surface energy (obtained from water contact angle) of blend films of PS (M.W.= 290 kg/mol) and PB (M.W.= 3 kg/mol).

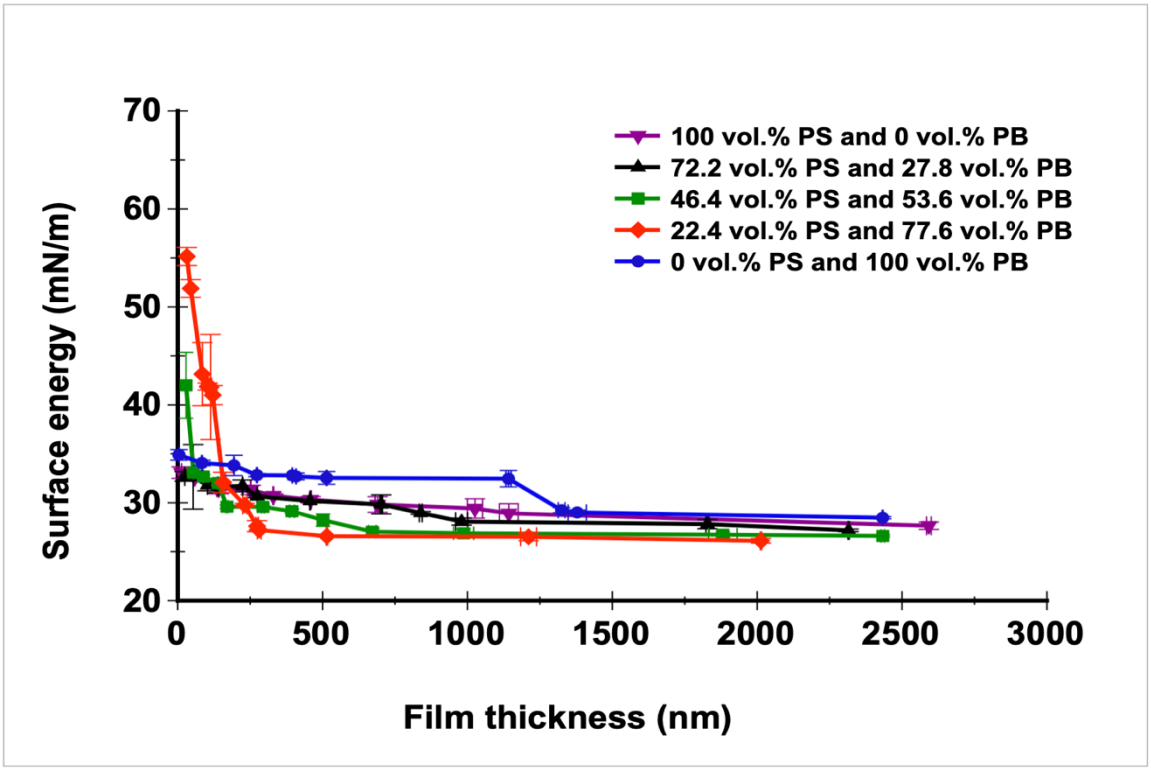

Figure 4.32 A plot of the relation of film thickness and surface energy (obtained from glycerol contact angle) of blend films of PS (M.W.= 290 kg/mol) and PB (M.W.= 3 kg/mol).

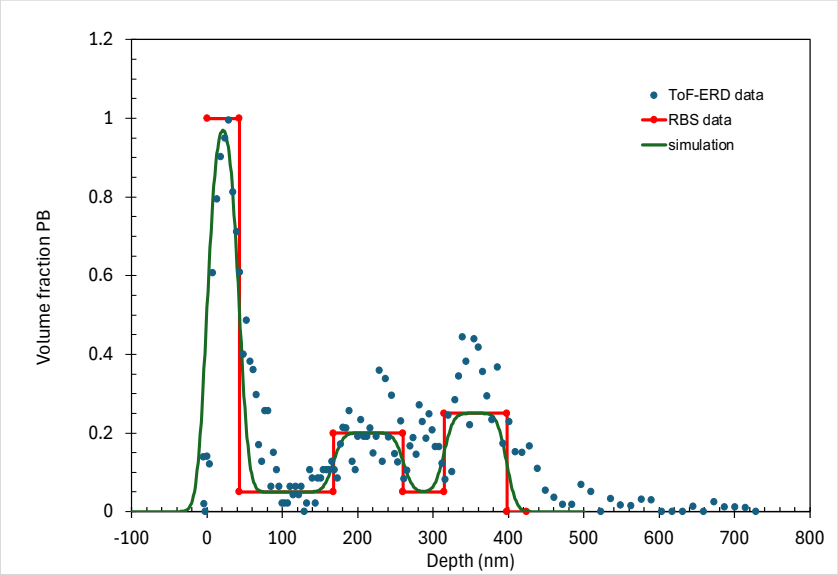

A. 27.8 vol.% PB

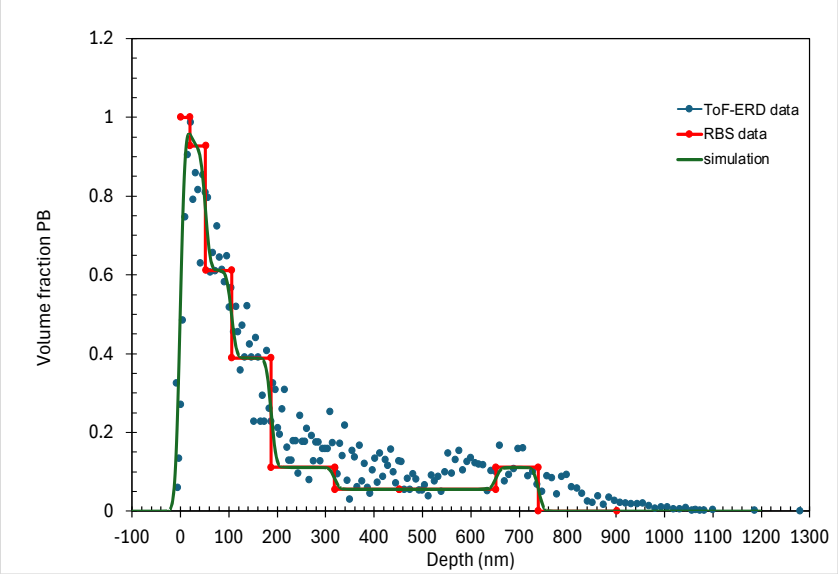

B. 53.6 vol.% PB

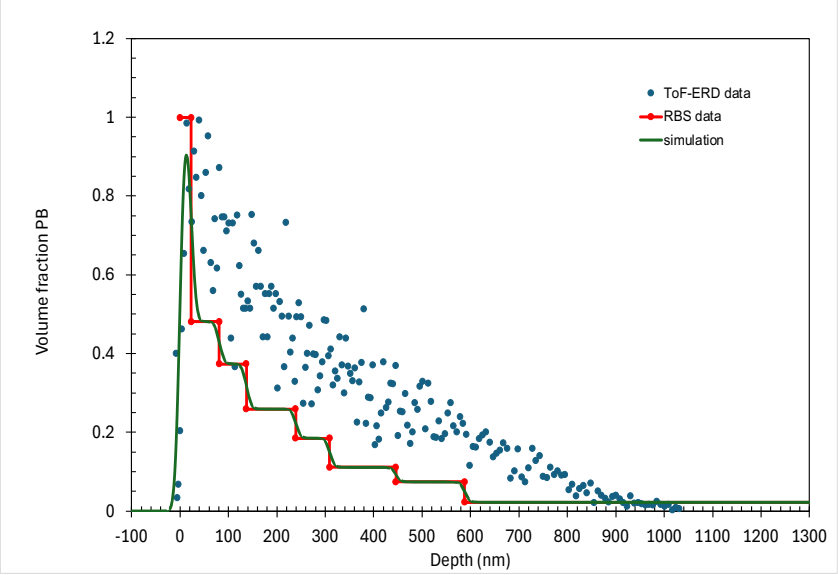

C. 77.6 vol.% PB

Figure 4.33 ToF-ERD data compared with volume fraction profiles obtained by RBS for blend films of PS (M.W.= 290 kg/mol) and PB (M.W.= 3 kg/mol).

PS M.W. (kg/mol)	PB M.W. (kg/mol)	PB (vol. %)	Polymers (vol. %)	Thickness (nm)	Surface energy (water) (mN/m)	Average roughness (nm)	PB amount at the surface (%)
290.0	3.0	0.0	2.9	690.0 ± 8.8	29.9 ± 0.4	1.4 ± 0.1	
		27.8	4.3	702.4 ± 4.4	30.1 ± 0.2	4.5 ± 1.6	85.2 ± 4.4
		53.6	6.3	671.7 ± 13.0	27.3 ± 0.5	46.0 ± 11.4	104.0 ± 5.7
		77.6	18.6	514.6 ± 2.0	27.1 ± 0.3	21.1 ± 7.3	94.4 ± 4.5
		100.0	4.7	513.8 ± 1.6	33.4 ± 0.2	5.0 ± 0.5	

Table 4. 8 Summarising some data of five blend films PS (M.W.= 290 kg/mol) and PB (M.W.= 3 kg/mol).

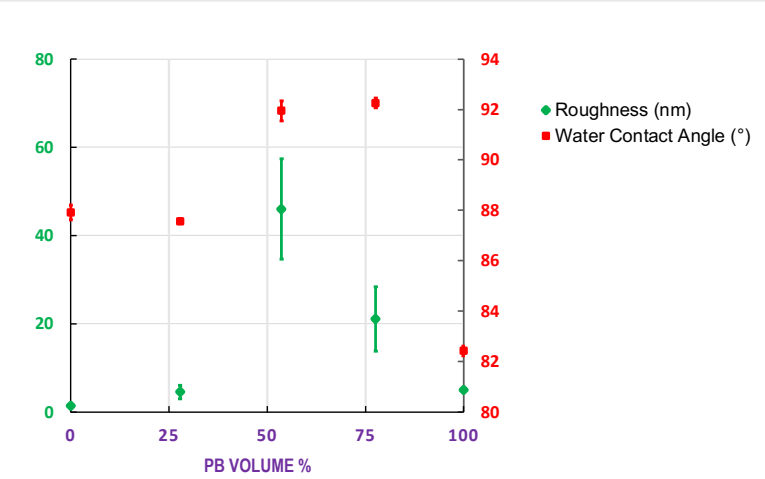

Figure 4.34 PB volume %, roughness, and water contact angle for blend films of PS (M.W.= 290 kg/mol) and PB (M.W.= 3 kg/mol).

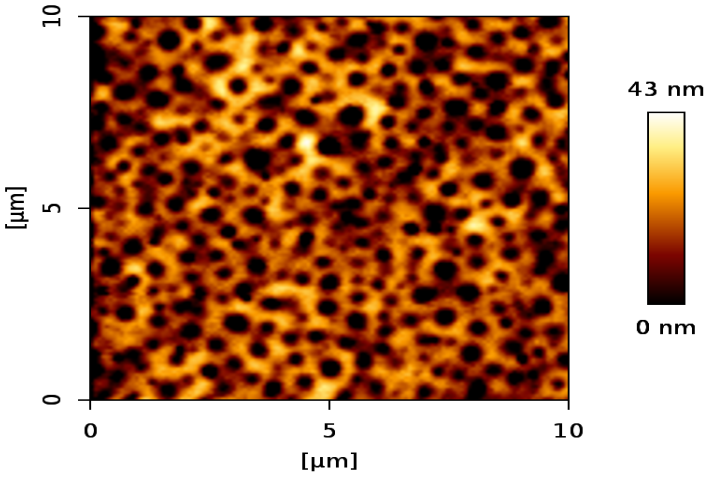

Figure 4.35 AFM topography of the unstained film surface containing 72.2 vol.% PS (M.W. 290 kg/mol) and 27.8 vol.% PB (M.W. 3 kg/mol). The roughness is 4.5 ± 1.6 nm. The thickness is 702.4 ± 4.4 nm. Surface energy is 30.1 ± 0.1 mN/m.

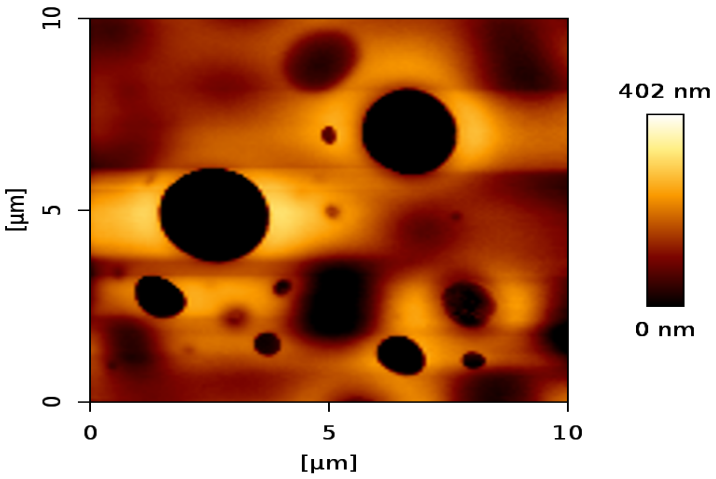

Figure 4.36 AFM topography of the unstained film surface containing 46.4 vol.% PS (M.W. 290 kg/mol) and 53.6 vol.% PB (M.W. 3 kg/mol). The roughness is 46.0 ± 11.4 nm. The thickness is 671.7 ± 12.9 nm. Surface energy is 27.3 ± 0.5 mN/m.

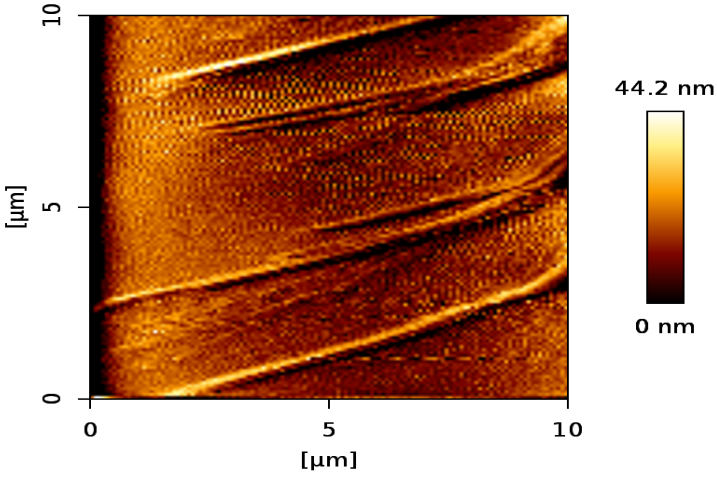

Figure 4.37 AFM topography of the unstained film surface containing 22.4 vol.% PS (M.W. 290 kg/mol) and 77.6 vol.% PB (M.W. 3 kg/mol). The roughness is 21.1 ± 7.3 nm. The thickness is 514.6 ± 2.0 nm. Surface energy is 27.1 ± 0.3 mN/m.

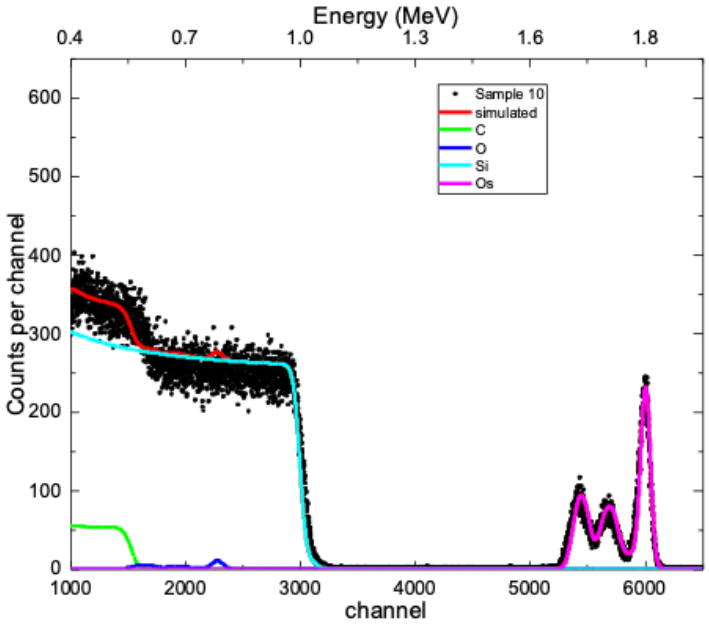

(A)

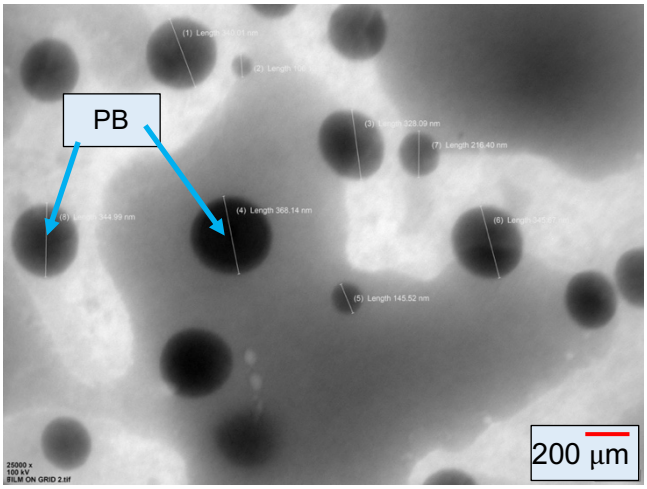

(B)

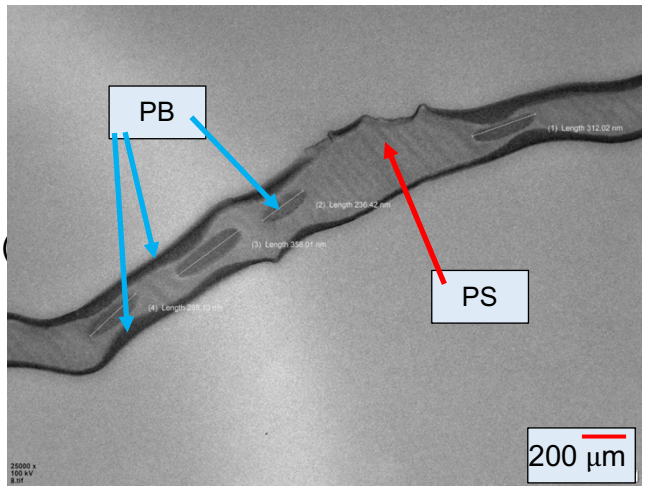

Figure 4.38 (A) RBS spectrum for a thin film comprises 72.2 vol.% PS (M.W. 290 kg/mol) and 27.8 vol.% PB (M.W. 3 kg/mol). (B) TEM micrograph of the top surface (C) TEM cross-section micrograph of the stained film containing 72.2 vol.% PS (M.W. 290 kg/mol) and 27.8 vol.% PB (M.W. 3 kg/mol). The roughness is 4.5 $\pm$ 1.6 nm. The thickness is 702.4 $\pm$ 4.4 nm. Surface energy is 30.1 $\pm$ 0.1 mN/m. The scale bar is 200 nm.

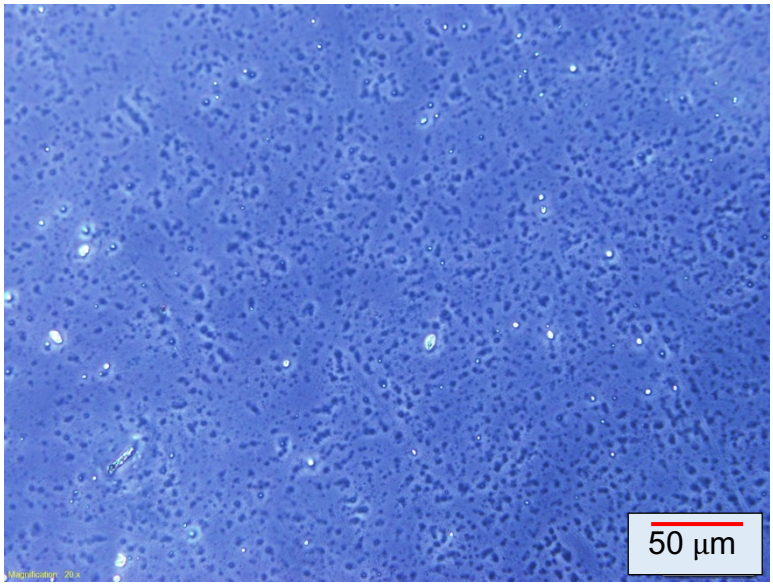

A. 274.5 ± 0.4 nm thick

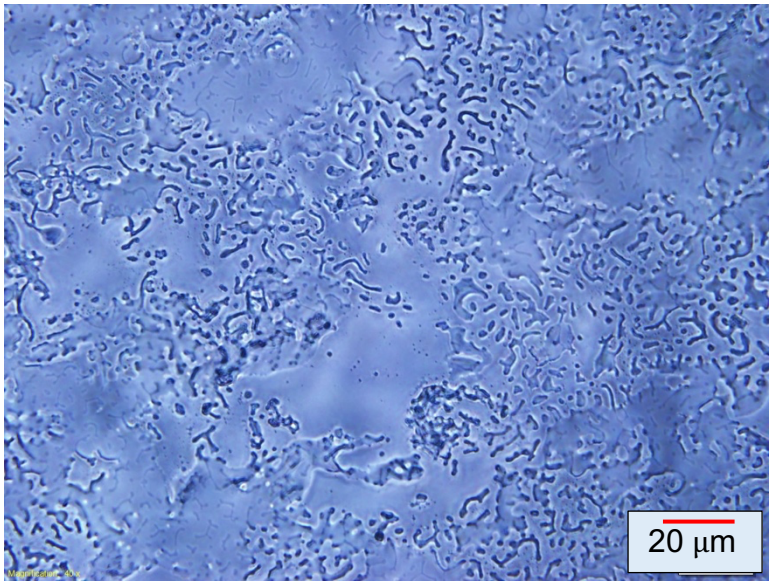

B. 838.7 ± 5.1 nm thick

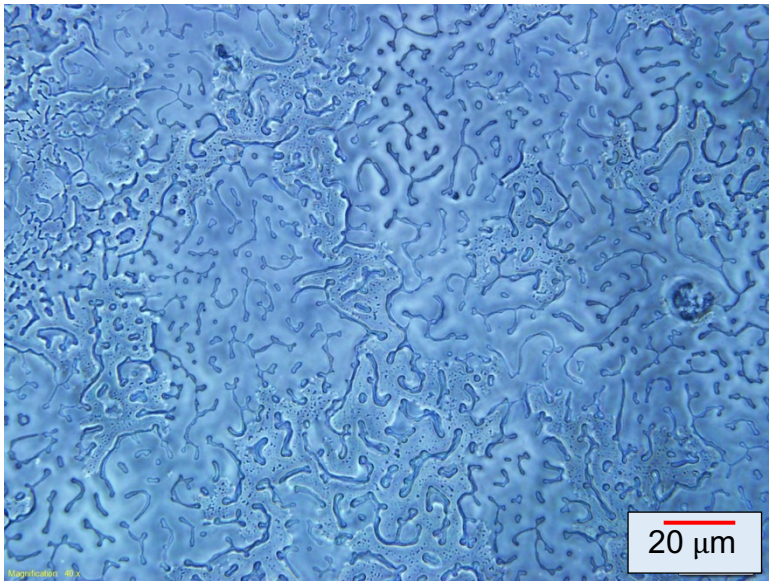

C. 979.8 ± 20.6 nm thick

Figure 4.39 Three optical micrographs of three unstained films containing 72.2 vol.% PS (M.W. 290 kg/mol) and 27.8 vol.% PB (M.W. 3 kg/mol). The scale bar is 20 μm unless A has a scale bar of 50 μm.

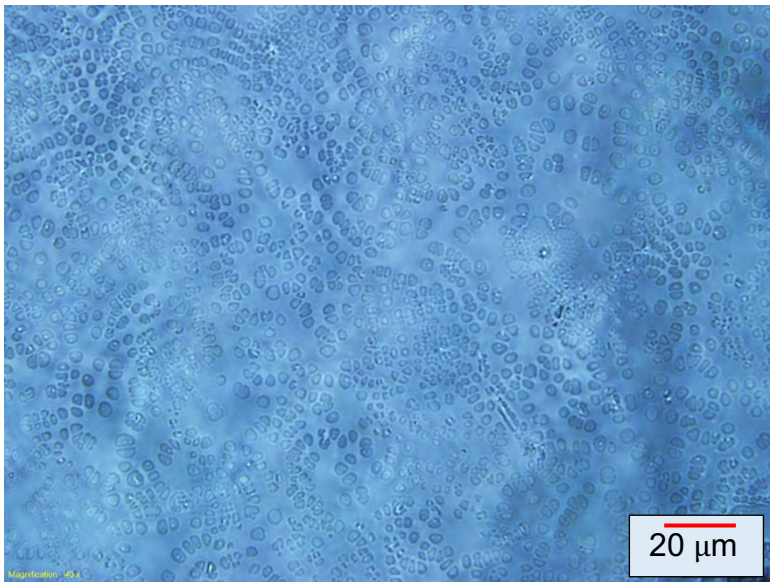

A. 88.2 ± 0.9 nm thick

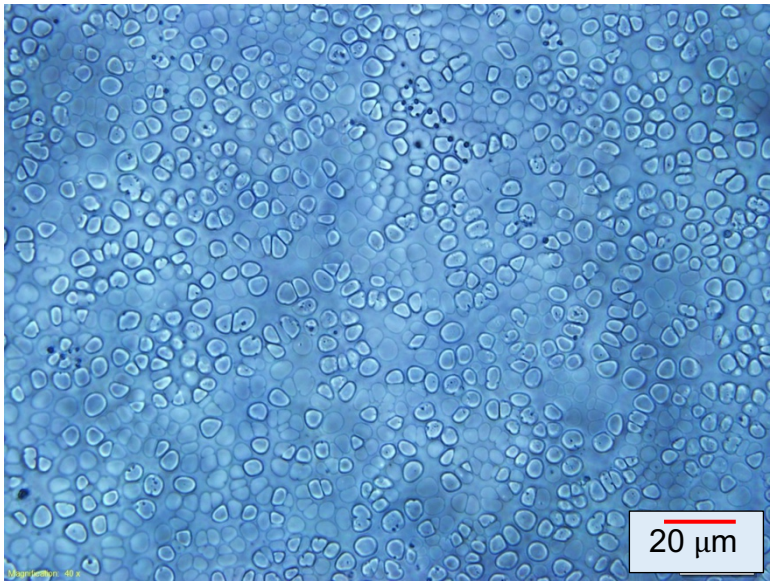

B. 294.1 ± 4.6 nm thick

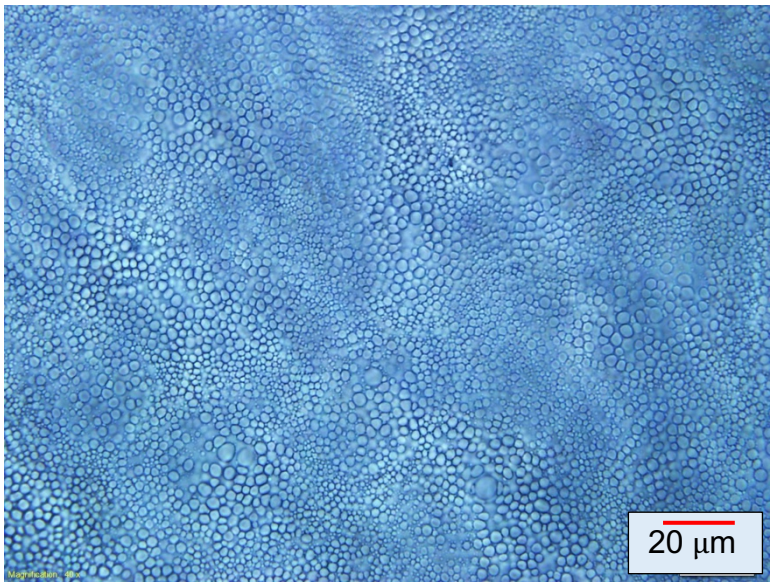

C. 986.7 ± 34.7 nm thick

Figure 4.40 Three optical micrographs of three unstained films containing 46.4 vol.% PS (M.W. 290 kg/mol) and 53.6 vol.% PB (M.W. 3 kg/mol). The scale bar is 20 µm.

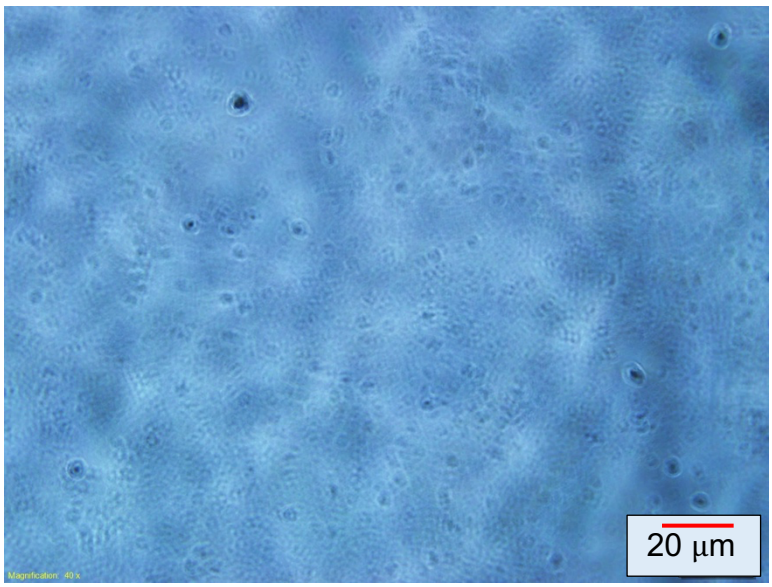

A. 31.4 ± 0.1 nm thick

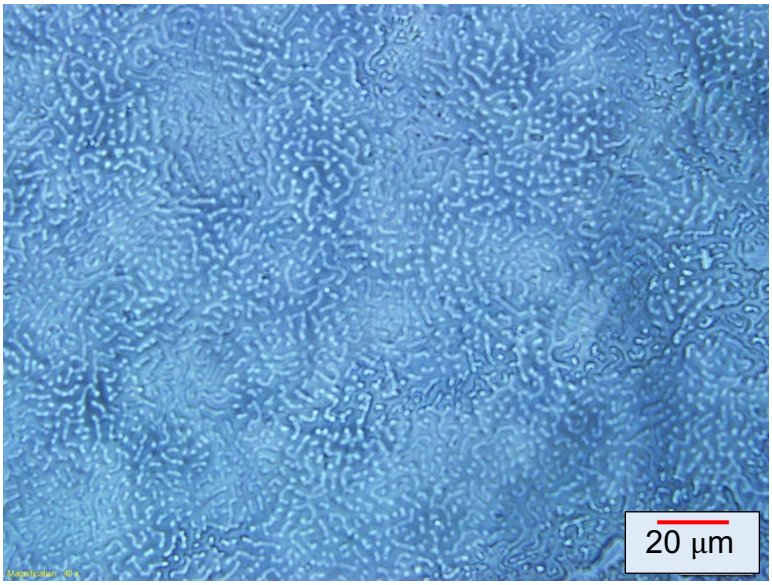

B. 113.3 ± 3.7 nm thick

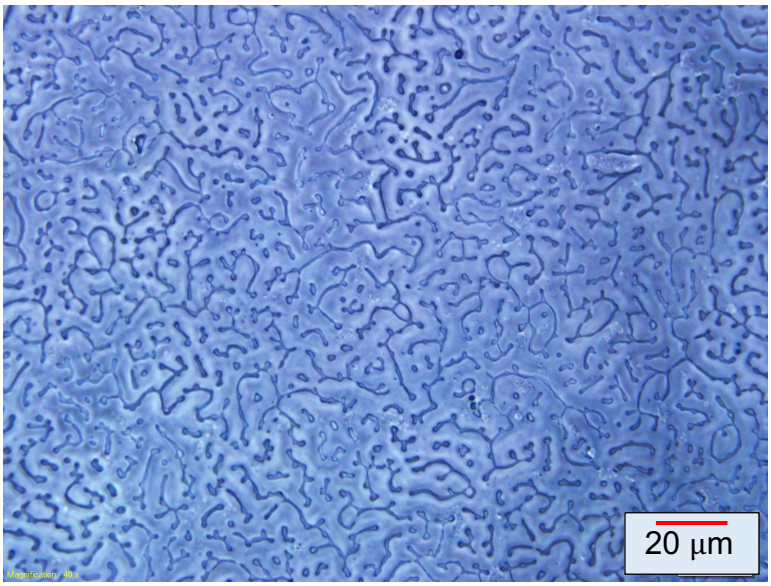

C. 156.9 ± 7.1 nm thick

Figure 4.41 Three optical micrographs of three unstained films containing 22.4 vol.% PS (M.W. 290 kg/mol) and 77.6 vol.% PB (M.W. 3 kg/mol). The scale bar is 20 µm.

The cross-section in TEM micrographs of Figure 4.38 (C) shows no PB domain formation other than in the bulk of the film. These domains have different sizes and lengths, around 106 nm to 368 nm, as in Figure 4.38 (B). Also, there is surface segregation to both surfaces, the air and substrate interface. A central polystyrene-rich layer surrounds the PB domains, possibly caused by surface-directed spinodal decomposition. We conclude that lamellar phase separation occurs when a low molecular weight polymer is blended with a high molecular weight polymer, irrespective of which polymer is low or high in molecular weight. Both Figure 4.33 (A) and Figure 4.38 (A) demonstrate the presence of five distinct layers, a conclusion that is further corroborated by TEM Figure 4.38 (C).

The optical microscope revealed that the phase separation changed as the film thickness changed, as illustrated in Figures 4.39, 40, and 41. It is worth noting that Figures 4.39-C and 4.41-C exhibited a similar pattern of structures. These two optical images showcased different surface energies, measuring 29.2 ± 0.2 mN/m and 33.5 ± 0.5 mN/m, respectively.

4.5 Blend films of PS (M.W.= 4 kg/mol) and PB (M.W.= 200 kg/mol)

For direct comparison, the focus was on the 4 kg/mol PS blend films and 200 kg/mol PB (Figure 4.42). The results indicate that films thinner than 80 nm exhibit the highest hydrophobicity at 53.6 vol.% PB blend, while films made of a single polymer are more hydrophilic, as illustrated in Figure 4.43.

The findings indicated that within the 80 to 2400 nm thickness range, the blend film with 77.6 vol.% PB exhibited the lowest surface energy. In contrast, the 53.6 vol.% PB blend film demonstrated surface energy levels between those of the individual polymer films within the 150 nm to 2600 nm thickness range. The highest surface energy was recorded in the 27.8 vol.% PB blend film (Figure 4.43). Furthermore, the results highlighted that PS (low molecular weight) films are less hydrophobic than PB (high molecular weight) films (Table 4.9).

The X-ray photoelectron spectroscopy (XPS) analysis revealed that the surface composition of the films with polymer blend ratios of 27.8 vol.% PB, 53.6 vol.% PB, and 77.6 vol.% PB is 3.1 ± 0.2%, 3.0 ± 0.1%, and 50.5 ± 2.1% PB, respectively. This indicates that the surface layer of the films containing 27.8 vol.% PB and 53.6 vol.% PB is predominantly composed of PS. However, in the case of the film with 77.6 vol.% PB, the surface layer consists of an equal mix of PB and PS (Table 4.10). From these

results, we conclude that the low molecular weight polymer (4 kg/mol PS) segregates to the surface when the two polymers separate.

Blend of	Polymer weight fraction	Polymer volume fraction	Water contact angle (°)	Surface energy((mN)/m)-water	Glycerol contact angle (°)	Surface energy((mN)/m)- glycerol	The Thickness (nm)
100 vol.% PS (M.W. 4 kg/mol)	0.50%	0.42%	19.9 ± 2.3	68.8 ± 1.7	65.5 ± 1.4	37.2 ± 1.6	4.4 ± 1.4
	1.00%	0.83%	30.7 ± 1.6	64.1 ± 1.5	69.5 ± 0.8	34.9 ± 0.9	41.7 ± 0.1
	2.00%	1.67%	83.62 ± 0.05	32.6 ± 0.1	74.5 ± 0.4	32.0 ± 0.5	80.2 ± 0.1
	2.50%	2.08%	84.2 ± 0.1	32.2 ± 0.1	74.8 ± 0.4	31.8 ± 0.5	90.52 ± 0.03
	3.50%	2.92%	85.9 ± 0.1	31.1 ± 0.1	76.6 ± 0.9	30.7 ± 1.0	141.55 ± 0.04
	4.00%	3.33%	86.6 ± 0.1	30.7 ± 0.1	76.9 ± 1.3	30.6 ± 0.4	160.7 ± 0.1
	5.00%	4.17%	87.3 ± 0.1	30.3 ± 0.1	77.66 ± 0.03	30.12 ± 0.03	197.9 ± 0.1
	7.50%	6.25%	87.8 ± 0.1	29.9 ± 0.1	78.4 ± 0.2	29.7 ± 0.3	277.0 ± 0.2
	10.00%	8.34%	88.2 ± 0.1	29.7 ± 0.1	78.4 ± 0.5	29.4 ± 0.6	399.4 ± 0.9
	25.00%	20.84%	89.4 ± 0.1	28.9 ± 0.2	79.8 ± 0.5	28.9 ± 0.6	1415.9 ± 35.1
	35.00%	29.18%	89.6 ± 0.3	28.8 ± 0.4	80.1 ± 0.1	28.7 ± 0.1	1808.5 ± 28.9
	45.00%	37.51%	90.4 ± 0.2	28.3 ± 0.3	80.2 ± 0.1	28.8 ± 0.1	3588.5 ± 3.0
72.2 vol.% PS (M.W. 4 kg/mol) and 27.8 vol.% PB (M.W.200 kg/mol)	0.25%	0.22%	38.3 ± 1.0	60.2 ± 1.1	51.5 ± 3.2	45.1 ± 3.5	13.6 ± 0.1
	0.50%	0.43%	62.3 ± 2.0	46.1 ± 2.4	66.9 ± 1.0	36.4 ± 1.2	33.8 ± 0.1
	1.00%	0.87%	71.1 ± 2.0	40.5 ± 2.4	69.8 ± 0.5	34.7 ± 0.6	48.1 ± 0.3
	1.50%	1.30%	80.9 ± 0.7	34.3 ± 0.9	72.1 ± 0.4	33.4 ± 0.5	66.5 ± 0.1
	2.00%	1.73%	83.1 ± 0.1	32.9 ± 0.2	73.6 ± 0.1	32.5 ± 0.1	88.9 ± 0.1
	2.50%	2.17%	83.8 ± 0.1	32.5 ± 0.2	74.2 ± 0.2	32.1 ± 0.2	138.3 ± 0.1
	3.50%	3.03%	85.2 ± 0.3	31.6 ± 0.4	75.7 ±0.6	31.3 ± 0.7	197.4 ± 0.3
	5.00%	4.33%	86.3 ± 0.2	30.9 ± 0.3	76.5 ± 0.6	30.8 ± 0.7	310.1 ± 1.2
	7.00%	6.06%	87.0 ± 0.2	30.5 ± 0.2	77.0 ± 0.4	30.5 ± 0.5	490.3 ± 2.3
	10.00%	8.66%	87.3 ± 0.3	30.2 ± 0.4	77.4 ± 0.7	30.3 ± 0.8	732.8 ± 9.1
	20.00%	17.32%	88.4 ± 0.2	29.5 ± 0.2	79.8 ± 0.2	28.9 ± 0.2	1103.5 ± 2.7
	25.00%	21.65%	88.8 ± 0.2	29.3 ± 0.2	80.02 ± 0.04	28.8 ± 0.04	1671.5 ± 4.3
	35.00%	30.31%	89.8 ± 0.2	28.7 ± 0.2	81.1 ± 0.3	28.2 ± 0.4	2548.8 ± 95.9
46.4 vol.% PS (M.W. 4 kg/mol) and 53.6 vol.% PB (M.W. 200 kg/mol)	0.25%	0.22%	44.9 ± 1.1	56.5 ± 1.3	57.6 ± 0.6	41.6 ± 0.7	14.5 ± 0.1
	0.50%	0.45%	62.3 ± 1.1	46.0 ± 1.3	71.3 ± 2.0	33.8 ± 2.3	29.7 ± 0.1
	1.00%	0.90%	84.5 ± 0.3	32.0 ± 0.3	75.2 ± 1.4	31.5 ± 1.6	61.96 ± 0.05
	1.50%	1.35%	86.1 ± 0.7	31.0 ± 0.9	76.7 ± 0.2	30.7 ± 0.3	100.6 ± 0.5
	2.00%	1.80%	87.2 ± 0.3	30.3 ± 0.4	77.830±0.004	30.02 ± 0.01	173.8 ± 0.8
	2.50%	2.25%	88.3 ± 0.2	29.6 ± 0.3	78.6 ± 0.2	29.6 ± 0.2	203.3 ± 1.8
	3.50%	3.14%	88.8 ± 0.1	29.3 ± 0.1	79.4 ± 0.1	29.1 ± 0.2	263.8 ± 0.3
	5.00%	4.49%	89.0 ± 0.3	29.2 ± 0.4	79.5 ± 0.1	29.0 ± 0.1	480.3 ± 2.7
	7.00%	6.29%	89.6 ± 0.4	28.8 ± 0.5	80.2 ± 0.5	28.7 ± 0.6	760.9 ± 4.6
	10.00%	8.98%	90.6 ± 0.2	28.2 ± 0.3	81.1 ± 0.2	28.1 ± 0.2	1370.2 ± 19.1
	15.00%	13.48%	90.7 ± 0.1	28.1 ± 0.1	81.1 ± 0.1	28.1 ± 0.1	2705.8 ± 41.2
22.4 vol.% PS (M.W. 4 kg/mol) and 77.6 vol.% PB (M.W. 200 kg/mol)	0.25%	0.23%	55.6 ± 1.5	50.1 ± 1.9	65.7 ± 1.5	37.0 ± 1.7	27.5 ± 0.1
	0.50%	0.47%	64.6 ± 0.2	44.6 ± 0.2	72.7 ± 0.7	33.0 ± 0.9	33.3 ± 0.1
	1.00%	0.93%	87.4 ± 0.1	30.2 ± 0.2	78.0 ± 0.3	29.9 ± 0.3	80.2 ± 0.1
	1.50%	1.40%	89.1 ± 0.3	29.1 ± 0.3	79.8 ± 0.4	28.9 ± 0.5	116.9 ± 0.1
	2.00%	1.86%	90.0 ± 0.2	28.6 ± 0.2	80.5 ± 0.2	28.5 ± 0.2	138.5 ± 0.4
	2.50%	2.33%	90.6 ± 0.2	28.2 ± 0.2	81.13 ± 0.03	28.12 ± 0.03	248.0 ± 0.5
	3.50%	3.26%	90.9 ± 0.5	28.0 ± 0.6	81.4 ± 0.1	27.9 ± 0.1	400.0 ± 0.9
	5.00%	4.65%	91.2 ± 0.4	27.8 ± 0.5	81.59 ±0.03	27.85 ± 0.03	739.0 ± 3.5
	7.00%	6.52%	91.2 ± 0.7	27.8 ± 0.9	81.9 ± 0.1	27.7 ± 0.1	1314.3 ± 22.7
	10.00%	9.31%	91.8 ± 0.4	27.4 ± 0.5	82.2 ± 0.1	27.5 ± 0.1	2347.9± 28.7
100 vol.% PB (M.W. 200 kg/mol)	0.25%	0.24%	35.9 ± 2.1	61.4 ± 2.2	49.6 ± 2.8	46.1± 3.0	13.7 ± 0.3
	0.50%	0.48%	48.3 ± 0.9	54.5 ± 1.1	66.2 ± 1.1	36.8 ± 1.2	32.1 ± 0.1
	1.00%	0.96%	55.0 ± 3.4	50.5 ± 4.1	77.5 ± 0.5	30.2 ± 0.6	92.59 ± 0.03
	1.50%	1.45%	88.6 ± 0.7	29.5 ± 0.9	79.5 ± 0.2	29.1 ± 0.2	152.90 ± 0.05
	2.00%	1.93%	89.2 ± 0.4	29.1 ± 0.6	79.7 ± 0.7	28.9 ± 0.8	206.2 ± 0.1
	2.50%	2.41%	89.8 ± 0.2	28.7 ± 0.2	79.8 ± 0.2	28.9 ± 0.2	504.2 ± 0.7
	3.50%	3.37%	89.9 ± 0.3	28.6 ± 0.3	80.5 ± 0.6	28.5 ± 0.7	648.7 ± 1.1
	5.00%	4.82%	90.0 ± 0.2	28.5 ± 0.2	80.9 ± 0.8	28.2 ± 0.3	1104.7 ± 8.1
	7.50%	7.23%	90.7 ± 0.4	28.1 ± 0.5	81.3 ± 0.1	28.0 ± 0.1	2240.9 ± 2.0
	10.00%	9.63%	91.2 ± 0.2	27.8 ± 0.2	81.8 ± 0.1	27.7 ± 0.1	2640.0 ± 72.8

Table 4.9 Data from the contact angle experiment of blend films of PS 4 kg/mol and PB 200 kg/mol.

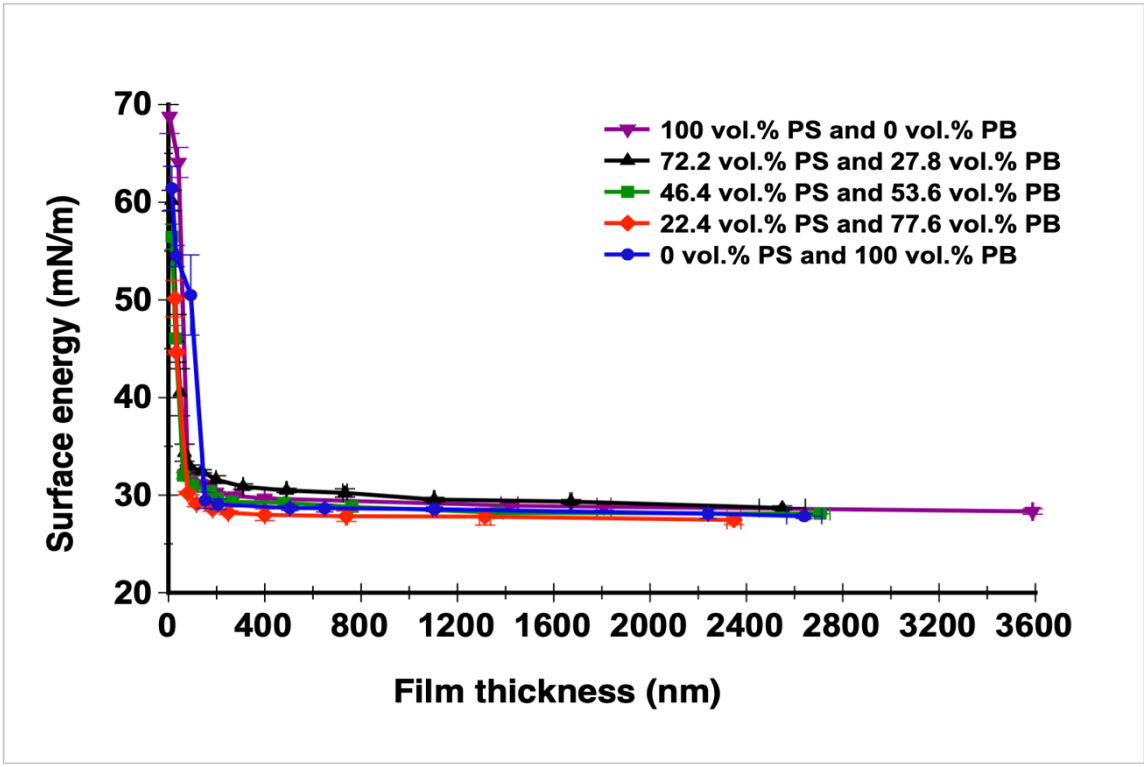

Figure 4.42 A plot of the relation of film thickness and surface energy of blend films of PS (M.W.= 4 kg/mol) and PB (M.W.= 200 kg/mol).

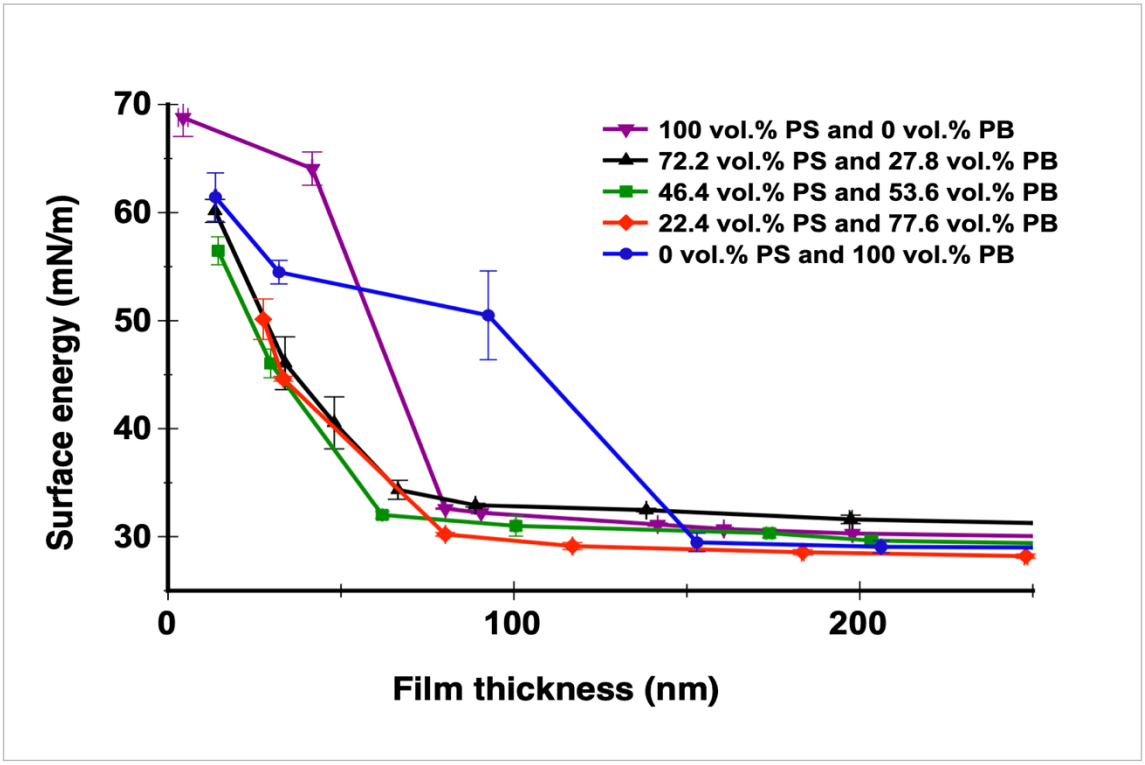

Figure 4.43 A zoom-in of the previous plot of the relation of film thickness and surface energy of blend films of PS (M.W.= 4 kg/mol) and PB (M.W.= 200 kg/mol). The data are the same as those shown in Figure 4.42.

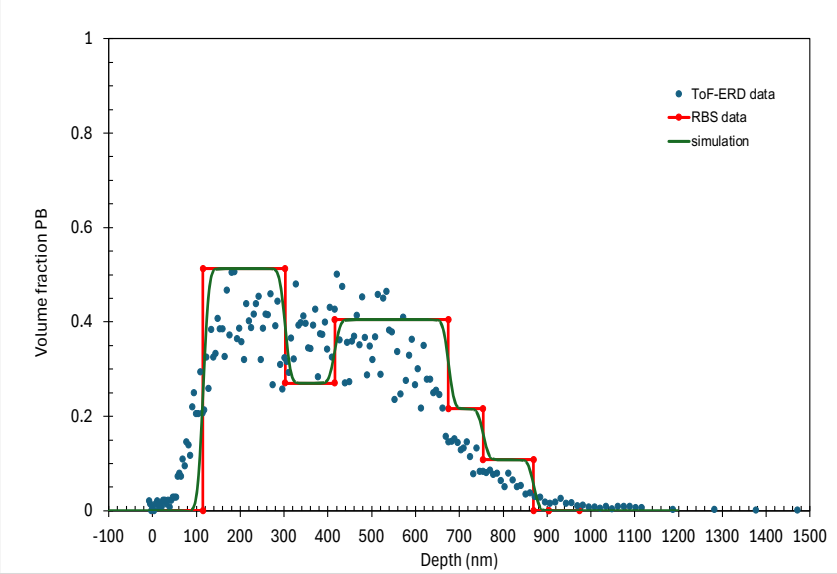

A. 27.8 vol.% PB

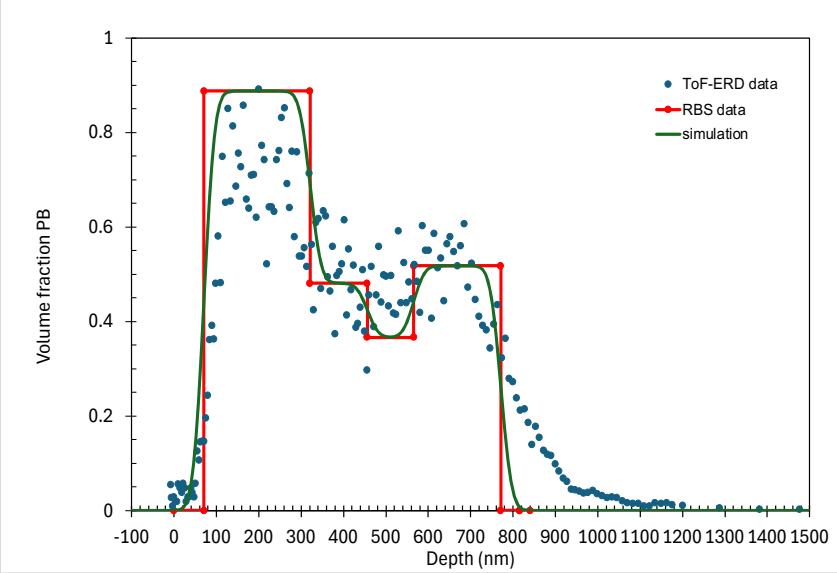

B. 53.6 vol.% PB

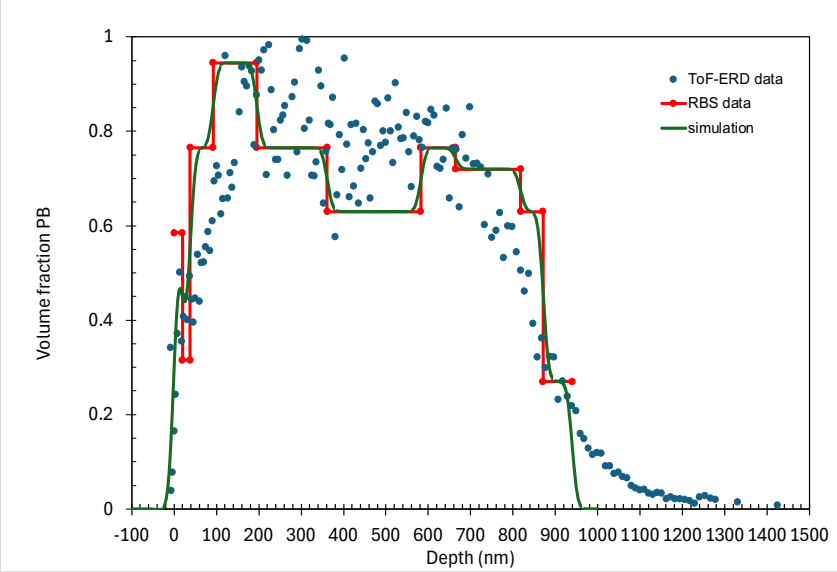

C. 77.6 vol.% PB

Figure 4.44 ToF-ERD data compared with volume fraction profiles obtained by RBS for blend films of PS (M.W.= 4 kg/mol) and PB (M.W.= 200 kg/mol).

PS M.W. (kg/mol)	PB M.W. (kg/mol)	PB (vol. %)	Polymers (vol. %)	Thickness (nm)	Surface energy (water) (mN/m)	Average roughness (nm)	PB amount at the surface (%)
4.0	200.0	0.0	8.3	399.4 ± 0.9	29.7 ± 0.1	1.03 ± 0.02	
		27.8	6.1	490.3 ± 2.3	30.5 ± 0.2	11.7 ± 1.1	3.1 ± 0.2
		53.6	4.5	480.3 ± 2.7	29.2 ± 0.4	3.6 ± 0.2	3.0 ± 0.1
		77.6	4.7	739.0 ± 3.5	27.8 ± 0.5	160.0 ± 5.0	50.5 ± 2.1
		100.0	3.4	648.7 ± 1.1	28.6 ± 0.3	2.3 ± 0.2	

Table 4.10 Summarising some data of five blend films PS (M.W.= 4 kg/mol) and PB (M.W.= 200 kg/mol).

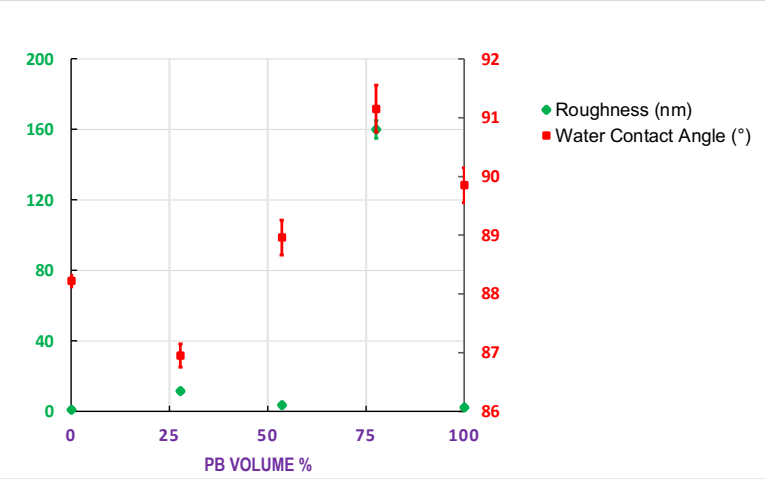

Figure 4. 45 PB volume %, roughness, and water contact angle for blend films of PS (M.W.= 4 kg/mol) and PB (M.W.= 200 kg/mol).

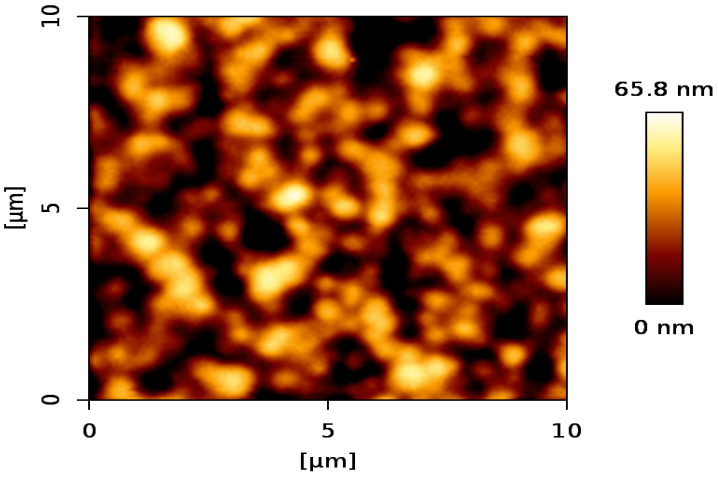

Figure 4.46 AFM topography of the unstained film surface containing 72.2 vol.% PS (M.W. 4 kg/mol) and 27.8 vol.% PB (M.W. 200 kg/mol). The roughness is 11.7 ± 1.1 nm. The thickness is 490.3 ± 2.3 nm. Surface energy is 30.5 ± 0.2 mN/m.

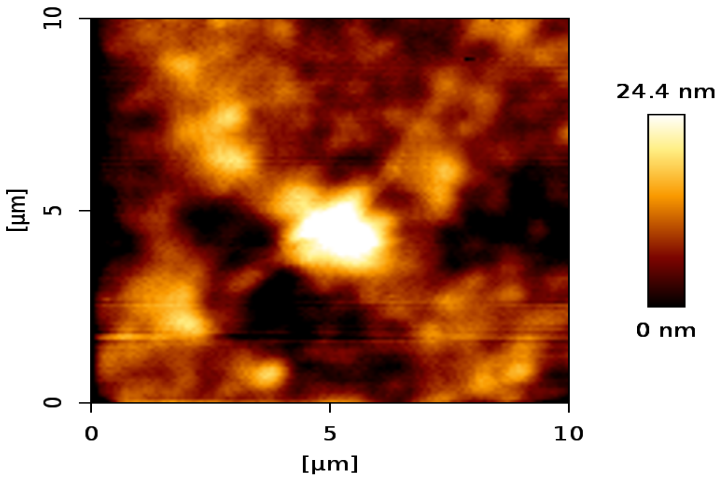

Figure 4.47 AFM topography of the unstained film surface containing 46.4 vol.% PS (M.W. 4 kg/mol) and 53.6 vol.% PB (M.W. 200 kg/mol). The roughness is 3.6 $\pm$ 0.2 nm. The thickness is 480.3 $\pm$ 2.7 nm. Surface energy is 29.2 $\pm$ 0.4 mN/m.

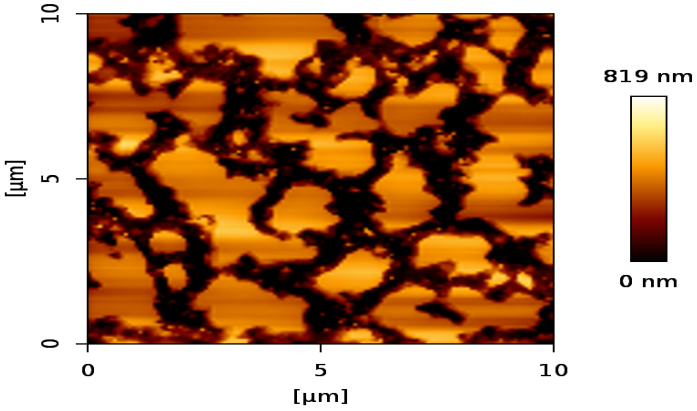

Figure 4.48 AFM topography of the unstained film surface containing 22.4 vol.% PS (M.W. 4 kg/mol) and 77.6 vol.% PB (M.W. 200 kg/mol). The roughness is 160.0 $\pm$ 5.0 nm. The thickness is 739.0 $\pm$ 3.5 nm. Surface energy is 27.8 $\pm$ 0.5 mN/m.

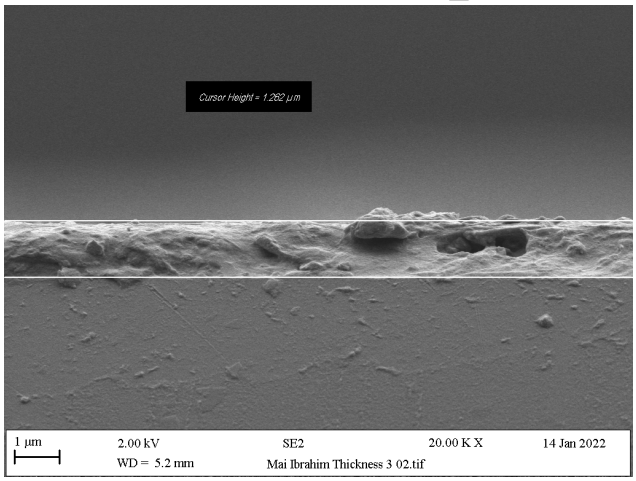

Figure 4.49 SEM cross-section micrograph of the surface of an unstained film containing 46.4 vol.% PS (M.W. 4 kg/mol) and 53.6 vol.% PB (M.W. 200 kg/mol) on a glass substrate. The roughness is 3.6 $\pm$ 0.2 nm. The thickness is 480.3 $\pm$ 2.7 nm (as measured using ellipsometry). The surface energy is 29.2 $\pm$ 0.4 mN/m. The scale bar is 1 µm, and the cursor height (the distance between the two white lines) is 1.262 µm.

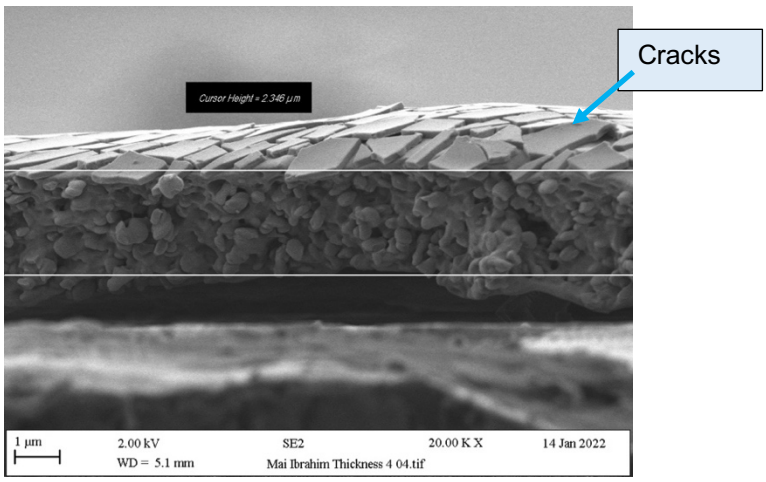

Figure 4.50 SEM cross-section micrograph of an unstained film containing 46.4 vol.% PS (M.W. 4 kg/mol) and 53.6 vol.% PB (M.W. 200 kg/mol) on a glass substrate. The thickness is 760.9 ±4.6 nm (as measured using ellipsometry). The surface energy is 28.8 ± 0.5 mN/m. The scale bar is 1 µm, and the cursor height (the distance between the two white lines) is 2.346 µm.

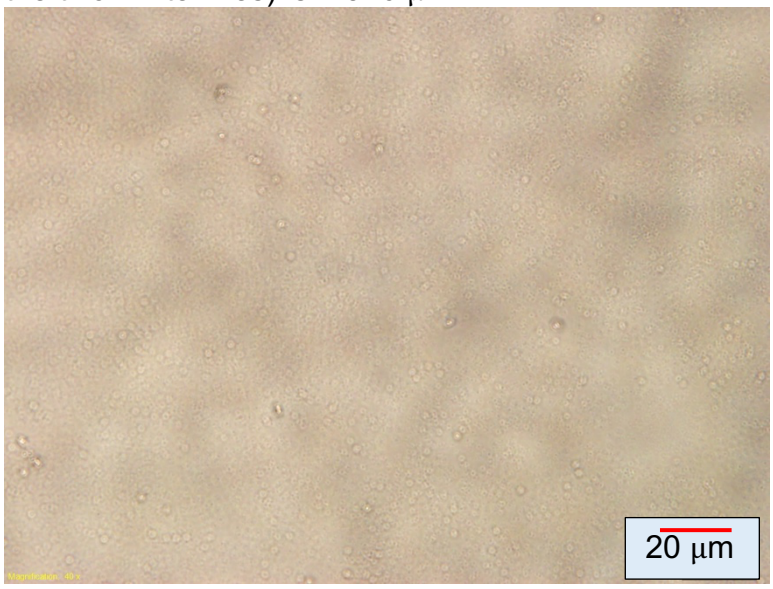

A. 33.8 ± 0.1 nm thick

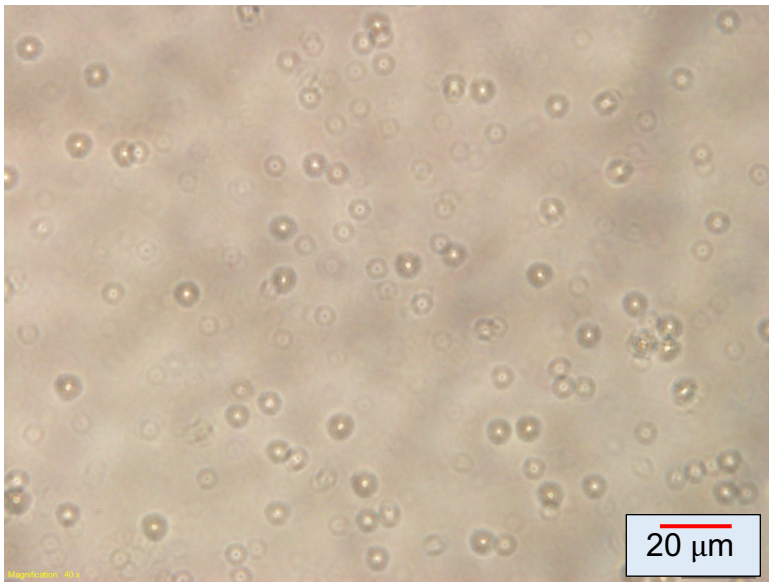

B. 310.1 ± 1.2 nm thick

Figure 4.51 Two optical micrographs of two unstained films containing 72.2 vol.% PS (M.W. 4 kg/mol) and 27.8 vol.% PB (M.W. 200 kg/mol). The scale bar is 20 µm.

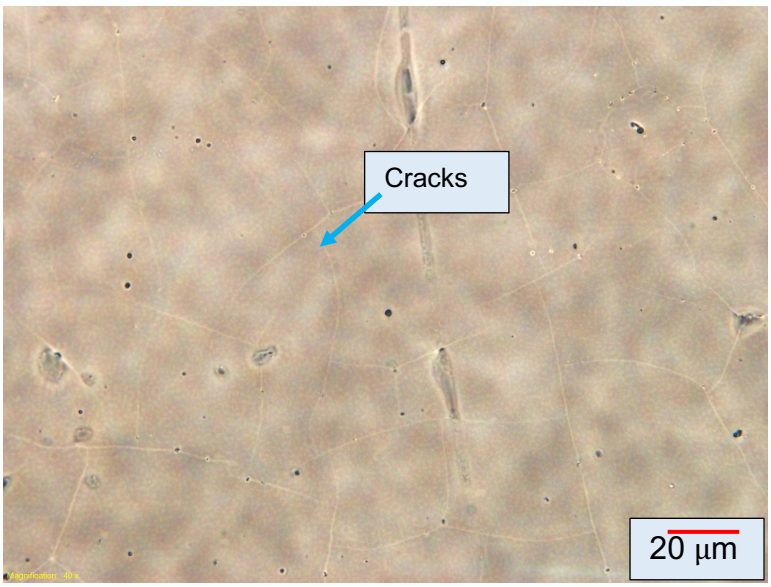

A. 173.8 ± 0.8 nm thick

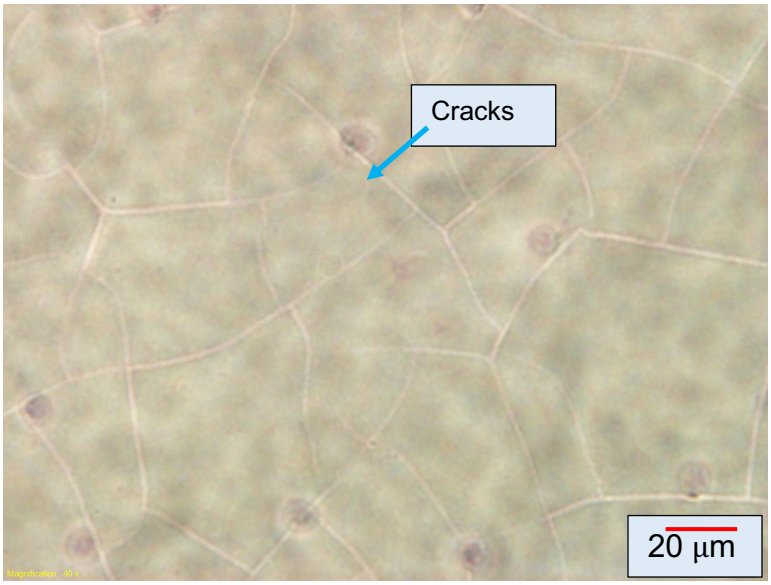

B.263.8 ± 0.3 nm thick

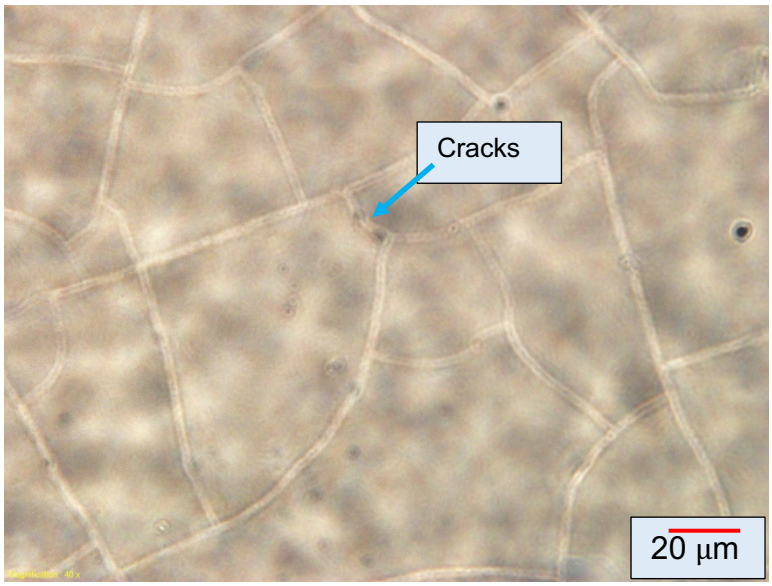

C. 760.9 ± 4.6 nm thick

Figure 4.52 Six optical micrographs of six unstained films containing 46.4 vol.% PS (M.W. 4 kg/mol) and 53.6 vol.% PB (M.W. 200 kg/mol). The scale bar is 20 μm.

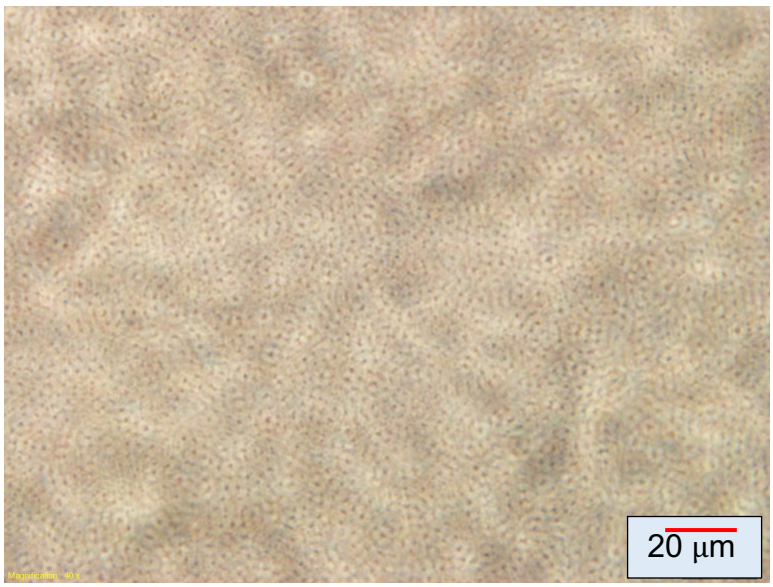

A. 27.5 ± 0.1 nm thick

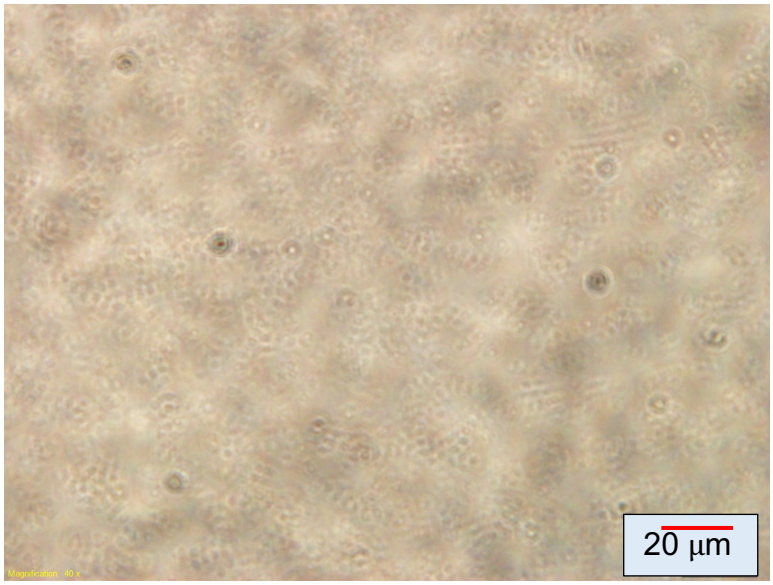

B. 33.3 ± 0.1 nm thick

Figure 4.53 Six optical micrographs of six unstained films containing 22.4 vol.% PS (M.W. 4 kg/mol) and 77.6 vol.% PB (M.W. 200 kg/mol). The scale bar is 20 μm.

The analysis of ToF-ERD and RBS data shows that a blend film containing 27.8 vol.% PB has a surface volume fraction of PB of 0.025, which then increases to a range of 0.3 - 0.53 at the bulk and 0.1 at the back of the film (Figure 4.44, A). In contrast, a blend film with 53.6 vol.% PB has a surface volume fraction of PB of 0.05, increasing to 0.9 at the bulk and decreasing to 0.5 towards the back of the film (Figure 4.44, B). For a blend film with 77.6 vol.% PB, most of the bulk is PB, with only 0.5 at the air interface and close to the substrate interface (Figure 4.44, C).

The AFM analysis revealed that the surface roughness for films with 27.8 vol.% PB, 53.6 vol.% PB, and 77.6 vol.% PB is 11.7 ± 1.1 nm, 3.6 ± 0.2 nm, and 160.0 ± 5.0 nm, respectively (Figures 4.45 - 4.48 and Table 4.10). Notably, the film with 77.6 vol.% PB

exhibited the highest surface roughness among these blends, which also got the highest PB content at the surface and the lowest surface energy, as mentioned before. It has structures typically on the scale of a few microns, which is known to influence the contact angle (Figure 4.48). These structures are similar to those in the optical image Figure 4.53 (A).

We had the opportunity to acquire two scanning electron microscope (SEM) cross-section images for 53 vol.% PB unstained films, which are displayed in Figures 4.49 and 4.50. Figure 4.50 revealed the presence of cracks, which develop as thickness increases, as shown in the optical microscopic images in Figures 4.52, A to C. This behaviour has a similar explanation to our previous findings discussed in section 4.1 for Figures 4.10, A to C, for blend films containing 72.2 vol.% PS (M.W. 4 kg/mol) and 27.8 vol.% PB (M.W. 3 kg/mol). In addition, the optical microscope results revealed that the film's structure exhibited varying behaviour as the thickness of the blend films increased (see Figures 4.51, 52, and 53).

4.6 Additional work.

In this thesis, we did not cover a particular film morphology observed in Figure 4.54, A and B. We obtained two TEM images of a stained blend film containing 48.1 kg/mol PS and 572.1 kg/mol PB. The images distinctly reveal that the PS (lower molecular weight) segregated to both surfaces, with some domains in the bulk, while the PB (higher molecular weight) predominantly occupied the bulk. This supports earlier comments in section 4.5 that the higher molecular weight PB is kinetically limited.

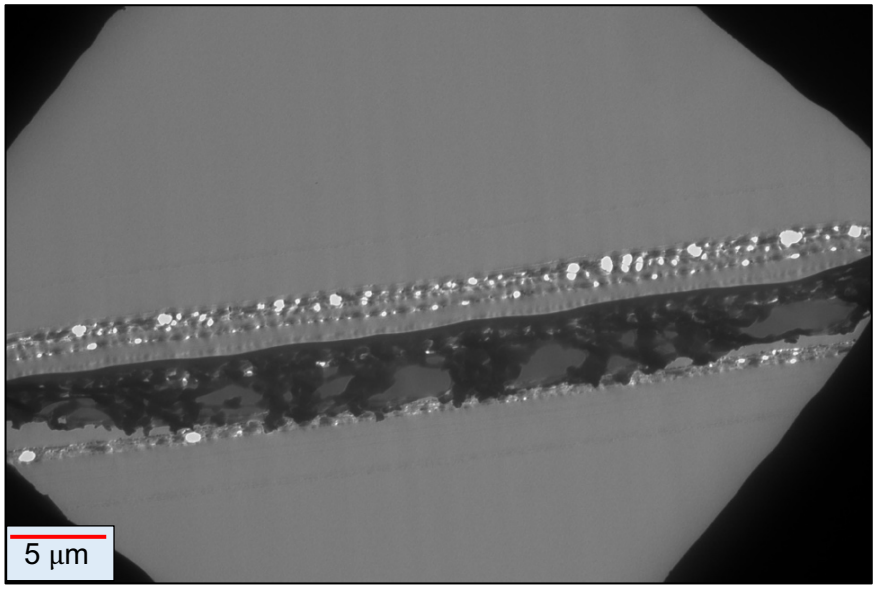

(A)

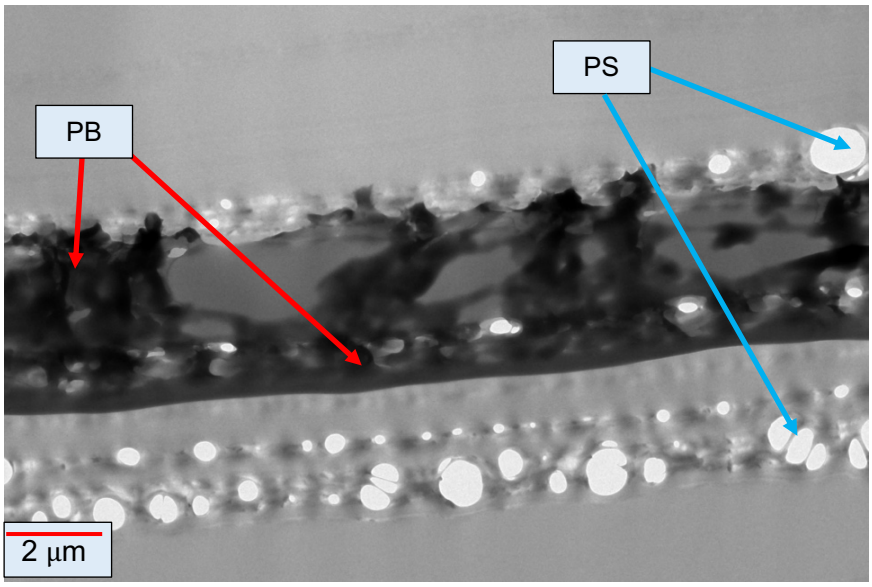

(B)

Figure 4.54 TEM cross-section micrograph of the stained film containing 14.8 vol.% PS (M.W. 48.1 kg/mol) and 85.2 vol.% PB (M.W. 572.1 kg/mol). The polymer volume is 3.53%. The scale bar is (A) 5 μm and (B) 2 μm.

Chapter 5. Discussion

The previous chapter presented complicated film morphologies resulting from five different immiscible blends of thin films. Here we discuss these results in terms of molecular weight, relative polymer concentration in the film, the amount of polybutadiene at the surface, and film roughness, as well as considering the presence of lamellar structure or bicontinuous structures.

5.1 The Impact of Molecular Weight

Many polymer properties, such as viscosity, depend on molecular weight, which includes surface tension. Moreover, surface tension plays an important role in processes such as the film structure of polymers blends. In 1969, researchers provided polymer surface tension data and proposed a relation linking polymer surface tension and molecular weight M_w (equation 5-1) [116],

$$\gamma = \gamma_\infty - \frac{k}{{M_w}^{2/3}} \tag{5-1}$$

where γ_∞ is the surface tension at infinite number-average molecular weight and k is a constant. They measured the surface tension of a series of poly(isobutylenes) with molecular weight between 400- 3000 units at 24°C. Also, they collected values of surface tension of different poly(dimethyl siloxane)s from the literature. Using experimental results and literature data, they found a linear relationship between the surface tension and the inverse of the molecular weight raised to the power of (2/3). It was suggested that a free-volume argument could explain this relationship, as the molecular weight affects the available free volume in the polymer (extra space within a polymer that is not occupied by the polymer chains) due to the existence of chain ends, which influences surface tension. These chain ends introduce more free volume than the middle of the chains. When the molecular weight is low, a higher number of chain ends leads to increased free volume, reducing the density of molecular interactions at the surface. This results in lower surface tension for lower molecular weight polymers. Conversely, higher molecular weight results in fewer chain ends relative to the polymer mass, reducing the free volume and leading to tighter molecular packing and higher surface tension.

Our observations of the surface tension of each homopolymer, PS and PB, showed variations in relation to their molecular weight. We noted a decrease in surface tension with an increase in molecular weight (refer to Figure 5.1), which does not align with equation (5-1). One possible explanation is the different topologies and chain end

structures exhibited by the polymers; for example, PB can have a branched configuration. However, there is a complex interplay among all the components (such as roughness and the amount of PB at the surface) that governs the surface tension of our films.

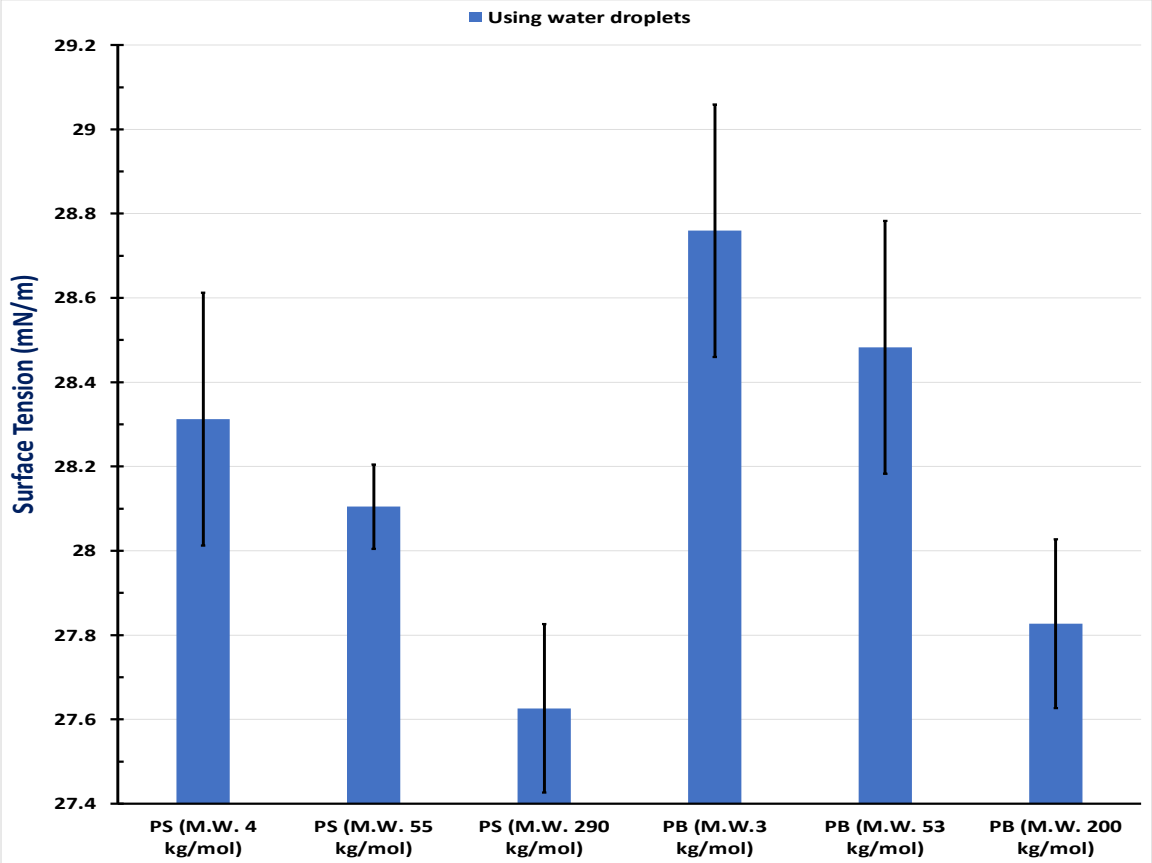

Figure 5.1 A histogram illustrates that as the molecular weight of pure PS or PB increases, the surface tension decreases.

In accordance with equation (5.1), it is unsurprising that a polymer with a higher molecular weight would not prefer the surface. In our study of two asymmetric blend thin films (blend films of PS M.W.=290 kg/mol and PB M.W. = 3 kg/mol, and blend films PS M.W.=4 kg/mol and PB M.W. = 200 kg/mol), we observed that the lower molecular weight polymer segregated to the air and substrate interfaces, leaving some domains in the bulk. This segregation of the lower molecular weight polymer can be attributed to differences in solubility between PS and PB in toluene, as evidenced by ToF-ERD and TEM results in Figures 4.33, 4.38-B, 4.44, A and B, and Figure 4.54 for the blend film of 48.1 kg/mol PS and 572.1 kg/mol PB. As the toluene evaporates during spin casting, the polymer solution concentration will eventually reach a critical point where the single-phase becomes unstable, resulting in phase separation. This is consistent with previous findings: upon casting the film, the ternary phase with lower surface

energy polymer favours the surface, PS (M.W. 4.55 kg/mol) rich phase, while PB (M.W. 53 kg/mol) rich phase is left in bulk [22].

After examining three symmetric blend films with varying molecular weights (**low** 4 kg/mol PS and 3 kg/mol PB, **medium** 55 kg/mol PS and 53 kg/mol PB, and **high** 290 kg/mol PS and 200 kg/mol PB), it was observed that in the first two cases, PB segregated to the air interface as observed using XPS (Figure 5.2) and ToF-ERD (Figures 4.5 and 4.14). Still, even in these two cases, PB rarely (in the first case) or partially (in the second case) covered the substrate interface. This indicates a different interaction between the polymers and the substrate. This observation is consistent with a previous study on blend films of *d*-PS (M.W. 49 kg/mol) and PB (M.W. 53 kg/mol), which found a bilayer structure where PB wets the air interface, and *d*-PS favours the substrate interface [22].

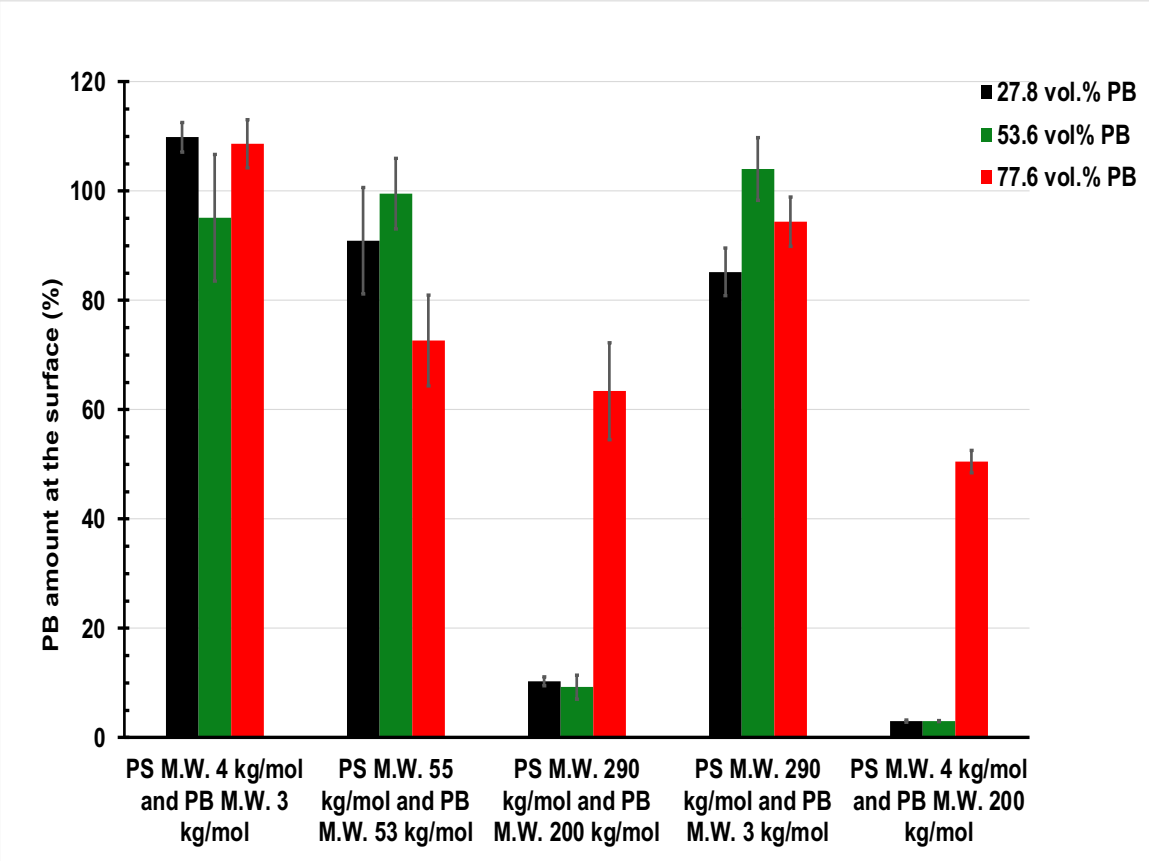

Figure 5.2 A histogram displays the PB concentration at the surface for three different blend mass ratios of the five blends in this study, as obtained from XPS results.

An exception was observed in the case of symmetric blend films with high molecular weight (PS M.W. 290 kg/mol and PB M.W. 200 kg/mol). It was found that for 27.8 vol.% PB and 53.6 vol.% PB blend films, the PS segregates to the air interface, and for 77.6 vol.% PB films, the surface structure is phase-separated, with PB covering 63.4 ± 8.9%

of the surface (see Figure 5.2). This phase separation could be attributed to the different solubility of the polymers in toluene. Specifically, PS remains in solution longer than PB due to its better solubility in toluene. As a result, PB emerges more quickly, while PS continues to dissolve from the film at the surface, ultimately leading to some PS remaining on the surface (Figure 4.23). Additionally, as shown in Figure 5.1, the surface tension of PB 200 kg/mol is higher than that of PS 290 kg/mol, causing PB to favour the bulk.

The significant error bars observed in certain blend conditions, particularly those involving low molecular weight polymers or high PB content, are likely due to an uneven distribution of phases at the film surface. Such blends frequently undergo phase separation or exhibit poor interfacial compatibility, resulting in localised domains of PB or PS, which in turn affect the average surface composition. Furthermore, variability in film thickness and instability during spin-coating may exacerbate this high standard deviation. In blends with very low surface percentages of PB (for instance, PS with a molecular weight of 4 kg/mol combined with PB of 200 kg/mol), even minor measurement errors can become disproportionately large in percentage terms.

To test the quality of the XPS data, we did a single-factor ANOVA *F*-test based upon the hypothesis that the PB surface concentration is the same for each blend. A one-way ANOVA was conducted to compare the means of PB concentration on the surface of three blends: PS M.W. 4 kg/mol and PB M.W. 3 kg/mol, PS M.W. 50 kg/mol and PB M.W. 53 kg/mol, and PS M.W. 290 kg/mol and PB M.W. 3 kg/mol. The analysis revealed **no statistically significant difference** among the blends' means, $\boldsymbol{F(2, 6) = 1.87}$, $\boldsymbol{p = 0.234}$. Since the *p*-value exceeds the conventional alpha level of 0.05, we **fail to reject the null hypothesis**. This suggests that any observed differences in the group means are likely due to random variation rather than a systematic effect of the group factor.

5.2 The Impact of PB concentration at the surface and roughness

In Figure 5.2, it is observed that the majority of blends have a surface concentration of PB that is either less than 20% or more than 80%, with only three falling closer to 70%, 65%, and 50%. In these instances, there is a notable mixing of the highly immiscible PS and PB, which suggests that these concentrations are likely to undergo phase separation. Additionally, the second and fifth blends (PS M.W. 55 kg/mol and PB M.W. 53 kg/mol) and (PS M.W. 4 kg/mol and PB M.W. 200 kg/mol) respectively exhibit the

most significant roughness (Figure 5.4) attributed to the phase separation. It is clear that other parameters also contribute to this phenomenon.

However, the data show little correlation between surface PB concentration and contact angle (Figure 5.3). Contact angle results showed that the surface of the first two symmetric blend films (PS M.W. 4 kg/mol and PB M.W. 3 kg/mol) and (PS M.W. 55 kg/mol and PB M.W. 53 kg/mol) is more hydrophobic than the rest (Figure 5.3). Conversely, the two asymmetric blends of a film containing 27.8 vol.% PB exhibit a contact angle that is less than the contact angle of the 0 vol.% PB.

A single-factor ANOVA *F*-test was conducted to compare the water contact angle of different blends. There was a statistically significant difference between blends: **$F(4,10) = 8.35$**, **$p = 0.0031$**. These results indicate that molecular weight combinations and other parameters significantly impact water contact angle.

The first and the fourth combination blend films in Figure 5.3 (PS M.W. 4 kg/mol and PB M.W. 3 kg/mol) and (PS M.W. 290 kg/mol and PB M.W. 3 kg/mol), respectively, have 100 vol.% PB films are higher surface energy than films 0 vol.% PB, therefore one would expect to see an increase in surface energy with increasing volume fraction of PB. However, this is not observed, which implies that some other parameters, such as the roughness, morphology, structure of the film, or the mechanism of the film formation, must also play a role.

Our findings suggest that it is difficult to determine a correlation between the contact angle and surface roughness (Figures 5.3. and 5.4). In 1999, researchers studied how surface roughness and texture affect the contact angle of water droplets on hydrophobic surfaces [114]. They specifically focused on hydrophobic surfaces that

trap air pockets under the droplet, enhancing its spherical shape. The researchers concluded that increased roughness does not always lead to higher contact angles. Instead, they found that the surface design and the quantity of trapped air beneath the droplet determine its wetting behaviour. However, another study focused on using Teflon, a hydrophobic material, as the research subject [117]. Teflon surfaces with different roughness levels were created through abrasive polishing, and contact angle measurements were taken using ultra-pure water. In conclusion, it was found that surface roughness significantly affects wetting behaviour.

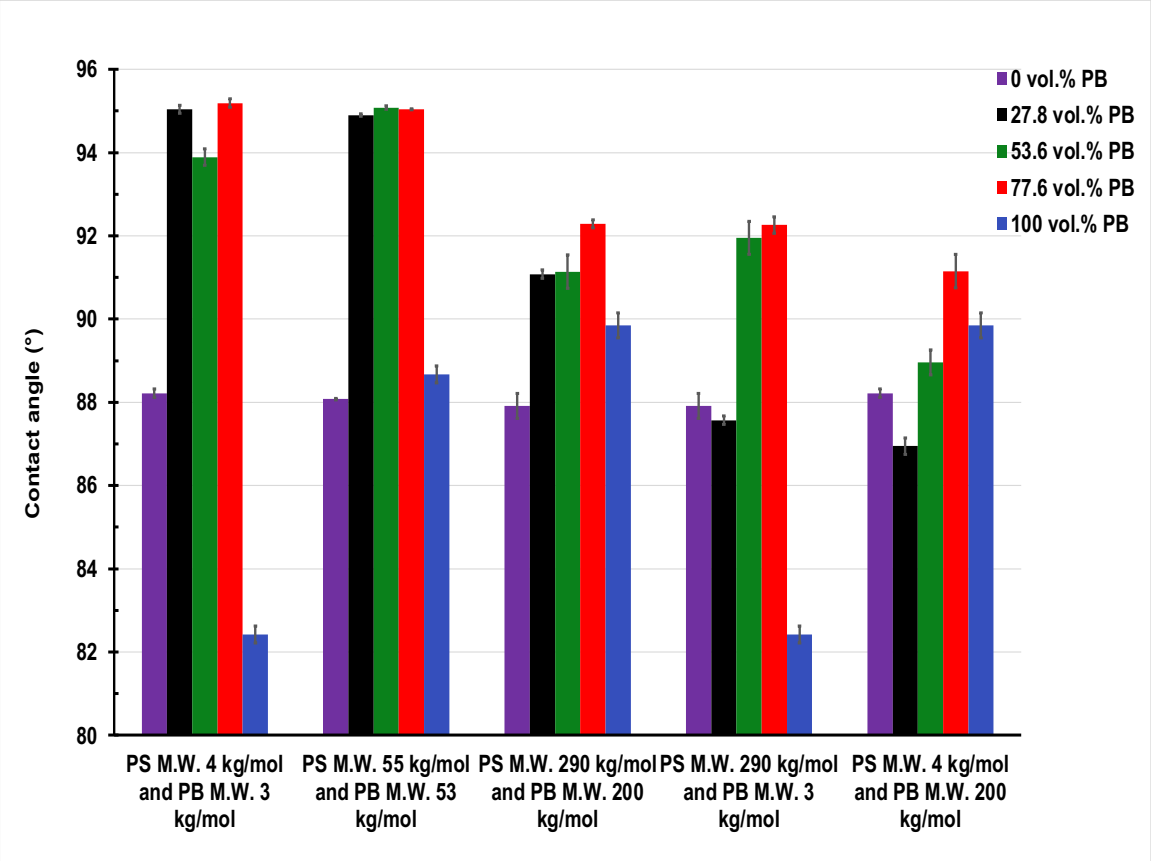

Figure 5.3 A histogram displays the water contact angle for five different blend mass ratios of the five blends in this study.

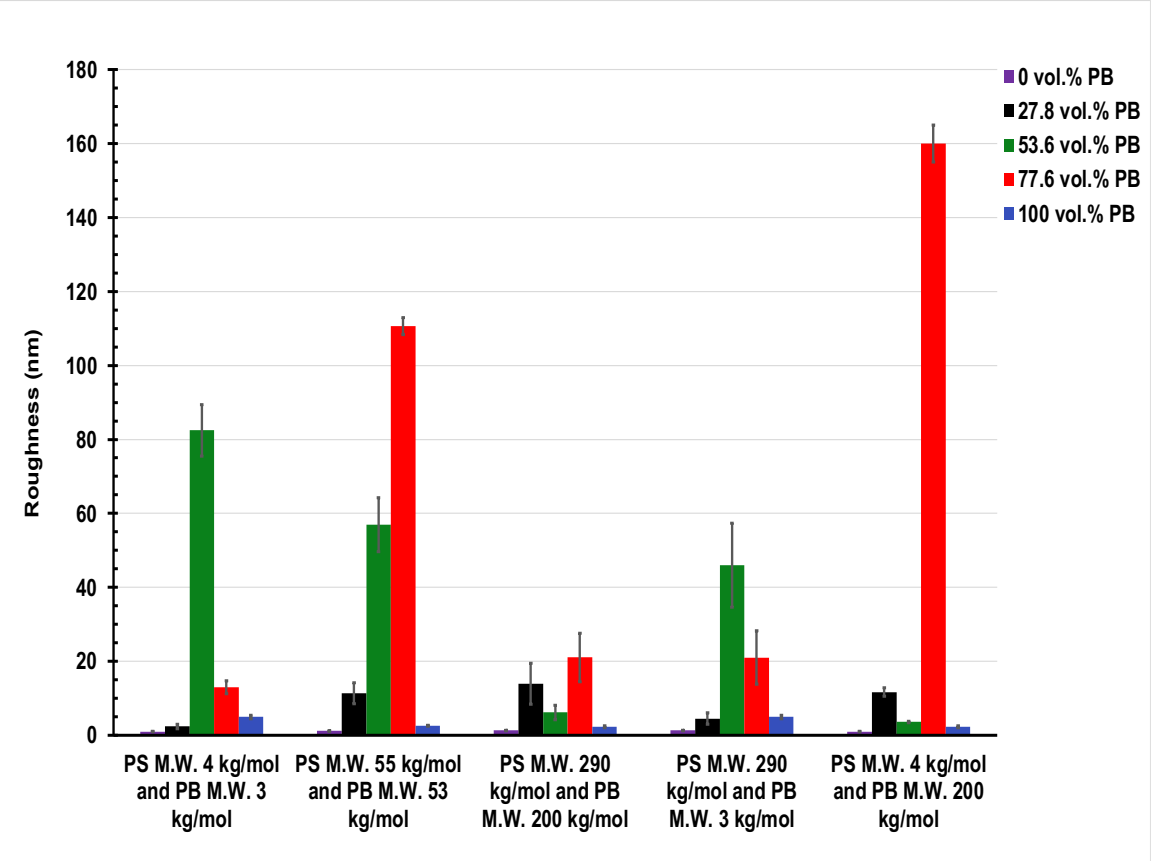

Figure 5.4 A histogram displays surface roughness for five different blend mass ratios of the five blends in this study.

5.3 The Impact of Polymer Concentrations

Since the morphology of the films exhibited variations with changes in the PB volume ratio, we will proceed by discussing the films with 27.8 vol.%, 53.6 vol.%, and 77.6 vol.% PB, highlighting the differences. In 2007, researchers demonstrated that polyetherimide (PEI) and polycaprolactone (PCL) form immiscible blends that separate into distinct surface patterns during spin-coating [118]. These patterns are influenced by the flow of the solution during spinning and the different evaporation rates of the solvents for the two polymers. The size and structure of the separated domains are significantly affected by the composition of the polymer blend, with higher PCL content causing a shift from PEI-rich domains to PCL-rich ones.

5.3.1 Films with 27.8 vol.% PB

The films in the black column (Figure 5.4) displayed the smoothest surfaces out of all the blend film combinations we tested. However, these films exhibited significant contact angles (above 90°) for the three symmetric blends films, indicating that their surfaces are more hydrophobic than the two asymmetric blends with the same mass ratio (refer to Figure 5.3). However, the contact angles for 27.8 vol.% PB films in asymmetric blends were lower than those of the pure PS in the same blend.

Looking at the fourth combination blend, the film containing 72.2 vol.% PS (M.W. 290 kg/mol) and 27.8 vol.% PB **(M.W. 3 kg/mol)** displayed a well-defined lamella structure, as shown in ToF-ERD and TEM results in Figures 4.33, A and 4.38, B. This film showed a clear segregation for PB **(M.W. 3 kg/mol)** to both air and substrate interfaces. In comparison, at the first combination blend, the film comprising 72.2 vol.% PS (M.W. 4 kg/mol) and 27.8 vol.% **PB (M.W. 3 kg/mol)** exhibited a thin layer of **PB (M.W. 3 kg/mol)** at the air interface (refer to Figure 4.5, A).

At the third combination, the blend film consisting of 72.2 vol.% of PS (M.W. 290 kg/mol) and 27.8 vol.% of PB **(M.W. 200 kg/mol)** displayed a lower volume fraction of PB (ranging from 0.1 to 0.4) throughout the bulk compared to the blend film containing 72.2 vol.% of PS (M.W. 4 kg/mol) and 27.8 vol.% of PB **(M.W. 200 kg/mol)**, which exhibited a volume fraction of PB between 0.2 to 0.55 throughout the bulk (refer to ToF-ERD results in Figures 4.23, A and 4.44, A). ToF-ERD and XPS results (Figure 5.2) reveal that these two films have a thinner surface layer of PS for the first and a thicker surface layer of PS for the second, which indicating that **PS (M.W. 290 kg/mol)** takes more time to go to the surface than **PS (M.W. 4 kg/mol)**.

5.3.2 Films with 53.6 vol.% PB

Films with 53.6 vol.% PB (green column in Figure 5.3) exhibit surface energy values that are close to those of films with 77.6 vol.% PB (red column in Figure 5.3) across all five blend films. When a PB layer is present on the surface (Figure 5.2), films in the green column develop rougher surfaces (Figure 5.4) compared to those with the same PB volume fraction, increasing their contact angles relative to films with the same PB volume fraction (Figure 5.3).

The PB profile in these films exhibits similar characteristics in the first two symmetric blends, with 46.4 vol.% PS (M.W. 4 kg/mol) and 53.6 vol.% PB (M.W. 3 kg/mol), and 46.4 vol.% PS (M.W. 55 kg/mol) and 53.6 vol.% PB (M.W. 53 kg/mol), as indicated by the ToF-ERD results (Figures 4.5, B and 4.14, B). However, in contrast, the last two asymmetric blends, 46.4 vol.% PS (M.W. 290 kg/mol) and 53.6 vol.% PB (M.W. 3 kg/mol), and 46.4 vol.% PS (M.W. 4 kg/mol) and 53.6 vol.% PB (M.W. 200 kg/mol), do not exhibit a similar PB profile, as shown in the ToF-ERD results (Figures 4.33, B and 4.44, B). In the blend film containing 46.4 vol.% PS (M.W. 290 kg/mol) and 53.6 vol.% PB (M.W. 200 kg/mol), there is a segregation of PS at the substrate, followed by a layer rich in PB. This layer is depleted in PS because PS is preferentially segregating towards the substrate interface (see Figure 4.23, B).

A film containing 46.4 vol.% PS (M.W. 4 kg/mol) and 53.6 vol.% PB (M.W. 200 kg/mol), with a mostly PS surface layer, displayed cracks in both SEM results and optical microscope images (Figures 4.50 and Figure 4.52, C to E). This was attributed to the formation of a PS-rich phase during toluene evaporation while spin coating. As the toluene evaporated, the PS-rich phase transitioned to a glassy state, causing it to shrink. In contrast, the neighbouring PB-rich phases, which remained in a non-glassy state, did not shrink, resulting in the formation of cracks due to the different volume expansivities of the two layers.

5.3.3 Films with 77.6 vol.% PB

The blend films with a volume concentration of 77.6% PB display the lowest surface energy among all five different blends and their corresponding mass ratios, as illustrated by the red columns in Figure 5.3. Furthermore, the air interface of these films is covered 50-100% by PB, in contrast to the surface of films with other ratios (Figure 5.2).

Moreover, a film blend containing 77.6 vol.% PB of PS with a molecular weight of 4 kg/mol and PB with a molecular weight of 200 kg/mol exhibits significant roughness at the surface. This roughness is likely due to the 50% presence of PB at the surface, suggesting phase separation at this level (Figure 5.4).

5.4 Lamellar structured blend film

Researchers observed a well-defined lamellar structure caused by surface-driven phase separation in PS and PB blend thin films cast from toluene solution [14]. Another lamellar structure was observed in spin-cast thin films made from polyaniline (PANI) doped with camphorsulfonic acid (CSA) and polystyrene (PS) [15]. They found that PANI tended to segregate near the gold substrate, forming an enrichment layer at the substrate interface. In thinner films, this led to a single layer of PANI near the substrate, whereas thicker films showed multiple layers of altering enrichment and depletion. These authors proposed that substrate-directed phase separation drives the formation of these lamellar structures.

In this work, the lamellar structure in the blend films is hard to observe when there is a high concentration of PB. However, the segregation becomes more noticeable when the solution contains less PB. In this case, we can see a clear difference with a good amount of PB covering the surfaces and a smaller amount in the bulk. For instance, a blend film containing 72.2 vol.% PS (M.W. 290 kg/mol) and 27.8 vol.% PB (M.W. 3 kg/mol) exhibited a distinct lamellar structure (Figures 4.33, A and 4.38, B). Conversely, a blend film containing 22.4 vol.% PS (M.W. 4 kg/mol) and 77.6 vol.% PB (M.W. 200 kg/mol) showed a lateral phase-separated structure with no surface layer (Figure 4.44, C). This lateral phase-separated structure may be attributed to the drying time of the high molecular weight PB (M.W. 200 kg/mol) with a high mass ratio (77.6 vol.% PB) during the spin coating process.

5.5 Bicontinuous morphology

Prior research has concentrated on studying the structural changes in thin films of two polymers, PS and PMMA [119]. On the native silicon oxide surface, the film's phase transformation was influenced by the substrate-wetting of PMMA. In the case of the PS:PMMA blend ratio of 60:40, the initial morphology displayed dome-like PMMA domains. After annealing, PMMA formed a continuous wetting layer, while PS formed droplets on top of this layer. The morphology was influenced by capillary fluctuations, resulting in isolated PS droplets.

Films with a composition close to the critical composition may form bicontinuous structures, at least in bulk. Here, we are considering whether or not a bicontinuous structure has been observed.

Films consisting of a blend of PS (M.W.= 4 kg/mol) and PB (M.W.= 3 kg/mol) exhibit a critical composition at a PS volume fraction of 0.48 (refer to eq. 2.27 in 2.4), suggesting that one could expect a bicontinuous structure at this ratio. Looking at the optical images of films containing 46.4 vol% PS (M.W.= 4 kg/mol) and 53.6 vol.% PB (M.W.= 3 kg/mol) in Figure 4.11, A to C appear to show bicontinuous structures. It is worth noting that these optical images are likely to represent the layer near the surface of the films because of the significant topography observed with AFM (Figure 4.8), which is consistent with the optical images. They are likely to represent the exact surface because there is a very thin layer of PB at the surface based on the ToF-ERD result (Figure 4.5, B). Additionally, films composed of PS (M.W.= 55 kg/mol) and PB (M.W.= 53 kg/mol) have a critical composition at a PS volume fraction of 0.51. It is likely that the structure of films containing 46.4 vol.% PS (M.W.= 55 kg/mol) and 53.6 vol.% PB (M.W.= 53 kg/mol) in Figure 4.20, B, represents a bicontinuous structure. However, the thicker film containing 46.4 vol% PS (M.W.= 55 kg/mol) and 53.6 vol.% PB (M.W.= 53 kg/mol) shown in Figure 4.20, C, does not indicate a bicontinuous structure, potentially this might be due to a strongly segregated surface layer that contains the majority of the PB, resulting in less PB throughout the rest of the film, causing it to no longer appear continuous. The same discussion applies to the blend film of PS (M.W. 290 kg/mol) and PB (M.W. 200 kg/mol), which have a critical composition at a PS volume fraction of 0.47. A film containing 46.4 vol% PS (M.W.= 290 kg/mol) and 53.6 vol.% PB (M.W.= 200 kg/mol) in Figure 4.29, A showed a bicontinuous structure.

In the context of asymmetric blend films of PS (M.W.= 290 kg/mol) and PB (M.W.= 3 kg/mol), a critical composition is calculated at a PS volume fraction of 0.1. However, in Figures 4.41 C and D, the morphology appears to resemble a bicontinuous blend film consisting of 22.4 vol.% PS (M.W.= 290 kg/mol) and 77.6 vol.% PB (M.W.= 3 kg/mol). Also, Figures 4.41 C and D may show what can interrupt the structure as the cracking of a PS-rich phase after it has gone through the glass transition. As for the second asymmetric blend film of PS (M.W.= 4 kg/mol) and PB (M.W.= 200 kg/mol), which demonstrates a critical composition at a PS volume fraction of 0.88, there is no evidence within our observed mass ratios to suggest the presence of any bicontinuous structure.

Chapter 6. Summary and Future Work

6.1 Summary

Polystyrene and polybutadiene are widely used polymers with distinct mechanical and surface properties, making them valuable in various industrial applications. The blend films of these immiscible polymers have attracted considerable interest for their potential in coatings, nanotechnology, and diverse material science applications. The structure and surface energy of PS and PB blend films play essential roles in influencing their behaviour in applications, including wetting, adhesion, and chemical resistance. This thesis has presented the surface energy as a function of the thickness of five different polystyrene and polybutadiene spin-coated blend films. The blends included three symmetric blends: PS (M.W. = 4 kg/mol) and PB (M.W. = 3 kg/mol); PS (M.W. = 50 kg/mol) and PB (M.W. = 53 kg/mol); PS (M.W. = 290 kg/mol) and PB (M.W. = 200 kg/mol); and two asymmetric blends: PS (M.W. = 290 kg/mol) and PB (M.W. = 3 kg/mol); and PS (M.W. = 4 kg/mol) and PB (M.W. = 200 kg/mol). The measurements were taken at polymer mass ratios (PS:PB) of 0:1, 1:3, 1:1, 3:1, and 1:0. Contact angles of water and glycerol on thin films were analysed as a function of polymer concentration at room temperature. The contact angles of water and glycerol revealed nearly identical surface energies, confirming the reliability of the measurements. The surface energy decreases as the film thickness increases, but the relationship with concentration was inconsistent. Generally, blend film surfaces showed more hydrophobic surfaces than those of the individual homopolymers.

Moreover, in terms of structural behaviour, the study investigated the impact of changing the polymer's molecular weight and changes in polymer concentration on the surface energy and final morphology. PS and PB films displayed different morphologies. The results have been presented and compared with the contact angle measurements. The depth profile of polybutadiene for all different ratios of the blend thin films under investigation was obtained and discussed. Surface segregation phenomena, bicontinuous structure and well-defined lamellar structures have been explained, and their properties were discussed. We have explained these morphologies based on the spin coating conditions, such as polymer solubility, polymer evaporation time, or the effect of polymer chain ends. The films showed significant roughness, particularly in the blends, indicating significant phase separation, confirmed through atomic force microscopy.

6.2 Future Work

6.2.1 Ageing and Environmental Effects

Understanding how ageing and environmental factors impact the performance of PS and PB films is crucial for designing them to withstand long-term use in various applications. Over time, these films have been exposed to environmental elements such as humidity, ultraviolet (UV) light, and temperature fluctuations, which have affected their structural and surface properties.

For instance, PS, being more rigid and less flexible, tends to degrade under UV light as the exposure can break the polymer chains, leading to a loss of mechanical strength, yellowing, and changes in surface energy. On the other hand, PB, with its unsaturated carbon-carbon double bonds, is particularly prone to oxidation and chain breakage when exposed to UV light, air, or heat, resulting in reduced mechanical performance and altered elasticity. Additionally, ageing may increase surface roughness and alter the film's surface energy and wettability.

Therefore, it is important to focus on enhancing the longevity and stability of PS and PB films, especially in predicting their behaviour in applications subject to environmental fluctuations over extended periods, such as outdoor coatings and packaging.

6.2.2 Multilayered Thin Films

The study of multilayer PS and PB blend films presents a promising engineering approach. These films possess adjustable surface energy, as well as mechanical and physical properties. By designing multilayered films with alternating layers of PS and PB, it becomes possible to create distinct regions with varying energies, stiffness, and barrier properties. This approach is essential for applications that demand gradient properties, such as barrier coatings, functional surfaces, and protective films [120], [121].

The interaction between PS and PB layers at the interfaces in multilayered structures is significant due to the immiscibility of PS and PB and the formation of either sharp or diffused interfaces, both of which impact the film's performance. By controlling the thickness of each layer and the number of these interfaces, it becomes possible to adjust the final film morphology and surface properties. For instance, thicker PS layers can contribute to a more rigid structure with a higher glass transition temperature, while thinner PB layers can enhance flexibility.

Multilayered thin films have diverse applications, such as in hydrophobic coatings, where the PB surface layer can be customised for low surface energy to enhance water repellency. In contrast, the PS bulk layer provides structural support. Additionally, alternating PS and PB layers could enhance resistance to gas permeation by slowing the diffusion of gases through the film, thereby creating a more effective barrier. The order and thickness of the layers can also be adjusted to achieve specific optical properties, such as anti-reflective or reflective coatings.

6.2.3 Conclusion

The investigation of polystyrene and polybutadiene thin films has demonstrated their highly adjustable structural and surface properties, offering diverse applications in coatings, adhesives, and functional surfaces. By modifying parameters such as processing methods, blending ratios, or integrating functional polymers, the morphology, mechanical properties, and surface energy of these films can be tuned to meet specific needs.

An exploration of environmental and ageing effects is essential for enhancing the durability and dependability of these films in practical conditions. Moreover, multi-layered films enable precise control over gradient properties, making them valuable for protective coatings and barrier materials.

Continued examination of the interplay between structure, morphology, and surface energy in PS and PB thin films will yield deeper insights into polymer science and lead to the development of next-generation materials with highly customised properties for a wide range of industries.

References

[1] R. A. L. Jones and R. W. Richards, *Polymers at Surfaces and Interfaces*, 1st ed. New York: Cambridge University Press, 1999.

[2] S. Wu, *Polymer Interface and Adhesion*, 1st ed. New York: Marcel Dekker, Inc, 1982.

[3] M. Rubinstein and R. H. Colby, *Polymer Physics*. New York: Oxford University Press, 2003.

[4] L. C. Sawyer, D. T. Grubb, and G. F. Meyers, *Polymer Microscopy*, 3rd ed. Springer , 2008.

[5] G. R. Strobl, *The Physics of Polymers: Concepts for Understanding Their Structures and Behavior*, 3rd ed. Berlin: Springer, 2007.

[6] A. Kaştan and Ş. Talaş, "Abrasive wear behaviour of SBR/HIPS (%35–55) polymer blends," *Mater. Res. Express*, vol. 6, no. 10, p. 105353, 2019.

[7] M. Geoghegan and G. Krausch, "Wetting at polymer surfaces and interfaces," *Prog. Polym. Sci.*, vol. 28, no. 2, pp. 261–302, 2003.

[8] S. Y. Heriot and R. A. L. Jones, "An interfacial instability in a transient wetting layer leads to lateral phase separation in thin spin-cast polymer-blend films," *Nat. Mater.*, vol. 4, no. 10, pp. 782–786, 2005.

[9] P. Mokarian-Tabari, M. Geoghegan, J. R. Howse, S. Y. Heriot, R. L. Thompson, and R. A. L. Jones, "Quantitative evaluation of evaporation rate during spin-coating of polymer blend films: Control of film structure through defined-atmosphere solvent-casting," *Eur. Phys. J. E*, vol. 33, no. 4, pp. 283–289, 2010.

[10] S. Walheim, M. Böltau, J. Mlynek, G. Krausch, and U. Steiner, "Structure Formation via Polymer Demixing in Spin-Cast Films," *Macromolecules*, vol. 30, no. 17, pp. 4995–5003, 1997.

[11] S. Nilsson, A. Bernasik, A. Budkowski, and E. Moons, "Morphology and Phase Segregation of Spin-Casted Films of Polyfluorene/PCBM blends," *Macromolecules*, vol. 40, no. 23, pp. 8291–8301, 2007.

[12] H. Cai *et al.*, "Regulation of dewetting and morphology evolution in spin-coated PS/PMMA blend films via graphene-based Janus nanosheets," *Appl. Surf. Sci.*, vol. 630, p. 157393, Sep. 2023.

[13] T. Afzal *et al.*, “Tuning phase separation in DPPDTT/PMMA blend to achieve molecular self-assembly in the conducting polymer for organic field effect transistors,” *J. Chem. Phys.*, vol. 160, no. 3, Jan. 2024.

[14] M. Geoghegan, R. A. L. Jones, R. S. Payne, P. Sakellariou, A. S. Clough, and J. Penfold, “Lamellar structure in a thin polymer blend film,” *Polymer*, vol. 35, no. 10, pp. 2019–2027, 1994.

[15] A. Bernasik *et al.*, “Lamellar structures formed in spin-cast blends of insulating and conducting polymers,” *Synth. Met.*, vol. 144, no. 3, pp. 253–257, 2004.

[16] S. Kang, W.-G. Koh, and Y. K. Joung, “Enhancing surface segregation with cyclic polymer additives: A facile approach to surface modification,” *Eur. Polym. J.*, vol. 205, p. 112759, 2024.

[17] K. Dalnoki-Veress, J. A. Forrest, J. R. Stevens, and J. R. Dutcher, “Phase separation morphology of thin films of polystyrene/polyisoprene blends,” *J. Polym. Sci. Part B Polym. Phys.*, vol. 34, no. 17, pp. 3017–3024, 1996.

[18] D. A. Winesett, H. Ade, J. Sokolov, M. Rafailovich, and S. Zhu, “Substrate dependence of morphology in thin film polymer blends of polystyrene and poly (methyl methacrylate),” *Polym. Int.*, vol. 49, no. 5, pp. 458–462, 2000.

[19] J. Jaczewska *et al.*, “Humidity and Solvent Effects in Spin-Coated Polythiophene–Polystyrene Blends,” *J. Appl. Polym. Sci.*, vol. 105, no. 1, pp. 67–79, 2007.

[20] P. C. Jukes, S. Y. Heriot, J. S. Sharp, and R. A. L. Jones, “Time-Resolved Light Scattering Studies of Phase Separation in Thin Film Semiconducting Polymer Blends during Spin-Coating,” *Macromolecules*, vol. 38, no. 6, pp. 2030–2032, 2005.

[21] K. Dalnoki-Veress, J. A. Forrest, J. R. Stevens, and J. R. Dutcher, “Phase separation morphology of spin-coated polymer blend thin films,” *Elsevier Sci. Phys. A*, vol. 239, pp. 87–94, 1997.

[22] M. Geoghegan, R. A. L. Jones, A. S. Clough, and J. Penfold, “The Morphology of As-Cast Films of a Polymer Blend: Dependence on Polymer Molecular Weight,” *J. Polym. Sci. Part B Polym. Phys.*, vol. 33, no. 8, pp. 1307–1311, 1995.

[23] X. Li, Y. Han, and L. An, “Surface morphology control of immiscible polymer-blend thin films,” *Polymer*, vol. 44, no. 26, pp. 8155–8165, 2003.

[24] T. Kikuchi, M. Kudo, C. Jing, T. Tsukada, and M. Hozawa, “Electrohydrodynamic Effect on Phase Separation Morphology in Polymer Blend Films,” *Langmuir*, vol. 20, no. 4, pp. 1234–1238, 2004.

[25] P. Wang and J. T. Koberstein, “Morphology of Immiscible Polymer Blend Thin Films Prepared by Spin-Coating,” *Macromolecules*, vol. 37, no. 15, pp. 5671–5681, 2004.

[26] X. Li, Y. Han, and L. An, “Annealing effects on the surface morphologies of thin PS/PMMA blend films with different film thickness,” *Appl. Surf. Sci.*, vol. 230, no. 1–4, pp. 115–124, 2004.

[27] L. A. Utracki, P. Mukhopadhyay, and R. K. Gupta, “Polymer Blends: introduction,” in *Polymer Blends Handbook*, 2nd ed., L. A. Utracki and C. A. Wilkie, Eds. Dordrecht: Springer Netherlands, 2014, pp. 3–170.

[28] L. M. Robeson, “Fundamentals of Polymer Blends,” in *Polymer blends A Comprehensive review*, vol. 641, Hanser Gardner Pub Cincinnati, OH, 2007, pp. 11–23.

[29] M. Geoghegan and G. Hadziioannou, *Polymer electronics*, 1st ed. Oxford University Press, 2013.

[30] R. A. L. Jones, *Soft Condensed Matter*. Oxford University Press, 2002.

[31] E. Manias and L. A. Utracki, “Thermodynamics of polymer blends,” in *Polymer blends handbook*, 2nd ed., vol. 282, L.A. Utracki and C.A. Wilkie, Eds. Dordrecht: Springer Netherlands , 2014, pp. 171–289.

[32] H. B. Eitouni and N. P. Balsara, “Thermodynamics of Polymer Blends,” in *Physical Properties of Polymers Handbook*, 2nd ed., J. E. Mark, Ed. New York, NY: Springer New York, 2007, pp. 339–356.

[33] J. H. Wei, D. C. Coffey, and D. S. Ginger, “Nucleating pattern formation in spin-coated polymer blend films with nanoscale surface templates,” *J. Phys. Chem. B*, vol. 110, no. 48, pp. 24324–24330, 2006.

[34] D. Bonn and D. Ross, “Wetting transitions,” *Reports Prog. Phys.*, vol. 64, no. 9, pp. 1085–1163, 2001.

[35] H. Tavana, R. Gitiafroz, M. L. Hair, and A. W. Neumann, “Determination of solid surface tension from contact angles: The role of shape and size of liquid molecules,” *J. Adhes.*, vol. 80, no. 8, pp. 705–725, Aug. 2004.

[36] D. Y. Kwok and A. W. Neumann, “Contact angle measurement and contact angle interpretation,” *Adv. Colloid Interface Sci.*, vol. 81, no. 3, pp. 167–249, 1999.

[37] T. Young, “III. An essay on the cohesion of fluids,” *Philos. Trans. R. Soc. London*, vol. 95, pp. 65–87, 1805.

[38] D. K. Owens and R. C. Wendt, “Estimation of the Surface Free Energy of Polymers,” *J. Appl. Polym. Sci.*, vol. 13, no. 8, pp. 1741–1747, 1969.

[39] F. K. Hansen and G. Rødsrud, “Surface Tension by Pendant Drop: I. A Fast Standard Instrument Using Computer Image Analysis,” *J. Colloid Interface Sci.*, vol. 141, no. 1, pp. 1–9, 1991.

[40] J. D. Berry, M. J. Neeson, R. R. Dagastine, D. Y. C. Chan, and R. F. Tabor, “Measurement of surface and interfacial tension using pendant drop tensiometry,” *J. Colloid Interface Sci.*, vol. 454, pp. 226–237, 2015.

[41] R.-J. Roe, “Surface Tension of Polymer Liquids,” *J. Phys. Chem.*, vol. 72, no. 6, pp. 2013–2017, 1968.

[42] D. LI and A. W. Neumann, “Contact Angles on Hydrophobic Solid Surfaces and Their Interpretation,” *J. Colloid Interface Sci.*, vol. 148, no. 1, 1992.

[43] D. Y. Kwok, C. N. C. Lam, A. Li, K. Zhu, R. Wu, and A. W. Neumann, “Low-Rate Dynamic Contact Angles on Polystyrene and the Determination of Solid Surface Tensions,” *Polym. Eng. Sci.*, vol. 38, no. 10, pp. 1675–1684, 1998.

[44] D. Li and A. W. Neumann, “Contact Angles on Hydrophobic Solid Surfaces and Their Interpretation,” *J. Colloid Interface Sci.*, vol. 148, no. 1, pp. 190–200, 1992.

[45] H. Tavana, N. Petong, A. Hennig, K. Grundke, and A. W. Neumann, “Contact Angles and Coating Film Thickness,” *J. Adhes.*, vol. 81, no. 1, pp. 29–39, Jan. 2005.

[46] R. N. Shimizu and N. R. Demarquette, “Evaluation of Surface Energy of Solid Polymers Using Different Models,” *J. Appl. Polym. Sci.*, vol. 76, pp. 1831–1845, 2000.

[47] A. W. Neumann, R. David, and Y. Zuo, *Applied Surface Thermodynamics, Second Edition*. 2010.

[48] J. Spelt, *Applied Surface Thermodynamics*. Crc Press, 1996.

[49] L. M. Matuana, J. J. Balatinecz, and C. B. Park, “Effect of Surface Properties on

the Adhesion between PVC and Wood Veneer Laminates," *Polym. Eng. Sci.*, vol. 38, no. 5, pp. 765–773, 1998.

[50] J. Genzer and E. J. Kramer, "Pretransitional thinning of a polymer wetting layer," *Europhys. Lett.*, vol. 44, no. 2, p. 180, 1998.

[51] M. Geoghegan, H. Ermer, G. Jüngst, G. Krausch, and R. Brenn, "Wetting in a phase separating polymer blend film: quench depth dependence," *Phys. Rev. E*, vol. 62, no. 1, pp. 940–950, 2000.

[52] M. Geoghegan *et al.*, "Surface segregation from polystyrene networks," *J. Phys. Condens. Matter*, vol. 12, no. 24, pp. 5129–5142, 2000.

[53] M. Geoghegan, R. A. L. Jones, D. S. Sivia, J. Penfold, and A. S. Clough, "Experimental study of surface segregation and wetting in films of a partially miscible polymer blend," *Phys. Rev. E*, vol. 53, no. 1, pp. 825–837, 1996.

[54] L. Sung, A. Karim, J. F. Douglas, and C. C. Han, "Dimensional Crossover in the Phase Separation Kinetics of Thin Polymer Blend Films," *Phys. Rev. Lett.*, vol. 76, no. 23, pp. 4368–4371, 1996.

[55] G. Krausch, "Surface induced self assembly in thin polymer films," *Mater. Sci. Eng. R14*, vol. 14, no. 1, pp. 1–94, 1995.

[56] H. Wang and R. J. Composto, "Thin film polymer blends undergoing phase separation and wetting: Identification of early, intermediate, and late stages," *J. Chem. Phys.*, vol. 113, no. 22, pp. 10386–10397, 2000.

[57] M. Geoghegan, R. A. L. Jones, and A. S. Clough, "Surface directed spinodal decomposition in a partially miscible polymer blend," *J. Chem. Phys.*, vol. 103, no. 7, pp. 2719–2724, 1995.

[58] J. Rysz *et al.*, "Depth profiling studies of the surface directed phase decomposition in thin polymer films," *Vacuum*, vol. 54, pp. 303–307, 1999.

[59] S. Puri and H. L. Frisch, "Surface-directed spinodal decomposition: modelling and numerical simulations," *J. Phys. Condens. Matter*, vol. 9, no. 10, pp. 2109–2133, 1997.

[60] M. Geoghegan, T. Nicolai, J. Penfold, and R. A. L. Jones, "Kinetics of surface segregation and the approach to wetting in an isotopic polymer blend," *Macromolecules*, vol. 30, no. 14, pp. 4220–4227, 1997.

[61] R. A. L. Jones, L. J. Norton, E. J. Kramer, F. S. Bates, and P. Wiltzius, "Surface-

Directed Spinodal Decomposition," *Phys. Rev. Lett.*, vol. 66, no. 23, pp. 1326–1329, 1991.

[62] A. Karim, J. F. Douglas, L. P. Sung, and B. D. Ermi, "Self-assembly by phase separation in polymer thin films," *Encycl. Mater. Sci. Technol.*, p. 8319, 2002.

[63] J. Koo, S. Satija, J.-S. Lee, and Y.-S. Seo, "Spontaneous Bilayer Phase Separations of Spin-Coated Polymer BlendThinFilms: A Neutron Reflectivity Study," *Macromol. Res.*, vol. 24, no. 12, pp. 1105–1110, 2016.

[64] A. Budkowski, A. Bernasik, P. Cyganik, J. Rysz, and R. Brenn, "Surface-directed phase separation in nanometer polymer films: self-stratification and pattern replication," *e-Polymers*, vol. 2, no. 1, p. 005, 2002.

[65] A. M. Higgins *et al.*, "Surface segregation and self-stratification in blends of spin-cast polyfluorene derivatives," *J. Phys. Condens. Matter*, vol. 17, no. 8, pp. 1319–1328, 2005.

[66] A. J. Parnell *et al.*, "Depletion of PCBM at the Cathode interface in P3HT/PCBM Thin Films as Quantified via Neutron Reflectivity Measurements," *Adv. Mater.*, vol. 22, no. 22, pp. 2444–2447, 2010.

[67] C. M. Björström *et al.*, "Vertical phase separation in spin-coated films of a low bandgap polyfluorene/PCBM blend—Effects of specific substrate interaction," *Appl. Surf. Sci.*, vol. 253, no. 8, pp. 3906–3912, 2007.

[68] C. M. Björström *et al.*, "Multilayer formation in spin-coated thin films of low-bandgap polyfluorene: PCBM blends," *J. Phys. Condens. Matter*, vol. 17, no. 50, pp. L529–L534, 2005.

[69] E. Pavlopoulou, G. Fleury, D. Deribew, F. Cousin, M. Geoghegan, and G. Hadziioannou, "Phase separation-driven stratification in conventional and inverted P3HT: PCBM organic solar cells," *Org. Electron.*, vol. 14, no. 5, pp. 1249–1254, 2013.

[70] L. Hou *et al.*, "Lateral Phase Separation Gradients in Spin-coated Thin Films of High-Performance Polymer: Fullerene Photovoltaic Blends," *Adv. Funct. Mater.*, vol. 21, no. 16, pp. 3169–3175, 2011.

[71] S. Linde, A. Carella, and R. Shikler, "New Approach for Analyzing the Vertical Structure of Polymer Thin Films Based on Surface-Enhanced Raman Scattering," *Macromolecules*, vol. 45, no. 3, pp. 1476–1482, 2012.

[72] G. Lu *et al.*, “Moderate doping leads to high performance of semiconductor/insulator polymer blend transistors,” *Nat. Commun.*, vol. 4, no. 1, p. 1588, 2013.

[73] X. Ren, L.-T. Weng, C.-M. Chan, and K.-M. Ng, “Hollow Interior Structure of Spin-Coated Polymer Thin Films Revealed by ToF-SIMS Three-Dimensional Imaging,” *Anal. Chem.*, vol. 84, no. 20, pp. 8497–8504, 2012.

[74] G. H. Michler and S. Hennning, “Special Preparation Techniques,” in *Electron Microscopy of Polymers*, H. Pasch, Ed. Berlin, Heidelberg: Springer Berlin Heidelberg, 2008, pp. 219–230.

[75] A. R. Hall and M. Geoghegan, “Polymers and biopolymers at interfaces,” *Reports Prog. Phys.*, vol. 81, no. 3, 2018.

[76] R. Ramos-Hernández, E. Pérez-Gutiérrez, F. D. Calvo, M. F. Beristain, M. Cerón, and M. J. Percino, “Solvent Effect on Small-Molecule Thin Film Formation Deposited Using the Doctor Blade Technique,” *Coatings* , vol. 13, no. 2, p. 425, 2023.

[77] A. M. Schrand, “Polymer Sample Preparation for Electron Microscopy,” *Microsc. Microanal.*, vol. 11, no. S02, pp. 702–703, Aug. 2005.

[78] Y. Yuan and T. R. Lee, “Contact Angle and Wetting Properties,” in *Surface Science Techniques*, G. Bracco and B. Holst, Eds. Berlin, Heidelberg: Springer Berlin Heidelberg, 2013, pp. 3–34.

[79] G. Lamour *et al.*, “Contact Angle Measurements Using a Simplified Experimental Setup,” *J. Chem. Educ.*, vol. 87, no. 12, pp. 1403–1407, 2010.

[80] R. F. Egerton, *Physical Principles of Electron Microscopy*, vol. 56. Springer, 2005.

[81] D. B. Murphy, *Fundamentals of Light Microscopy and Electronic Imaging / Douglas B. Murphy*. Wiley-Liss, 2001.

[82] Z. Luo, *A Practical Guide to Transmission Electron Microscopy*, 1st ed., vol. 2. Momentum Press, 2016.

[83] D. W. Grainger and D. G. Castner, “3.1 Surface Analysis and Biointerfaces: Vacuum and Ambient In Situ Techniques,” in *Comprehensive Biomaterials II*, vol. 3, P. Ducheyne, Ed. Oxford: Elsevier, 2017, pp. 1–24.

[84] H. Fujiwara, *Spectroscopic ellipsometry : principles and applications*.

Chichester, England ; Hoboken, NJ: John Wiley & Sons, 2007.

[85] H. Wang and P. K. Chu, “Surface Characterization of Biomaterials,” in *Characterization of Biomaterials*, A. Bandyopadhyay and S. Bose, Eds. Elsevier, 2013.

[86] D. Gonçalves and E. A. Irene, “Fundamentals and applications of spectroscopic ellipsometry,” *Quim. Nova*, vol. 25, no. 5, pp. 794–800, 2002.

[87] G. H. Michler and R. Godehardt, “Atomic Force Microscopy (AFM),” in *Electron Microscopy of Polymers*, H. Pasch, Ed. Berlin, Heidelberg: Springer Berlin Heidelberg, 2008, pp. 121–144.

[88] H. Schönherr, “Imaging Polymer Morphology using Atomic Force Microscopy,” in *Polymer Morphology: Principles, Characterization, and Processing*, 1st ed., Q. Guo, Ed. Hoboken, New Jersey: John Way & Sons, 2016, pp. 100–117.

[89] P. Agarwal and M. V Salapaka, “Control and Systems Approaches to Atomic Force Microscopy,” *IFAC Proc. Vol.*, vol. 41, no. 2, pp. 10456–10467, 2008.

[90] G. Alberti and G. Nuzzaci, “1.6.5 SEM and TEM techniques,” in *World Crop Pests*, vol. 6, E. E. Lindquist, M. W. Sabelis, and J. Bruin, Eds. Elsevier Science, 1996, pp. 399–410.

[91] P. W. Atkins and J. De Paula, “Processes on solid surfaces,” in *Atkins’ Physical Chemistry*, 10th ed., Oxford university press, 2014, pp. 937–959.

[92] G. H. Michler and R. Godehardt, “Transmission Electron Microscopy: Fundamentals of Methods and instrumentation,” in *Electron Microscopy of Polymers*, H. Pasch, Ed. Berlin, Heidelberg: Springer Berlin Heidelberg, 2008, pp. 15–50.

[93] L. Reimer and H. Kohl, “1.1 Transmission Electron Microscopy,” in *Transmission Electron Microscopy Physics of mage Formation*, 5th ed., vol. 36, W. T. Rhodes, Ed. Springer , 2008, pp. 1–3.

[94] T. Oku, “1.1 Characteristic of Electron Microscopy,” in *Structure Analysis of Advanced Nanomaterials - Nanoworld by High-Resolution Electron Microscopy*, De Gruyter, 2014, pp. 1–7.

[95] G. H. Michler and W. Lebek, “Electron Microscopy of Polymers,” in *Polymer Morphology: Principles, Characterization, and Processing*, 1st ed., Q. Guo, Ed. Hoboken, New Jersey: John Wiley & Sons, 2016, pp. 37–53.

[96] M. Kunz and K. Shull, “Improved technique for cross-sectional imaging of thin polymer films by transmission electron microscopy,” *Polymer*, vol. 34, no. 11, pp. 2427–2430, 1993.

[97] J. F. Moulder, W. F. Stickle, P. E. Sobol, and K. D. Bomben, *Handbook of X-ray Photoelectron Spectroscopy*. Perkin-Elmer Corporation, 1992.

[98] S. Hofmann, *Auger-and X-ray Photoelectron Spectroscopy in Materials Science: a User-Oriented Guide*, vol. 49. Springer Science & Business Media, 2012.

[99] J. F. Watts and J. Wolstenholme, *An Introduction to Surface Analysis by XPS and AES*. John Wiley & Sons, 2019.

[100] C. Jeynes and J. L. Colaux, “Thin film depth profiling by ion beam analysis,” *Analyst*, vol. 141, no. 21, pp. 5944–5985, 2016.

[101] J. Perrière, “Rutherford backscattering spectrometry,” *Vacuum*, vol. 37, no. 5–6, pp. 429–432, 1987.

[102] W. K. Chu, J. W. Mayer, M.-A. Nicolet, T. M. Buck, G. Amsel, and F. Eisen, “Principles and applications of ion beam techniques for the analysis of solids and thin films,” *Thin Solid Films*, vol. 17, no. 1, pp. 1–41, 1973.

[103] H. J. Whitlow, P. Jeanneret, E. Guibert, L. Wang, and M. Van Der Meer, “Time detector design for Time-of-Flight Elastic Recoil Detection Analysis (ToF-E ERDA),” *Nucl. Instruments Methods Phys. Res. Sect. B Beam Interact. with Mater. Atoms*, vol. 450, pp. 385–389, Jul. 2019.

[104] C. McAleese *et al.*, “Physics & Applications of the new TOF-ERD System Installed at Surrey Ion Beam Centre.” Zenodo, Jun-2022.

[105] J. Julin and T. Sajavaara, “Conceptual study of a heavy-ion-ERDA spectrometer for energies below 6 MeV,” *Nucl. Instruments Methods Phys. Res. Sect. B Beam Interact. with Mater. Atoms*, vol. 406, pp. 61–65, 2017.

[106] Y. Shi *et al.*, “Characterization of solar cell passivating contacts using time-of-flight elastic recoil detection analysis,” *Appl. Phys. Lett.*, vol. 123, no. 26, 2023.

[107] G. G. Politano and C. Versace, “Variable Angle Spectroscopic Ellipsometry Characterization of DMOAP-Functionalized Graphene Oxide Films,” *Coatings*, vol. 13, no. 12, p. 2066, 2023.

[108] G. H. Michler, “Problems Associated with the Electron Microscopy of Polymers,” in *Electron Microscopy of Polymers*, H. Pasch, Ed. Berlin, Heidelberg: Springer

Berlin Heidelberg, 2008, pp. 175–183.

[109] S. M. Park, S. H. Yun, and B. H. Sohn, “Variations of the Lamellar Period in Thin Films of Diblock Copolymers by Selective Staining Agents,” *Macromol. Chem. Phys.*, vol. 203, no. 14, pp. 2069–2074, 2002.

[110] L. Staniewicz, A. M. Donald, and D. J. Stokes, “The effect of osmium staining on lamellar spacing in thin polystyrene-polyisoprene diblock copolymer films,” *J. Phys. Conf. Ser. 241 012077*, pp. 1–4, Jul. 2010.

[111] H. A. Davies, “General Preparation of Material and Staining of Sections,” in *Electron Microscopy Methods and Protocols*, vol. 117, M. A. N. Hajibagheri, Ed. Totowa, New Jersy: Humana Press, 1999, pp. 1–11.

[112] K. M. Ashley, D. Raghavan, J. F. Douglas, and A. Karim, “Wetting-DewettingTransition Line in Thin Polymer Films,” *Langmuir*, vol. 21, no. 21, pp. 9518–9523, 2005.

[113] A. C. Balazs, T. Emrick, and T. P. Russell, “Nanoparticle polymer composites: where two small worlds meet,” *Science (80-.).*, vol. 314, no. 5802, pp. 1107–1110, 2006.

[114] J. Bico, C. Marzolin, and D. Quéré, “Pearl drops,” *Europhys. Lett.*, vol. 47, no. 2, pp. 220–226, 1999.

[115] Y. Li, J. Q. Pham, K. P. Johnston, and P. F. Green, “Contact Angle of Water on Polystyrene Thin Films: Effects of CO2 Environment and Film Thickness,” *Langmuir*, vol. 23, no. 19, pp. 9785–9793, 2007.

[116] D. G. Legrand and G. L. Gaines, “The Molecular Weight Dependence of Polymer Surface Tension,” *J. Colloid Interface Sci.*, vol. 31, no. 2, pp. 162–167, 1969.

[117] J. Wang, Y. Wu, Y. Cao, G. Li, and Y. Liao, “Influence of surface roughness on contact angle hysteresis and spreading work,” *Colloid Polym. Sci.*, vol. 298, no. 8, pp. 1107–1112, 2020.

[118] T. Liu, R. Ozisik, and R. W. Siegel, “Phase separation and surface morphology of spin-coated films of polyetherimide/polycaprolactone immiscible polymer blends,” *Thin Solid Films*, vol. 515, no. 5, pp. 2965–2973, Jan. 2007.

[119] D. U. Ahn, Z. Wang, I. P. Campbell, M. P. Stoykovich, and Y. Ding, “Morphological evolution of thin PS/PMMA films: Effects of surface energy and blend composition,” *Polymer*, vol. 53, no. 19, pp. 4187–4194, 2012.

[120] D. Langhe and M. Ponting, *Manufacturing and Novel Applications of Multilayer Polymer Films*. William Andrew is an imprrint of Elsevier, 2016.

[121] A. R. Ajitha, M. K. Aswathi, H. J. Maria, J. Izdebska, and S. Thomas, “Multilayer Polymer Films,” in *Multicomponent Polymeric Materials*, J. K. Kim, S. Thomas, and P. Saha, Eds. Springer, 2016, pp. 229–258.

Appendix

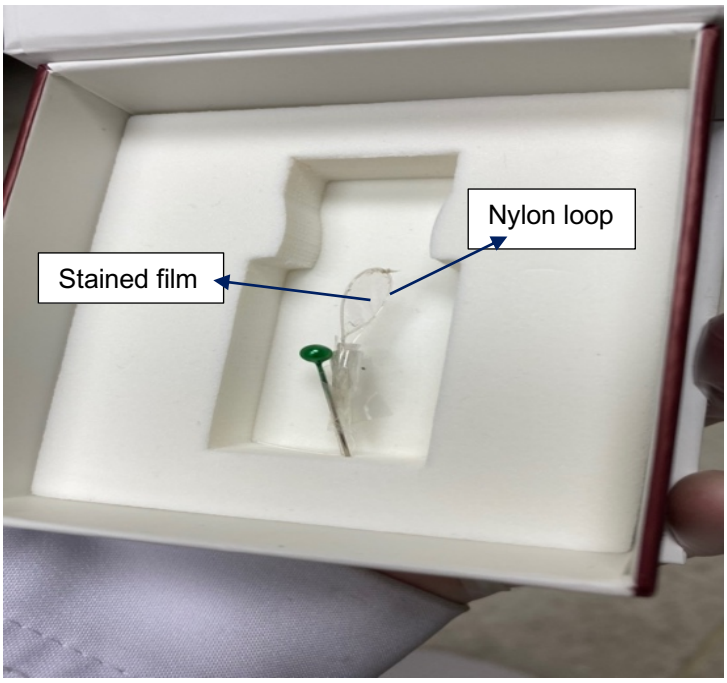

Figure A.1 An image of a stained film containing 72.2 vol.% PS (M.W. 290 kg/mol) and 27.8 vol.% PB (M.W. 3 kg/mol). The film was floated on distilled water and

To test the staining and its effect, staining for four different blends of thin films was done for 10, 20 and 30 minutes each (Table A.7). The optical images of the films were taken before and after staining. These images were used to obtain information on the structure length scale using a fast Fourier transform (FFT) analysis (see Figure A.2). The radial intensity distribution from the FFT was obtained to determine the length scale inherent in the film structure (Figure A.3).

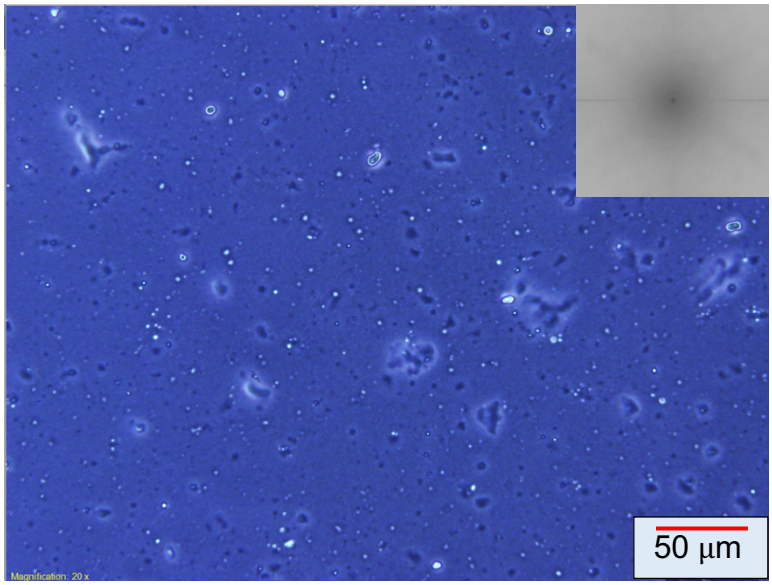

Figure A.2 An optical micrograph of unstained film containing 14.3 wt.% PS (M.W. 48 kg/mol) and 85.7 wt.% PB (M.W. 572 kg/mol), and its FFT (Film No. 1 in Table A.1). The scale bar is 50 µm.

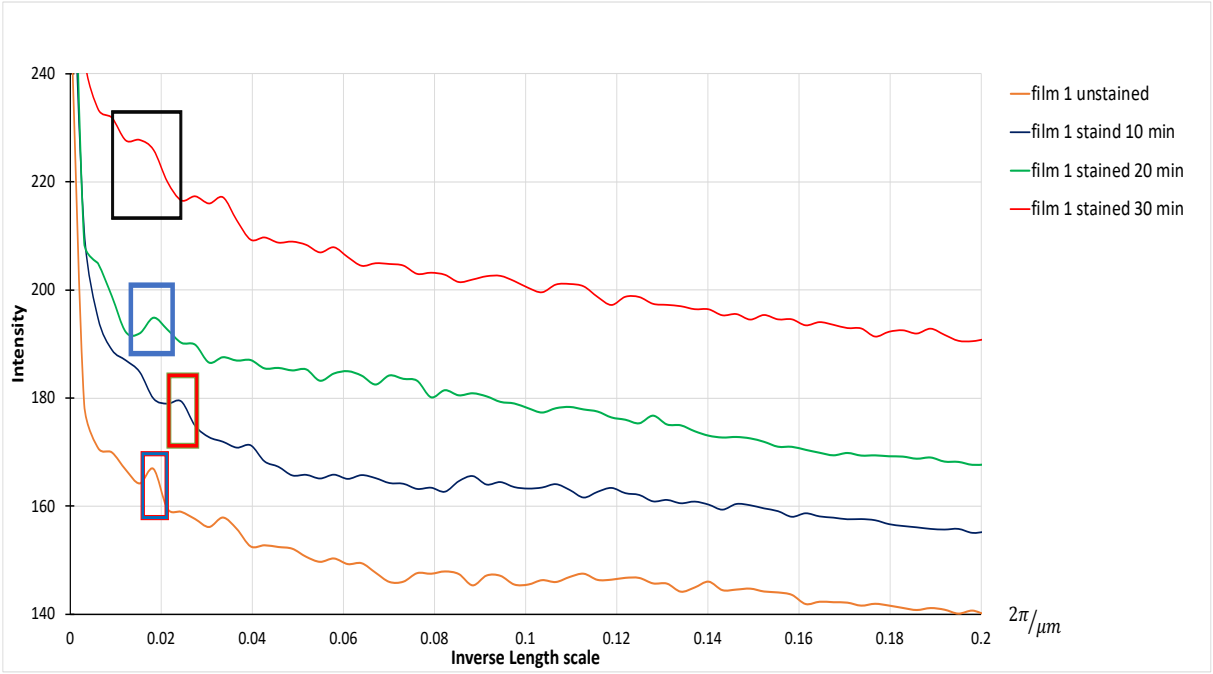

Figure A.3 The average radial distribution for staining Film No.1 (in Table A.1) as a function of time. Note that the plots are staggered by 20 counts for clarity. The unstained film has not been adjusted.

Film No.	Weight fraction	Polymer	Product No.	M_w (kg/mol)	M_n (kg/mol)	M_w/M_n	Weight of the Polymers
1	3.50%	PS	330345	48.1	47.5	1.01	14.3 %
		PB	P18646-Bd	572	543	1.05	85.7 %
Length scale in microns			Unstained			8.71	
			10 min stained			6.53	
			20 min stained			7.46	
			30 min stained			8.71	
Film No.	**Weight fraction**	**Polymer**	**Product No.**	**M_w** (kg/mol)	**M_n** (kg/mol)	**M_w/M_n**	**Weight of the Polymers**
2	3.50%	PS	327727	4.13	4.11	1.01	14.3 %
		PB	P2481-Bd	53.0	50.0	1.06	85.7 %
Length scale in microns			Unstained			6.53	
			10 min stained			10.45	
			20 min stained			5.80	
			30 min stained			6.53	
Film No.	**Weight fraction**	**Polymer**	**Product No.**	**M_w** (kg/mol)	**M_n** (kg/mol)	**M_w/M_n**	**Weight of the Polymers**
3	3.75%	PS	330345	48.1	47.5	1.01	16.7 %
		PB	P18646-Bd	572	543	1.05	83.3 %
Length scale in microns			Unstained			5.22	
			10 min stained			8.71	
			20 min stained			5.22	
			30 min stained			10.45	
Film No.	**Weight fraction**	**Polymer**	**Product No.**	**M_w** (kg/mol)	**M_n** (kg/mol)	**M_w/M_n**	**Weight % of the Polymers**
4	3.75%	PS	327727	4.13	4.11	1.01	16.7 %
		PB	P18646-Bd	572	543	1.05	83.3 %
Length scale in microns			Unstained			5.80	
			10 min stained			7.46	
			20 min stained			5.80	
			30 min stained			6.53	

Table A.1 Specification of PS and PB in each film was used to investigate whether the staining duration is not damaging the films.

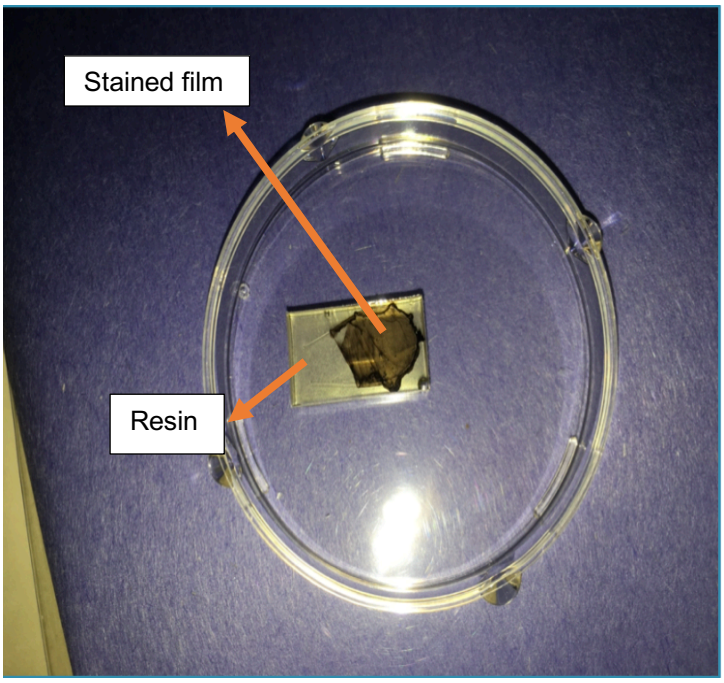

Figure A.4 An image of a stained film with 14.8 vol.% PS (M.W. 48.1 kg/mol) and 85.2 vol.% PB (M.W. 572.1 kg/mol). The film was embedded into LR white medium acrylic resin, pipetted into a mold hole, and then cured.

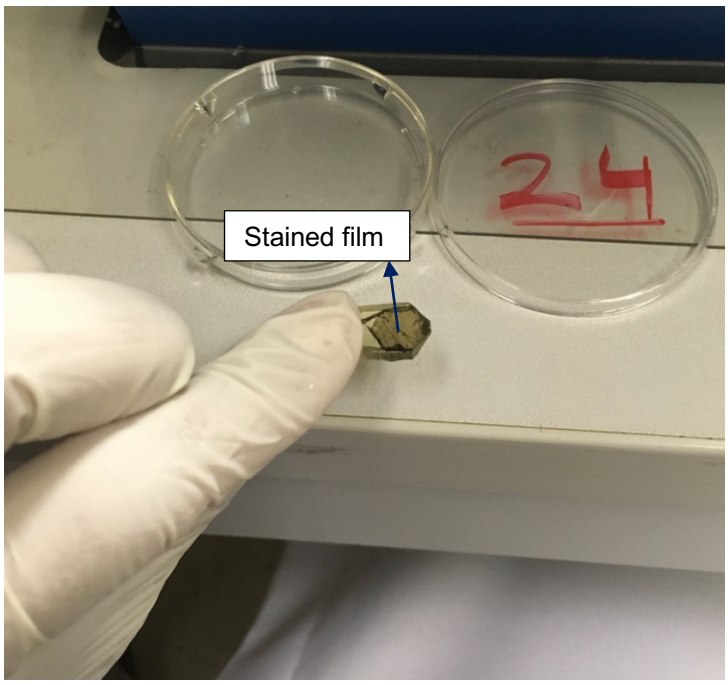

Figure A.5 An image of the film in Figure A.4 after trimming the excess resin from the block face and the edges of the block using a single-edged razor blade.